Silesian University of Technology

Augustine Nana Sekyi Appiah, MPhil.

Deformation-Induced Size Effects on the Structure and Mechanical Properties of Heterogenous L-PBF Fabricated AlSi10Mg Alloys

PhD dissertation

Supervisor:

Marcin Adamiak, PhD, DSc Eng.

Co-supervisor:

Przemysław Snopiński, PhD Eng.

Gliwice, 2025

Acknowledgments

First and foremost, I would like to express my deepest gratitude to my supervisors, Prof. Marcin Adamiak and Dr. Przemysław Snopiński, for their exceptional guidance, support, and encouragement throughout the course of this research. Their expertise, insightful feedback, and unwavering patience have been invaluable to both my academic development and the successful completion of this thesis.

I am also immensely thankful to my family for their unconditional love and support, even across distances. Their belief in my abilities and constant encouragement have been a source of strength during the most challenging moments of this journey. To my friends, both near and far, thank you for the laughter, the check-ins, and the thoughtful distractions that helped me maintain balance and perspective.

Completing this thesis would not have been possible without the collective influence and support of all these incredible individuals. I am sincerely grateful.

This research received financial support from the National Science Center (NCN), Poland, project number 2021/43/D/ST8/01946 "Toward obtaining strength-ductility synergy: Novel Generation of Heterostructured Nanostructured Al-Si alloys - Investigation of Microstructure, Mechanical Properties, and Deformation Mechanisms"

Abstract

Additive manufacturing (AM) of AlSi10Mg via laser-based powder bed fusion of metals (PBF-LB/M) produces a unique hierarchical microstructure characterized by a fine, interconnected network of eutectic Si within an α-Al matrix. While this cellular architecture imparts high strength, its inherent brittleness severely limits ductility, creating a fundamental trade-off that constrains its use in demanding structural applications. This thesis presents a systematic investigation into overcoming this limitation through a multi-stage thermomechanical processing strategy designed to tailor microstructural heterogeneity and control deformation mechanisms. The research methodology integrates advanced manufacturing with targeted post-processing. PBF-LB/M was used to fabricate AlSi10Mg samples, which were then subjected to low-temperature annealing (LTA) protocols (280 °C for 9 mins and 300 °C for 30 mins) to create three distinct initial states: one with a continuous Si network (As-built), one with a partially ruptured network (LTA_280), and one with a fragmented and spheroidized Si particulate structure (LTA_300). These conditioned samples were then subjected to both gradual uniaxial compression and severe plastic deformation (SPD) via Equal Channel Angular Pressing (ECAP) and Twist Channel Angular Pressing (TCAP) at various temperatures and passes. A comprehensive multi-scale characterization suite, including LOM, SEM, EDS, EBSD, TEM, XRD, and mechanical testing (uniaxial, hardness, and cyclic loading-unloading-reloading), was employed to correlate processing, microstructure, and properties. The results demonstrate that the continuity of the Si network is the dominant factor governing the alloy's mechanical response. The continuous network in the as-built condition promotes high initial strain hardening and significant kinematic hardening (back stress up to ~351 MPa post-ECAP), driven by the generation of geometrically necessary dislocations (GNDs) to accommodate strain gradients at the Al/Si interface. However, this same network acts as a conduit for premature fracture. The LTA_300 treatment was identified as a critical pre-conditioning step; by fragmenting the brittle network, it sacrifices some initial strength but unlocks exceptional ductility (failure strain increasing from 35.1% to 47.2%) by enabling more homogeneous deformation and extensive storage of statistically stored dislocations (SSDs), reaching densities of $1.48 \times 10^{14}\ m^{-2}$ at fracture. Applying SPD to the ductile LTA_300 pre-conditioned material proved to be a promising key to achieving superior properties. In contrast, SPD processing of the

as-built material led to embrittlement. High-temperature ECAP ($\geq 350°C$) was found to be detrimental, causing substantial softening due to Si particle coarsening and dynamic recovery. This work establishes a clear, mechanism-based framework for designing high-performance AM alloys. It demonstrates that by strategically pre-conditioning the brittle reinforcing phase before applying severe plastic deformation, it is possible to leverage the full potential of grain boundary and dislocation strengthening to overcome the paradoxical strength-ductility trade-off. These findings provide a validated pathway to produce lightweight, damage-tolerant aluminum components for advanced aerospace and automotive applications.

Streszczenie

Stop AlSi10Mg wytwarzany przyrostowo metodą PBF-LB/M charakteryzuje się hierarchiczną mikrostrukturą, składającą się z sieci eutektycznego krzemu (Si) w osnowie α-Al. Taka budowa, choć zapewnia wysoką wytrzymałość, prowadzi do niskiej ciągliwości. Ten konflikt między wytrzymałością, a plastycznością, stanowi barierę w zaawansowanych zastosowaniach konstrukcyjnych. W niniejszej pracy podjęto próbę przełamania tego ograniczenia poprzez wieloetapową obróbkę termomechaniczną, której celem była świadoma modyfikacja morfologii mikrostruktury komórkowej. Materiałem wyjściowym były próbki stopu AlSi10Mg w stanie po wydruku (*as-built*), które następnie poddano dwóm wariantom wyżarzania niskotemperaturowego (LTA): 280°C/9 min oraz 300°C/30 min. Uzyskano w ten sposób trzy stany mikrostrukturalne: z ciągłą siecią Si (a*s-built*), z częściowo przerwaną siecią Si (*LTA_280*) oraz ze sferoidalnymi, rozdrobnionymi wydzieleniami Si (*LTA_300*). Tak przygotowane próbki poddano następnie intensywnemu odkształceniu plastycznemu metodą przeciskania przez kanał kątowy ECAP/TCAP. Ewolucję mikrostruktury zbadano wykorzystując zaawansowane techniki takie jak: LOM, SEM, EDS, EBSD, TEM, XRD, natomiast własności mechaniczne określono w badaniach twardości i próbach jednoosiowego ściskania. Wykazano, że kluczowym czynnikiem determinującym odpowiedź mechaniczną stopu jest ciągłość sieci Si. W stanie wyjściowym (a*s-built)* sprzyja ona generowaniu dyslokacji geometrycznie niezbędnych (GND) i silnemu umocnieniu kinematycznemu (naprężenie wsteczne do ~351 MPa po ECAP). W pracy wykazano również, że modyfikacja morfologii sieci Si, a w szczególności przerwanie jej ciągłości i sferoidyzacja, aktywuje nowe mechanizmy poślizgu dyslokacji. Zamiast kumulować się na granicy międzyfazowej Al/Si, dyslokacje napotykające na dyskretne cząstki krzemu są zmuszone do ich omijania zgodnie z mechanizmem Orowana. Prowadzi to do pozostawiania pętli dyslokacyjnych wokół cząstek i odmiennego charakteru umocnienia odkształceniowego. Wyniki badań dowodzą, że odpowiednie przygotowanie mikrostruktury, a w szczególności modyfikacja morfologii kruchej fazy wzmacniającej przed intensywnym odkształceniem plastycznym, stanowi skuteczną strategię przełamania fundamentalnego konfliktu między wytrzymałością, a plastycznością w stopach Al-Si. Opracowana, dwuetapowa ścieżka procesowa (LTA + SPD)

otwiera perspektywy wytwarzania lekkich i wytrzymałych komponentów dla zaawansowanych zastosowań w przemyśle lotniczym i motoryzacyjnym.

Table of Contents

List of Abbreviations

AM	Additive Manufacturing
BF	Bright-Field
CT	Computed Tomography
DDW	Dense Dislocation Wall
DF	Dark-Field
DMLS	Direct Metal Laser Sintering
DRX	Dynamic Recrystallization
EBM	Electron Beam Melting
EBSD	Electron Backscatter Diffraction
ECAP	Equal Channel Angular Pressing
EDS	Energy Dispersive X-ray Spectroscopy
FFT	Fast Fourier Transform
FIB	Focused Ion Beam
GNDs	Geometrically Necessary Dislocations
HAADF	High-Angle Annular Dark-Field
HAGBs	High-Angle Grain Boundaries
HAZ	Heat-Affected Zone
HPT	High Pressure Torsion
HRTEM	High-Resolution Transmission Electron Microscopy
IPF-Z	Inverse Pole Figure (in the Z direction)
KAM	Kernel Average Misorientation
LAGBs	Low-Angle Grain Boundaries
LOF	Lack of Fusion
LOM	Light Optical Microscopy
LTA	Low-Temperature Annealing

LUR	Loading-Unloading-Reloading
MP	Melt Pool
MPB	Melt Pool Boundary
NC	Nanocrystalline
PBF-LB/M	Powder Bed Fusion - Laser Beam / Metal
SAED	Selected Area Electron Diffraction
SEM	Scanning Electron Microscopy
SLA	Stereolithography
SLM	Selective Laser Melting
SPD	Severe Plastic Deformation
SSDs	Statistically Stored Dislocations
STEM	Scanning Transmission Electron Microscopy
TCAP	Twist Channel Angular Pressing
TEM	Transmission Electron Microscopy
UCS	Ultimate Compressive Strength
UFG	Ultrafine-Grained
XRD	X-Ray Diffraction
YS	Yield Strength

Chapter One

1.0 Introduction

1.1 Background

The transportation industry has undergone substantial technological evolution in recent decades, emerging as a major contributor to climate change due to escalating carbon emissions [1]. While policy initiatives and economic incentives have accelerated engineering innovations, existing solutions fall short of achieving comprehensive sustainability targets. Among mitigation strategies, structural optimization of vehicles – particularly through advanced material selection – offers substantial potential to enhance energy efficiency and minimize environmental impact. Lightweighting, which replaces conventional steel with low-density alternatives such as aluminum alloys, remains a well-documented method for curbing emissions. Empirical studies indicate a linear relationship between mass reduction and fuel savings, with roughly 0.5 L of fuel conserved per 100 km for every 100 kg of weight reduction [2]. Nevertheless, practical implementation is constrained by conflicting performance requirements – demanding concurrent high strength and ductility – alongside the inherent property limitations of conventional aluminum alloys. Furthermore, multi-material assemblies often introduce recycling complications at end-of-life stages. These challenges have motivated materials science research toward heterostructured metallic systems.

Heterostructured materials, characterized by deliberately engineered microstructural gradients, have gained prominence due to their exceptional mechanical performance and enhanced strain-hardening capabilities. These materials exhibit a bimodal distribution of "soft" (coarse-grained, CG) and "hard" (ultrafine-grained, UFG, $d < 1$ μm) domains, where flow stress disparities can exceed 100% [3]. Common architectural configurations include lamellar [4], [5], graded [6], and core-shell (harmonic) [7] geometries. The superior properties of heterostructured metals arise from synergistic interactions between microstructural heterogeneities, mediated by back stress hardening, geometrically necessary dislocations (GNDs), and evolving dislocation substructures [8]. Under deformation, strain partitioning between domains generates plastic incompatibility, necessitating GND accumulation (**Figure 1**). These dislocations act as barriers to conventional dislocation motion, simultaneously elevating strength and sustaining strain-hardening rates [8].

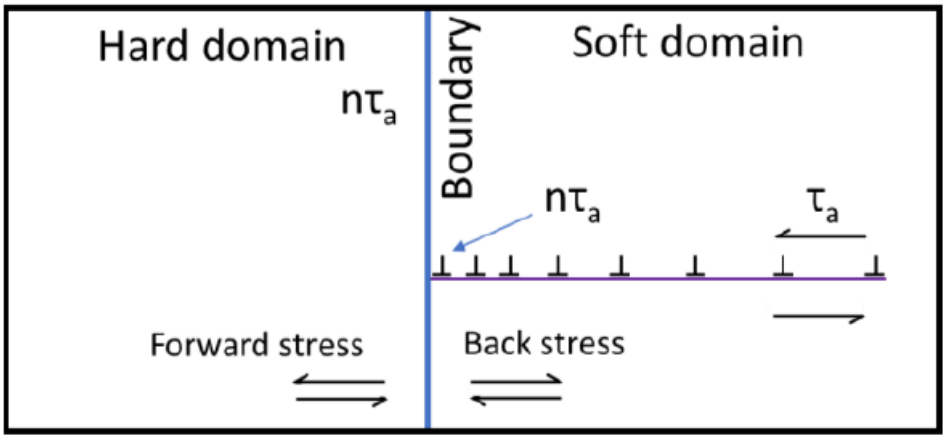

Figure 1. Schematics of a GND pile-up, inducing back stress in the soft domain, which in turn induces forward stress in the hard domain Adapted from [9].

Additive manufacturing (AM) techniques, with specific emphasis on laser-based powder fusion of metals or powder bed fusion – laser beam/metal (PBF-LB/M), present compelling ecological and resource optimization benefits when fabricating lightweight heterostructured alloys. Yet, the formation of heterogeneous microstructures remains limited to select additively manufactured lightweight materials, primarily observed in magnesium alloys AZ61 and AZ91[10], [11], and aluminum-silicon compositions containing 4-16% Si [12], [13], [14]. Determining the most suitable PBF-LB/M materials requires evaluation across multiple parameters: distinctive microstructural characteristics, interface concentration between domains, mechanical property differentials between hard and soft regions, and spatial configuration of these domains. While both PBF-LB/M processed AZ61/AZ91 and Al-Si systems demonstrate potential for weight-critical automotive and aerospace applications, their fundamental properties diverge significantly. The magnesium-based alloys (AZ61/AZ91) exhibit a relatively modest strength differential of approximately 0.235 GPa between the softer α-Mg and harder β-Mg17Al12 phases [15]. By contrast, the Al-Si system develops high-density cellular architectures (comprising 21-35% of the microstructure, depending on precise chemical formulation) characterized by Si-enriched cell boundaries surrounding Al-rich cellular interiors [16], [17]. This microstructural arrangement produces a substantially greater flow stress disparity of approximately 9.45 GPa between constituent domains [18]. Given these comparative attributes, PBF-LB/M processed Al-Si alloys emerge as superior candidates for lightweight structural components in transportation sectors, thus being the central focus of this investigation.

The industry demand for PBF-LB/M processed Al-Si alloys in aerospace and automotive structural applications stems from their exceptional specific strength values and thermal conductivity performance. These additively manufactured Al-Si materials have attracted particular attention due to their superior mechanical property profiles – including enhanced strength, formability, and durability metrics – when compared against conventionally cast counterparts, as quantified in **Table 1**. Among the Al-Si alloy spectrum, AlSi10Mg has gained particular prominence owing to its optimized performance characteristics. The approximately 10% silicon content enhances melt fluidity during processing, minimizing defect formation related to incomplete fusion or balling phenomena, thereby promoting consistent layer consolidation [19]. Furthermore, the magnesium addition enables Mg_2Si precipitate formation during subsequent aging treatments, which contributes to improved tensile strength and hardness values. This microstructural feature positions AlSi10Mg as a balanced composition offering advantageous strength-ductility combinations for structural applications when compared with alternative formulations such as AlSi7Mg and AlSi12Mg [20]. Based on these performance advantages, AlSi10Mg constitutes the primary material focus of this research investigation.

Table 1. Comparison of the mechanical properties of cast and additively manufactured Al-Si alloys

Alloy	Condition	Yield Strength [MPa]	Tensile Strength [MPa]	Elongation at break, [%]	Reference
AlSi7Mg	PBF-LB/M	290	388	6.1	[21], [22]
	Cast	271	321	2.9	
AlSi10Mg	PBF-LB/M	268	391	1.4	[23]
	Cast	170	320	3.0	
AlSi12Mg	PBF-LB/M	260	380	3.0	[14]
	Cast	90	190	9.5	

1.2 Problem Statement

The pursuit of lightweight, high-performance structural materials frequently encounters the fundamental strength-ductility paradox. Established strengthening mechanisms, such as grain

refinement [24], solutioning, dislocation accumulation, and precipitation [25], reliably increase yield strength but concurrently diminish ductility, often due to suppressed strain hardening. Sustained plastic deformation, indicative of good ductility, requires a high strain-hardening capacity, which originates from the intricate interplay between mobile dislocations and various microstructural features acting as obstacles across multiple length scales [26], [27]. While heterostructured materials offer a promising route to co-optimize strength and ductility, and PBF-LB/M provides unique capabilities for fabricating such structures in alloys like AlSi10Mg, the precise mechanisms by which tailored heterogeneity, induced via post-processing, influences dislocation dynamics and strain hardening behavior in these additively manufactured alloys remain insufficiently elucidated. This research addresses this deficiency by focusing on the strategic optimization of microstructural heterogeneity in PBF-LB/M AlSi10Mg through controlled post-processing. By systematically correlating post-processing conditions with detailed microstructural characterization and mechanical property assessment, this work seeks to uncover the fundamental principles governing strain hardening in these specific heterostructures. The goal is to provide a mechanism-based understanding for designing lightweight automotive and aerospace components that transcend the performance limitations of conventional aluminum alloys, without compromising end-of-life recyclability.

Chapter Two

2.0 Literature Review

2.1 Additive Manufacturing

Additive Manufacturing (AM), commonly known as 3D printing, has fundamentally transformed the design and production landscape across multiple sectors by enabling the layer-by-layer construction of complex parts directly from digital models. Initially developed in the 1980s with Charles Hull's invention of stereolithography (SLA), AM has progressed from producing basic prototypes to fabricating end-use components across aerospace, automotive, and healthcare industries [28], [29]. This technological evolution is well-documented, laying a foundation for understanding AM's substantial impact and future potential across various industrial applications. The historical technological roadmap of AM, showcasing its transition from prototype development to advanced industrial applications, is illustrated in **Figure 2**.

The scope of materials used in AM has significantly broadened from plastics and resins to include a wide range of metals and ceramics, selected based on the unique properties required for specific applications. Metals such as titanium and nickel alloys have become prevalent due to their high strength and corrosion resistance, properties that are particularly advantageous in aerospace and medical implants. AlSi10Mg exemplifies the benefits of metal powders in AM due to its excellent mechanical properties and favorable post-processing surface finish [30].

AM technologies encompass a variety of distinct processes, each characterized by specific approaches to material handling and energy application. Powder bed fusion (PBF), including PBF-LB/M and electron beam melting (EBM), is especially significant for its capacity to produce highly dense and mechanically robust metal parts. PBF-LB/M, for example, is extensively used in applications requiring precision, as it melts metal powders layer by layer to fabricate parts with complex internal structures and intricate geometries. This precision and the ability to produce parts with fine features are invaluable in high-demand sectors such as aerospace and medical device manufacturing, where component integrity and dimensional accuracy are critical [31], [32].

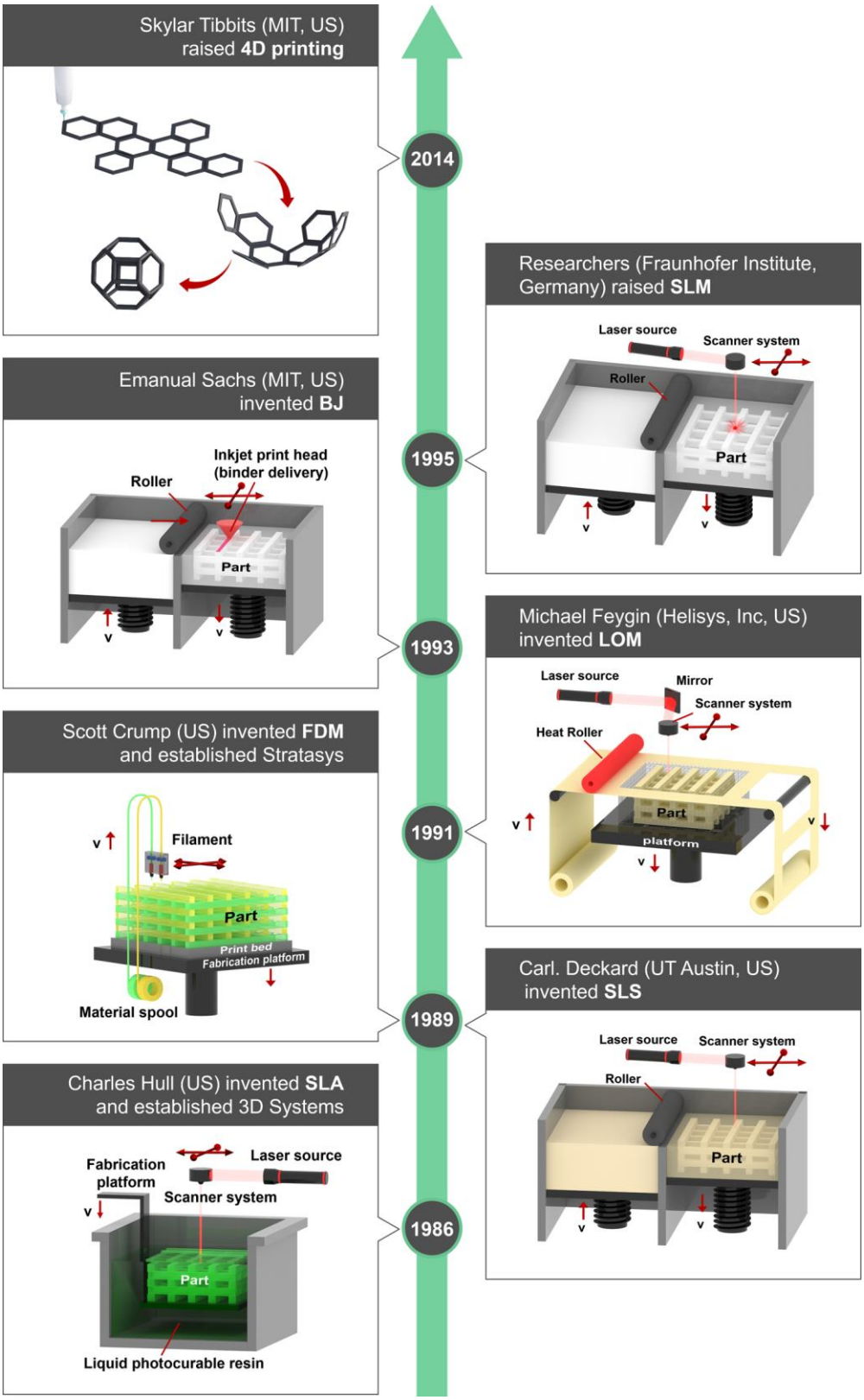

Figure 2. Technological roadmap of additive manufacturing Adapted from [33].

Overall, AM's evolution from a prototyping tool to a versatile manufacturing process reflects its transformative role in modern engineering. Continuous advancements in AM technologies and materials, coupled with a growing understanding of process-microstructure-property relationships, are expanding AM's applicability, enabling industries to meet stringent requirements in terms of strength, weight reduction, and customization. This ongoing progress ensures that AM remains at the forefront of manufacturing innovation, particularly in high-stakes sectors like aerospace and healthcare, where both reliability and performance are paramount [34]. The application of AM technologies has profoundly impacted various industries by enabling innovative designs, reducing material wastage, and improving efficiency. In aerospace, AM facilitates lightweight designs for aircraft components, which directly contributes to fuel savings and reduced emissions, essential considerations in today's environmentally conscious landscape [35]. The automotive industry also leverages AM, especially for rapid prototyping, which accelerates development cycles and allows for the production of complex, geometrically intricate parts that would be challenging and costly to manufacture through traditional means [36]. A notable example of AM in aerospace is the production of fuel nozzles for jet engines, which have been optimized to improve performance while reducing both weight and manufacturing complexity. The ability to consolidate multiple components into a single AM-produced part, as in jet engine fuel nozzles, simplifies assembly processes, enhances reliability, and enables more efficient fuel flow [37]

However, despite these benefits, AM technologies face certain limitations. Issues such as porosity and anisotropy in printed parts can adversely impact mechanical properties and durability, making it challenging to ensure consistent quality in AM-fabricated components. Porosity, for instance, can introduce weaknesses within the material that compromise load-bearing capacity, while anisotropy due to directional solidification affects mechanical performance along different orientations [38]. Additionally, the economic viability of AM, especially for large-scale production, remains a concern. High machine and material costs, coupled with slower production rates compared to traditional manufacturing methods, present substantial obstacles to AM's widespread adoption in high-volume applications [39].

2.2 Laser-Based Powder Bed Fusion of Metals (PBF-LB/M)

Laser-based powder bed fusion of metals or powder bed fusion – laser beam/metal (PBF-LB/M) is an additive manufacturing technology where a high-power laser selectively melts and

fuses metallic powders layer by layer to create complex 3D parts. It is also known as direct metal laser sintering (DMLS) or selective laser melting (SLM). PBF-LB/M has become the preferred technology for many industries because of its ability to achieve consistent quality and control over microstructure, which directly influences mechanical properties. The process's rapid cooling rates lead to refined microstructures with higher strength characteristics, which is advantageous for high-performance applications [40]. However, challenges such as residual stress accumulation and anisotropic mechanical properties persist, often necessitating post-processing techniques to improve part durability and dimensional accuracy. Consequently, significant research efforts have been directed towards optimizing process parameters and developing new alloy compositions tailored to AM processes, enhancing performance and reducing failure risks in applications [41]. **Figure 3** depicts a typical workflow for the PBF-LB/M process, emphasizing the step-by-step progression from initial design to final post-processing in a standard PBF-LB/M operation. The PBF-LB/M process initiates with the **Design** phase, wherein a 3D CAD model is created to encapsulate all required geometrical details of the part. This is followed by the **Conversion** stage, where the CAD file is transformed into an STL file format, enabling slicing in preparation for printing. In the **File Transfer** stage, the STL file is uploaded to slicing software, which generates the machine instructions essential for guiding the print process. Next, the **Configuration** phase entails optimizing parameters, such as layer thickness, laser power, and scanning strategy, to ensure optimal print quality and mechanical characteristics. The **Print** stage follows, marking the actual printing process where the part is constructed from the metal powders, layer by layer, with precision in each successive layer contributing to the overall integrity and precision of the final component.

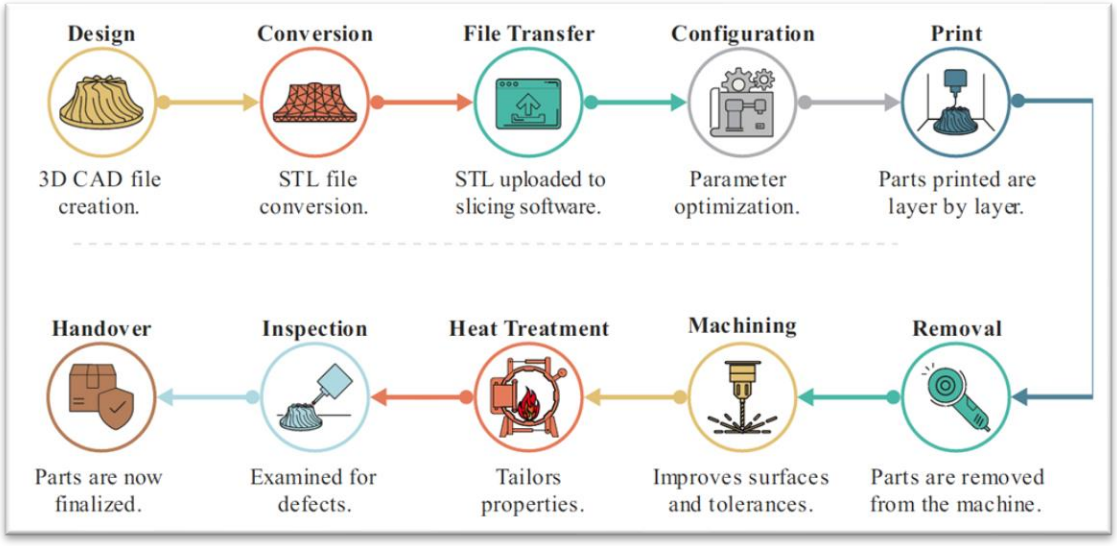

Figure 3. An example of a typical PBF-LB/M process workflow. Adapted from [42].

Post-printing operations proceed through a series of meticulously structured steps to uphold the integrity and functionality of printed parts. The **Removal** stage involves detaching the printed parts from the build platform and cleaning them, followed by **Machining** to achieve precise dimensions and improve surface finishes. **Heat Treatment**, an optional phase, serves to tailor the mechanical properties such as strength and ductility, particularly important in applications requiring customized material performance. In the subsequent **Inspection** phase, quality assurance protocols are employed to examine the parts for defects and verify dimensional accuracy, ensuring that each component meets stringent standards. The final **Handover** stage involves preparing the parts for delivery to their respective applications or inventory, concluding the L-PBF workflow and readying the components for functional use. [43], [44], [45]. Paramount to the success of PBF-LB/M is the management of process parameters such as laser power, scan speed, layer thickness, and hatch spacing – these factors collectively influence the energy density imparted to the powder bed and are crucial for achieving optimal material properties and minimizing defects such as porosity or residual stresses. For instance, inappropriate energy input can lead to issues like poor surface finish, internal stresses, and structural weaknesses [46].

PBF-LB/M technology has evolved significantly, incorporating advanced features such as multi-laser systems to increase build rates and improve part quality across larger build areas. Modern PBF-LB/M machines are equipped with dynamic scanning strategies and sophisticated software that allows for real-time adjustments and monitoring, enhancing the reliability and efficiency of the process. The integration of in-situ monitoring systems using cameras and sensors

facilitates the detection of defects during the build process, enabling corrective measures to be implemented promptly. For instance, in a study detailed by Chowdhury et al. [47], it is suggested that using advanced numerical modeling can enhance the understanding of the complex interactions between process parameters and resulting material properties in PBF-LB/M, providing insights that can lead to more predictable and repeatable manufacturing outcomes.

In terms of material options, PBF-LB/M is versatile, capable of processing a wide range of metals and alloys, including difficult-to-machine and high-strength materials. Recent advancements have expanded the material portfolio to include high-entropy alloys and complex metallic composites, opening new avenues for applications in aerospace, biomedical, and automotive industries.

2.2.1 Microstructure of PBF-LB/M Alloys

The alloy solidification sequence is schematically represented in **Figure 4** [48]. The first solid forms from liquid and acts as a nucleus for solid phase growth, forming a dendrite (**Figure 4a**). the size of the dendrite increases in subsequent stages of solidification, before grains are formed (**Figure 4b, c**). Owing to the fact that alloys solidify within a range of temperatures, the first metal to solidify has the highest melting point composition, while the last has the lowest eutectic composition. As a result, the alloy fraction with the lowest melting point is moved ahead of the solidifying dendrite until it becomes stuck between the grain boundaries (**Figure 4d**).

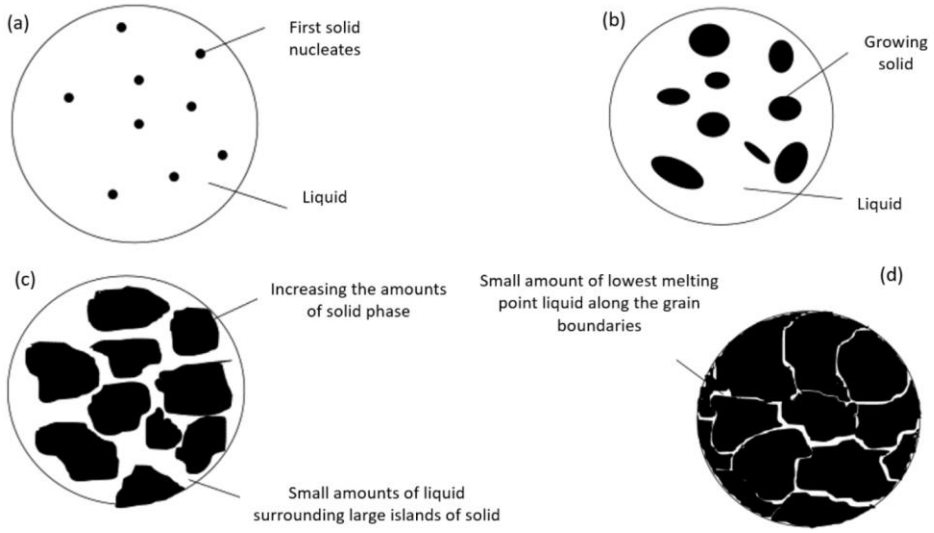

Figure 4. Schematic showing how a PBF-LB/M alloy solidifies (a) the beginning of solidification, (b,c) solid phase growth, (d) final stage of solidification. Adapted from [48].

A defining characteristic of materials produced by PBF-LB/M is their complex and often unique hierarchical microstructure. This term refers to a structural organization featuring distinct morphological or crystallographic features arranged across multiple, vastly different length scales, ranging from the nanometer scale up to the scale of the entire component [49]. This intricate hierarchy is a direct consequence of the complex and highly non-equilibrium thermal history imposed by the PBF-LB/M process, specifically the interplay of rapid solidification, directional heat extraction, and repeated thermal cycling [50].

The typical levels constituting this hierarchy can be broadly categorized as follows:

- **Macroscale (mm to cm)**: This level encompasses the overall geometry of the printed part and can include large-scale defects such as distortion due to residual stress accumulation or significant cracks that may form during or after the build process [51].
- **Mesoscale (µm to mm)**: At this scale, the microstructure is dominated by the pattern of solidified melt pools, reflecting the laser scanning strategy. Features include the shape and overlap of individual melt pools, the distinct boundaries between them, and associated heat-affected zones (HAZs) formed by the reheating of underlying material [49]. Process-induced porosity or lack-of-fusion defects often manifest at this scale.
- **Microscale (µm)**: This level is characterized by the grain structure of the solidified material. This includes the morphology (shape) of the grains, which are often columnar (elongated) due to directional solidification but can sometimes be equiaxed, their size distribution, and their crystallographic orientation (texture) [49].
- **Sub-Microscale (nm to µm)**: Within the grains, finer sub-structures are typically observed. These include cellular or dendritic solidification structures resulting from instabilities at the solid-liquid interface during rapid cooling. The spacing between these cells or dendrite arms is a key feature at this scale. Additionally, dense networks or cells formed by dislocations generated during solidification and subsequent thermal straining are prominent [49].
- **Nanoscale (nm)**: The finest level of the hierarchy involves features such as nanoscale precipitates, solute clusters, or the distribution of different phases within the cellular or dendritic sub-structures. These features often arise from the extended solid solubility achieved during rapid solidification and subsequent low-temperature thermal cycling or deliberate post-processing heat treatments [49].

The existence of this hierarchical structure carries profound implications for the material's properties. Mechanical behavior, such as strength, ductility, and fatigue resistance, is not governed by features at a single length scale but rather emerges from the complex interplay and interactions between structures across the entire hierarchy [52]. For instance, Maeshima et al., [53] have postulated that the overall strength might be dictated by fine cellular structures and nanoprecipitates, while fatigue life, according to Kan et al., [54], could be limited by mesoscale defects like pores, and fracture toughness might be influenced by the tortuosity of crack paths navigating melt pool boundaries and grain structures, as reported by Zhao et al., [52]. Consequently, achieving optimal performance in LPBF components necessitates a holistic understanding of the microstructure across all relevant scales and developing strategies to control features at each level of the hierarchy.

2.2.2 Residual Defects

The inherent anisotropy in mechanical properties associated with PBF-LB/M processes resulting from residual defects due to directional cooling and layer-wise building also affects the mechanical behavior of PBF-LB/M parts. Despite continuous advancements in PBF-LB/M, achieving complete microstructurally defect-free parts remains a challenge due to the intricate nature of the solidification process and the resulting complex geometries. Residual defects, often in the form of pores, are nearly inevitable [55], [56]. The most common types include gas-entrapped pores, keyhole pores, and lack of fusion (LOF) defects. The formation mechanisms and consequences of these defects on mechanical properties have been a focal point of recent research [55], [56], [57]. Many studies utilize porosity volume as a key metric to assess the quality and predict the performance of PBF-LB/M parts [58], [59], [60]. However, the relationship between porosity and mechanical properties in additively manufactured components requires further exploration, as conventional research has not fully addressed the three-dimensional anisotropic characteristics of these defects. Consequently, specimens with identical volumetric porosity can exhibit substantially different mechanical responses depending on build orientation and loading conditions [61], [62]. This research area has garnered significant attention recently. For example, Wu et al. [63] examined failure mechanisms during tensile testing of additively manufactured AlSi10Mg, specifically investigating how LOF defects oriented perpendicular to the build direction influence performance. Their work showed the directional impact of these defects on

tensile ductility and emphasized the importance of minimizing both their dimensions and aspect ratios.

2.3 AlSi10Mg in Additive Manufacturing

The microstructural evolution in AlSi10Mg alloys during PBF-LB/M is profoundly influenced by the rapid cooling and solidification inherent to the process. The microstructure formed during solidification of the printed alloys is heavily influenced by the interplay between the temperature gradient (G) and the solidification rate (R), as illustrated in **Figure 5** [64]. While the cooling rate, represented by the product G*R, governs the scale of the solidification structure, the ratio G/R dictates the morphology of the solidification front. In the context of the PBF-LB/M process, cooling rates within the melt pool have been reported to reach the order of 10^6 K/s. This rapid cooling can be attributed to the small dimensions of the melt pool and the efficient heat sinking provided by the underlying bulk metal [65]. For AlSi10Mg alloy, the G/R parameter is estimated to be around 20 Ks/mm^2. The combination of a high cooling rate and a moderate temperature gradient places the solidification process of aluminum alloys during PBF-LB/M near the transition zone between columnar dendritic and equiaxed dendritic growth [66], as depicted in **Figure 5**. Specifically, the high cooling rate promotes the formation of a very fine microstructure. Furthermore, solidification conditions can exhibit subtle variations from the bottom to the top of the melt pool. This is due to the gradual reduction in the temperature gradient, which can trigger a shift from columnar to equiaxed morphology. This transition has been numerically predicted and experimentally validated in AlSi10Mg alloy through EBSD analysis by Liu et al. [67].

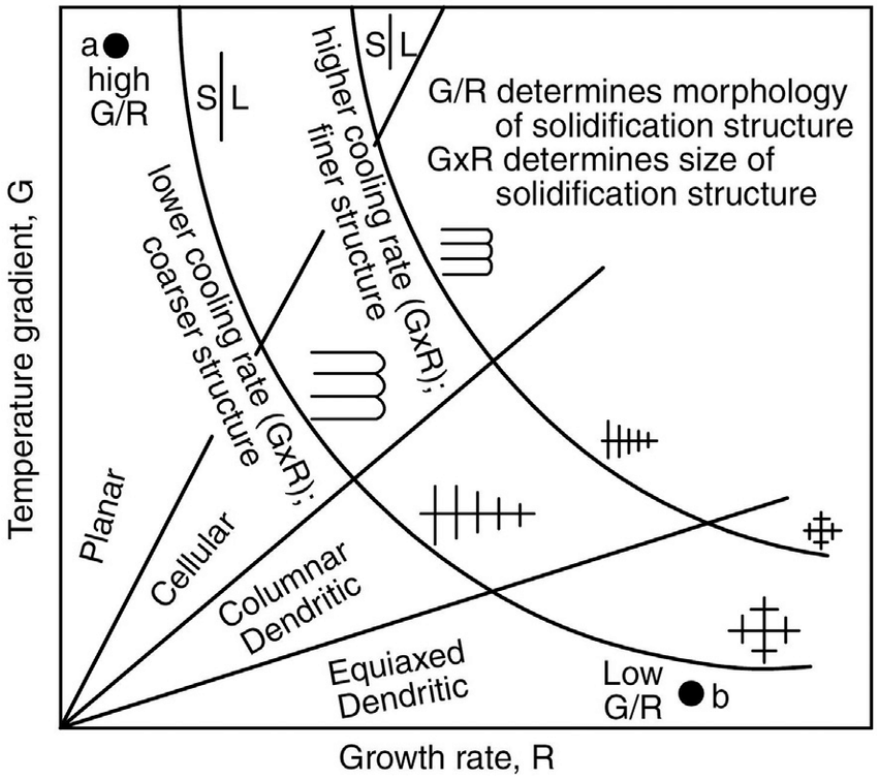

Figure 5. Influence of growth rate (R) and temperature gradient (G) on the morphology and size of solidification microstructure. Adapted from [64].

Post-processing treatments such as heat treatment and plastic deformation processes play significant roles in modifying the microstructural attributes and mechanical properties of PBF-LB/M-fabricated AlSi10Mg alloys. Heat treatments, including annealing, solution treating and aging, can homogenize the alloy's microstructure, dissolve undesirable precipitates, and alleviate residual stresses, thereby improving ductility and toughness. These treatments must be meticulously controlled to avoid negative impacts on part dimensions and properties, as emphasized by Li et al. [68]. Such post-processing steps are often indispensable for tailoring the material properties to meet specific application requirements, enhancing the usability of AlSi10Mg alloy components in critical applications.

2.4 The Cellular Microstructure of AlSi10Mg Produced by PBF-LB/M

Figure 6 compares the microstructure of a cast AlSi10Mg (**Figure 6a**) to a PBF-LB/M fabricated AlSi10Mg (**Figure 6b**) as observed under the scanning electron microscope (SEM). The

microstructure of the cast AlSi10Mg is characterized by a coarse-grained hypoeutectic solidification structure with dispersed microconstituents in the interdendritic regions. On the other hand, the microstructure of the as-built PBF-LB/M AlSi10Mg alloy is dominated by a fine cellular or cellular-dendritic sub-structure. This structure consists of a primary α-Al phase regions which are enveloped by a continuous or semi-continuous network rich in silicon [69]. The characteristic size of these α-Al cells is typically in the sub-micron range, often measuring several hundred nanometers [70].

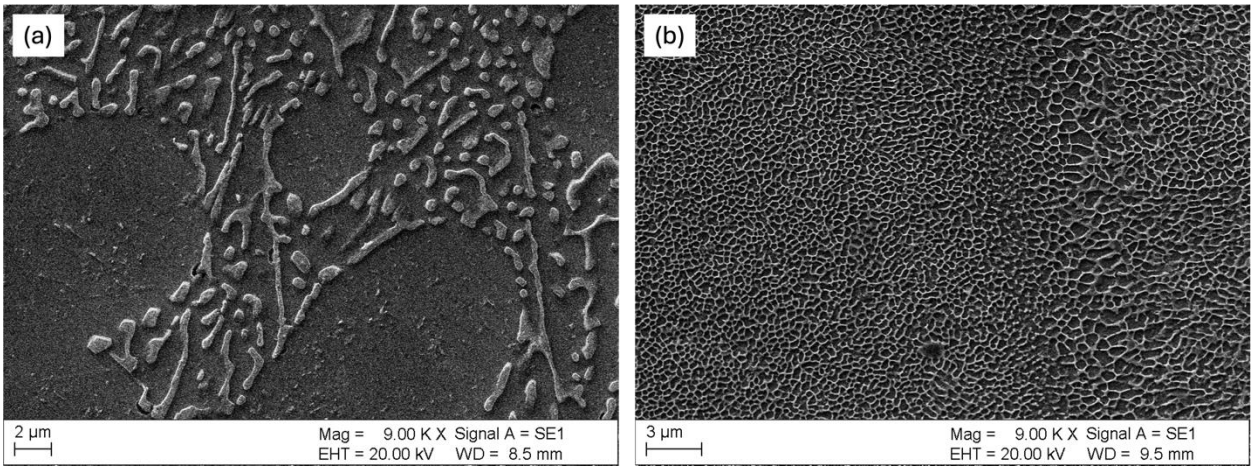

Figure 6. Microstructure of AlSi10Mg alloy (a) alloy fabricated by casting, exhibiting a typical coarse-grained hypo-eutectic solidification structure with various types of dispersed microconstituents in the interdendritic regions, and **(b)** alloy fabricated by L-PBF, exhibiting a cellular structure [from own experiments].

The formation of this cellular network is fundamentally driven by the high thermal gradients and high solidification front velocities, resulting in high cooling rates [71]. Under these non-equilibrium conditions, as the α-Al phase solidifies rapidly, the slower-diffusing Si atoms are 'rejected' from the advancing solid-liquid interface. The limited time for diffusion prevents the rejected Si from homogenizing in the remaining liquid ahead of the interface. This leads to a build-up of Si concentration in the liquid adjacent to the solidification front, a phenonomenon known as constitutional undercooling [72]. This undercooling destabilizes the planar solidification front, promoting cellular growth morphologies. The rejected Si becomes trapped in the intercellular regions, eventually solidifying as a Si-rich eutectic phase, forming the characteristic network structure observed at the cell boundaries. The resulting cellular structure is often considered

metastable due to the supersaturation of Si within the α-Al cell and the fine, non-equilibrium nature of the eutectic network [72].

Importantly, the cellular morphology is not uniform throughout the solidified material. Variations are commonly observed within individual melt pools, typically characterized by finer cells in the melt pool interior and coarser cells near the melt pool boundaries (MPB) or in the heat-affected zone (HAZ) of the underlying previously solidified material [73]. The size of the cellular structure has been inversely correlated with the local cooling rate, suggesting that the regions experiencing the highest cooling rates develop the finest cells [74]. However, the transition between fine and coarse cellular regions, particularly at the MPB, may not always be gradual. Zhang et at., [69] propose a more complex picture involving distinct microstructural zones within a melt pool, namely the liquid solidification zone (LSZ), the mushy solidification zone (MSZ), and the heat affected zone (HAZ), potentially arising from abrupt changes in solidification conditions (G/R ratio) or grain growth transitions at the boundary, challenging simpler models based solely on smooth thermal gradients.

Beyond the cellular morphology, the as-built AlSi10Mg is characterized by a high initial density of dislocations. These dislocations are often organized into networks or walls, frequently associated with the cellular boundaries [72]. This pre-existing dislocation structure arises during the rapid cooling phase due to thermal mismatch stresses between the α-Al matrix and the Si-rich phase, as well as stresses generated by the constrained shrinkage during solidification. In a study by Eskandari Sabzi et al., [75], it is reported that the multiplication and annihilation of these dislocations during the complex thermal cycling of the PBF-LB/M process play a paramount role in establishing the initial yield strength of the PBF-LB/M materials. In some complex alloys processed by PBF-LB/M, dislocation networks have even been observed to be coupled with phase separation phenomena within cellular structures, highlighting the intricate defect structures that can form [72].

2.4.1 Cellular Network Continuity and Morphology in Mechanical Properties

The continuity of the Si-rich network forming the cellular structure influences the mechanical properties of PBF-LB/M AlSi10Mg alloys notably its strength, work hardening behavior, and most importantly, its ductility. The cellular network acts as a potent strengthening agent where the fine α-Al cell size contributes to strength through a Hall-Petch type mechanism, in which case the cell boundaries impede dislocation motion, similar to grain boundaries [76]. As

cell size decreases, the density of these barriers increases, leading to higher yield strength [77]. Additionally, the Si-rich phase forming the network constitutes hard obstacles dispersed within the softer α-Al matrix. Dislocations moving within the α-Al cells encounter this network, and overcoming it requires increased stress, primarily through the Orowan looping mechanism, where dislocations bow out between the Si particles or network segments [78]. This Orowan strengthening contribution is considered significant, with Chen et al., [78] identifying it as the dominant mechanism related to the Si phase. The combined effect of fine cell size and Si network barrier results in the substantially higher yield strength observed in as-built PBF-LB/M AlSi10Mg compared to its cast counterpart [69].

The cellular structure is also central to the material's work hardening response. During plastic deformation, dislocations generated within the α-Al cells move and interact with the cell boundaries (Si network) [70]. Snopiński et al., [79] have reported that these boundaries act as effective obstacles, hindering dislocation movement and promoting dislocation accumulation and storage. This accumulation leads to an increase in the overall dislocation density and the formation of complex dislocation arrangements, such as pile-ups and tangles, requiring progressively higher stress for further deformation, thus contributing to work hardening [80]. Furthermore, the significant difference in hardness and elastic modulus between the α-Al matrix and the Si-rich network leads to strain incompatibility during deformation. This incompatibility necessitates the generation of GNDs near the cell boundaries to accommodate the localized strain gradients and maintain lattice continuity [70]. Shi et al., [81] have shown that finer cell boundaries lead to higher back stress and a more pronounced work hardening ability. Conversely, Salandari-Rabori et al., [82], [83], [84] have shown that if the cellular structure is eliminated or significantly coarsened, for instance through heat treatment, the work hardening rate tends to decrease due to the loss of these potent dislocation-obstacle interactions. The unique cellular structure is thus identified as a primary origin of the high strain-hardening rate observed in PBF-LB/M AlSi10Mg [52].

While the cellular network significantly enhances strength and work hardening, its rigid (brittle) nature can limit the material's overall ductility. The continuous network restricts dislocation motion across cell boundaries, potentially leading to stress concentrations and premature failure initiation. The morphology and continuity of the network can influence deformation localization patterns and the path of crack propagation. For instance, a highly continuous and brittle network might provide an easy path for inter-cellular fracture, limiting

tensile elongation. Snopiński [85] has also suggested that the Si network can induce the formation of stacking faults during deformation, which are typically rare in coarse-grained aluminum but can influence plasticity. Modifying the network, for example, by partial spheroidization through heat treatment, can sometimes improve ductility, albeit usually at the expense of strength [86].

2.5 Dislocations

A dislocation is a one-dimensional (linear) defect within the crystal structure around which some of the atoms are misaligned [87]. There are two basic types of dislocations: edge and screw dislocations. In edge dislocation, as shown in **Figure 7**, an extra portion of a plane of atoms, or half-plane, the edge of which terminates within the crystal [88].

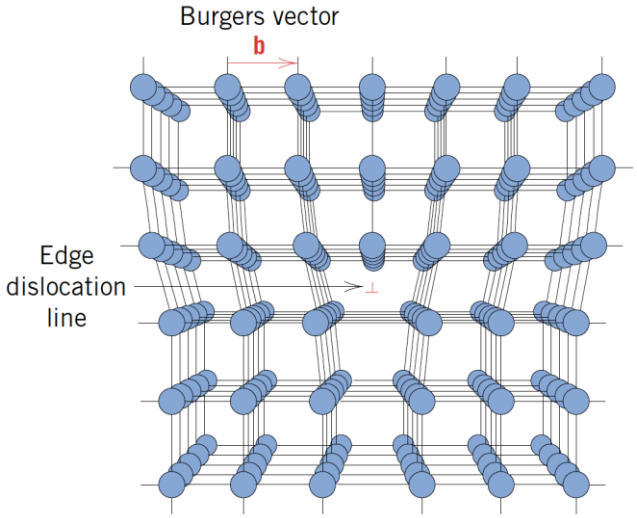

Figure 7. Schematic diagram of Edge dislocation. Adapted from [88].

An important characteristic of any dislocation is its Burgers vector (b), which represents the magnitude and direction of the lattice distortion, or the atomic displacement required to close a loop (a Burgers circuit) drawn around the dislocation line the defective crystal, compared to a perfect crystal. For an edge dislocation, the Burgers vector is oriented perpendicular (⊥) to the dislocation line. Under an applied shear stress, edge dislocations move within the crystal. This movement, termed glide or slip, occurs within a specific crystallographic plane known as the slip plane [89]. For an edge dislocation, the slip plane is the plane containing both the dislocation line and its Burgers vector. The direction of glide for an edge dislocation is parallel to its Burgers vector. The movement involves the sequential breaking and reforming of atomic bonds along the slip plane, effectively shifting the extra half-plane through the crystal one atomic spacing at a time [88].

Another type of dislocation is called screw dislocation. This is formed by shear stress that is applied to produce the distortion shown in **Figure 8a**, where the upper front region of the crystal is shifted one atomic distance to the right relative to the bottom portion. The atomic distortion associated with a screw dislocation is also linear and along a dislocation line (line AB in **Figure 8b**) [88]. As it moves, the screw dislocation effectively unzips the lattice along the slip plane [90]. It is noteworthy that most dislocations found in crystalline materials are usually neither pure edge nor pure screw but exhibit components of both types. These are termed mixed dislocations [91].

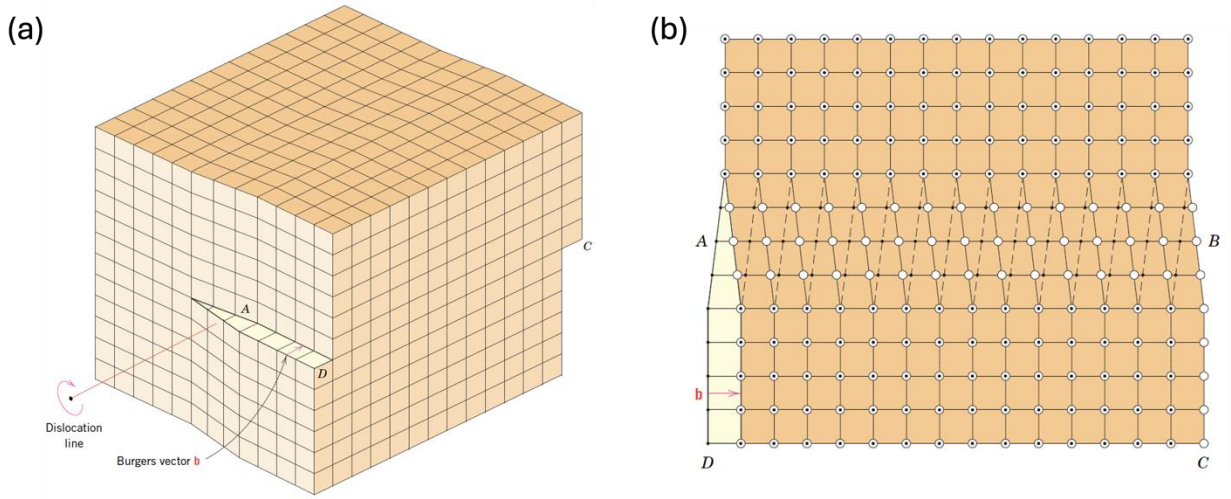

Figure 8. Schematic diagram of screw dislocation. Adapted from [88].

2.6 Dislocation Dynamics During Deformation

In polycrystalline materials, adjacent grains usually have different crystallographic orientations and a common grain boundary (**Figure 9**) [88]. During plastic deformation, slip or dislocation motion must take place across this common boundary, for example, from grain A to grain B in **Figure 9**. The grain boundary acts as a barrier to dislocation motion. Two major reasons account for this: Firstly, because the two grains are of different orientations, a dislocation passing into one grain from another must change its direction of motion and this becomes difficult as the crystallographic misorientation increases. The other reason is that the atomic disorder within a grain boundary region results in a discontinuity of slip plane from one grain into the other. For high-angle grain boundaries, it may not be the case that dislocations traverse grain boundaries during deformation; rather, dislocations tend to pile up at the boundaries. These pile-ups introduce stress concentrations ahead of their slip planes, which generate new dislocations in adjacent grains [92], [93].

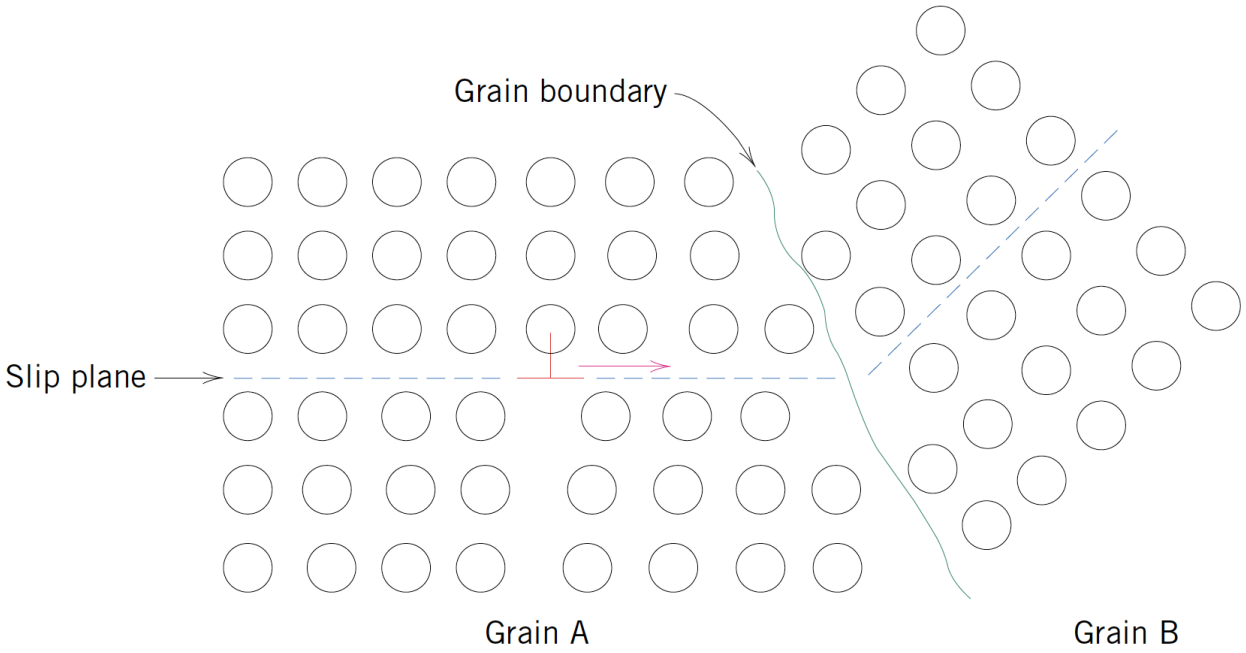

Figure 9. The motion of a dislocation as it encounters a grain boundary. Adapted from [88].

Understanding the dynamic interaction between the boundaries of the cellular sub-structures in PBF-LB/M alloys and dislocations during deformation is essential to explaining the unique properties of these alloys. While focused on a different material system – a refractory high-entropy alloy (RHEA) – a recent study by Liu et al. [94] has provided compelling visual evidence and mechanistic insights directly relevant to this interaction, reproduced in **Figure 10**. This figure tracks the evolution of the cellular structure and associated dislocation distributions within an L-PBF TiNbTaZrMo alloy under increasing compressive strain.

Initially, in the as-built state (0% strain, **Figure 10a-b**), dislocations resulting from thermal stresses during fabrication are present within the cell interiors. As deformation begins (~10% strain, **Figure 10c-d**), the cell walls act primarily as barriers to dislocation motion. This impedance leads to the accumulation and pile-up of dislocations near these boundaries (**Figure 10d1**), significantly contributing to the elevated yield strength commonly observed in L-PBF materials.

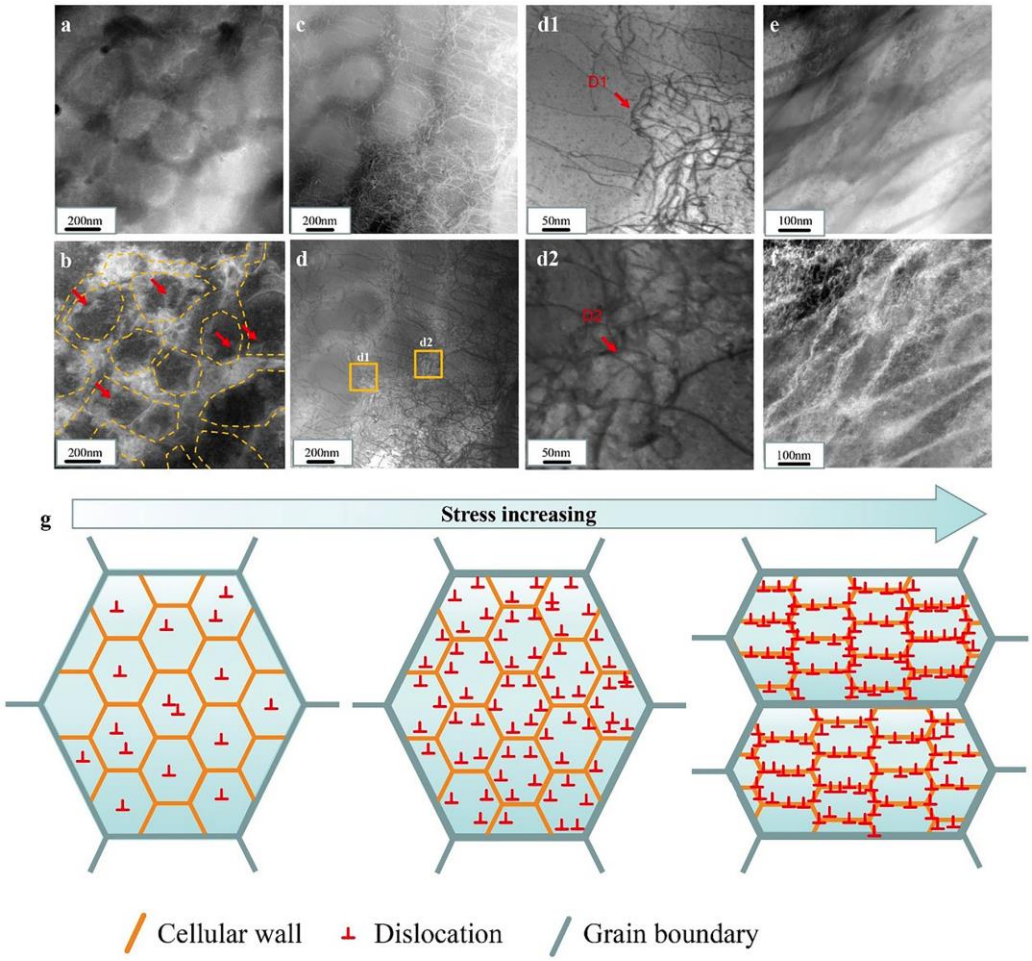

Figure 10. Evolution of dislocation interaction with the cellular microstructure in L-PBF TiNbTaZrMo RHEA during compression. (a, b) As-built state showing initial dislocations. (c, d) At ~10% strain, cell walls hinder dislocation motion leading to pile-ups. (e, f) At ~45% strain, cell walls absorb and store dislocations. (g) Schematic summarizing the transition from hindrance to absorption. Adapted from [94].

However, the role of the cellular structure evolves as plastic deformation progresses. At higher strains (~45% strain, **Figure 10e-f**), the cell walls transition from being primarily obstacles to acting as sites for dislocation absorption and storage. Dense dislocation tangles and networks form along and within the cell walls (**Figure 10f**), indicating their capacity to accommodate significant plastic strain. This mechanism (**Figure 10g**) is crucial for enabling sustained work hardening and promoting more homogeneous deformation, which can delay strain localization and potentially enhance ductility.

Although the specific chemical composition of the cell boundaries in the RHEA studied by Liu et al. [94] (Ti/Ta-Nb segregation) differs from the Si-rich eutectic network found in L-PBF AlSi10Mg, the principle of dislocation interaction with a strengthening phase at cell/dendrite boundaries is analogous. The dual role observed – initial impedance contributing to yield strength, followed by dislocation storage facilitating work hardening and accommodating strain – provides a framework.

2.6.1 Dislocation Formation and Accumulation in PBF-LB/M AlSi10Mg

The PBF-LB/M AlSi10Mg in the as-built state already possesses a high density of dislocations, typically organized within or around the cellular sub-structure [95]. Upon the application of external stress leading to plastic deformation, new dislocations are generated within the α-Al matrix primarily through the operation of dislocation sources, such as the Frank-Read mechanism [77]. This generation leads to a significant increase in the total dislocation density as plastic strain accrues [95]. These newly generated dislocations, along with the pre-existing ones, move through the lattice until they encounter obstacles. In PBF-LB/M AlSi10Mg, the primary obstacles include the Si-rich network at the cell boundaries, precipitates (if present, especially after heat treatment), grain boundaries, and other dislocations (forest hardening) [79]. Interactions with these obstacles impede dislocation motion, causing dislocations to accumulate. The Si network is particularly effective in hindering dislocation movement and facilitating efficient dislocation storage [79]. Dislocation pile-ups readily form against the relatively impenetrable Si phase [96].

Dislocation accumulation is highly heterogenous and the patterns can vary even at the microstructural scale, sometimes manifesting as shear bands, particularly in heat-treated conditions [71]. Modeling studies by Rohoman and Zhou [77] have shown that factors like the volume fraction of the cell wall, the cell diameter, and the initial difference in dislocation density between the cell wall and interior significantly influence the pattern and extent of GND accumulation within the cellular structure. Experimental observations by Liu et al. [97] and Zhu et al. [98] confirm incompatible plastic deformation at the microscale, leading to localized residual strains/stress and dislocation pile-ups, particularly at interfaces like the Al/Si cell boundaries, grain boundaries, and melt pool boundaries.

2.6.2 Accumulation Sites

Dislocations do not accumulate uniformly; specific microstructural features serve as primary sites for their concentration. These accumulation sites include cell boundaries/Si network, grain boundaries, melt pool boundaries (MPBs), and cell/grain interiors.

2.6.2.1 Cell Boundaries/Si Network

These interfaces represent the most significant barriers to dislocation motion within the grains/cells and as a consequence, they are major sites for dislocation accumulation [79]. Dislocation pile-ups against the Si network are commonly observed [96], and the network itself acts as a storage location [79]. The hindrance of dislocation movement by the cell walls directly leads to accumulation, further aiding in subsequent grain refinement processes [99].

2.6.2.2 Grain boundaries

Similar to cell boundaries but typically at a larger length scale, grain boundaries act as effective barriers to dislocation glide, particularly high-angle grain boundaries. Dislocation pile up at grain boundaries, contributing to strengthening and work hardening. Grain boundaries are also primary sites for the accumulation of GNDs, which are necessary to accommodate the misorientation between adjacent grains experiencing different slip system activations [70]. The role of low-angle grain boundaries or subgrain boundaries, often formed by dislocation arrangements [8], is also significant in strengthening PBF-LB/M materials.

2.6.2.3 Melt Pool Boundaries (MPBs)

These mesoscale interfaces serve as another site for dislocation accumulation. MPBs often feature different microstructures (e.g. coarser cells, HAZ) compared to the melt pool interiors, leading to mechanical property variations across the boundary [69]. This mismatch can cause strain localization and incompatibility between dislocation accumulation, likely enriched in GNDs needed to accommodate the localized strain gradients and potential crystallographic misorientations across the boundary interface [100]. The accumulation of dislocations and associated stress concentrations at MPBs contributes to their observed behavior as preferential sites for damage initiation and propagation [100], [101], [102].

2.6.2.4 Cell/Grain Interiors

Dislocations also accumulate within the α-Al cellular or grain interiors. This occurs through random trapping events involving interactions between moving dislocations and forest

dislocations leading to the storage of statistically stored dislocations (SSDs) [70]. This contributes to the overall flow stress and isotropic hardening of the alloy. Crystal plasticity models, for instance, as presented by Rohoman and Zhou [77] often account for dislocation density evolution separately within cell interiors and at cell walls/boundaries.

2.6.3 Heat Treatment

Post-process heat treatments are commonly applied to PBF-LB/M AlSi10Mg to modify its microstructure and mechanical properties. Low-temperature annealing (LTA), typically conducted at temperatures ~200 – 300°C (e.g. 225°C for 2 hours [103] or 280°C for 9 minutes [104]), is often employed primarily for stress relief. However, even these relatively low temperatures induce some changes in the dislocation structure and precipitate state.

During LTA, thermal energy facilitates recovery processes. Dislocations rearrange and annihilate, leading to a noticeable decrease in the overall dislocation density compared to the as-build state. This reduction in dislocation density directly lowers the contribution of dislocation hardening to the alloy's yield strength [70]. Concurrently, the supersaturated α-Al matrix begins to decompose. Silicon atoms precipitate out of solution, often forming fine Si particles within the α-Al cells [86]. Existing Si particles within the eutectic network may coarsen [103], and the continuity of the Si network itself can be disrupted, leading to partial spheroidization or breakup [104]. For example, annealing at 225°C for 2 hours was associated with secondary precipitation, solute depletion, and Ostwald ripening phenomena [103].

These microstructural changes impact subsequent dislocation behavior during deformation. While the overall initial dislocation density is lower, the newly formed or coarsened precipitates within the cell interiors act as new obstacles to dislocation motion. Dislocations must bypass these precipitates, often via the Orowan looping mechanism [78], which contributes to strengthening. The effectiveness of these precipitates as obstacles depends on their size, spacing, and coherency with the matrix. Salandari-Rabori et al. [83] have noted transitions in dislocation-precipitate interaction mechanisms (e.g., from shearing of very fine precipitates to looping around larger ones) as annealing progresses or strain increases.

The net effect of LTA on mechanical properties is typically a trade-off. The reduction in dislocation density tends to decrease yield strength and hardness, while the increased potential of dislocation motion and potentially the modification of the constraining Si network often leads to

an improvement in ductility [86]. However, the precipitation effects can partially offset the strength loss or even influence properties in complex ways. For instance, annealing at 225°C was found to reduce creep resistance (increase in minimum creep rate) compared to the as-built state, particularly at lower testing temperatures (150°C), suggesting that the microstructural changes induced by LTA are not necessarily beneficial for elevated temperature performance [103]. In some cases, LTA might be used strategically as a pre-treatment before other processes; for example LTA followed by ECAP resulted in increased hardness and strength, suggesting the annealed structure was amenable to significant work hardening [104]. **Table 2** compares the microstructural features and mechanical properties of as-built and low-temperature annealed PBF-LB/M AlSi10Mg

Table 2. Comparison of microstructural features and mechanical properties for as-built vs. heat-treated (LTA) PBF-LB/M AlSi10Mg

Feature	**As-built**	**Heat-treated (LTA ~200 – 300°C)**	**Reference(s)**
Microstructural Features			
Cellular Structure	Fine (sub-micron) α-Al cells, intact structure	Cells largely retained, potential network modifications	[70], [104]
Si Network	Continuous/semi-continuous eutectic structure	Network potentially modified/partially broken up	[69], [104]
Dislocation Density	High, organized networks	Reduced due to recovery	[70], [77]
Precipitate State	Supersaturated α-Al matrix	Fine Si/Mg_2Si precipitates within α-Al cells	[86], [103]
Mechanical Properties			
Yield Strength (MPa)	~250 – 300+	Decreased (e.g. ~90 – 200)	[74], [86]

Ultimate Tensile Strength (MPa)	~400 – 460+	Decreased (e.g. ~290)	[74], [104]
Elongation (%)	~2 – 10	Increased (e.g., factor of 4 increase, ~6 post-ECAP)	[79], [86]
Hardness (HV)	~115 – 120+	Decreased (except followed by deformation)	[80], [104]
Creep Strength (>150°C)	Baseline	Reduced	[103]

2.7 Statistically Stored Dislocations (SSDs) and Geometrically Necessary Dislocations (GNDs)

During plastic deformation, two main types of dislocations contribute to the evolving microstructure and mechanical properties: statistically stored dislocations (SSDs) and geometrically necessary dislocations (GNDs) [79].

SSDs are generated by various mechanisms within the microstructure, such as Frank-Read sources or grain boundary ledges, and serve to carry plastic deformation. As short-range obstacles, SSDs can hinder the movement of mobile dislocations along the slip plane [105], [106]. GNDs, conversely, are formed during the relaxation of strain gradients; their primary function is to maintain lattice compatibility by reducing deformation inhomogeneity [83]. GNDs are categorized as long-range obstacles and, unlike SSDs, do not facilitate the accommodation of plastic strain [106]. In the as-built AlSi10Mg microstructure created by PBF-LB/M – which contains non-equilibrium eutectic phases, cell boundaries, and Si-rich nano-precipitates with numerous defects like stacking faults (SFs) and microstrains – GNDs are known to exist owing to pronounced strain gradients [76], [107]. Li et al. [76] demonstrated that GNDs, rather than SSDs, are the principal contributors to hardening. By inducing partial and complete dissolution of the eutectic phases and cell boundaries through heat treatment, they observed a significant decrease in work hardening resulting from GND reduction, even when SSDs were still present. Consequently, with increasing strain levels (irrespective of strain rate), GND density consistently rises at the eutectic phases and

cell boundaries. These GNDs fundamentally influence the deformation behavior by enhancing interactions with mobile dislocations. Mobile dislocations moving through these dense GND regions undergo absorption and annihilation at cell and eutectic boundaries. Subsequently, the eutectic phases and cell boundaries act as key mediators in plastic deformation mechanisms by continuously generating GNDs nearby. Therefore, as deformation progresses, the formation of these dense GND regions and their continued interaction with mobile dislocations become the most dominant rate-controlling mechanism, regardless of the strain rate [83].

2.8 Dislocation Exhaustion Rates Across Deformation Stages

The work hardening behavior of a material is also governed by the rate at which dislocations are removed from the structure through annihilation or dynamic recovery processes [77]. These exhaustion mechanisms counteract storage, leading to a decrease in the work hardening rate as deformation progresses. Key mechanisms include the annihilation of dislocations with opposing Burgers vectors on the same or intersecting slip planes [108].

The balance between storage and exhaustion typically defines the stages of work hardening. In many metals, an initial stage of rapid hardening is followed by a relatively constant, high work hardening rate (linear hardening), where storage dominates. Subsequently, a decreasing work hardening rate as dynamic recovery/annihilation processes become more active [83]. Eventually, at large strains, the dislocation density may saturate when the rate of generation equals the rate of annihilation, leading to steady-state flow [109].

The rate of dislocation exhaustion is influenced by several factors, including temperature, strain rate, material properties like stacking faults energy, and the existing dislocation structure itself. The crystal plasticity models presented by Rohoman and Zhou [77] incorporate terms for dynamic recovery or annihilation to capture the evolution of dislocation density accurately. In PBF-LB/M materials, dynamic recovery and recrystallization processes occurring during the build process itself, driven by the intense thermal cycles, are thought to be paramount in controlling the initial yield strength [110]. Furthermore, interactions between dislocations and solute atoms can also influence hardening behavior, sometimes leading to phenomena like dynamic strain aging (DSA), which can cause fluctuations in the work hardening rate [83].

A particular notable finding from in-situ neutron diffraction studies on PBF-LB/M AlSi10Mg, by Zhang et al. [96], is the occurrence of significant dislocation annihilation during unloading stages. The magnitude of this annihilation increases with the amount of prior plastic

deformation experienced during unloading. Macroscopically, this phenomenon is associated with the observation of reverse plastic strain (Bauschinger effect) upon unloading. Microscopically, the annihilation is driven by the internal residual stresses that develop due to incompatible plastic deformation between different microstructural constituents (e.g., compressive stress in the Al matrix balanced by tensile stress in the Si phase). These internal stresses can drive the backward motion or rearrangement of dislocations, particularly screw dislocations, leading to their annihilation and a measurable decrease in the total dislocation density upon unloading [96], [111], [112], [113], [114], [115].

2.9 Melt Pool Boundaries (MPBs) vs. Melt Pool Interiors

2.9.1 MPBs vs. Interiors: Behavior Under Stress

The grain structure at MPBs can differ, sometimes featuring a thin layer of fine equiaxed grains formed at the solidification front, contrasting with the columnar grains often dominating the pool interior and growing along the thermal gradient [81]. Studies indicate that MPBs frequently act as mechanically weaker zones or preferential sites for strain localization and damage initiation under tensile loading [116], [117]. Direct measurements using nanoindentation by Chen et al. [100] have shown lower hardness-to-modulus ratios (H/E) at MPBs compared to interiors, suggesting that MPBs tend to yield plastically before the bulk of the melt pool. Digital image correlation (DIC) analyses by Zhu et al. [98] have revealed higher strain accumulation at MPBs compared to interiors, even in regions free from obvious defects. This localized strain is attributed to microstructural weakening effects at the boundary, such as potential strain recrystallization or Si phase precipitation/coarsening due to remelting and thermal cycling [98].

The consequence of this localized yielding and strain accumulation is that MPBs often become preferential sites for damage nucleation and propagation. Chen et al. [100] performed in-situ tensile testing combined with synchrotron-based X-ray microtomography and directly observed microvoid nucleation, growth, and coalescence occurring predominantly in the regions of MPBs. Fracture analyses have shown cracks initiating at defects (like pores, which can also be concentrated near MPBs) and then propagating along the MPB paths [116], [117]. Studies have demonstrated a direct correlation between the density (area fraction) of MPBs and the overall tensile ductility of PBF-LB/M AlSi10Mg. For example, Chen et al. [100] showed that reducing the area fraction of MPBs (e.g. by increasing hatch spacing while maintaining overall density)

leads to significant increase in elongation fracture. This strongly implies that MPBs act as detrimental features limiting ductility.

Furthermore, the geometric and microstructural discontinuity across the MPB interface creates inherent stress and strain concentrations. The mismatch in properties and deformation behavior between the yielding MPB region and the more resistant melt pool interior leads to localized stress build-up, further promoting plastic flow and damage initiation at the boundary [98].

2.9.2 MPBs vs. Interiors: GNDs Accumulation

The relatively higher localized strain at the MPBs and being the preferential sites for the initiation of plastic yielding creates sharp gradients in plastic strain across the interface between the yielding MPB zone and the adjacent, less-deformed melt pool interior. Maintaining lattice continuity across such a gradient geometrically necessitates the presence of higher density of GNDs localized within the MPB region [100]. Furthermore, potential crystallographic misorientation between the grains within the MPB/HAZ and the columnar grains of the interior provide another source requiring GND accommodation. The observed stress concentrations at MPBs [81] drive the localized plasticity that generates these GNDs. Therefore, based on the principles of crystal plasticity and the observed mechanical behavior, GNDs are expected to accumulate at significantly higher densities near MPBs compared to within the bulk of the melt pool interiors.

2.10 Dislocation Accumulation and Grain Refinement

The high dislocation densities generated during PBF-LB/M and subsequent plastic deformation play a crucial role in phenomena beyond just strengthening and hardening; they are intimately linked to processes of grain refinement. This is particularly relevant when considering post-processing techniques like severe plastic deformation (SPD) and advanced PBF-LB/M strategies aimed at producing finer, more equiaxed grain structures. Grain refinement during plastic deformation typically involves the transformation of the initial grain structure into smaller grains or subgrains bounded by high-angle grain boundaries (HAGBs). High densities of dislocations, especially GNDs, are the driving force behind this transformation. Several interrelated mechanisms contribute, including subgrain formation, misorientation increase, and dynamic recrystallization (DRX).

2.10.1 Subgrain Formation

Dislocations accumulated during deformation tend to rearrange into lower-energy configurations, forming arrays or walls that define regions of low crystallographic misorientation. These structures are known as low-angle grain boundaries (LAGBs) or subgrain boundaries [110]. The formation of such subgrains effectively subdivides the original larger grains. The strengthening effect of these LAGBs can be significant, sometimes described as a unified Hall-Petch relationship relating yield strength to subgrain size [118]. Snopiński et al. [99] observed the formation of new subgrain boundaries with misorientations in the range of 2 – 8° in ECAP-processed AlSi10Mg.

2.10.2 Misorientation Increase

Continued plastic deformation leads to further dislocation accumulation at these LAGBs. GNDs, in particular, contribute to progressive lattice rotation within the subgrains [70]. As more dislocations are incorporated into the LAGBs, the misorientation angle across the boundary increase. Eventually, when the misorientation exceeds a critical value (typically ~15°), the LAGB transforms into a HAGB, effectively creating new, smaller grains [119]. Intensive dislocation accumulation during SPD has been directly linked to grain size reduction down to the sub-micrometer scale (e.g., ~500 nm after a single ECAP pass) [99].

2.10.3 Dynamic Recrystallization (DRX)

Under conditions of high strain, high temperature, or very high stored energy associated with extremely high dislocation densities, dynamic recrystallization can occur [120]. DRX involves the nucleation and growth of new, strain-free grains within the deformed microstructure, consuming the deformed structure and leading to significant grain refinement and often texture modification. Evidence of DRX has been observed in PBF-LB/M alloys subjected to methods like KoBo extrusion, which resulted in a nearly dislocation-free, refined grain structure (~1.1 μm) with an increased fraction of HAGBs and specific recrystallization textures [80]. Even during ECAP processing, Snopiński et al. [99] have reported evidence of DRX alongside conventional dislocation-driven refinement mechanisms.

More importantly, the fine cellular structure plays an active role in the grain refinement process. The dense network of Al/Si cell boundaries acts as extremely effective obstacles to dislocation motion [79]. This promotes intense dislocation accumulation and interaction,

particularly near the boundaries, accelerating the formation of dislocation tangles, cell walls, and subgrain structures [99]. The constraints imposed by the cell walls also lead to localized lattice rotations and likely enhance GND generation, further driving the increase in misorientation across developing boundaries [81]. Direct observations using high-resolution Kikuchi diffraction after ECAP processing have shown that the Al/Si cellular walls themselves develop increased lattice orientation spread and contribute significantly to the overall grain refinement process [99].

2.11 Severe Plastic Deformation (SPD) and Strengthening Mechanisms

Severe plastic deformation (SPD) techniques involve imposing extremely large plastic strains on a material, sometimes without significant changes in the overall dimensions, to induce substantial microstructural refinement and modification [80]. Applying SPD to PBF-LB/M AlSi10Mg offers a potential pathway to overcome some of its inherent limitations, such as low ductility and defect sensitivity. Several SPD methods have been explored for post – processing PBF-LB/M Al-Si alloys. The most commonly studied SPD technique for PBF-LB/M AlSi10Mg/AlSi12 is equal channel angular pressing (ECAP). It involves pressing a billet through a die containing two channels of equal cross-section intersecting at an angle (typically 90° or 120°), imposing large shear strains [80]. Multiple passes can be applied to accumulate strain. Another SPD technique applied to this alloy is high pressure torsion (HPT). This method involves subjecting a thin disk-shaped sample to high pressure and concurrent torsional straining [121]. It can achieve very high strains and significant refinement but is limited to small sample sizes. Other techniques such as KoBo extrusion (involving an oscillating die) [122] and multi-axial forging [80] have also been investigated for PBF-LB/M AlSi10Mg, offering different strain paths and microstructural outcomes.

2.11.1 SPD Microstructural Evolution

SPD processing induces dramatic changes in the PBF-LB/M AlSi10Mg microstructure. The most significant effect is substantial grain refinement, often reaching the ultra-fine grained (UFG, < 1 μm) or even nanocrystalline (NC, < 100 nm) regime [80], [122]. For example, average grain sizes around 500 nm after one ECAP pass [99] and 240 nm after two ECAP passes [123] have been reported. This refinement occurs through the generation and accumulation of dislocations, which rearrange into LAGBs or subgrains. Multi-axial forging was reported to produce extremely fine subgrains [80]. Furthermore, the intense plastic deformation breaks down

the original PBF-LB/M cellular structure. The interconnected Si network is fragmented into finer, more dispersed particles, and the distinct α-Al cells are refined or eliminated [123].

SPD initially leads to a massive increase in dislocation density. However, depending on the processing temperature and accumulated strain, dynamic recovery or even dynamic recrystallization processes can occur, potentially leading to a saturation or even decrease in dislocation density in later stages [80]. Techniques like KoBo extrusion, involving cyclic strain paths, might result in a refined structure with relatively low stored dislocation density [80]. SPD processes involving hydrostatic pressure components, such as ECAP or HPT, can effectively reduce or eliminate the porosity inherent in the as-built PBF-LB/M material through pore collapse and closure [123]. This densification contributes to improved mechanical properties.

2.11.2 Strengthening Mechanisms

The yield strength (σ_y) of a metallic material is often modeled as a linear superposition of the intrinsic lattice friction stress (σ_0) and the strength increments ($\Delta\sigma_i$) from various microstructural features that impede dislocation motion according to **Equation 1** [123].

$$\sigma_y = \sigma_0 + \sum \Delta\sigma_i \tag{1}$$

For PBF-LB/M AlSi10Mg, the primary strengthening contributions ($\Delta\sigma_i$) typically considered are solid solution strengthening ($\Delta\sigma_{ss}$), grain boundary strengthening ($\Delta\sigma_{gb}$), precipitation or dispersion strengthening ($\Delta\sigma_{or}$ or $\Delta\sigma_{eutectic}$), and dislocation strengthening ($\Delta\sigma_{dis}$). The friction stress (σ_0) of pure aluminum is relatively small (e.g., ~5.5 MPa [124] or ~ 35 MPa [125]) and sometimes neglected or combined with other terms.

2.11.2.1 Solid Solution Strengthening ($\Delta\sigma_{ss}$)

The presence of solute atoms (Si, Mg) dissolved in the α-Al matrix creates local lattice distortions and strain fields that interact with the stress fields of dislocations, impeding their movement [53]. The strengthening effect is typically modeled by **Equation 2**.

$$\Delta\sigma_{ss} = \sum_i k_i C_i^m \tag{2}$$

Where k_i is the strengthening coefficient for solute i, C_i is the concentration of solute i in solid solution (wt% or at%), and m is an exponent, frequently taken as 1 or 2/3 [124]. Some studies place this contribution higher depending on the assumed concentrations and model [126]. Nonetheless, it is reported in the literature that this contribution is significantly reduced upon heat treatment as Si and Mg precipitate out of the solid solution [127].

2.11.2.2 Grain/Cell Boundary Strengthening (Hall-Petch) ($\Delta\sigma_{gb}$)

This mechanism describes the strengthening effect arising from boundaries hindering dislocation motion. The classical Hall-Petch equation relates the strength increase ($\Delta\sigma_{HP}$) to the inverse square root of the characteristic barrier spacing, d, according to **Equation 3**.

$$\Delta\sigma_{HP} = k_{HP} d^{-1/2} \tag{3}$$

Where k_{HP} is the Hall-Petch coefficient, a material constant [123]. For aluminum alloys, k_{HP} is typically in the range of 0.04 – 0.07 MPa·$m^{1/2}$ [124]. In the context of PBF-LB/M AlSi10Mg, due to the ultra-fine cellular structure (cell size $\lambda \approx 0.5$ μm) being significantly smaller that the grain size (d ≈ several μm), the cell boundaries are considered the dominant barriers limiting dislocation mean free path within grains. Therefore, the Hall-Petch relationship is often applied using the cell size instead of the grain size [123]. Similar to the solid solution strengthening ($\Delta\sigma_{ss}$), this contribution also diminishes after heat treatment that cause cell coarsening or grain growth [127].

2.11.2.3 Precipitation/Dispersion Strengthening (Orowan, $\Delta\sigma_{or}$ or $\Delta\sigma_{eutectic}$)

This mechanism accounts for the stress required for dislocations to bypass non-shearable second-phase particles [53]. In PBF-LB/M AlSi10Mg, the relevant obstacles are the eutectic Si network/particles at cell boundaries and the nano-sized precipitates within the cells. The Orowan strengthening contribution is commonly estimated using equations of the form given in **Equation 4**.

$$\Delta\sigma_{or} = M \frac{CGb}{\lambda_p} \ln\left(\frac{d_p}{r_0}\right) \tag{4}$$

Where M is the Taylor factor (~3.06 for FCC), G is the shear modulus of the matrix (~26 GPa for Al), b is the Burgers vector (~0.286 nm for Al), d_p is the effective particle diameter, λ_p is the

effective interparticle spacing on the slip plane, r_0 is the dislocation core radius, and C is a constant related to dislocation line tension [16].

It is worth noting that applying this model to PBF-LB/M AlSi10Mg comes with some challenges. Firstly, there is the challenge of dual obstacle population, where both the interconnected eutectic Si network and the discrete nano-precipitates contribute [128]. Their effects might need separate calculation or combined effective parameter approach. Additionally, determining approprioate values for d_p and λ_p for the continuous eutectic Si network is difficult and requires simplification, often relating them to the cell size or Si particle characteristics observed in 2D sections [16]. λ_p is related to the particle volume fraction (f) and size (d_p) roughly as $\lambda_p \approx d_p\left(\sqrt{\frac{\pi}{4f}} - 1\right)$ or simpler geometric relationships.

Despite these challenges, Orowan strengthening from the Si phase (particularly the network) is generally considered a major contributor to the high strength of PBF-LB/M AlSi10Mg [123].

2.11.2.4 Dislocation Strengthening ($\Delta\sigma_{dis}$)

The high density of dislocations present in the PBF-LB/M AlSi10Mg alloy acts as obstacles to the motion of other dislocations through entanglement and stress field interactions [95]. This contribution is typically described by the Taylor hardening model given in Equation 5.

$$\Delta\sigma_{dis} = M\alpha Gb\sqrt{\rho} \tag{5}$$

Where M is the Taylor factor, α is a constant (typically 0.2 – 0.5 for FCC), G is the shear modulus, b is the Burgers vector and ρ is the dislocation density (usually the sum of GNDs density and SSDs density). Given the high initial dislocation densities reported for PBF-LB/M AlSi10Mg, this mechanism provides a significant contribution to the as-built yield strength.

2.12 Objectives

The primary objective of this research is to elucidate the fundamental deformation mechanisms governing the mechanical properties of heterogeneous PBF-LB/M fabricated AlSi10mg alloys with competing material- and deformation-induced size effects. This investigation aims to enable the synthesis of novel Al-Si alloys that overcome traditionally limiting property combinations, specifically achieving both high strength and enhanced ductility simultaneously. In contemporary materials science and industry, alloys exhibiting exceptional strength while maintaining significant ductility represent a critical frontier for advanced structural applications. Conventionally, these properties exist in an inverse relationship, where improvements in strength typically occur at the expense of ductility. This trade-off stems from the fact that strengthening mechanisms often impede the microstructural features necessary for ductility. Despite numerous research efforts to reconcile these competing properties, designing metallic components that successfully combine both remains a significant challenge in materials engineering.

2.12.1 Research Approach

This research leverages the inherent heterogeneous microstructure of additively manufactured AlSi10Mg alloys, characterized by domains with substantially different flow stresses – specifically the 'soft' aluminum core and 'hard' silicon shell. During deformation, this microstructural heterogeneity generates inhomogeneous stress and strain partitioning between phases, resulting in heterogeneous distribution of plastic strains across phase interfaces. The interaction between these distinct phases necessitates the generation of geometrically necessary dislocations (GNDs) at phase interfaces to accommodate plastic strain gradients, potentially enhancing dislocation storage capacity and contributing significantly to strain hardening.

The methodology for developing high-strength, ductile Al-Si alloys in this research integrates three sequential processes:

- Laser-based powder bed fusion of metals (PBF-LB/M) manufacturing to establish the initial heterogeneous microstructure
- Targeted heat treatments designed to optimize microstructural gradients and enhance deformability
- Severe plastic deformation (SPD) processing to further refine the microstructure

2.12.2 Specific Objectives

The research will systematically address the following specific objectives:

1. **To systematically tailor the initial as-built microstructure through targeted low-temperature annealing (LTA) protocols.** This involves creating distinct microstructural starting conditions with varying degrees of Si network continuity, ranging from a fully intact cellular network to a partially ruptured network and a fragmented, spheroidized particulate structure. This objective seeks to precisely control the initial balance between network-derived strength and matrix ductility as a prerequisite for subsequent deformation processing.
2. **To conduct a comprehensive investigation into the deformation mechanisms as a function of the initial microstructural state and the mode of deformation.** This will be accomplished by:
    - Correlating the evolution of the dislocation substructure under gradual deformation with the macroscopic strain hardening response. This includes quantifying the relative contributions of statistically stored dislocations (SSDs) and geometrically necessary dislocations (GNDs) using multi-scale characterization techniques.
    - Analyzing the kinematic hardening behavior and the evolution of internal back stress through cyclic loading-unloading-reloading (LUR) tests to mechanically probe the influence of Si network continuity on long-range internal stress development.
3. **To develop and validate an optimized severe plastic deformation (SPD) processing route for achieving an unparalleled combination of strength and ductility.** This objective will focus on:
    - Evaluating the effectiveness of different SPD techniques, namely Equal Channel Angular Pressing (ECAP) and Twist Channel Angular Pressing (TCAP), on microstructural refinement and mechanical properties.
    - Establishing a viable processing window by investigating the influence of critical SPD parameters, including processing temperature and the number of deformation passes.

- Defining a complete, synergistic thermomechanical pathway that leverages the pre-conditioned microstructure to maximize the benefits of SPD while avoiding detrimental failure mechanisms.

Chapter Three

3.0 Methodology

This chapter presents the experimental approach undertaken in this research. The experimental design is centered on the Materials Science paradigm, which states that a material's properties are a direct function of its microstructure, which is in turn controlled by its processing history [129]. This relationship is fundamental to achieving desired characteristics in the industrial manufacturing of metallic products, as the control of process parameters is essential for obtaining a suitable microstructure that dictates the final mechanical properties [129], [130]. This research systematically explores each element of this paradigm to achieve a superior balance of strength and ductility in PBF-LB/M AlSi10Mg. The experimental approach is divided into four phases as outlined in **Figure 11**.

1. **Initial Additive Manufacturing and Material Selection – Comparative study**

This phase focuses on comparing different Al-Si alloy systems and choosing an alloy composition with the most desirable combination of as-built properties spanning microstructure, hardness and most importantly, defects. This phase takes into account initial characterization of powders of AlSi7Mg, AlSi10Mg, and AlSi12Mg. It then proceeds to fabricate parts from these powders using PBF-LB/M technology. The fabricated parts are then characterized and compared and an alloy composition, AlSi10Mg is selected as the focus of the thesis.

2. **Sample Conditioning: Creating three initial states**

In this phase, the as-built PBF-LB/M AlSi10Mg samples are divided and subjected to different LTA treatments to create different microstructural states for deformation studies.

3. **Deformation Processing**

In this phase, samples from all three initial conditions are subjected to various deformation techniques to study microstructural evolution and mechanical response. The two main approaches explored in this phase are gradual deformation, through compression studies at progressive strains: 5%, 20%, and maximum failure strain. The second is severe plastic deformation using ECAP and TCAP over a range of processing temperatures from ambient temperature to 450 °C.

4. **Comprehensive Characterization**

This phase uses a multi-faceted approach to analyze the materials after each processing step. The comprehensive suit encompasses microstructural analysis, mechanical testing and phase and dislocation analysis.

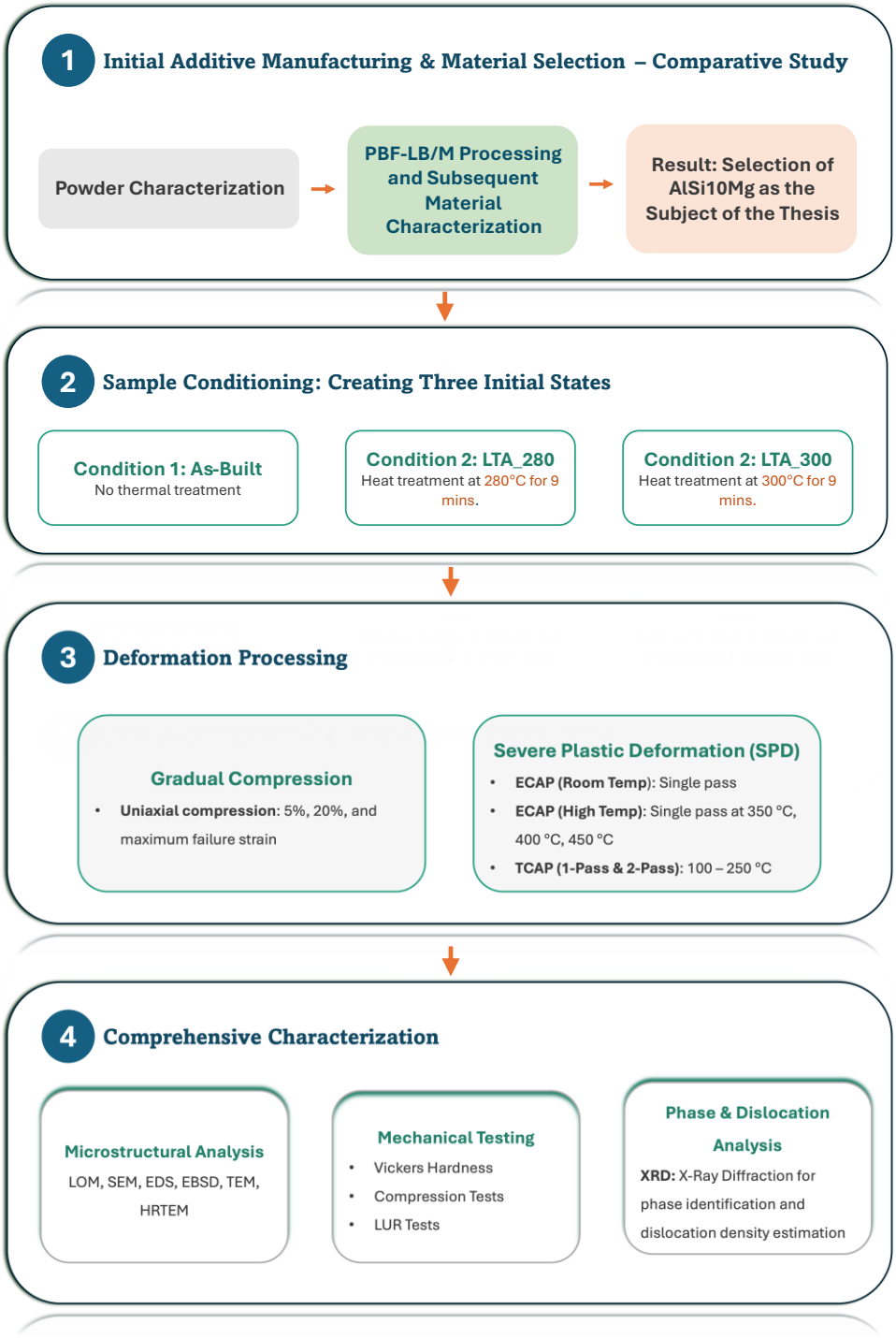

Figure 11. Visualization of the various experimental phases of the research

3.2. PBF-LB/M Sample Fabrication

The studied Al-Si alloy samples were fabricated using the Laser-based powder fusion of metals (PBF-LB/M) technique. The manufacturing process was conducted on a Trumpf TruPrint system, equipped with a high-precision ytterbium fiber laser, for fabricating parts from Al-Si powder systems. Prior to the build, the system's build chamber was purged with high-purity argon gas to ensure an oxygen concentration below 0.02%, minimizing oxidation during the melting and solidification of the powder. The key processing parameters were as follows:

- Laser power: 175 W
- Layer thickness: 20 µm
- Laser scan speed: 1400 mm/s
- Scan strategy: Zigzag pattern with a 67° rotation between successive layers

The printed samples were produced in two geometrical configurations to suit different experimental procedures:

- Cuboidal samples: Dimensions of 15 mm × 15 mm × 60 mm were prepared primarily for microstructural analysis, thermal treatments, high temperature ECAP processing, TCAP processing (single and double pass(es)) and hardness evaluations.
- Cylindrical samples: Dimensions of 10 mm diameter × 60 mm height were fabricated for room temperature ECAP experiments.

The quality and surface finish of the fabricated specimens are shown in **Figure 12**.

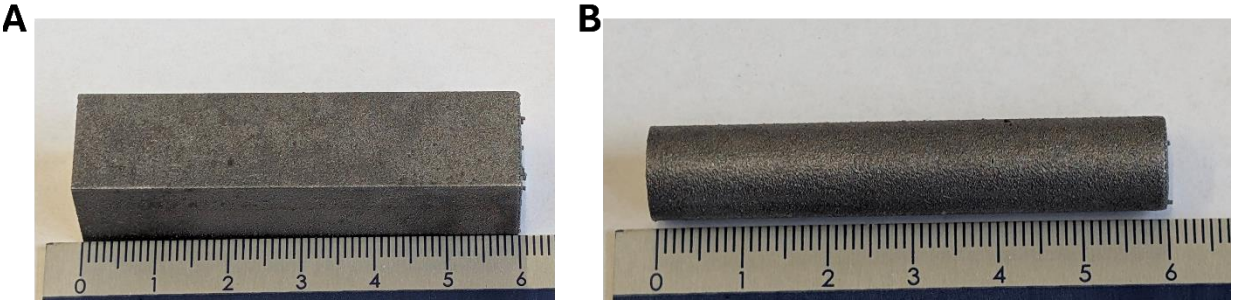

Figure 12. PBF-LB/M fabricated AlSi10Mg samples. A. Cuboidal sample with dimensions 15 mm x 15 mm x 60 mm and **B.** Cylindrical sample with 15 mm diameter and 60 mm height, used for ECAP processing

3.3. Heat Treatment

Initial post-processing of the PBF-LB/M fabricated AlSi10Mg samples was carried out through low-temperature annealing (LTA) for controlled modification of the eutectic cellular structure prior to SPD. The annealing treatments were performed in a laboratory-grade resistance furnace, under a continuous flow of argon gas to maintain an inert atmosphere and suppress surface oxidation during the thermal cycle. Two distinct heat treatment protocols were employed to investigate the effect of thermal exposure on microstructural evolution. The first batch of specimens was annealed at 280 °C for 9 minutes, designated as LTA_280. The thermal profile for this treatment is illustrated in **Figure 13A**. A second group of specimens underwent annealing at 300 °C for 30 minutes and was labeled LTA_300. The thermal profile for this treatment is shown in **Figure 13B**. All samples were furnace-heated at the respective treatment temperatures and subsequently air-cooled to room temperature prior to further processing.

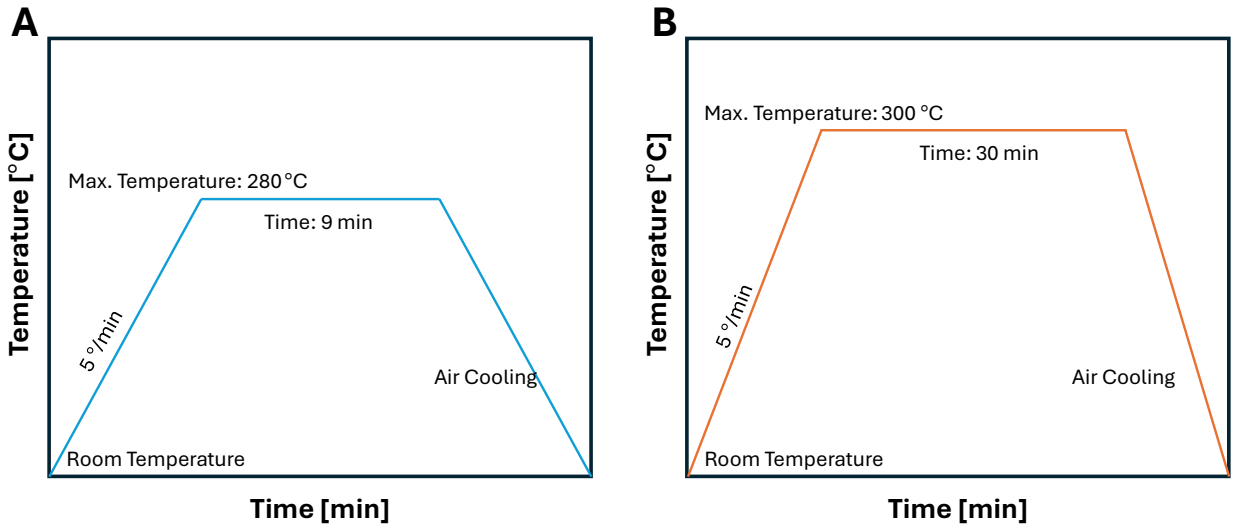

Figure 13. Schematic illustrations of the heat treatment profile A. LTA_280 condition, and **B**. LTA_300 condition (unscaled axes: for illustration purposes)

3.4 Microhardness Testing

To evaluate the local mechanical response and assess the influence of post-processing treatments on structural uniformity, Vickers microhardness testing was carried out along the cross-sections of all samples – As-built, heat-treated, and SPD-processed. Measurements were performed immediately following standard metallographic preparation, and right after final polishing using colloidal silica to ensure a mirror-like finish suitable for indentation testing. Microhardness measurements were conducted using a FM-ARS 9000 microhardness tester (FTC Tokyo, Japan). A constant load of 300 grams (2.94 N) was applied for each indentation, with a dwell time of 15 seconds to ensure full load application and accurate diagonal measurement. However, the load was reduced to 100 grams for the high temperature ECAP processed samples, due to their relatively "softer" nature after this post-processing treatment.

For spatial resolution of local hardness variations, an 8 × 8 matrix indentation pattern was employed across each sample's cross-section as shown schematically in **Figure 14**. The step size between adjacent indentations was fixed at 0.2 mm in both the horizontal and vertical directions. This grid-based approach was intended to capture heterogeneities in hardness due to melt pool morphology, microstructural variation, and the presence of residual stress or second-phase particulates.

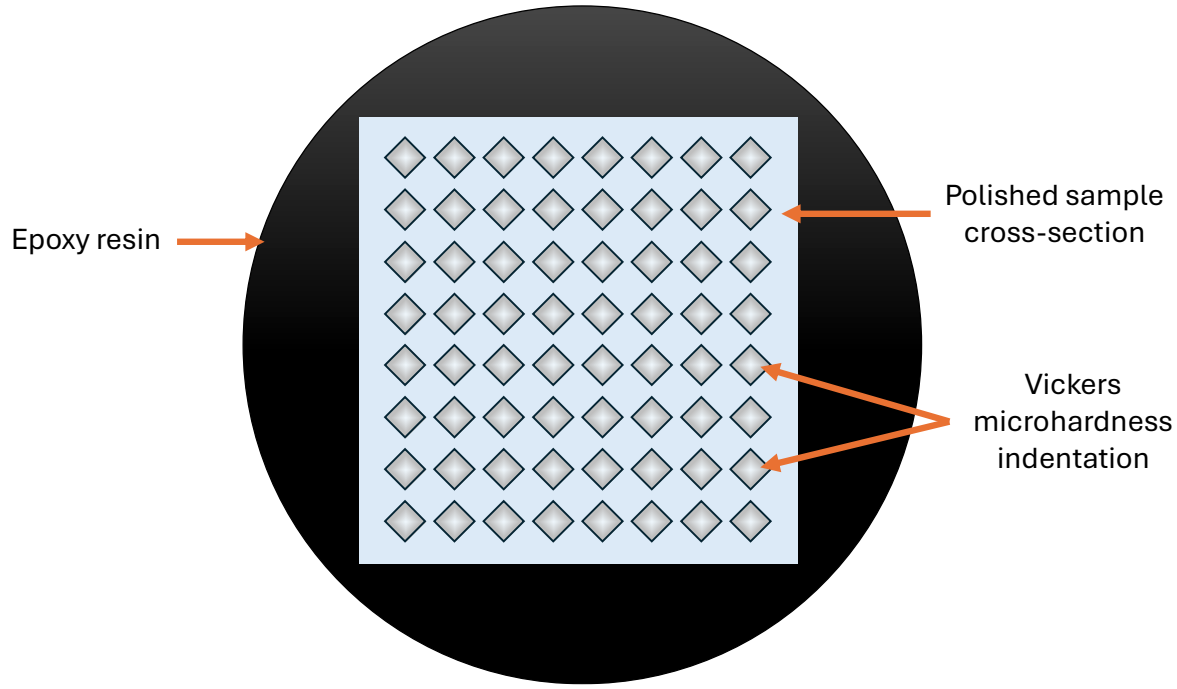

Figure 14. Schematic diagram of microhardness measurement approach

3.5. Compression Testing

To evaluate the mechanical response and deformation behavior of the PBF-LB/M fabricated and post-processed AlSi10Mg alloy samples, room temperature uniaxial compression tests were conducted using a Zwick/Roell Z020 universal testing machine (**Figure 15**). Cylindrical specimens with diameter of 6 mm and height of 9 mm (**Figure 16**) were machined from the As-built, heat-treated (LTA_280 and LTA_300), and SPD-processed (ECAP and TCAP) samples. All specimens were oriented such that the loading direction was aligned with the build direction to capture the anisotropic mechanical behavior arising from the layer-wise fabrication inherent to PBF-LB/M processing. To monitor the evolution of mechanical properties during deformation, tests were performed up to three different engineering strain levels:

- 5% strain
- 20% strain
- Until failure

Digital images of the samples after each compressive strain are shown in **Figure 17**.

In addition to uniaxial compression tests, cyclic loading-unloading-reloading (LUR) compression tests were performed to assess the kinematic hardening behavior and to estimate the evolution of back stress during plastic deformation. The same cylindrical specimen geometry and orientation were used. In each LUR cycle, the sample was compressed to a pre-defined strain, unloaded to near-zero loads, and then reloaded to a higher strain level in the subsequent cycle. Multiple LUR cycles were performed incrementally, until failure, to capture the strain evolution of the back stress. The area enclosed between the unloading and reloading curves in each cycle was used to estimate the Bauschinger effect and evaluate the strain path sensitivity of the material under compressive deformation.

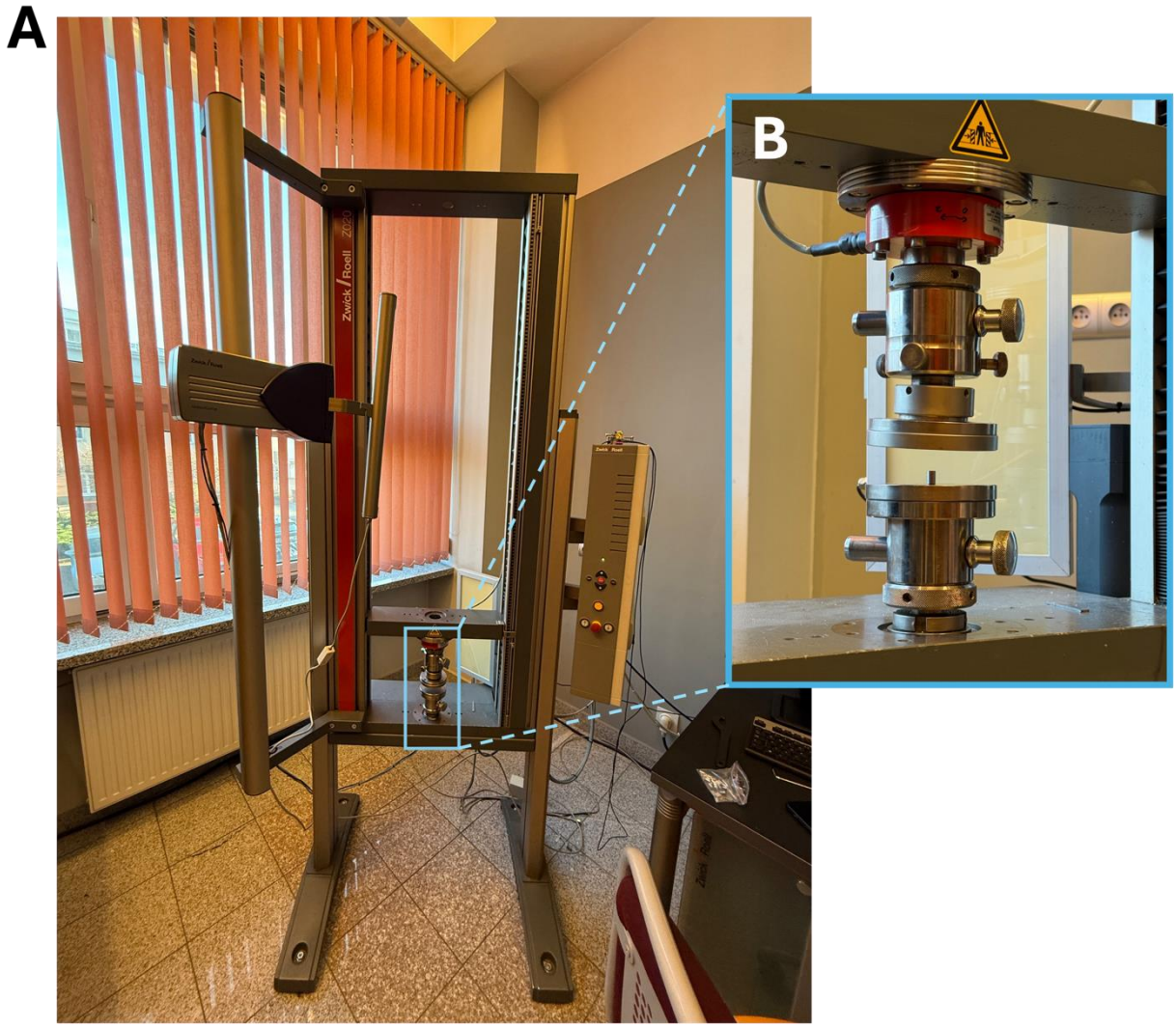

Figure 15. **Zwick/Roell Z020 universal testing machine used for compression testing**. **A**. View of the machine in the laboratory, and **B**. A closeup view of the crosshead of the compression testing system with a sample mounted on the lower head.

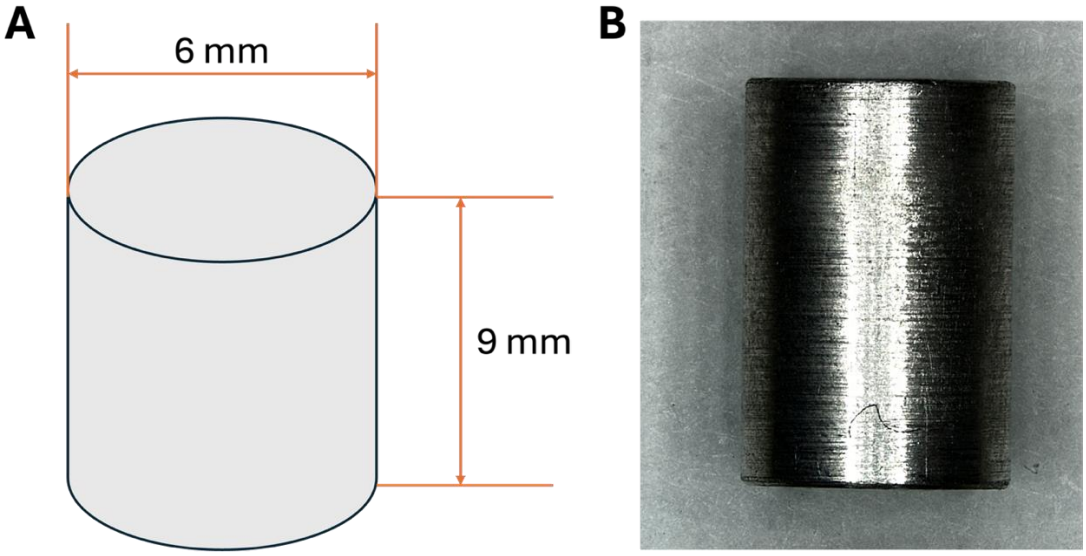

Figure 16. Compression testing specimen A. Dimensions of machined specimens used for compression testing and **B**. A digital image of the sample ready for compression testing.

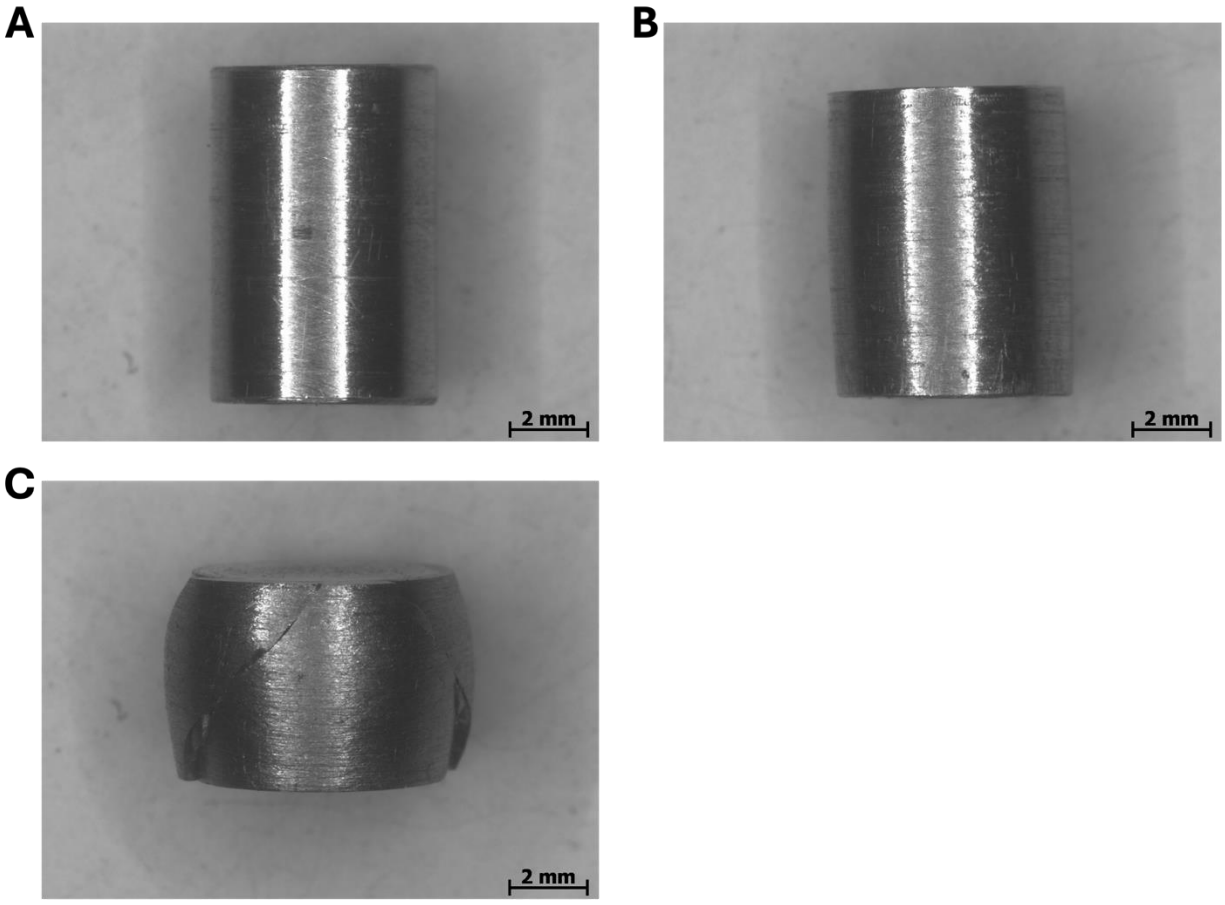

Figure 17. Images of specimens after compression testing **A**. After 5% strain, **B**. After 20% strain, and **C**. After maximum strain to failure.

3.6. Equal Channel Angular Pressing (ECAP)

3.6.1. Room Temperature ECAP processing

To investigate the influence of room temperature severe plastic deformation on the microstructure and mechanical behavior of PBF-LB/M fabricated AlSi10Mg alloys, ECAP was employed as a post-processing technique. The process was conducted using a custom-fabricated ECAP die designed with a channel intersection angle (φ) of 120° and an outer curvature angle (ψ) of 20°. A schematic diagram of this setup is shown in **Figure 18**.

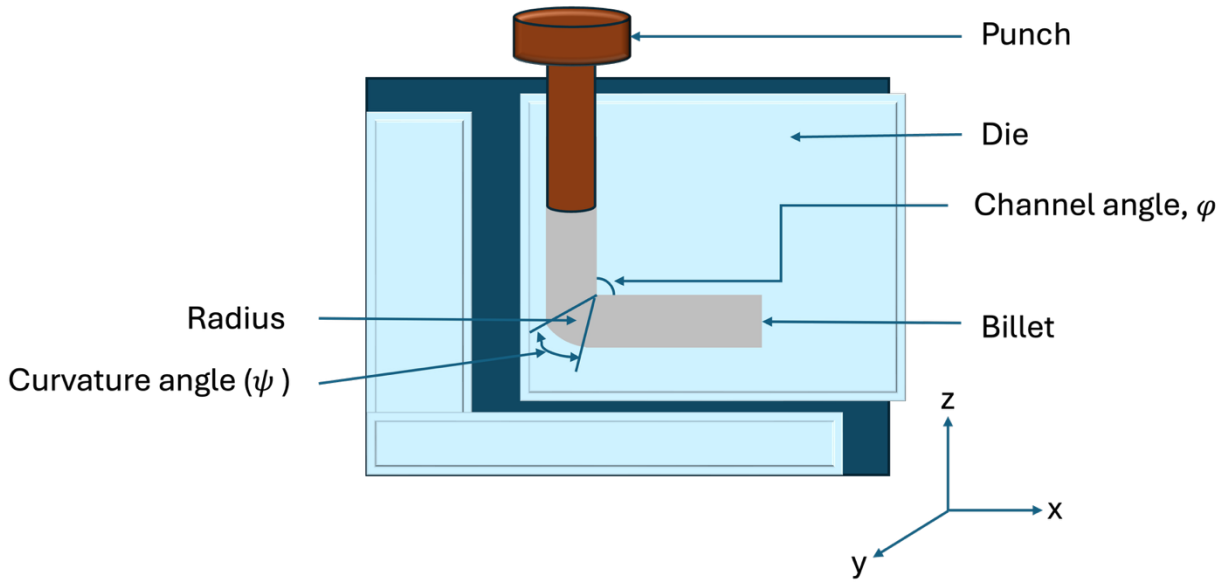

Figure 18. Schematic diagram of ECAP setup

Each sample was subjected to a single ECAP pass at ambient temperature. To minimize friction and material-die interaction during processing, the contact surfaces of both the die and the specimens were coated with a graphite-based lubricant prior to deformation. The accumulated plastic strain introduced by ECAP was estimated using the standard analytical expression for simple shear in angular channels, given by **Equation 6**:

$$\varepsilon_N = N\left[\frac{2}{\sqrt{3}} \cdot \cot\left(\frac{\varphi}{2}+\frac{\psi}{2}\right) + \psi \csc\left(\frac{\varphi}{2}+\frac{\psi}{2}\right)\right] \quad (6)$$

Where ε_N is the von Mises plastic strain, and *N* represents the number of ECAP passes. Based on this configuration, the equivalent von Mises equivalent plastic strain introduced per pass was calculated to be approximately 0.63.

3.6.2 High Temperature ECAP processing

High-temperature ECAP processing was carried out using a LabTest 5.2000 CT hydraulic press (**Figure 19**). The press is equipped with a maximum ram speed of 400 mm/min, which was regulated through an integrated servo valve-controlled oil pressure system, driven by an electric motor. This setup enabled consistent and repeatable pressing conditions during ECAP deformation.

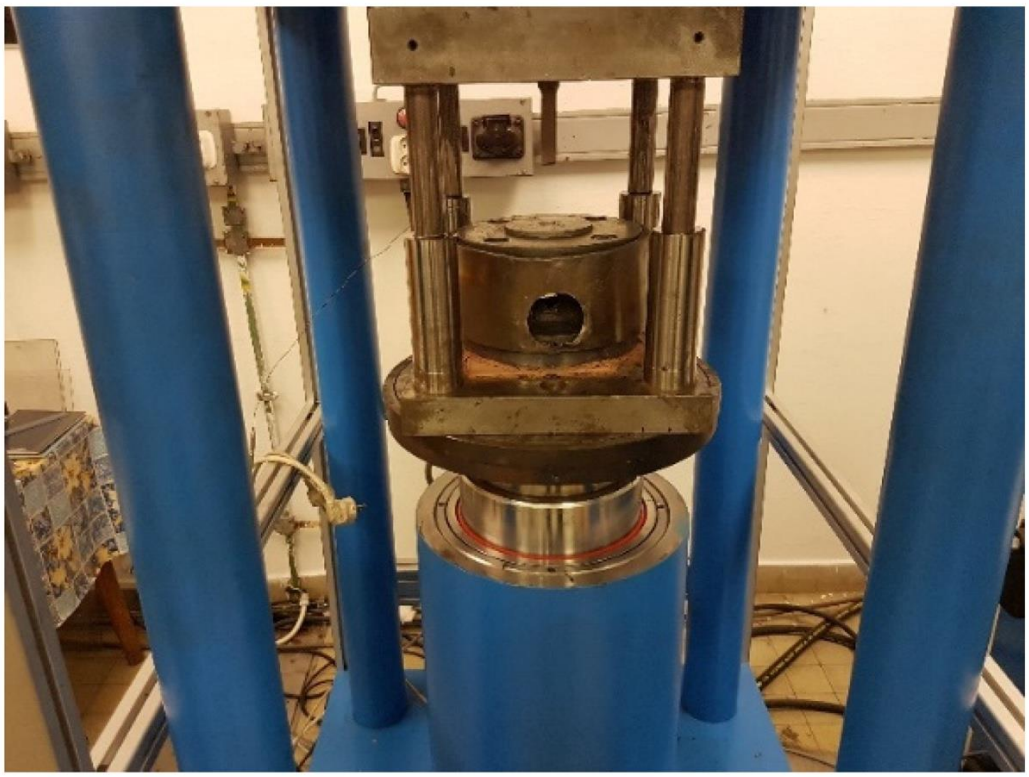

Figure 19. View of the LabTest 5.2000 CT hydraulic press workstation for material forming using high temperature ECAP process

The ECAP experiments were conducted at three elevated temperatures: 350 °C, 400 °C, and 450 °C, to investigate the influence of temperature on microstructural evolution and mechanical properties of the PBF-LB/M fabricated AlSi10Mg alloy. Heating of the die and the specimen was achieved using a dTRON 304 temperature controller, interfaced with a NiCr-Ni thermocouple, which provided precise thermal feedback and control. This thermal system was capable of reaching and maintaining temperatures up to 1350 °C, ensuring uniform heating

throughout the ECAP process. Given the significant role of friction in ECAP, particularly at high temperatures, appropriate lubrication was essential to prevent uneven flow, die sticking, or sample damage. Therefore, Nicro-Thermocup 1200, a high-temperature-resistant lubricant, was applied at the interface between the die and the sample.

3.7 Twist Channel Angular Pressing (TCAP)

The TCAP process was similarly employed to impart severe plastic deformation to the PBF-LB/M fabricated AlSi10Mg samples, with the aim of modifying their microstructure and improving mechanical properties at higher-than-ambient temperatures, below the alloy's eutectic temperature. All samples were subjected to a two-pass TCAP sequence. During the first pass, deformation was carried out at 100 °C for all sample conditions, including the as-built and LTA states. For the second pass, the deformation temperature was increased due to the significantly higher flow stress encountered during reprocessing. Specifically, the as-built samples were processed at a temperature of 250 °C and the heat-treated (LTA_280 and LTA_300) samples were processed at 150 °C. The increase in processing temperature during the second pass was necessitated by the elevated resistance encountered during deformation of previously processed samples. This adjustment was critical to avoid damage to the samples and die components, particularly for the non-heat-treated as-built samples, which exhibited the highest resistance due to their work-hardened microstructure.

The TCAP experiments were conducted using a hydraulic press with a maximum load capacity of 1600 kN. The PBF-LB/M samples with cuboidal geometry were pressed at a constant ram speed of 2 mm/s, following route A; a deformation route where no rotation is applied between successive passes. The TCAP die used in this study featured two intersecting channels with a 90° internal channel angle (φ) and a 9° curvature angle (ψ). Unlike traditional ECAP dies, the TCAP die incorporated a helical twist in the horizontal channel (**Figure 20**), designed to induce additional torsional strain during processing. This configuration results in a higher imposed equivalent strain per pass, calculated as $\varepsilon \approx 1.23$.

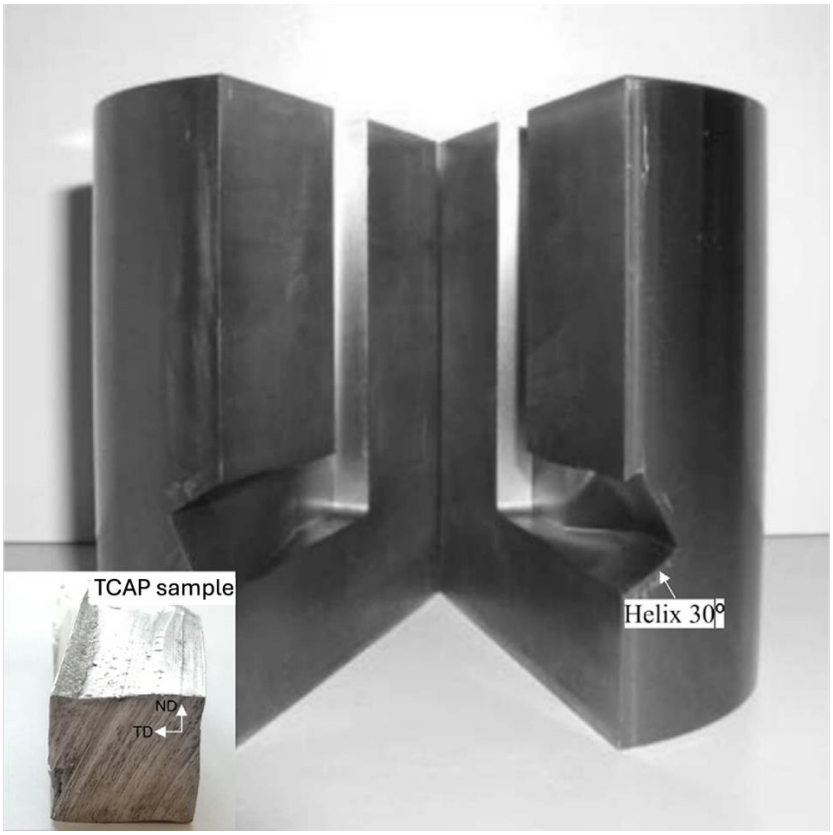

Figure 20. Twist Channel Angular Pressing Setup with a rotary channel (30° helix)

A summary of the sample designation used throughout the thesis and their post-processing conditions is presented in **Table 3**

Table 3. Investigated samples and their respective post-processing conditions

Sample	Heat Treatment	SPD	SPD Temperature	Number of SPD Passes
As-built	–	–	–	–
LTA_280	280 °C/9 minutes	–	–	–
LTA_300	300 °C/30 minutes	–	–	–
As-built_ECAP	–	ECAP	Ambient	1
As-built_ECAP350	–	ECAP	350 °C	1
As-built_ECAP400	–	ECAP	400 °C	1
As-built_ECAP450	–	ECAP	450 °C	1
LTA_280_ECAP	280 °C/9 minutes	ECAP	Ambient	1
LTA_300_ECAP	300 °C/30 minutes	ECAP	Ambient	1
As-built_1TCAP	–	TCAP	100 °C	1
LTA_280_1TCAP	280 °C/9 minutes	TCAP	100 °C	1
LTA_300_1TCAP	300 °C/30 minutes	TCAP	100 °C	1
As-built_2TCAP	–	TCAP	250 °C	2
LTA_280_2TCAP	280 °C/9 minutes	TCAP	150 °C	2
LTA_300_2TCAP	300 °C/30 minutes	TCAP	150 °C	2

3.8 Powder Particle Size Analysis

The particle size distribution of the as-received AlSi10Mg powder was analyzed using a laser diffraction particle size analyzer, specifically the ANALYSETTE 22 (Fritsch, East Windsor, NJ, USA). Prior to measurement, the powder was ultrasonically dispersed in a suitable liquid medium to minimize agglomeration and ensure accurate particle size detection. The system utilizes laser diffraction principles to measure a wide range of particle sizes, providing statistical parameters such as d_{10}, d_{50}, and d_{90}, which represent the particle diameters below which 10%, 50%, and 90% of the sample volume exists, respectively.

3.9 Microstructural Characterization

3.9.1 Sample Preparation and Etching

For metallographic examination, samples were sectioned along their cross-sections (X-Y and X-Z planes) using a precision cutting machine. The sectioned samples were then mounted in epoxy resin. Surface preparation was performed using an automated grinding and polishing system, adhering to a sequential protocol. Initial grinding was carried out using SiC abrasive papers with grit sizes of 600, 1200, and 2000, followed by polishing with diamond suspensions of decreasing particle size: 9 µm, 6 µm, 3 µm, and 1 µm. A final polishing stage was conducted using 0.04 µm colloidal silica to achieve a mirror-like finish. To reveal microstructural features, chemical etching was performed using Keller's reagent, composed of 95 ml H_2O, 2.5 ml HNO_3, 1.5 ml HCl, and 1.0 ml HF. The etching duration was 20 ± 5 seconds.

3.9.2 Optical and Scanning Electron Microscopy

Post-etching, microstructural analysis was conducted using both light optical (LOM) and scanning electron microscopy (SEM) techniques. LOM was performed using the AxioVision system (ZEISS, Jena, Germany) primarily for identification of mesoscale microstructural features such as melt pool (MP) and melt pool boundaries (MPBs). For high-resolution imaging and detailed surface morphology evaluation, SEM, specifically the EVO 15 MA series SEM was employed. SEM imaging facilitated the identification of microstructural features such as cellular structures, and the distribution of Si-rich phases.

To determine grain orientation, size, and for kernel average misorientation (KAM) analysis, electron backscatter diffraction (EBSD) was carried out within the SEM framework. EBSD measurements were conducted at an accelerating voltage of 20 kV and a step size of 0.2 µm.

3.9.2 Transmission Electron Microscopy (TEM)

For nanoscale structural analysis, transmission electron microscopy (TEM) was conducted. Thin lamellae (approximately 120 nm thick) were prepared using focused ion beam (FIB) milling, performed along the build direction using gallium (Ga) ion milling. The prepared lamellae were analyzed using a Titan 80-300 FEI S/TEM, operated at an accelerating voltage of 300 kV. The system was equipped with high-resolution TEM (HRTEM) and energy-dispersive X-ray spectroscopy (EDS) for atomic-scale imaging and elemental analysis, respectively. Electron

diffraction patterns were analyzed using Gatan Digital Micrograph and CrystBox software, allowing for crystallographic indexing and phase identification.

3.9.3 X-Ray Diffraction (XRD) Analysis

Crystallite size and dislocation density were evaluated using X-ray diffraction (XRD). The analysis was performed using a PANalytical X'Pert Pro diffractometer (Malvern Panalytical Ltd., Almelo, The Netherlands), operated with a cobalt anode X-ray source (KαCo, $\lambda = 0.179$ nm), at 40 kV and 30 mA. Scans were conducted in the Bragg-Brentano geometry, covering a 2θ range of 30° – 100°, with a step size of 0.05° and a count time of 100 s per step. Resulting diffractograms were processed using X'Pert HighScore Plus software (version 3.0e), and phase identification was conducted using databases from the Inorganic Crystal Structure Database (ICSD) provided by FIZ Karlsruhe.

3.9.4 Porosity Analysis

The internal porosity characteristics of the printed components were evaluated using a combination of image-based analysis and X-ray computed tomography (CT). This approach enabled the detailed visualization and quantification of pore morphology, size distribution, and spatial distribution throughout the volume of the samples. Image based analysis employed LOM imaging and further quantification using ImageJ software. The CT scans were carried out using a Nikon X-TH-25-St-2X microtomograph, paired with a computer reconstruction station equipped with dedicated reconstruction software. The system employed a reflective X-ray lamp with a rotating tungsten anode, operating at a rotational speed of 5500 RPM and maintained at a constant temperature of 25 °C to ensure stable imaging conditions. The imaging geometry was optimized based on the sample dimensions. X-ray projections were captured using a Gd_2O_2S:Tb (Gadox) scintillator-based panel detector with a resolution of 2850 × 2850 pixels. The X-ray source operated at a cathode voltage of 220 kV and a filament current of 210 μA. To reduce beam hardening effects and improve image contrast, copper filters with a thickness of 0.25 mm were employed. Each scan was conducted over a 360° rotation, during which 4450 individual projections were collected, with 4 frames per projection, and an exposure time of 250 ms per frame. The acquired projection data were reconstructed in a 16-bit grayscale range, utilizing the Butterworth filter for noise suppression, with a frequency cutoff above 75% of the absolute value,

enhancing image clarity and reducing artifacts. Post-reconstruction analysis was conducted using VGStudioMax 2023.1 (Volume Graphics GmbH, Heidelberg, Germany).

3.10 Justification for Experimental Parameters and Procedures

The selection of every experimental parameter within this study was guided by established scientific principles and the specific objectives of the study. This section provides a justification for the parameters used in the LTA heat treatment, deformation, and characterization stages.

3.10.1 Rationale for Controlled Initial Microstructural States via LTA

The selection of the two LTA protocols – 280 °C for 9 minutes (LTA_280) and 300 °C for 30 minutes (LTA_300), was based on a thorough understanding of the known precipitation and decomposition kinetics of the metastable Si network in PBF-LB/M AlSi10Mg. The goal was to create three distinct microstructural starting points to systematically study the influence of the network continuity. The scientific basis for these parameters is well-established in the literature. In-situ heating experiments and calorimetric analyses by Albu et al. [131] have shown that the metastable eutectic Si network in PBF-LB/M AlSi10Mg begins to break down and spheroidize at temperatures above 240 °C. Fiocchi et al. [20], through detailed DSC analysis, pinpointed the onset of significant Si network disintegration and globularization to a narrow temperature range of approximately 305 – 320 °C, driven by the increased diffusional activity of silicon atoms. This knowledge directly informed the selection of the LTA parameters. The LTA_280 protocol was selected to remain just below the critical Si network decomposition temperature, promoting partial recovery and localized Si network rupture while preserving the cellular structure. In contrast, the LTA_300 protocol was set within the decomposition range to fully fragment and spheroidize the Si network, resulting in discrete Si particles in a ductile α-Al matrix. Microstructural analyses confirmed the intended outcomes of both treatments.

3.10.2 Rationale for Deformation Processing

The deformation processing stage was designed to probe both the fundamental hardening behavior, and the ultimate performance limits of the conditioned microstructures. Uniaxial compression tests to progressive engineering strain levels of 5%, 20%, and maximum failure strain were chosen as the primary method to investigate the intrinsic strain hardening behavior and dislocation evolution. This multi-stage approach is critical because it allows for the capture of microstructural snapshots at different points along the stress-strain curve. For example,

characterization after 5% strain provides insight into early-stage plasticity, such as the initial accumulation of GNDs, which was quantified using KAM analysis. Characterization at higher strains and at failure reveals the evolution of the dislocation structure and the ultimate damage mechanisms. ECAP and TCAP were selected as the SPD methods because they are well-established techniques for imposing extremely large plastic strains, which is necessary to induce significant grain refinement and generate high dislocation densities, thereby pushing the material's properties beyond conventional limits [123], [132], [133], [134].

3.10.3 Rationale for a Multi-Scale Characterization Protocol

The mechanical properties of PBF-LB/M AlSi10Mg are determined by a complex, hierarchical microstructure that spans multiple length scales, making a single characterization method inadequate for capturing its full complexities. Therefore, a multi-scale characterization approach was scientifically essential to accurately elucidate the process-structure-property relationships central to this thesis [135], [136]. At the mesoscale (µm to mm), LOM was used to reveal melt pool morphology and large-scale defects such as porosity, which are critical for identifying potential sites of strain localization and failure. At the microscale (µm), SEM provided high-resolution imaging of the α-Al/Si cellular network, while EBSD enabled quantitative grain structure analysis, including grain size, morphology, and was further leveraged through KAM analysis to estimate the local density of GNDs. At the nanoscale (nm to µm), TEM and HRTEM were indispensable for observing nanoscale features such as Si precipitates, dislocations, and their configurations, confirming mechanisms like dislocation pile-ups, dense dislocation walls, and stacking faults. Complementing these localized techniques, XRD provided bulk crystallographic information and, through Williamson-Hall analysis, enabled estimation of average crystallite size and total dislocation density, bridging data from EBSD and TEM. This comprehensive microstructural insight was correlated with mechanical property measurements, including Vickers microhardness for rapid strength assessment, uniaxial compression tests for stress-strain behavior, and LUR tests to quantify kinematic hardening and back stress evolution.

Chapter Four

4.0 Results

4.1. Comparative Study of PBF-LB/M AlSi7Mg, AlSi10Mg, AlSi12Mg

4.1.1 Powder Characterization

4.1.1.1 Morphology

Figure 21 presents SEM images detailing the particle morphology and surface features of the investigated powders: AlSi7Mg (**Figure 21A**), AlSi10Mg (**Figure 21B**), and AlSi12Mg (**Figure 21C**). Each alloy powder is shown at progressively increasing magnifications (left to right). The powders are generally characterized by spherical particles, though some irregular shapes are present. A notable feature across all powder types is the presence of finer, satellite particles adhering to the surfaces of larger particles, indicative of agglomeration or particle interaction during powder production or handling. While visual inspection reveals a polydisperse nature, the detailed particle size distribution is provided in **Figure 21**.

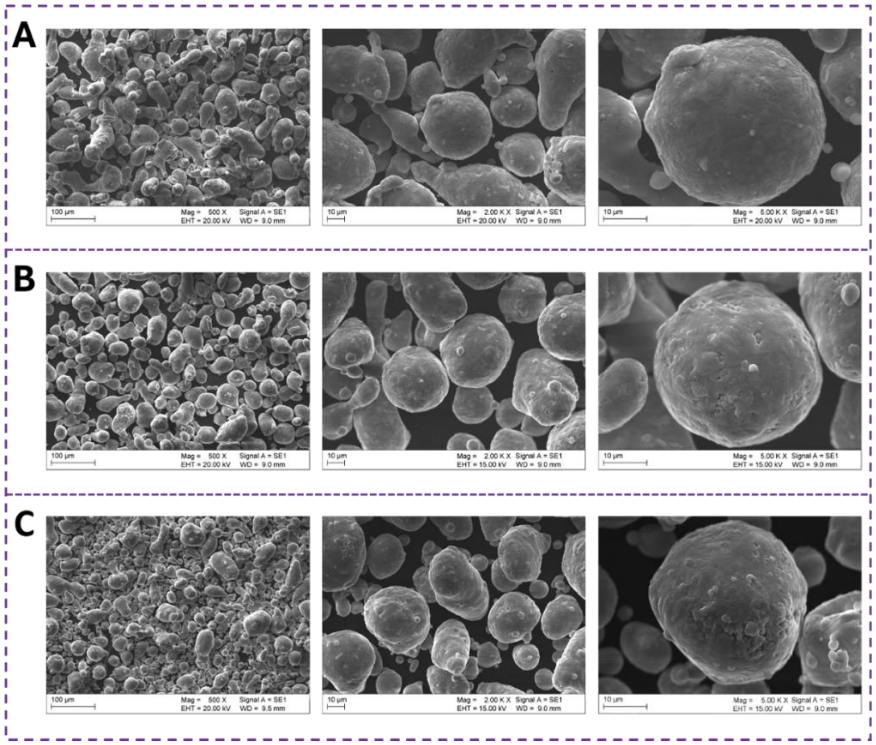

Figure 21. SEM images showing the morphologies of the Al-Si powders A. AlSi7Mg powder, **B**. AlSi10Mg powder, and **C**. AlSi12Mg powder.

4.1.1.2 Particle Size Analysis

The particle size distributions for the AlSi7Mg, AlSi10Mg, and AlSi12Mg powders are presented in **Figure 22**A – **22C** respectively, which display both volumetric frequency histograms and cumulative distributions. The uniformity of particle sizes was quantified by the span, calculated using **Equation (7)**

$$\text{span} = \frac{d_{90} - d_{10}}{d_{50}} \tag{7}$$

where d_{10}, d_{50} (median), and d_{90} are the particle diameters below which 10%, 50%, and 90% of the volumetric distribution lie, respectively. The AlSi10Mg powder (span = 1.06) exhibited the lowest span, indicating the highest particle size uniformity. The AlSi7Mg (span = 1.2) and AlSi12Mg (span = 1.3) powders also demonstrated good uniformity, supporting their suitability for the PBF-LB/M additive manufacturing process.

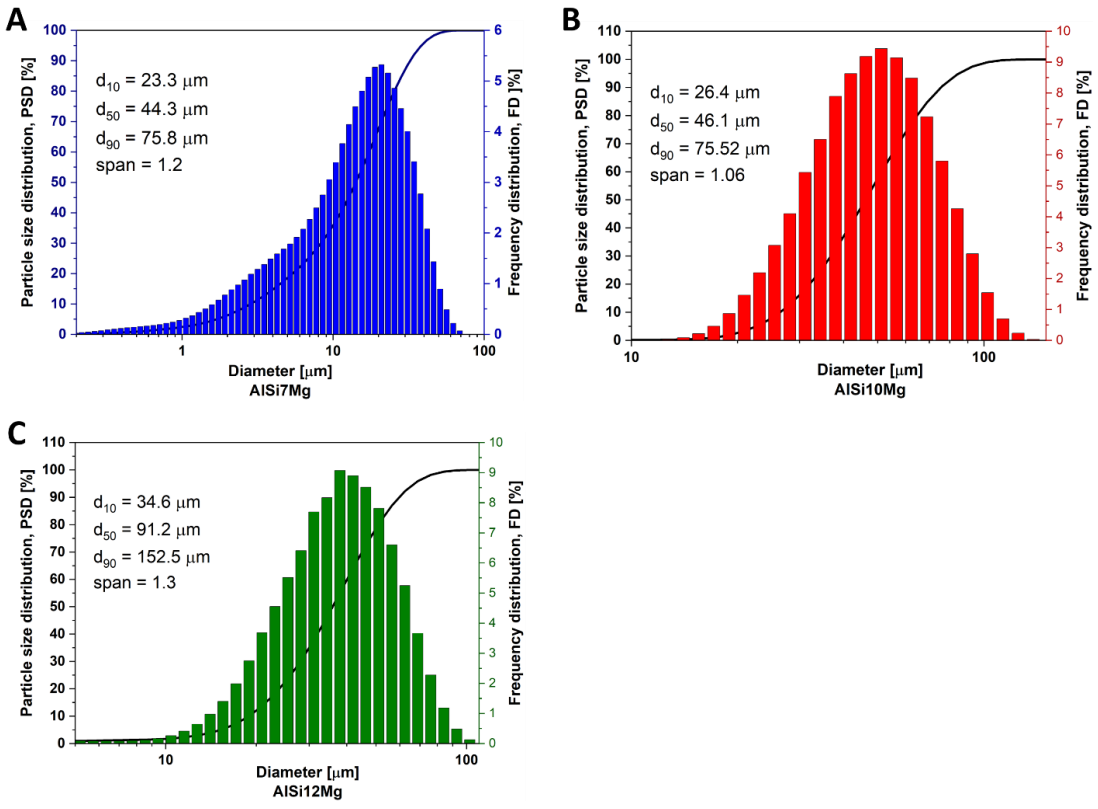

Figure 22. Powder particle size distribution A. AlSi7Mg powder, **B**. AlSi10Mg powder, and **C**. AlSi12Mg powder

4.1.1.3 Chemical Composition

The chemical composition of the powders was analyzed using energy dispersive x-ray spectroscopy (EDS). **Figure 23** presents the EDS elemental mapping results, while **Figure 24** displays the representative EDS spectra and corresponding quantitative chemical compositions for the powders. The analyses confirm the presence of the primary alloying elements – aluminum (Al), silicon (Si), and magnesium (Mg) – In proportions consistent with their respective alloy designations. Additionally, trace amounts of other elements, including iron (Fe), copper (Cu), and titanium (Ti), were identified.

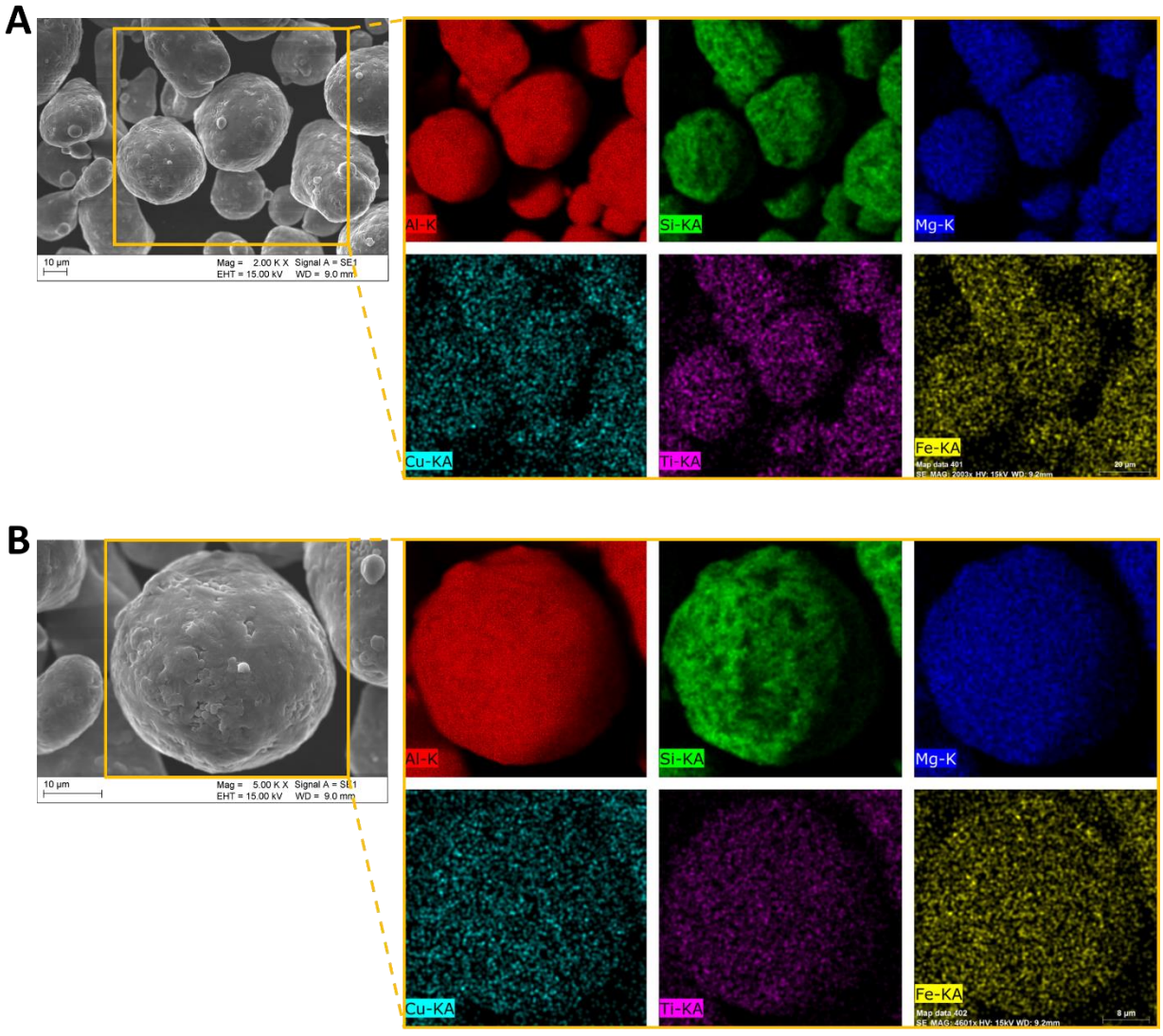

Figure 23. Energy dispersive x-ray spectroscopy (EDS) chemical composition mapping of Al-Si powder

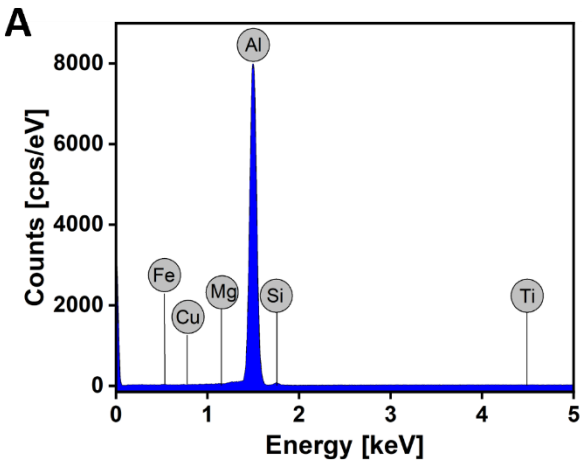

AlSi7Mg Chemical Composition						
Element	Si	Mg	Cu	Ti	Fe	Al
Weight%	6.8	0.3	0.04	0.22	0.18	Bal

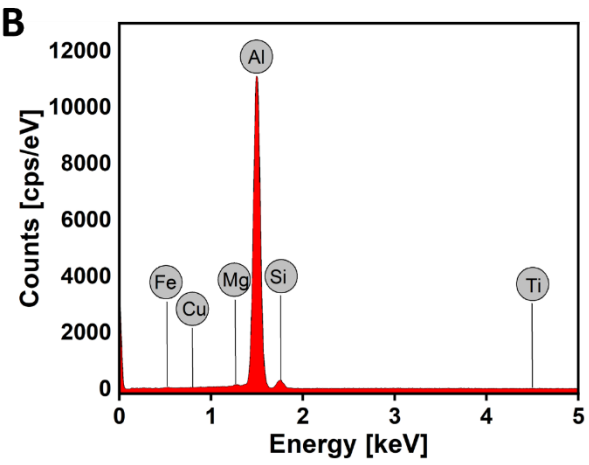

AlSi10Mg Chemical Composition						
Element	Si	Mg	Cu	Ti	Fe	Al
Weight%	10.5	0.5	0.15	0.15	0.09	Bal

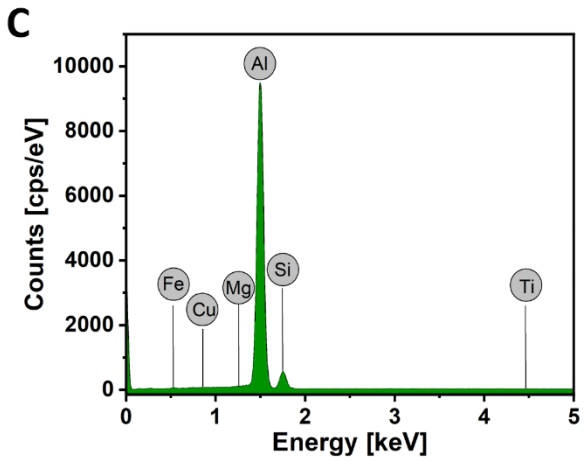

AlSi12Mg Chemical Composition						
Element	Si	Mg	Cu	Ti	Fe	Al
Weight%	12.8	0.25	0.08	0.18	0.55	Bal

Figure 24. EDS spectra and quantitative chemical composition analyses of the Al-Si powders
A. AlSi7Mg powder, **B.** AlSi10Mg powder, and **C.** AlSi12Mg powder

4.1.2 Microstructure

4.1.2.1 Light Optical Microscopy (LOM)

The microstructures of the as-built PBF-LB/M AlSi7Mg, AlSi10Mg, and AlSi12Mg alloys, observed under the light microscope are presented in **Figures 25, 26 and 27**, respectively. Across

all three alloys, the X-Z plane consistently exhibits a melt pool microstructure with elongated, wavy, or layered features, sometimes referred to in the literature as "fish-scale" pattern [137], [138], [139], indicative of the directional solidification inherent in the PBF-LB/M process. The X-Y plane for each alloy displays clear laser scan boundaries within the melt pools. As magnification increases from 50X to 200X and 500X, finer details of these microstructures, including cellular substructures, become progressively more resolved. The results further demonstrate that the AlSi7Mg alloy possesses several defects, in the form of porosity in the microstructure (**Figure 25A**). Nonetheless, a notable difference in the LOM microstructural observations in the dimensions of the melt pools in each alloy. The melt pool dimensions for AlSi7Mg were measured at a width of 140 ± 39 μm and a depth of 47 ± 8 μm. The melt pool dimensions for AlSi10Mg increased slightly to a width of 152 ± 15 μm and a depth of 50 ± 9 μm. Relatively, AlSi12Mg exhibited substantially larger melt pool dimensions, measuring 518 ± 158 μm in width and 79 ± 30 μm in depth.

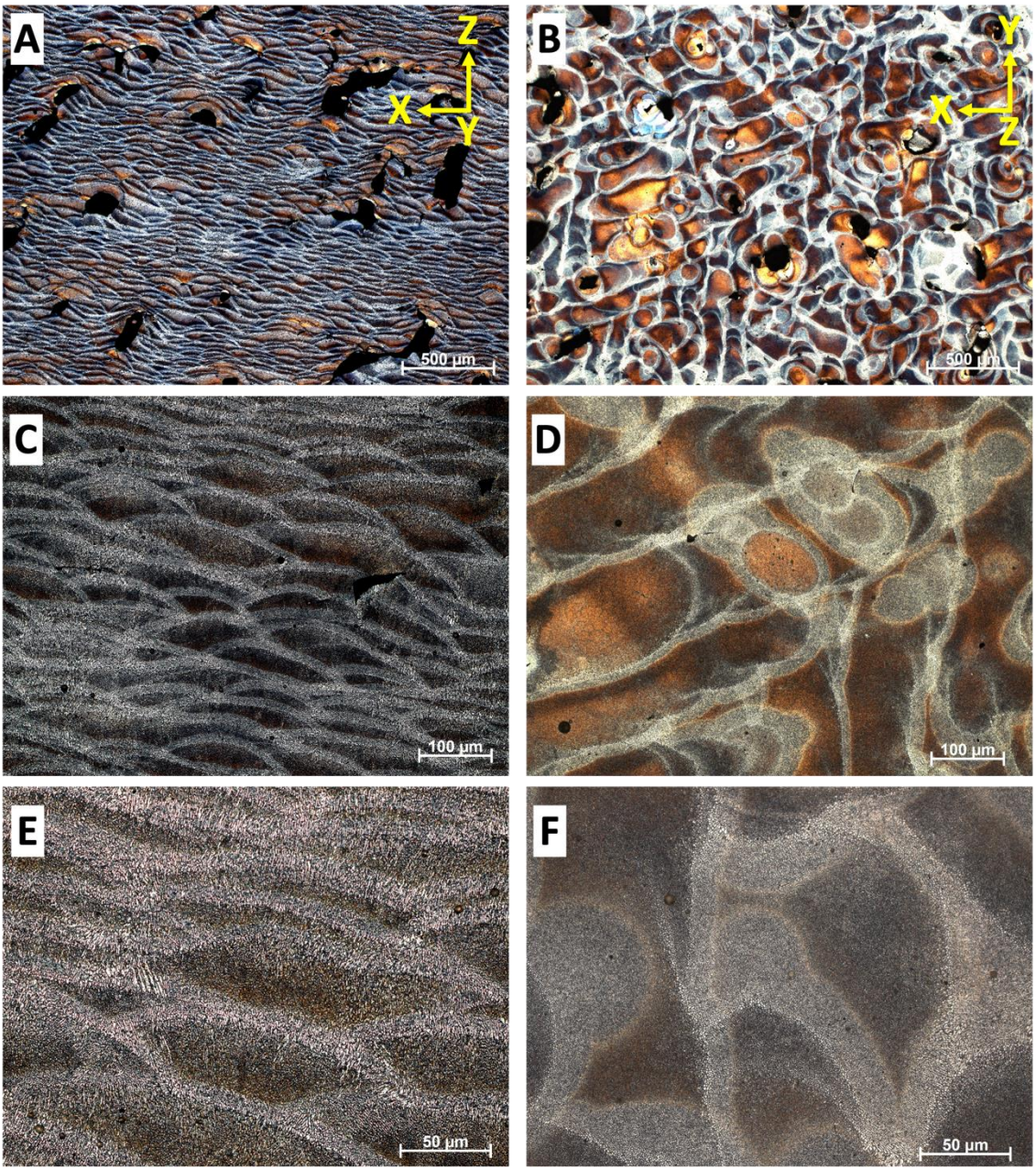

Figure 25. Microstructure of PBF-LB/M AlSi7Mg under the light microscope (LOM) A,B. Cross-section along the X-Z plane and X-Y plane respectively at 50X magnification, **C,D.** X-Z plane and X-Y plane respectively at 200X magnification, and **E,F.** X-Z plane and X-Y plane respectively at 500X magnification

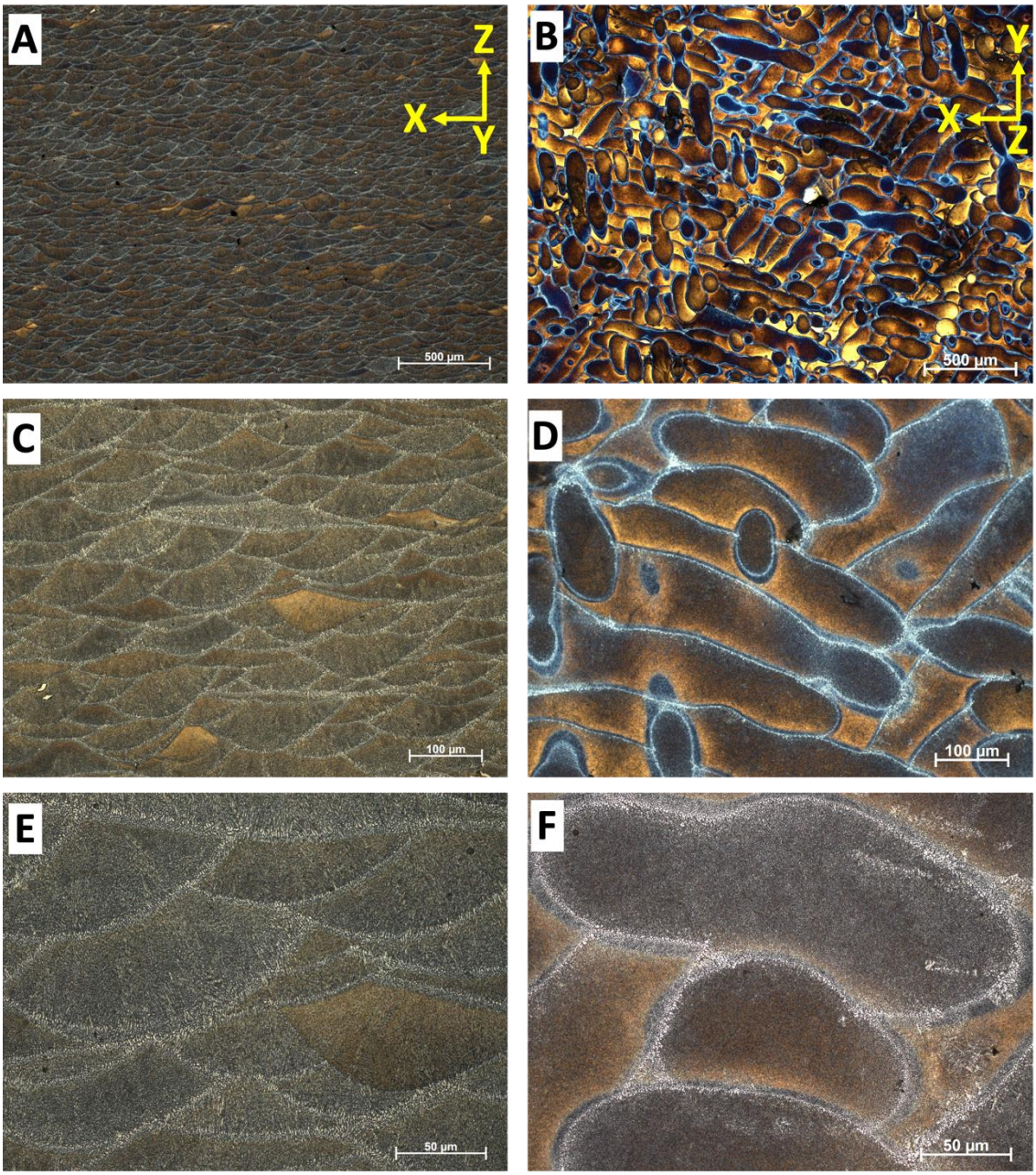

Figure 26. Microstructure of PBF-LB/M AlSi10Mg under LOM A,B. Cross-section along the X-Z plane and X-Y plane respectively at 50X magnification, **C,D.** X-Z plane and X-Y plane respectively at 200X magnification, and **E,F.** X-Z plane and X-Y plane respectively at 500X magnification

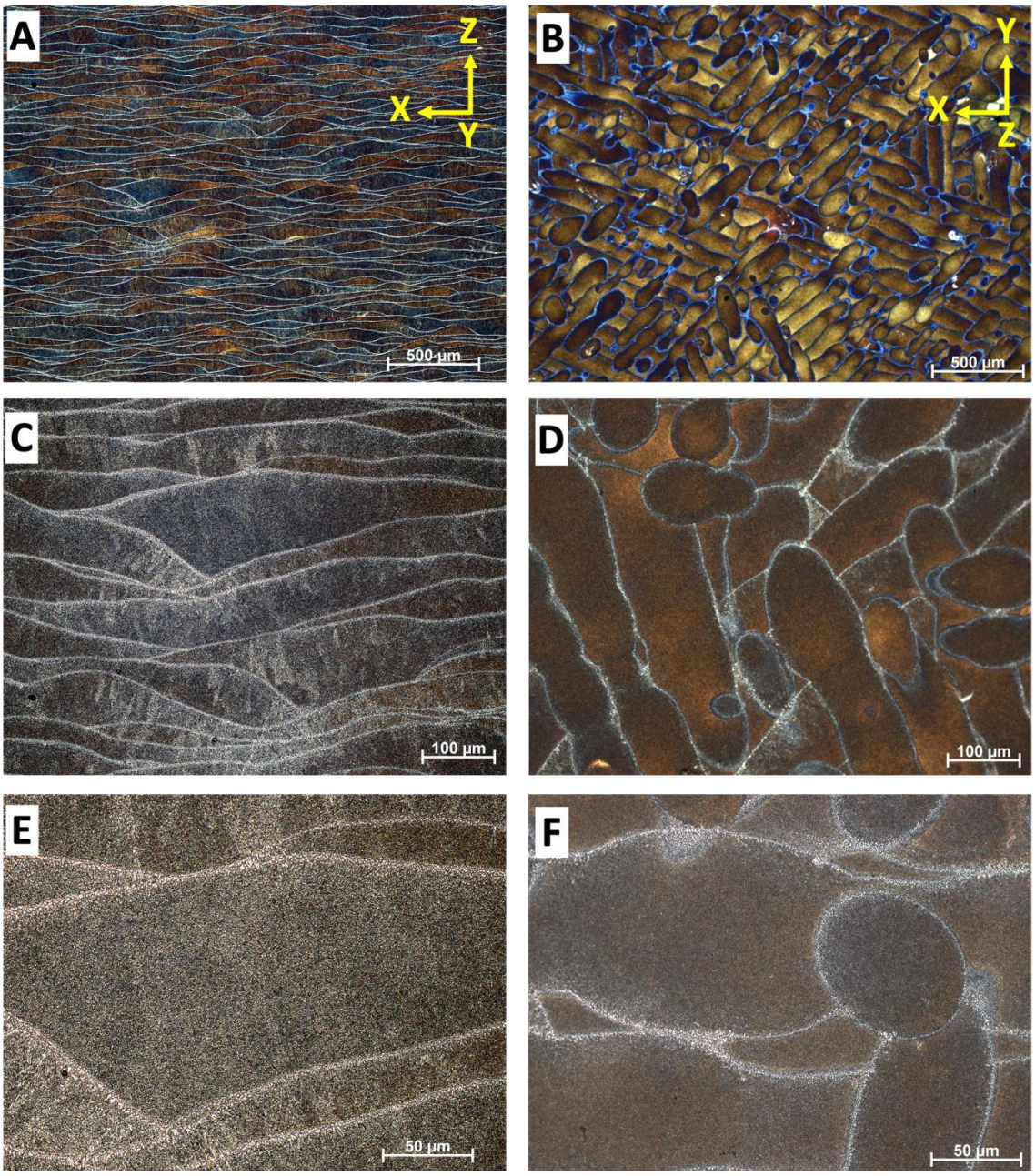

Figure 27. Microstructure of PBF-LB/M AlSi12Mg under LOM A,B. Cross-section along the X-Z plane and X-Y plane respectively at 50X magnification, **C,D.** X-Z plane and X-Y plane respectively at 200X magnification, and **E,F.** X-Z plane and X-Y plane respectively at 500X magnification

4.1.2.2 Scanning Electron Microscopy (SEM)

A more detailed examination of the microstructure of the PBF-LB/M Al-Si alloys was conducted using SEM. The results are presented in **Figures 28, 29, and 30**, corresponding to AlSi7Mg, AlSi10Mg, and AlSi12Mg, respectively. The SEM analysis consistently reveals a heterogeneous microstructure across all investigated samples. This heterogeneity is characterized by the presence of cells, which are formed as a direct consequence of the constitutional supercooling at the solidification front, which is driven by the high cooling rates of the PBF-LB/M process.

The observed heterogeneity stems from variations in the cell sizes within the microstructure. Specifically, three distinct regions are identified: a fine melt pool region (MP fine), a coarse melt pool region (MP coarse), and a heat-affected zone (HAZ). The MP fine region is characterized by the smallest cell sizes and constitutes most of the overall structure. The MP coarse region, in contrast, exhibits relatively larger cell sizes. The heat-affected zone (HAZ) is also discernible, and its presence is a direct consequence of the overlap of subsequent laser scans during the PBF-LB/M manufacturing process.

A key distinction in the microstructures of these alloys is found in the dimensions of the cells within the MP fine regions. For the AlSi7Mg alloy, as illustrated in **Figure 28**, the cell size measures 1.06 ± 0.25 μm. The AlSi10Mg alloy, depicted in **Figure 29**, exhibited the finest cells among the three, with dimensions of 0.88 ± 0.17 μm. Conversely, the AlSi12Mg alloy, shown in **Figure 30**, had the largest cell sizes, measuring 1.36 ± 0.38 μm.

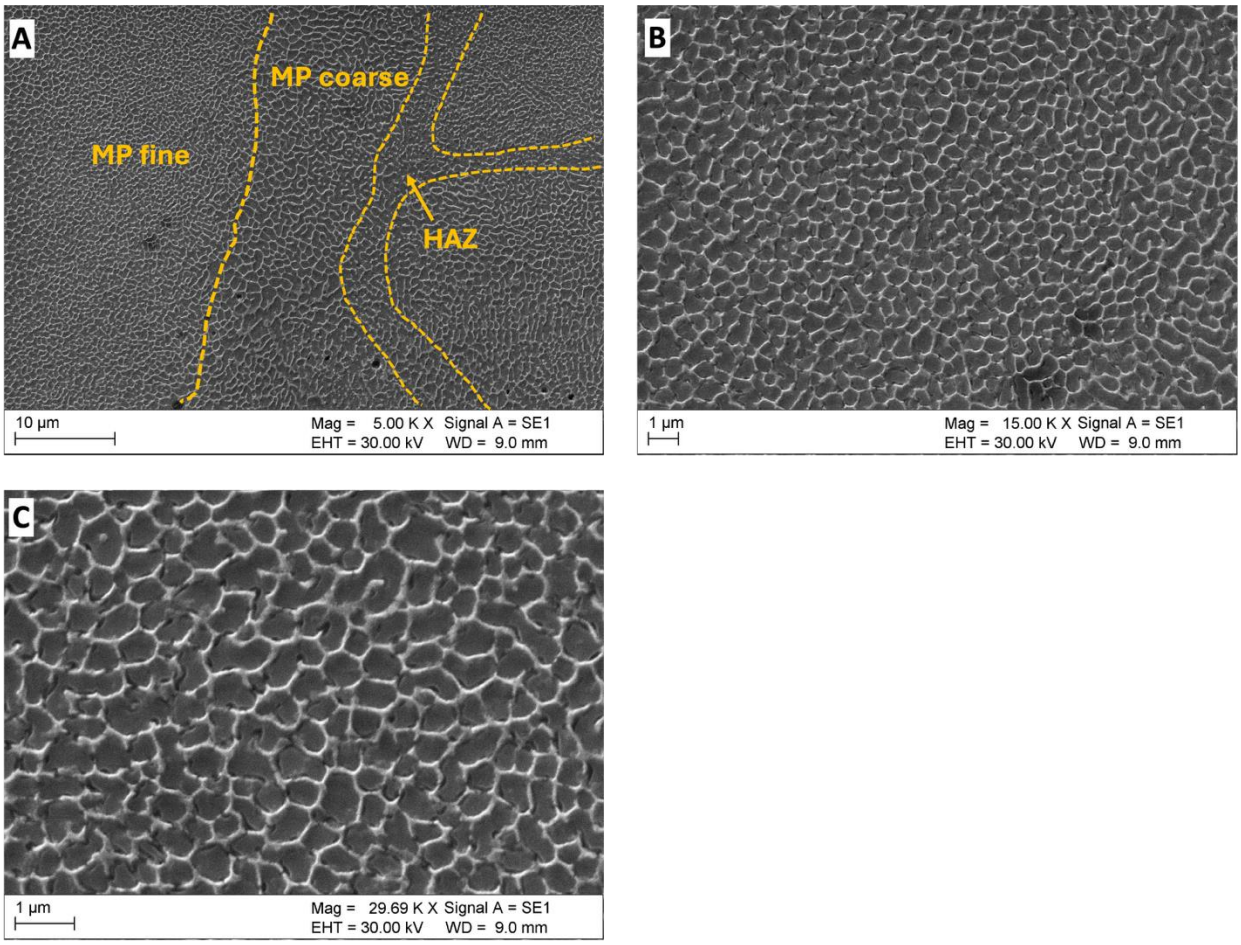

Figure 28. Microstructure of PBF-LB/M AlSi7Mg under the scanning electron microscope (SEM) A. SEM micrograph showing a heterogenous cellular microstructure with fine melt pool (MP fine), coarse melt pool (MP coarse) and heat-affected zone (HAZ), and **B and C** are higher magnification SEM images of the MP fine region.

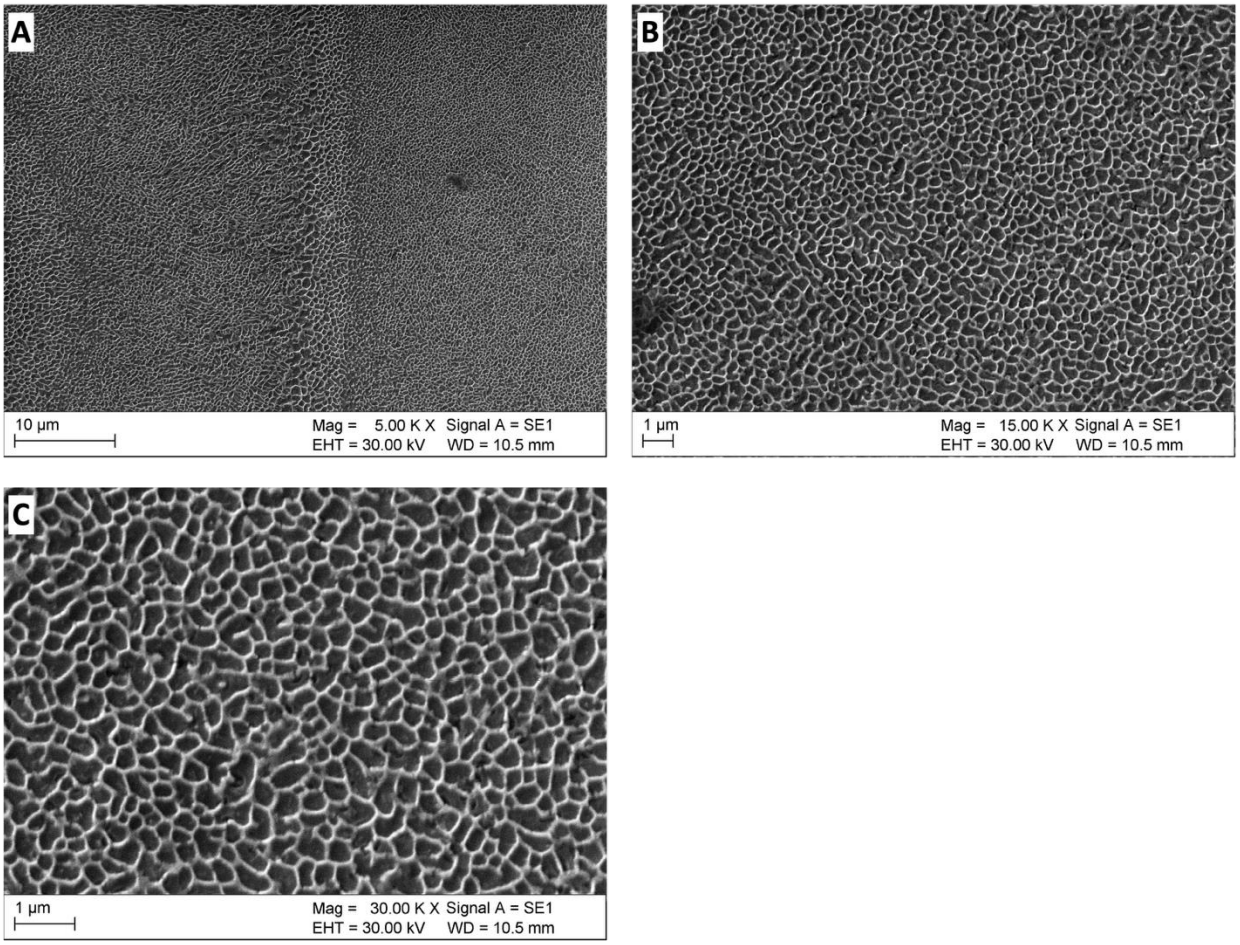

Figure 29. Microstructure of PBF-LB/M AlSi10Mg under the SEM A. SEM micrograph showing a heterogenous cellular microstructure with fine melt pool (MP fine), coarse melt pool (MP coarse) and heat-affected zone (HAZ), and **B and C** are higher magnification SEM images of the MP fine region.

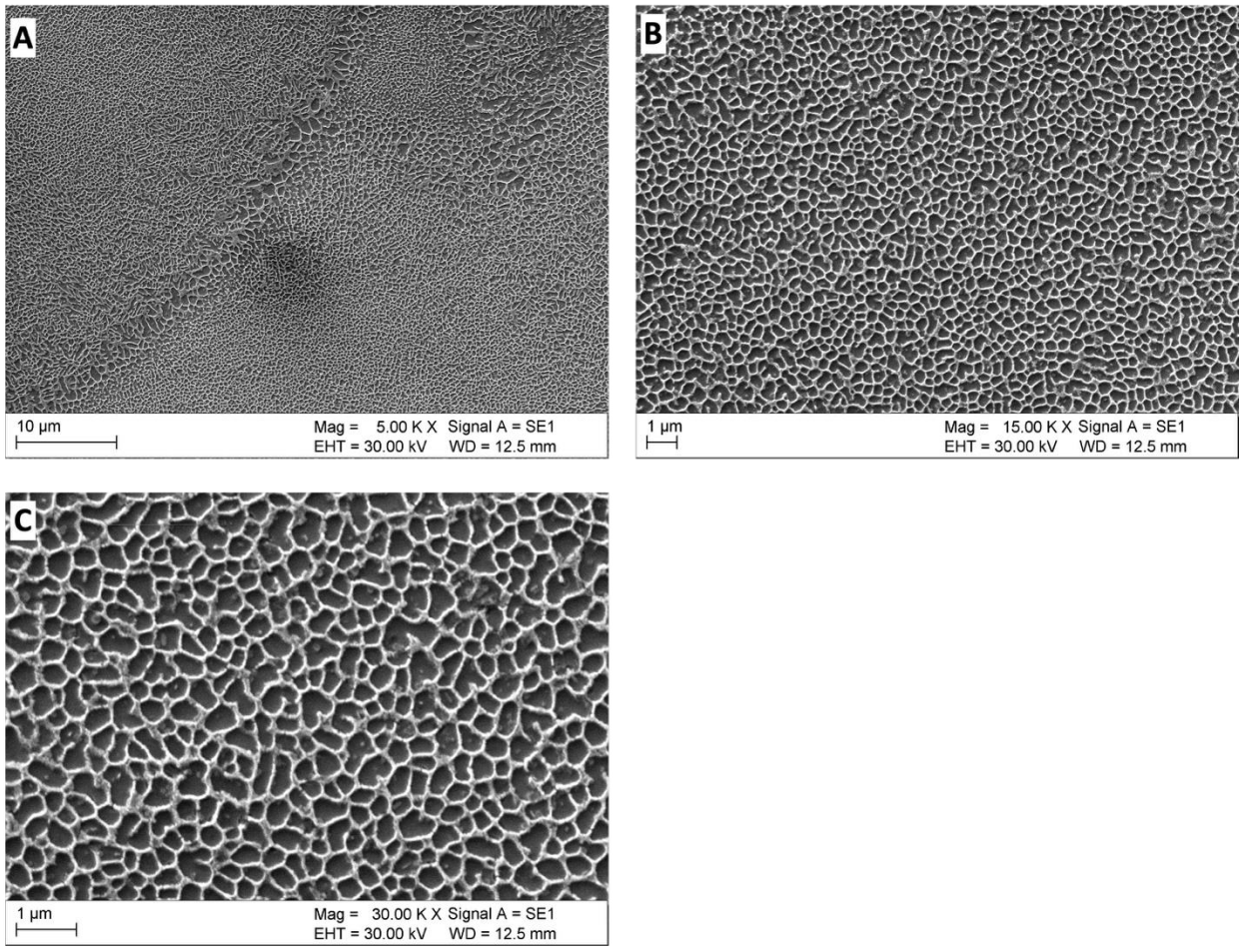

Figure 30. Microstructure of PBF-LB/M AlSi12Mg under the SEM A. SEM micrograph showing a heterogenous cellular microstructure with fine melt pool (MP fine), coarse melt pool (MP coarse) and heat-affected zone (HAZ), and **B and C** are higher magnification SEM images of the MP fine region.

4.1.3 Porosity

Investigations into the variations in porosity of the PBF-LB/M fabricated alloys were conducted using a combination of LOM and CT analysis. The results are presented in **Figures 31, 32 and 33** for the as-built AlSi7Mg, AlSi10Mg and AlSi12Mg, respectively. From LOM observations, the AlSi7Mg sample exhibited visibly higher levels of porosity in its cross-sectional microstructure (**Figure 31A**), while the AlSi10Mg and AlSi12Mg samples showed comparatively lower porosities (**Figures 32A and 33A**, respectively). These were further quantified through CT-based volumetric analysis. The total pore volume in the AlSi7Mg alloy was estimated at 2.39 mm^3 (**Figure 31B**), significantly higher than the values observed for the AlSi10Mg (0.45 mm^3, **Figure**

32B) and AlSi12Mg (1.76 mm^3, **Figure 33B**) counterparts. Furthermore, the average pore diameter in AlSi7Mg was measured at 0.13 ± 0.09 mm (**Figure 31C**), closely resembling the AlSi12Mg pores (0.13 ± 0.08 mm, **Figure 33C**), whereas the AlSi10Mg sample showed the smallest average pore diameter of 0.07 ± 0.02 mm (**Figure 32C**).

To further understand the nature of porosity, pore sphericity was analyzed – a key parameter in distinguishing between gas-induced and process-induced pores such as shrinkage or lack-of-fusion voids. Pores with sphericity values closer to 1 are typically indicative of gas porosity, having an almost perfect spherical morphology [140]. In this context, the AlSi10Mg sample exhibited the highest mean pore sphericity of 0.91 ± 0.05 (**Figure 32D**), strongly suggesting a dominance of nearly spherical gas pores. In contrast, the AlSi7Mg and AlSi12Mg samples showed lower average sphericities of 0.78 ± 0.13 (**Figure 31D**) and 0.72 ± 0.12 (**Figure 33D**), respectively, implying a higher proportion of irregularly shaped shrinkage or lack-of-fusion pores.

Sphericity was plotted against pore diameter and volume for each alloy, for insights into the relationship between pore shape and size. The AlSi10Mg sample consistently displayed pores with small diameters and high sphericity (**Figures 32E and 32F**), confirming a uniform distribution of gas pores and indicating high densification. On the other hand, the AlSi7Mg (**Figures 31E and 31F**) and AlSi12Mg (**Figures 33E and 33F**) samples exhibited broader pore sphericity distributions at varying diameters and volumes), consistent with more pronounced process-induced porosity. Overall, the porosity analysis confirms that AlSi10Mg exhibits superior structural integrity among the three alloys, with minimal total pore volume alongside smaller and more spherical pores.

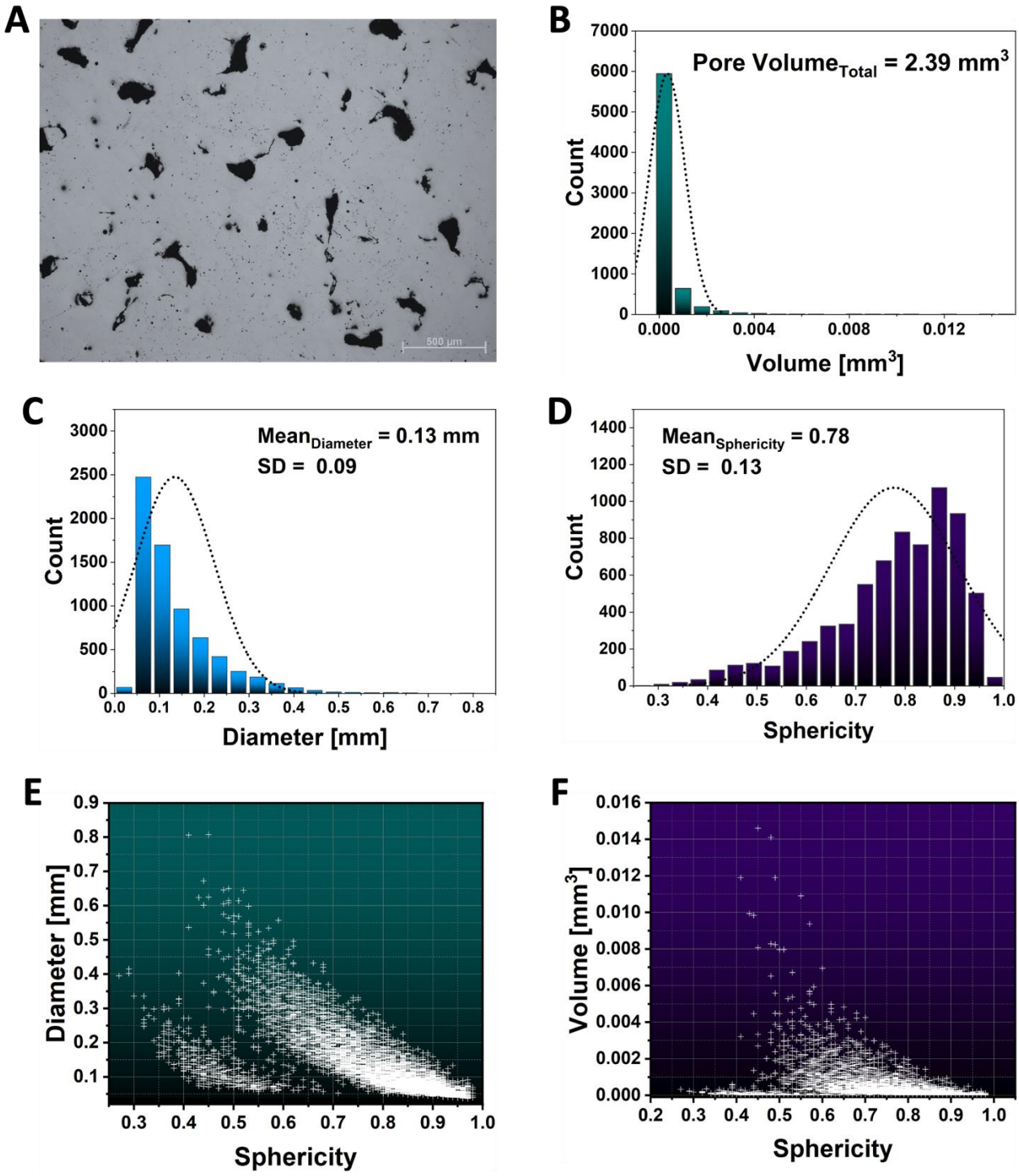

Figure 31. Porosity Analysis of PBF-LB/M AlSi7Mg A. LOM images showing porosity (in black) **B**. Pore volume distribution plot, **C**. Pore diameter distribution plot, **D**. Pore sphericity distribution plot, **E**. Diameter vs Sphericity plot, and **F**. Volume vs. Sphericity plot.

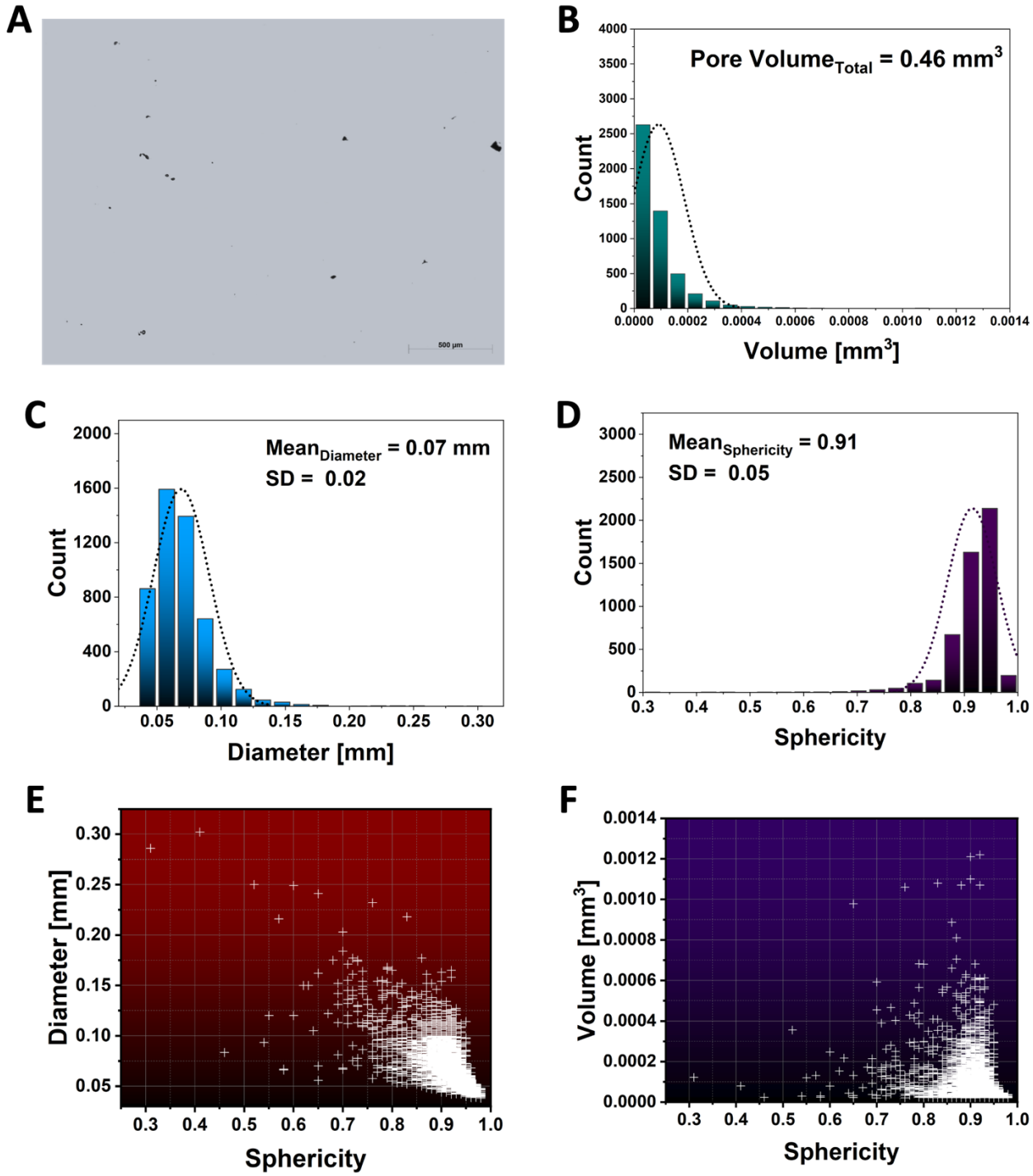

Figure 32. Porosity Analysis of PBF-LB/M AlSi10Mg A. LOM images showing porosity (in black) **B**. Pore volume distribution plot, **C**. Pore diameter distribution plot, **D**. Pore sphericity distribution plot, **E**. Diameter vs Sphericity plot, and **F**. Volume vs. Sphericity plot.

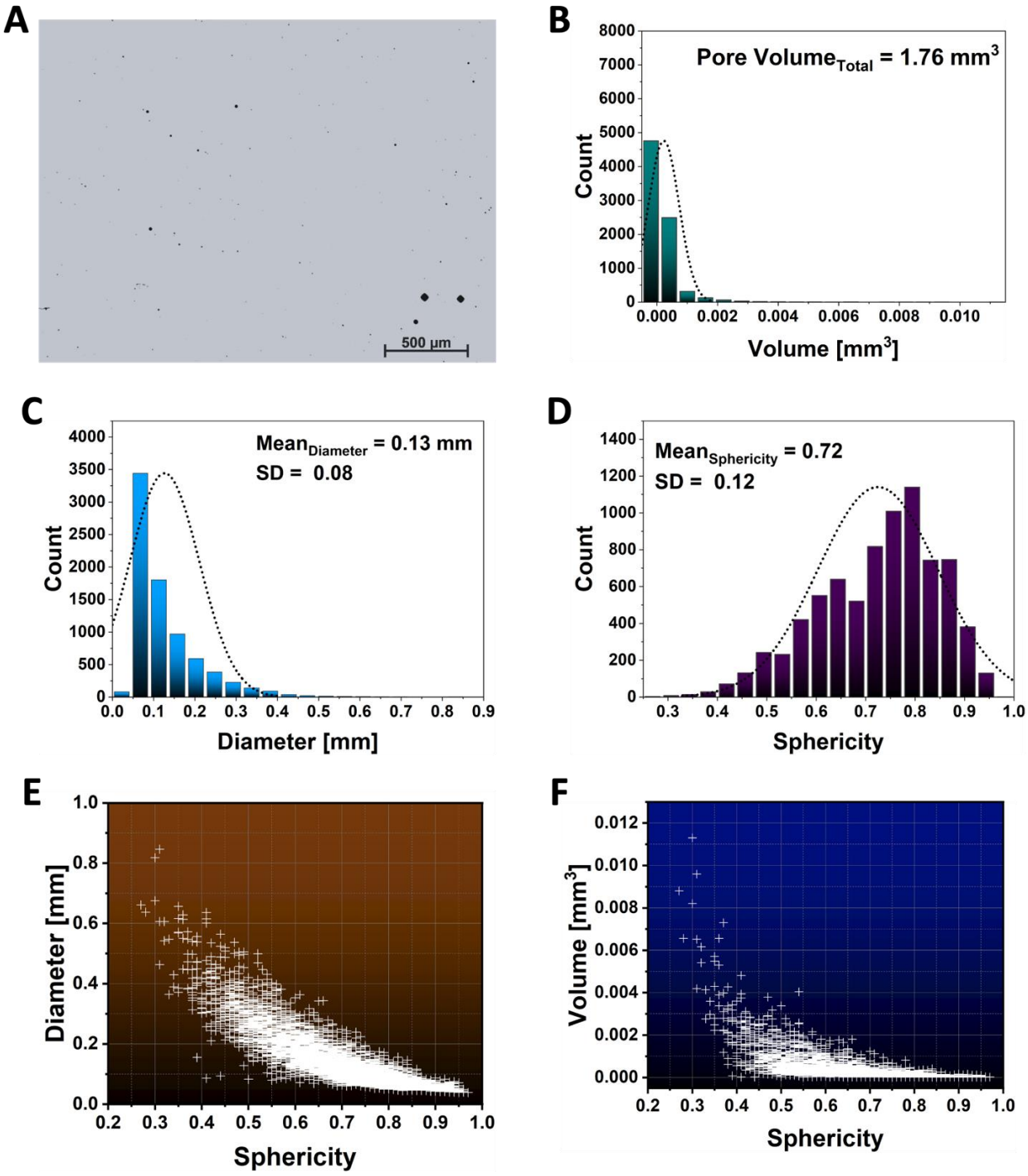

Figure 33. Porosity Analysis of PBF-LB/M AlSi12Mg A. LOM images showing porosity (in black) **B**. Pore volume distribution plot, **C**. Pore diameter distribution plot, **D**. Pore sphericity distribution plot, **E**. Diameter vs Sphericity plot, and **F**. Volume vs. Sphericity plot.

4.1.4 Hardness

Vickers microhardness tests were conducted to provide insights into the mechanical properties of the as-built samples. The results of these tests are presented in the hardness contour maps in **Figure 34**. The AlSi7Mg alloy exhibited the lowest mean microhardness value among the three, recorded at 96.77 $HV_{0.3}$. In contrast, the AlSi10Mg alloy demonstrated the highest mean hardness, reaching 115.77 $HV_{0.3}$. The AlSi12Mg alloy showed an intermediate microhardness value of 106.69 $HV_{0.3}$. The observed lowest microhardness value for the AlSi7Mg sample is directly influenced, in part, by its relatively high levels of porosity, which significantly impacts its mechanical integrity. Conversely, the superior hardness observed in the AlSi10Mg sample can be attributed to the refined nature of its cellular microstructure when compared to the AlSi12Mg sample. This finer cellular structure is understood to contribute to the overall strength of the alloy, operating under a mechanism analogous to the Hall-Petch effect, where a reduction in grain or cell size leads to an increase in material strength, consistent with observations by Bartošák et a. [141].

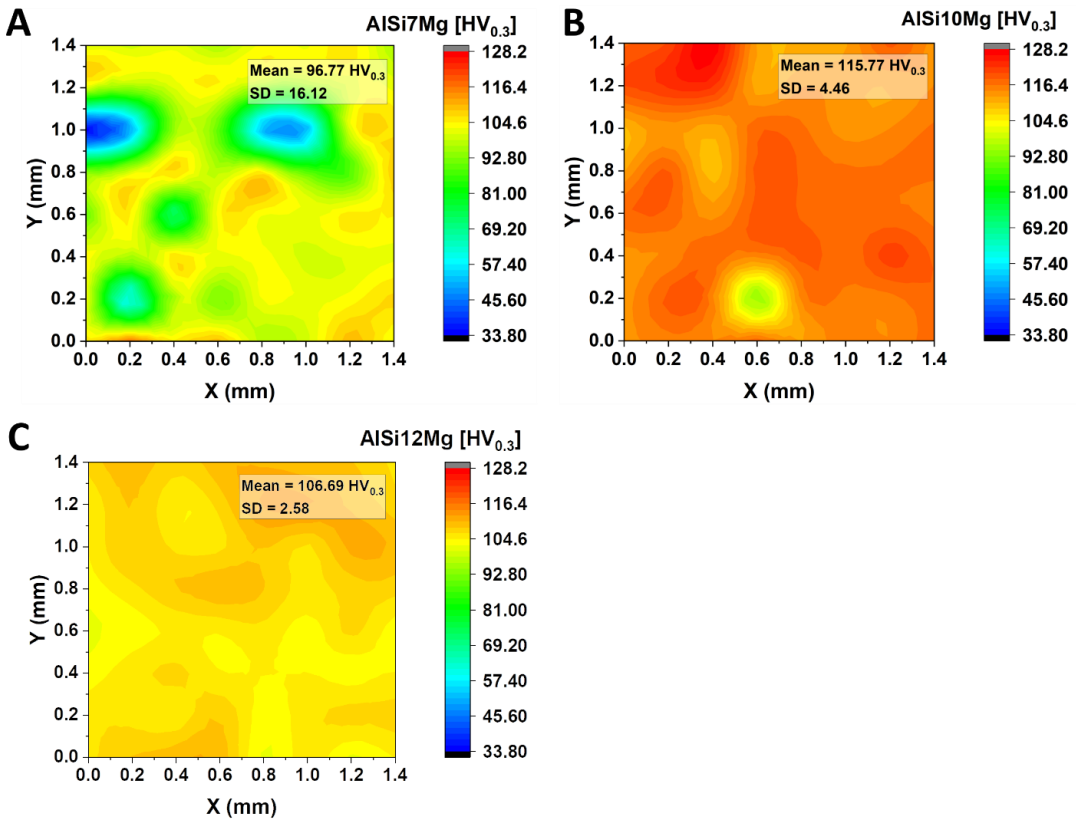

Figure 34. Vickers microhardness test results measured along the cross-section of the PBF-LB/M alloys A. AlSi7Mg, **B**. AlSi10Mg, and **C**. AlSi12Mg

4.1.5 Basis for Focusing on AlSi10Mg Alloy

The selection of PBF-LB/M fabricated AlSi10Mg alloy as the central focus of this thesis is grounded in both its scientific relevance and its potential to advance the design of structural materials that overcome the classical strength – ductility trade-off. AlSi10Mg is not only one of the most processable and industrially adopted aluminum alloys in the additive manufacturing domain, but also one that exhibits a heterogeneous microstructure – making it uniquely suited for exploring deformation-induced size effects and gradient-driven strengthening mechanisms.

From a powder metallurgy standpoint, the AlSi10Mg precursor powder offers excellent flowability and morphological consistency, which are critical for stable layer deposition and defect minimization during PBF-LB/M processing [142]. In the present comparative study with AlSi7Mg and AlSi12Mg, the AlSi10Mg powder demonstrated the narrowest particle size distribution, directly contributing to its superior build quality. As-built microstructural analysis revealed that AlSi10Mg formed the most refined cellular structure and exhibited the lowest porosity among the three, correlating strongly with higher Vickers microhardness values. These baseline characteristics position AlSi10Mg as an excellent candidate for subsequent microstructural tailoring via post-processing routes.

This thesis therefore investigates how the initial cellular microstructure of PBF-LB/M AlSi10Mg dictates its strain hardening behavior and grain refinement during SPD. The primary objective is to establish a fundamental understanding of how the characteristic cellular network, inherent to the PBF-LB/M process, mediates dislocation activity and the dynamic restoration processes that lead to grain refinement under large strain. By correlating the initial cellular morphology with the resulting mechanical response and microstructural evolution, this work provides a framework for tailoring the properties of AM AlSi10Mg through controlled thermomechanical processing.

4.2 Heat Treatment

This section investigates the effects of low-temperature annealing (LTA) on the microstructural evolution of PBF-LB/M AlSi10Mg, with particular attention to modifications in the nanoscale cellular architecture. Emphasis is placed on assessing the extent to which the characteristic cellular structure is retained or altered following thermal exposure. Microstructural analyses are conducted on three distinct conditions: the as-built sample prior to heat heat treatment

(hereafter referred to as As-built), a sample subjected to low-temperature annealing at 280 °C for 9 minutes (LTA_280), and a sample annealed at 300 °C for 30 minutes (LTA_300). Grain and cell morphologies in each condition are examined to elucidate the thermal stability of the hierarchical microstructure.

4.2.1 Grain and Cell Morphology of As-built PBF-LB/M AlSi10Mg

To gain a better understanding of the grain structure of the as-built PBF-LB/M AlSi10Mg alloy before heat treatment, the microstructure was examined using EBSD. **Figure 35A** presents the EBSD inverse pole figure in the Z direction (IPF-Z) of the sample in its as-built state. This map reveals a microstructure predominantly characterized by columnar grains. This columnar morphology is a direct consequence of the rapid solidification and directional cooling inherent to the PBF-LB/M process, which promotes the growth of elongated grains aligned with the heat dissipation path [143]. A notable feature within this bulk columnar structure is the presence of a heat-affected zone, indicated by the dashed black lines in **Figure 35A**, which shows an area containing more equiaxed grains. The formation of these equiaxed grains within the HAZ is attributed to localized reheating that occurs during the addition of subsequent layers. Further quantitative analysis of the grain structure is provided by the grain size histogram in **Figure 35B**. This histogram indicates that the majority of grains within the structure possess an area below 400 μm^2. The average grain size was estimated to be 23.18 ± 69 μm in diameter and 231.67 ± 250.15 μm^2 in area.

The grain boundary and misorientation angle distribution analyses results are presented **Figure 35C and D**. The analysis reveals a high fraction of high-angle grain boundaries (HAGBs), constituting approximately 86.4% of the total boundaries. The remaining 13.6% are identified as low-angle grain boundaries (LAGBs). Specifically, HAGBs are defined as those with misorientation angles ranging from 15° to 65°, while LAGBs are characterized by misorientation angles between 2° and 15°.

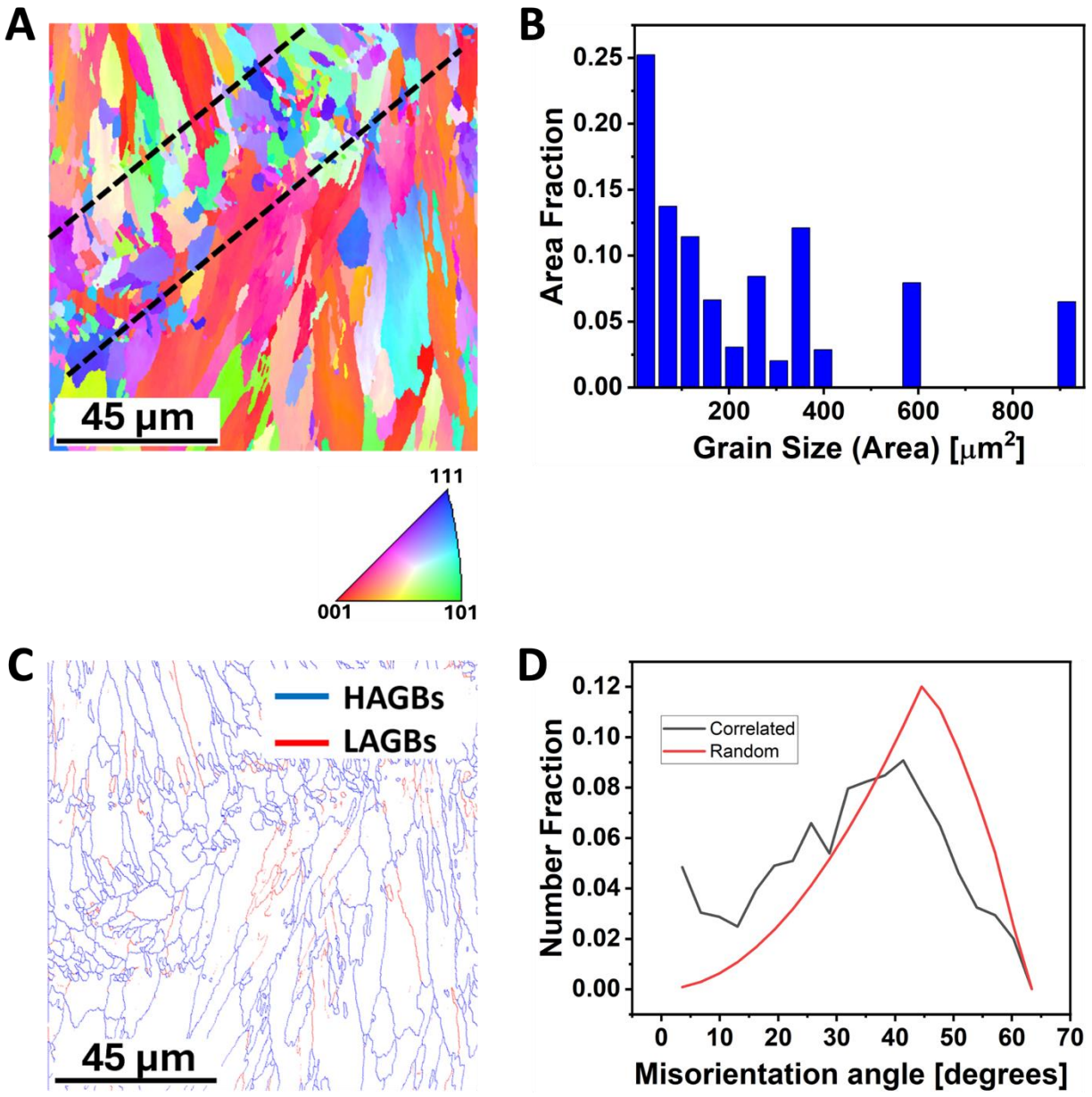

Figure 35. Microstructure of the as-built PBF-LB/M AlSi10Mg alloy from electron backscatter diffraction (EBSD) analysis. A. EBSD IPF-Z map of the sample, **B**. Grain size (area) histogram of the sample in the as-built state, **C**. Grain boundary map of the sample in as-built state (blue lines representing high angle grain boundaries (HAGBs) and red lines representing low angle grain boundaries (LAGBs)), and **D**. Misorientation angle histogram of the sample in the as-built state.

High magnification observation of the eutectic Si-rich cellular network was undertaken using TEM. The TEM image in **Figure 36A** shows the cellular structure to be well defined and

appearing fully intact with varying cell sizes in the range of 300 – 900 nm, and cell walls measuring 70 – 100 nm. Nonetheless, the higher magnification TEM image in **Figure 36B** shows that the Si network exhibits regions that are not fully continuous, with an intricate network of dislocations observed within the cells. EDS cell boundary analysis (**Figure 36C**) reveals the segregation of Si at the boundary, which corroborates the Si-rich nature of the eutectic cell boundaries.

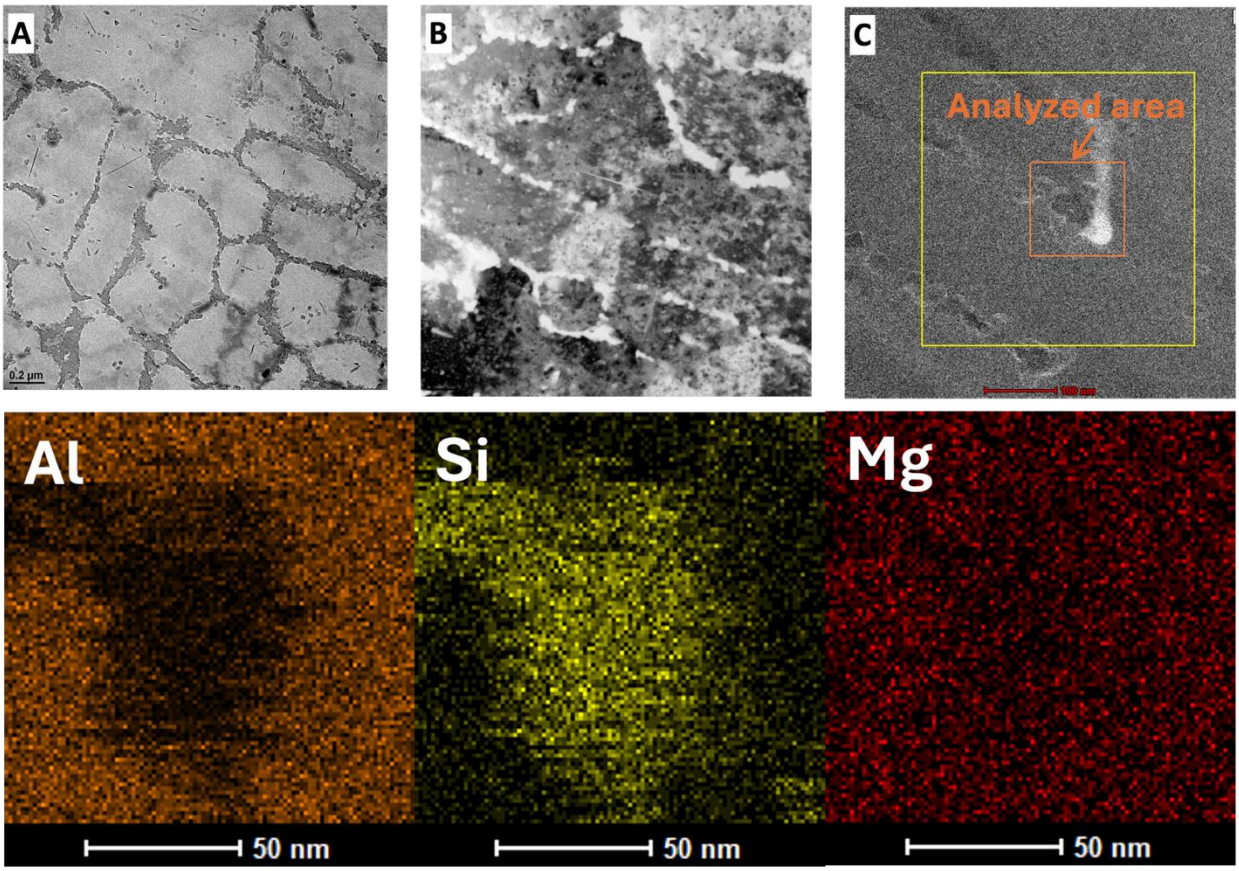

Figure 36. Cellular structure of As-built PBF-LB/M AlSi10Mg obtained from transmission electron microscopy (TEM) A. TEM image showing a magnified view of the full cellular structure, **B**. Higher magnification TEM image showing dislocation entanglements in the cell structure interiors, and **C**. STEM image and accompanying EDS mapping depicting Si segregation at the cell boundary.

4.2.2 Microstructure of After Annealing at 280 °C for 9 minutes

Figure 37 presents the LOM images of the LTA_280 sample in both the X–Y and X–Z planes at various magnifications. The observations indicate that low temperature annealing at 280 °C for 9 minutes does not lead to any substantial alteration of the mesoscale melt pool (MP)

and melt pool boundary (MPB) structures. The overall morphology closely resembles that of the As-built condition, with measured MP widths of 151 ± 17 μm and depths of 49 ± 11 μm.

SEM analysis further confirms the retention of the heterogeneous microstructure characteristic of the as-built state (**Figure 38A**). High-magnification SEM imaging of the fine cellular regions within the melt pools reveals localized disruptions in the continuity of the eutectic cellular network, evidenced by areas of ruptured cell walls marked by dashed circles in **Figure 38C**. This sample exhibits cell diameters in the range of approximately 300 – 900 nm, consistent with those observed in the As-built sample. These results suggest that the applied annealing condition (LTA_280) maintains the integrity of the nanoscale cellular architecture while inducing only minimal sub-cell disruptions.

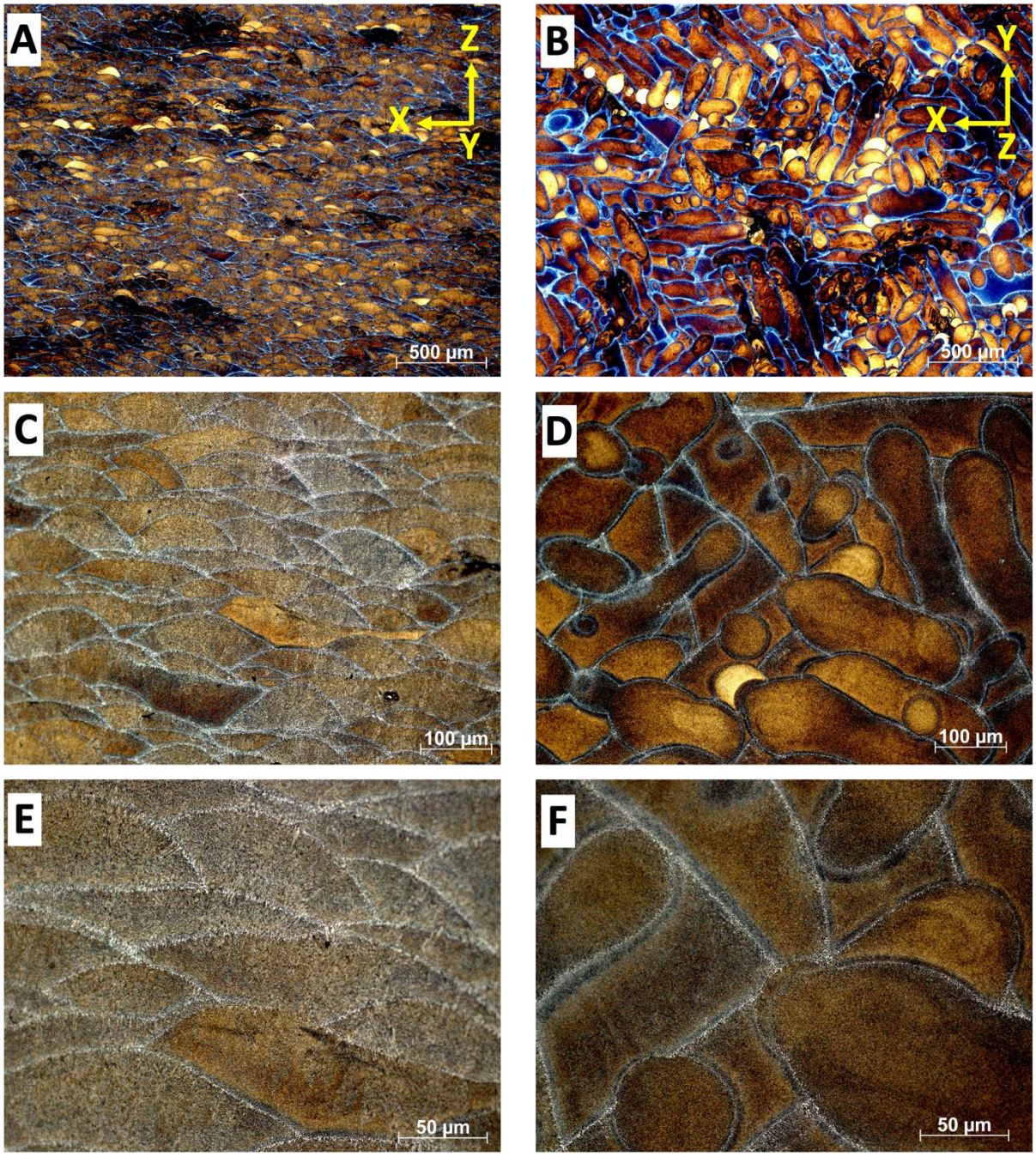

Figure 37. Microstructure of LTA_280 under LOM A,B. Cross-section along the X-Z plane and X-Y plane respectively at 50X magnification, **C,D.** X-Z plane and X-Y plane respectively at 200X magnification, and **E,F.** X-Z plane and X-Y plane respectively at 500X magnification

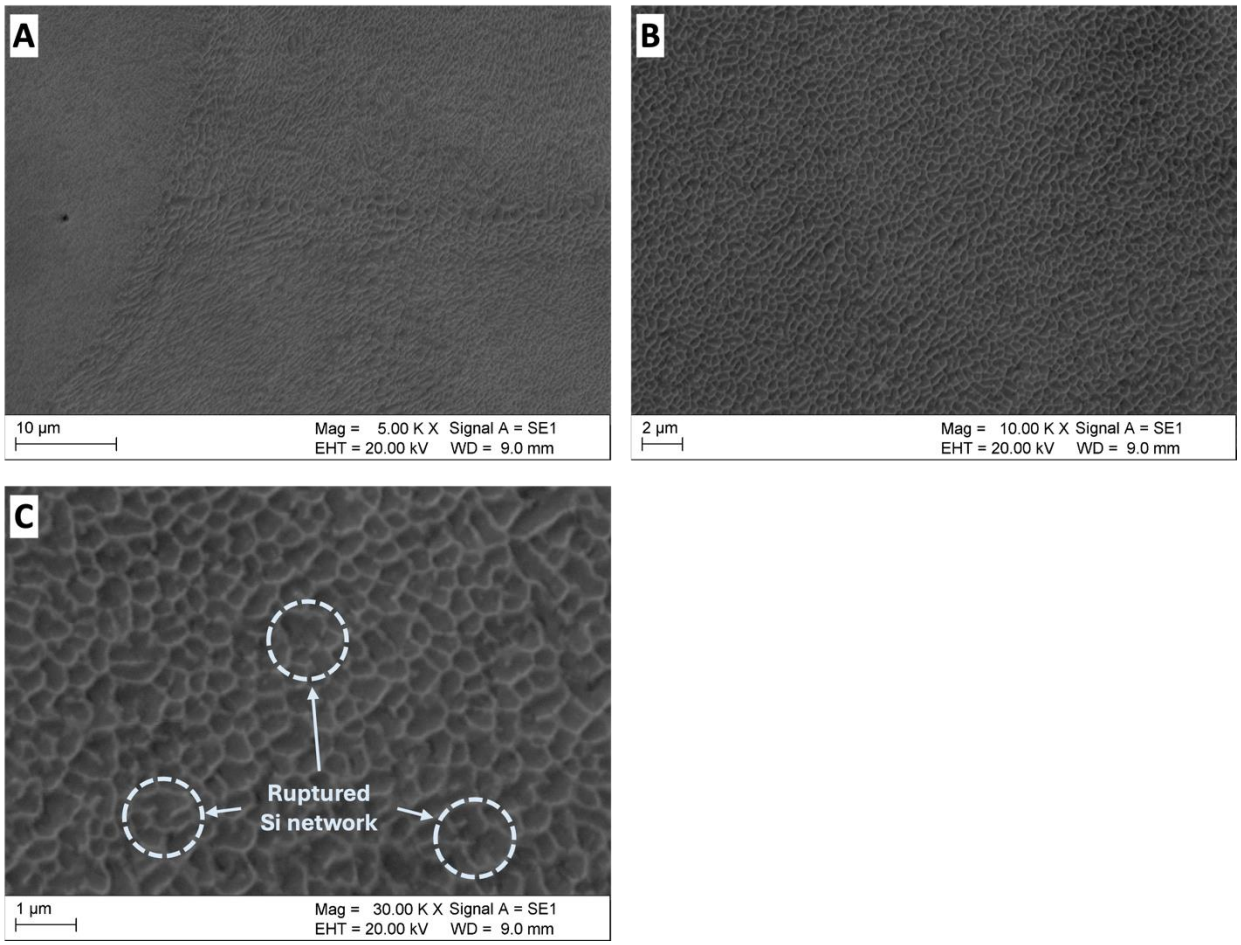

Figure 38. Microstructure of LTA_280 under the SEM A. SEM micrograph showing a heterogenous cellular microstructure, and **B and C** are higher magnification SEM images of the MP fine region.

EBSD results for the LTA_280 sample are presented in **Figure 39**. The IPF-Z map in **Figure 39A** reveals a predominantly columnar grain structure, characteristic of the solidification texture retained from the as-built condition. The grain size distribution shown in **Figure 39B** further confirms that the LTA treatment at 280 °C for 9 minutes does not induce significant grain growth. Quantitative boundary analysis indicates that HAGBs constitute approximately 82.6% of all grain boundaries, while LAGBs account for the remaining 17.4% (**Figures 39C and 39D**). These findings suggest that the applied annealing parameters preserve the microstructural features established during PBF-LB/M fabrication.

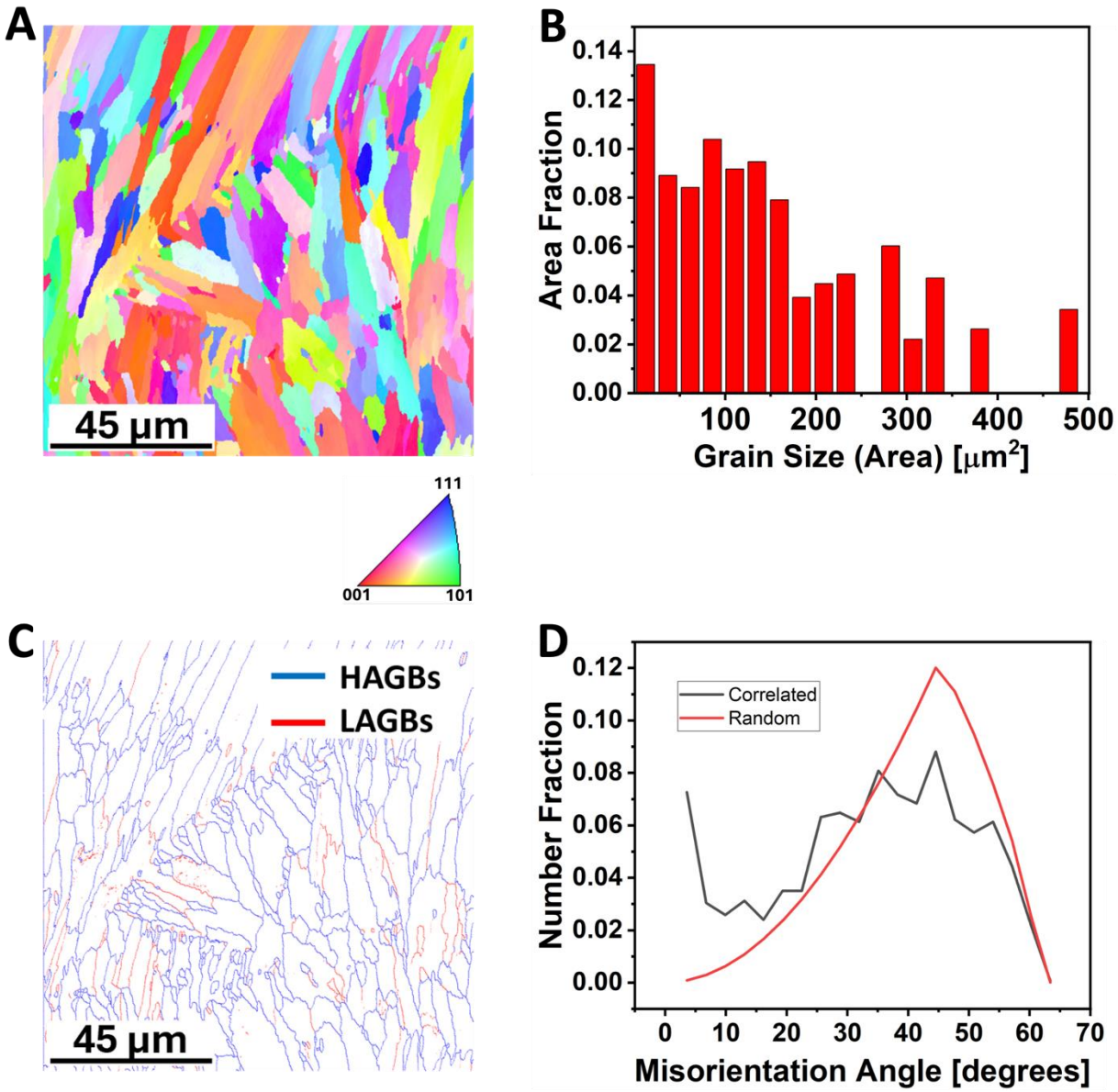

Figure 39. Microstructure of LTA_280 from EBSD analysis. A. EBSD IPF-Z map of the sample, **B**. Grain size (area) histogram of the sample, **C**. Grain boundary map of the sample (blue lines representing high angle grain boundaries (HAGBs) and red lines representing low angle grain boundaries (LAGBs)), and **D**. Misorientation angle histogram of the sample.

4.2.3 Microstructure of After Annealing at 300 °C for 30 minutes

Following annealing at 300 °C for 30 minutes, LOM analysis revealed that the mesoscale structure of the alloy, including the MPs and MPBs, remains largely unchanged from the as-built condition in both the X–Y and X–Z planes (**Figure 40**). However, higher-resolution imaging using SEM (**Figure 41**) revealed notable microstructural evolution at the nanoscale. Specifically, the

previously continuous eutectic Si network exhibited significant fragmentation (**Figure 41C**). This observed fragmentation of the Si network is consistent with literature reports documenting that annealing PBF-LB/M AlSi10Mg at temperatures ranging 260 °C – 320 °C fosters the precipitation of Si from the supersaturated matrix, resulting in the rupture of the Si network [64], [144].

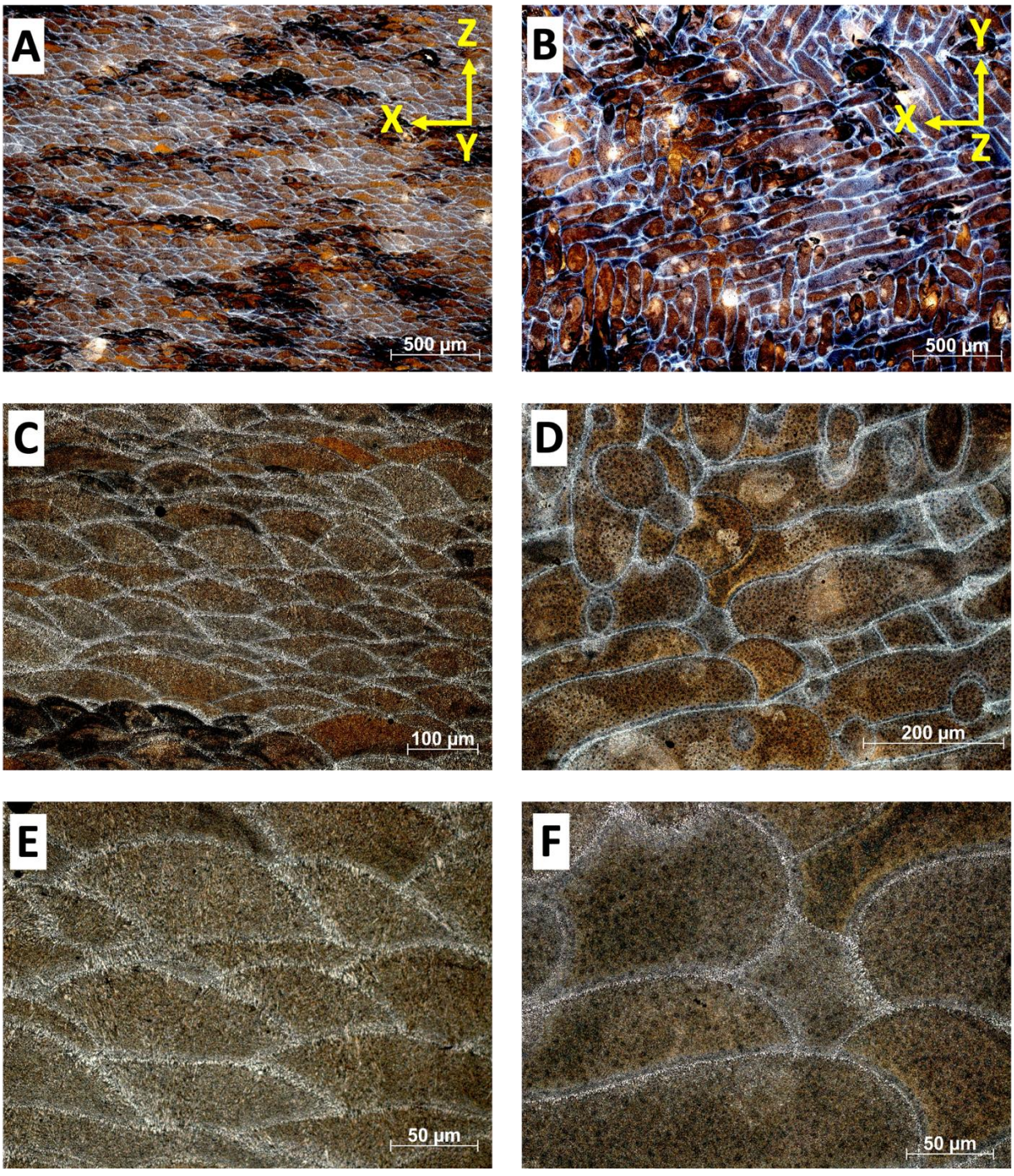

Figure 40. Microstructure of LTA_300 under LOM A,B. Cross-section along the X-Z plane and X-Y plane respectively at 50X magnification, **C,D.** X-Z plane and X-Y plane respectively at 200X magnification, and **E,F.** X-Z plane and X-Y plane respectively at 500X magnification

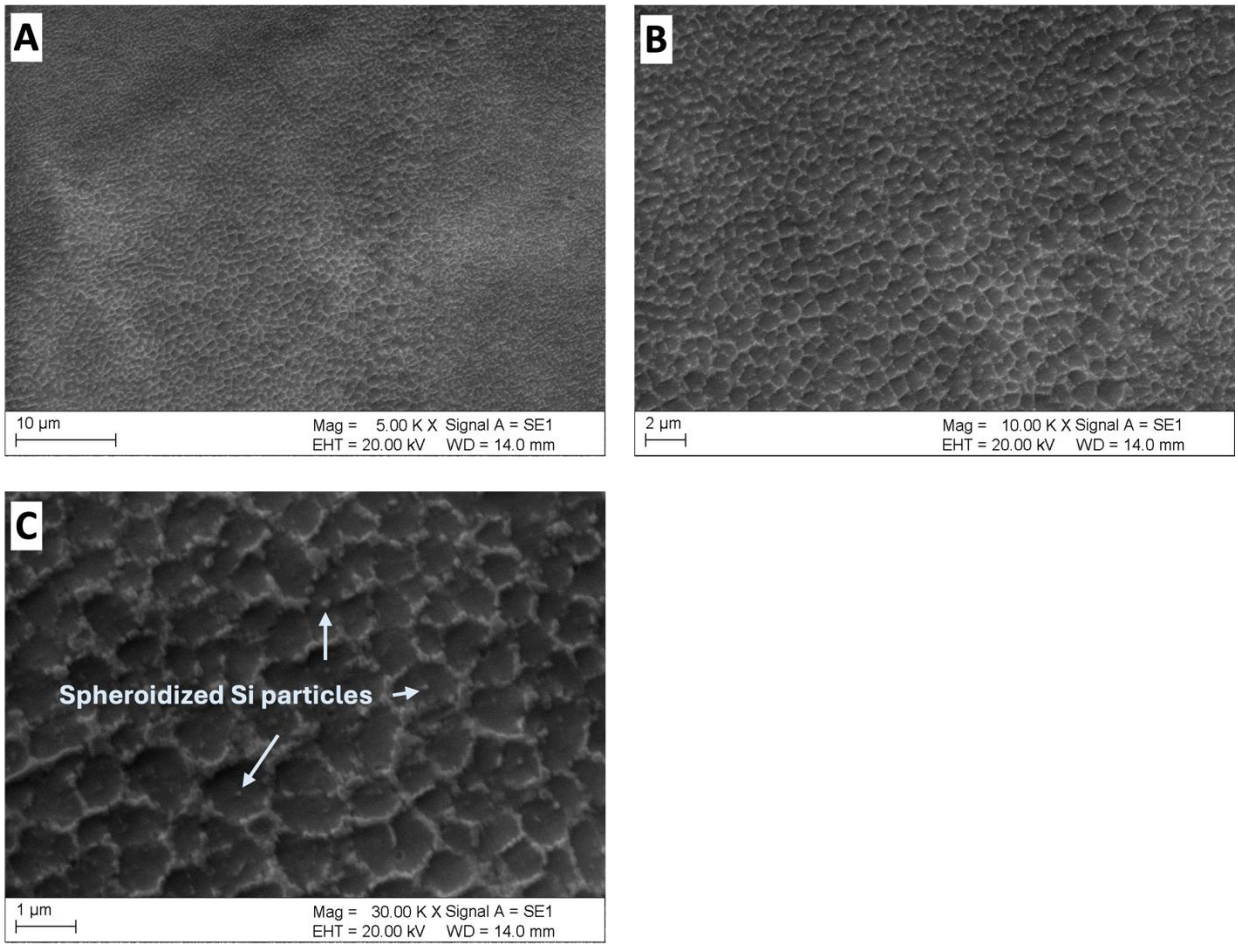

Figure 41. Microstructure of LTA_300 under the SEM A. SEM micrograph showing a heterogenous cellular microstructure, and **B and C** are higher magnification SEM images of the MP fine region.

Further investigation using TEM provided additional insight into the extent of eutectic network fragmentation. Bright-field TEM images in **Figures 42A and 42B** show the divorced Al/Si cell structure. EDS elemental mapping (**Figure 42C**) confirmed the Si-rich nature of these cell boundaries, with particle sizes averaging 95 ± 44 nm. These results suggest that upon annealing, the continuous Si network fragmented at its narrowest points. This was accompanied by a change in particle morphology, driven by the minimization of interfacial energy. The elongated fragments evolved into coarser, more spherical particles. This process is characteristic

of Ostwald ripening, where larger particles grow at the expense of smaller ones via the diffusion of silicon through the aluminum matrix [145], [146], [147].

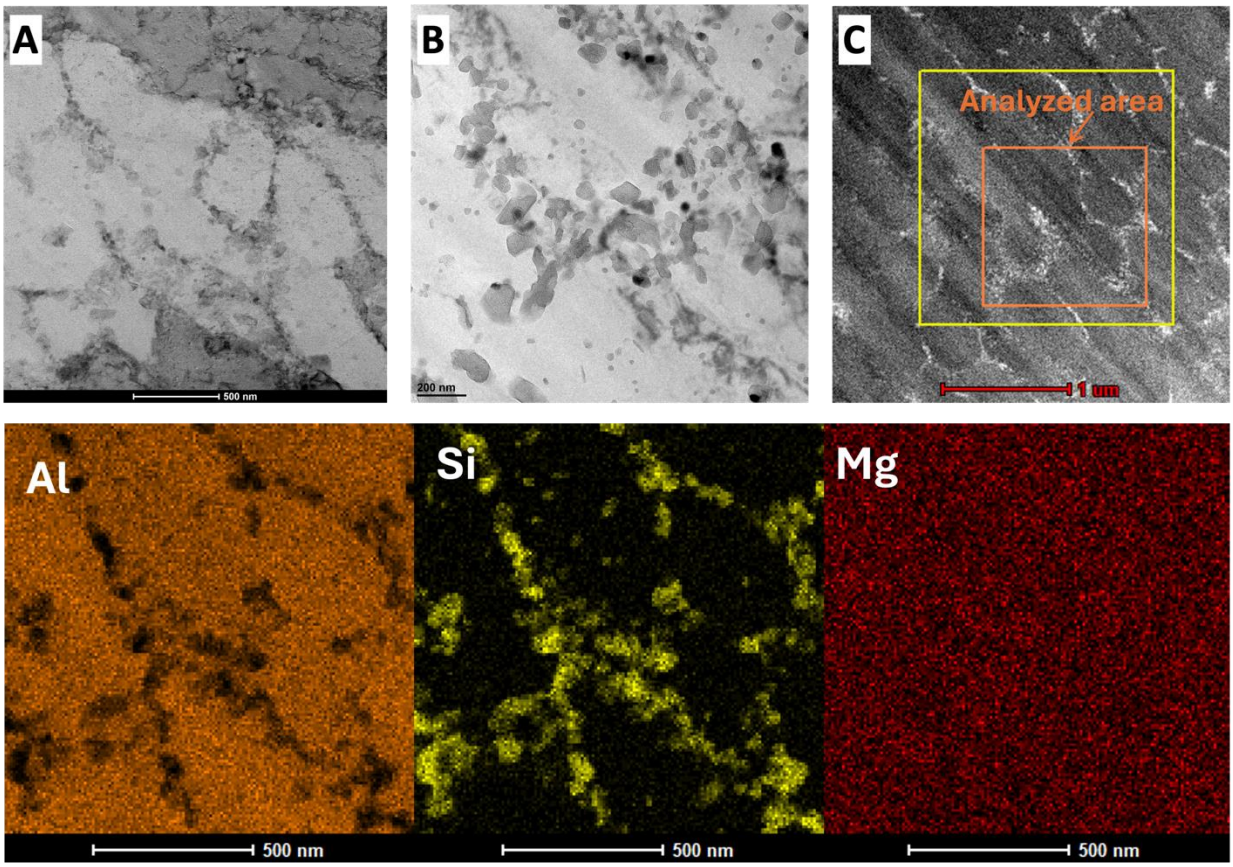

Figure 42. Cellular structure of LTA_300 obtained from transmission electron microscopy (TEM) A. TEM image showing a magnified view of the fragmented cellular structure, **B**. Higher magnification TEM image showing coarsened Si particles at the cell boundaries **C**. STEM image and accompanying EDS mapping of the fragmented cell boundaries.

EBSD analysis of the LTA_300 sample reveals that the overall grain morphology remains stable following annealing at 300 °C for 30 minutes. The IPF map in **Figure 43A** displays the characteristic columnar grain structure and HAZ previously observed in the As-built condition, indicating the preservation of the primary grain morphology. The grain size distribution also remains largely unchanged, with an average grain diameter of 23.48 ± 60.39 µm and an average grain area of 178.54 ± 180.25 µm² (**Figure 43B**). However, subtle evolution in grain boundary distribution is evident. Quantitative boundary analysis shows a slight increase in the fraction of

HAGBs, rising to 83.7%, while the proportion of LAGBs correspondingly decreases to 16.3% (**Figures 43C and 43D**).

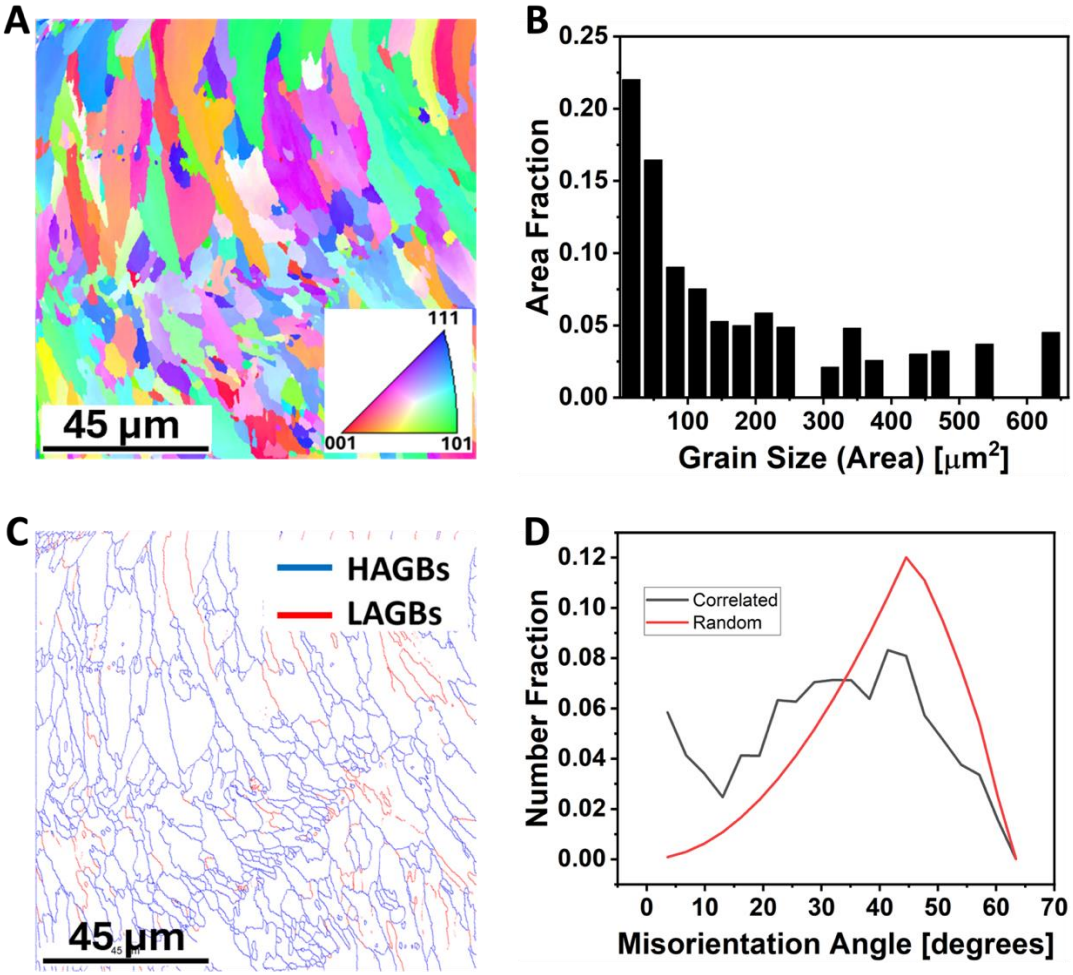

Figure 43. Microstructure of LTA_300 from EBSD analysis. A. EBSD IPF-Z map of the sample, **B**. Grain size (area) histogram of the sample, **C**. Grain boundary map of the sample, and **D**. Misorientation angle histogram of the sample.

4.3 Mechanical Properties of As-Built and Heat-Treated PBF-LB/M AlSi10Mg

This section presents an evaluation of the mechanical properties of PBF-LB/M AlSi10Mg samples in the as-built and heat-treated conditions. The investigation encompasses Vickers microhardness measurements, uniaxial compressive testing, and analysis of work hardening behavior to assess the influence of thermal treatments on mechanical performance. To provide mechanistic insight into the observed property variations, the mechanical testing results are correlated with supporting microstructural analyses. These include the evolution of microstructure

and dislocation structures under moderate to high strain levels, with particular emphasis on the accumulation of GNDs. Together, these analyses aim to elucidate the role of sub-cell network continuity on the plastic deformation mechanisms governing strength and strain hardening in PBF-LB/M AlSi10Mg alloys.

4.3.1 Hardness

Vickers microhardness results are compared for the samples before and after heat treatment and the results are presented in **Figure 44**. The As-built sample exhibits the highest average microhardness value, measured at 115.8 ± 4.5 $HV_{0.3}$. Following LTA heat treatment, a progressive decrease in microhardness is observed. The LTA_280 sample shows a moderate reduction to 105.5 ± 6.1 $HV_{0.3}$, while the LTA_300 sample demonstrates the lowest hardness, with an average value of 98.0 ± 3.3 $HV_{0.3}$. This trend correlates with the extent of fragmentation of the eutectic silicon network observed.

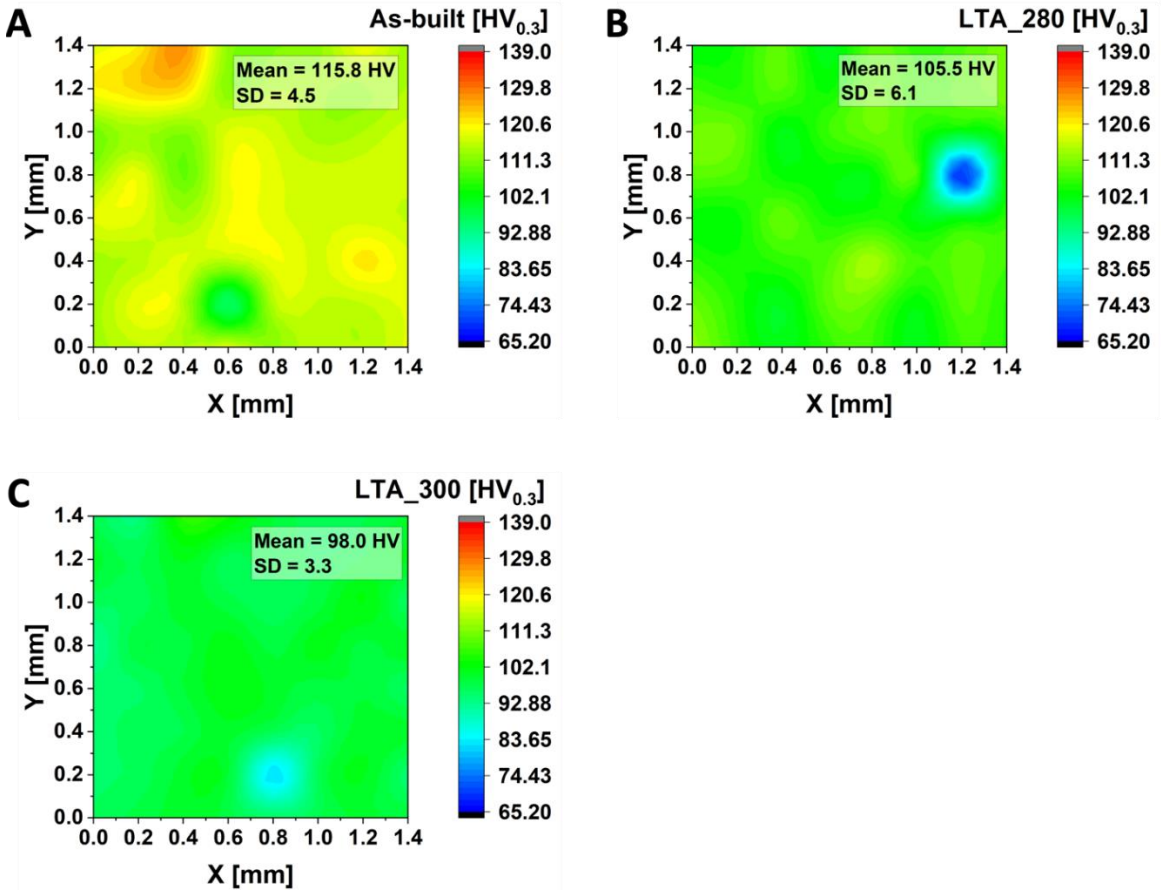

Figure 44. Vickers microhardness test results measured along the cross-section of the samples before and after heat treatment A. As-built, **B**. LTA_280, and **C**. LTA_300

4.3.2 Stress-Strain Behavior at Different Strain Levels

To evaluate the influence of Si cellular network modification on strain hardening behavior, uniaxial compression tests were conducted at room temperature across three strain levels: 5%, 20%, and maximum strain to fracture (max). The corresponding engineering and true stress-strain curves are presented in **Figures 45 – 47**, respectively. At 5% strain, all samples exhibited predominantly elastic behavior, as evidenced by the linear trend in the engineering stress-strain curves (**Figure 45**). Upon increasing the strain to 20%, noticeable yielding was observed (**Figure 46**). The as-built sample exhibited a yield strength of approximately 380 MPa, marking the point of deviation from linearity. In comparison, the LTA_280 and LTA_300 samples showed lower yield strengths of approximately 350 MPa and 280 MPa, respectively. At maximum strain (**Figure 47**), all samples demonstrated increased yield strength and underwent fracture. The as-built sample reached an estimated yield strength of 450 MPa, fracturing at 35.1% strain. The LTA_280 sample exhibited a yield strength of approximately 440 MPa, with a corresponding fracture strain of 36.8%. Nonetheless, although the LTA_300 sample maintained the lowest yield strength (~320 MPa), it showed the highest fracture strain of 47.2%, indicating improved ductility.

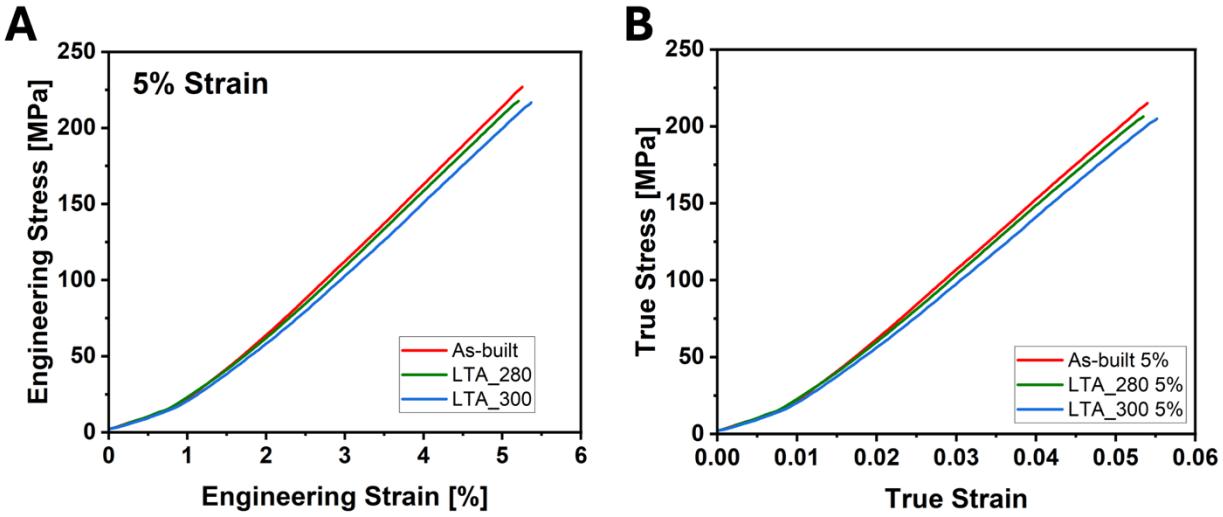

Figure 45. Engineering (**A**) and True (**B**) stress-strain plots corresponding to 5% strain compression for the samples before and after heat treatment.

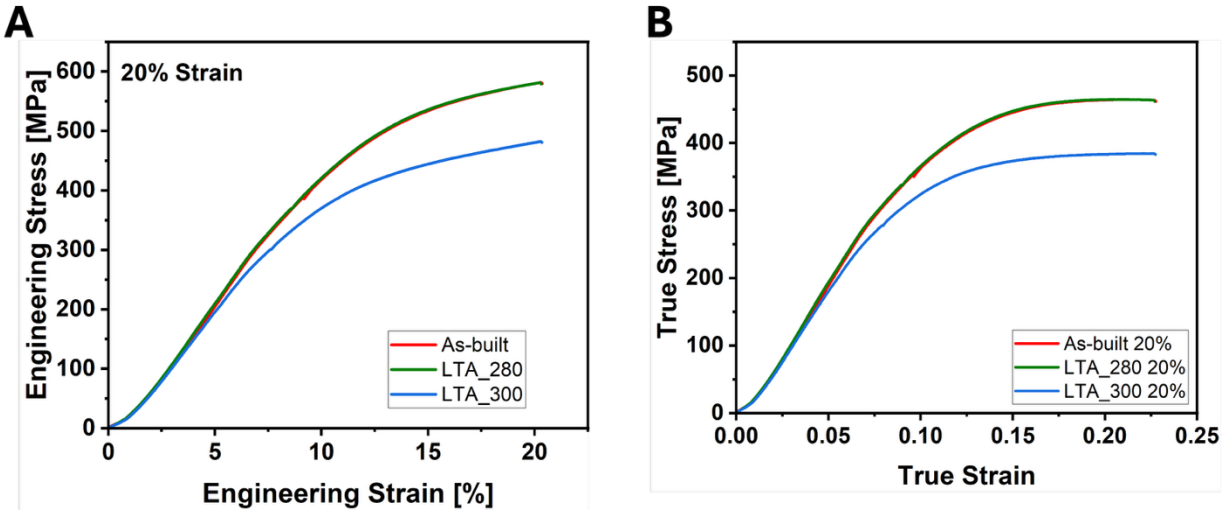

Figure 46. Engineering (**A**) and True (**B**) stress-strain plots corresponding to 20% strain compression for the samples before and after heat treatment.

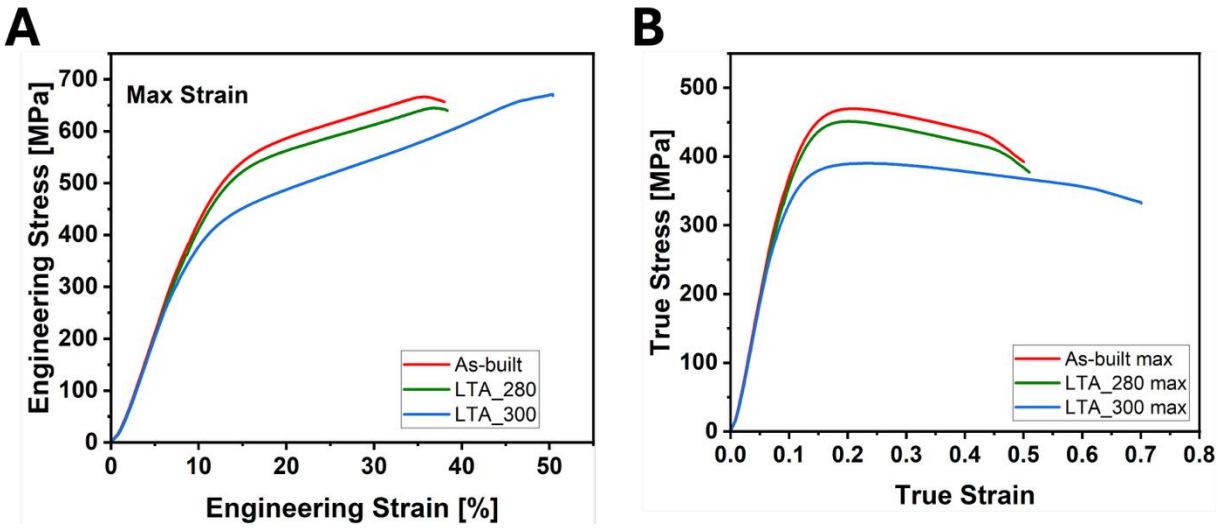

Figure 47. Engineering (**A**) and True (**B**) stress-strain plots corresponding to maximum strain compression for the samples before and after heat treatment.

4.3.2.1 Strain Hardening Behavior at Maximum Strain

To further understand the strain hardening behavior of the samples after reaching maximum strain, the strain hardening rate ($d\sigma/d\varepsilon$) was plotted as a function of true strain, as presented in **Figure 48**. Across all conditions, the strain hardening rate exhibited a decreasing trend with increasing true strain. This behavior is characteristic of plastically deforming AlSi10Mg alloys [78], [148], and reflects the material's progressively reduced ability to resist further plastic deformation as strain accumulates. At the onset of plastic deformation, the samples showed

relatively high strain hardening rates, indicative of significant initial work hardening. Among the three conditions, the As-built sample demonstrated the highest initial strain hardening rate, followed closely by the LTA_280 sample, whereas the LTA_300 sample showed the lowest. As true strain increased, the strain hardening rates for all samples gradually decreased. By approximately 0.22 true strain, the hardening rates of all conditions converged, suggesting that the material's capacity for further strain hardening had substantially diminished.

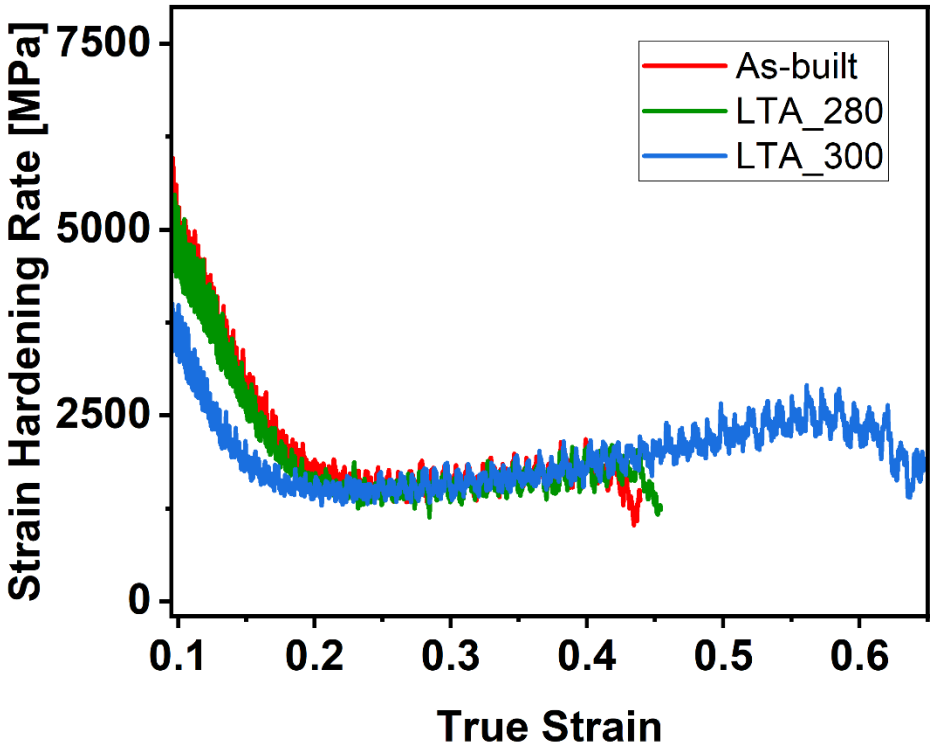

Figure 48. Strain hardening rate vs. True Strain plot for the compressed samples

The observed strain hardening behavior suggests that while the continuous or partially continuous Si cellular network enhances the material's initial resistance to plastic deformation, its capacity to resist localized deformation diminishes at larger strains, regardless of the structural integrity of the network. The LTA_300 sample, which possesses a fragmented cellular structure, was the last to undergo fracture, indicating a higher total strain-to-failure. To gain deeper insight into this behavior, the strain hardening exponent (n) was determined using the linearized form of Hollomon's power law (**Equation 8**):

$$\sigma = K\varepsilon^{n} \implies \log\sigma = \log K + n\log\varepsilon \quad (8)$$

The exponent was determined from the slope of the linear regression results in the log-log plot of true stress versus true plastic strain during uniform plastic deformation, as shown in **Figures 49 to 51** for the compressed As-built, LTA_280, and LTA_300 samples, respectively. The calculated strain hardening exponents were 0.250 for the As-built, 0.239 for LTA_280, and 0.215 for LTA_300. These results confirm that the As-built and LTA_280 samples exhibit a greater tendency for strain hardening, largely due to the barrier effect of the continuous or partially continuous Si network, which impedes dislocation motion and contributes to higher dislocation storage. Conversely, the lower strain hardening exponent of the LTA_300 sample is attributed to the fragmented nature of the cellular network. Nonetheless, its higher fracture strain shows that fragmentation of the Si network, while reducing the initial strain hardening rate, enhances ductility.

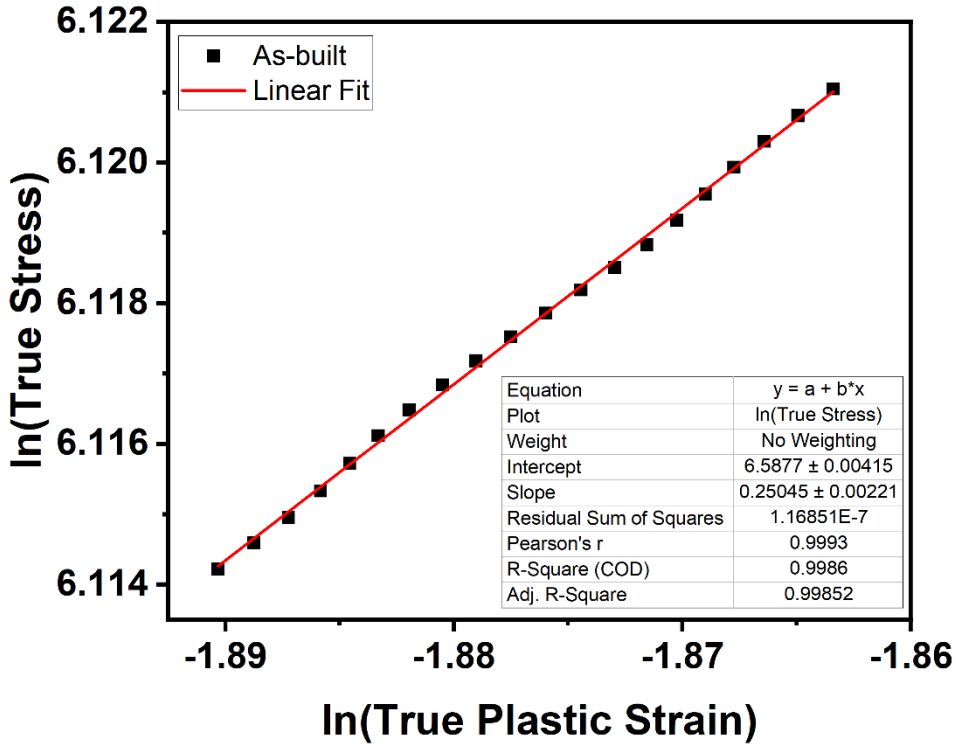

Figure 49. Strain hardening exponent plot for the compressed As-built sample

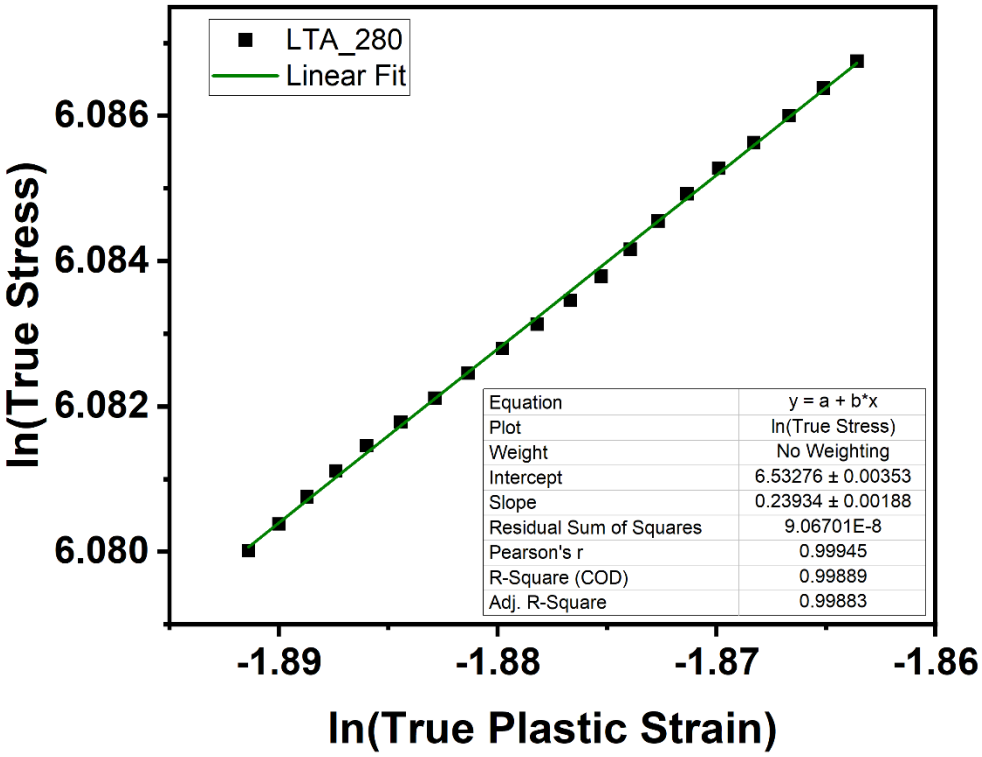

Figure 50. Strain hardening exponent plot for the compressed LTA_280 sample

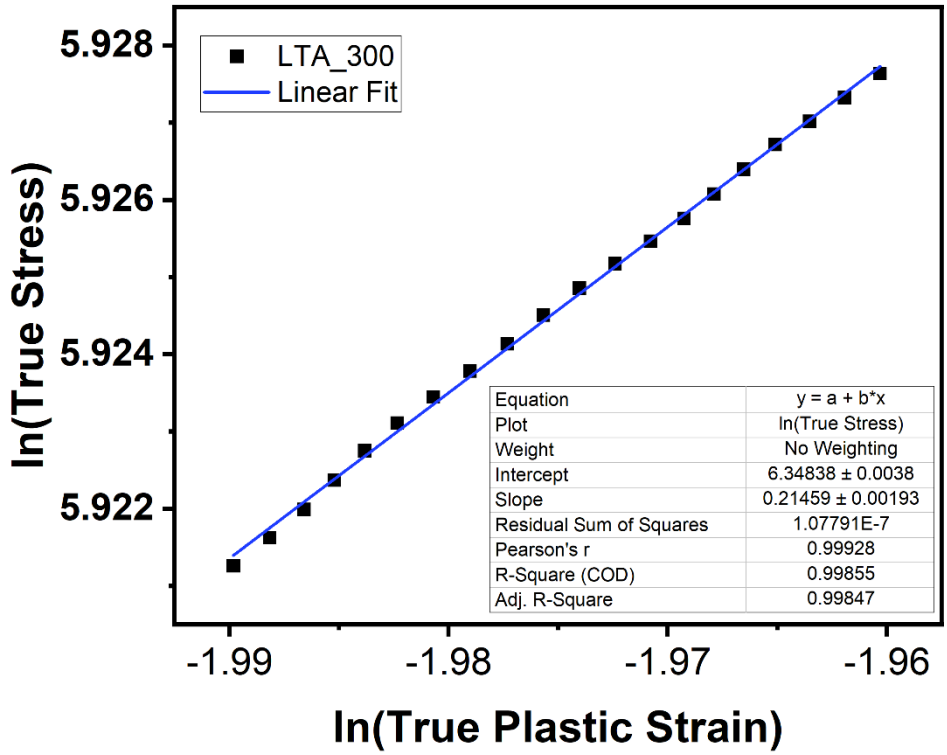

Figure 51. Strain hardening exponent plot for the compressed LTA_300 sample

A summary of the mechanical properties of the samples before and after heat treatment is given in **Table 4**.

Table 4. Mechanical Properties of as-built and heat-treated PBF-LB/M AlSi10Mg

Sample ID	**Hardness [$HV_{0.3}$]**	**Yield strength (σ_y) [MPa]**	**UCS [MPa]**	**Total strain at failure (ε_f) [%]**	**n**
As-built	115.8 ± 4.5	450	670.2	35.1	0.250
LTA_280	105.5 ± 6.1	440	666.3	36.8	0.239
LTA_300	98.0 ± 3.3	320	671.2	47.2	0.215

4.3.3 Dislocation Density

This section evaluates the evolution of dislocation densities in the As-built, LTA_280, and LTA_300 samples following compressive deformation. Dislocation densities were estimated using the Williamson–Hall (W–H) method (**Equations 9 and 10**), which enables the determination of crystallite size and microstrain from the broadening of X-ray diffraction peaks.

$$\beta\cos\theta = \frac{k\lambda}{D} + 4\varepsilon\sin\theta \tag{9}$$

Where β is full width at half maximum (FWHM) of the XRD peak (in radians); θ is Bragg angle; k is shape factor; λ is the wavelength of the X-ray; D is crystallite size; and ε is the microstrain, which is related to the dislocation density according to **Equation 10** where b is the magnitude of the Burgers vector and ρ is the dislocation density.

$$\rho = \frac{\varepsilon^2}{3b^2} \tag{10}$$

Table 5. Crystallite size and dislocation density from XRD.

Sample	**Crystallite Size (nm)**	**Dislocation density (m^{-2})**
As-built 5%	330.62	6.02×10^{13}
As-built 20%	203.81	9.67×10^{13}

As-built max strain	223.01	9.62×10^{13}
LTA_280 5%	268.80	7.12×10^{13}
LTA_280 20%	252.37	8.11×10^{13}
LTA_280 max strain	242.85	8.88×10^{13}
LTA_300 5%	311.43	6.14×10^{13}
LTA_300 20%	76.53	1.47×10^{14}
LTA_300 max strain	59.3	1.48×10^{14}

The corresponding XRD patterns, shown in **Figure 52**, capture diffraction from the Al matrix across different deformation levels (5%, 20%, and max strain), depicting peak broadening and intensity changes as strain increases.

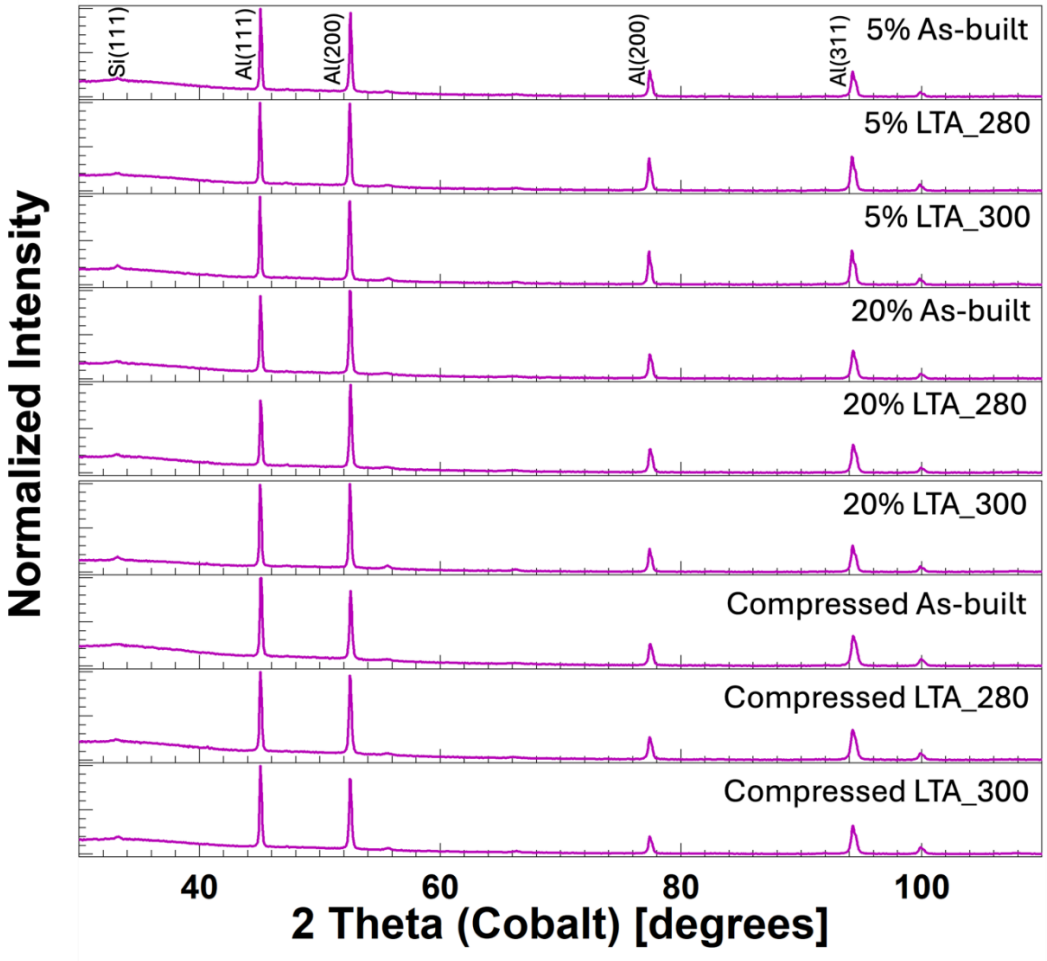

Figure 52. XRD spectra of the samples after compression at different 5%, 20%, and maximum strains.

At 5% strain, the As-built sample exhibited the largest crystallite size of 330.62 nm and a dislocation density of 6.02×10^{13} m^{-2}. The LTA_280 sample showed a smaller crystallite size of 268.80 nm and a slightly higher dislocation density of 7.12×10^{13} m^{-2}. The LTA_300 sample, which underwent eutectic network fragmentation during heat treatment, exhibited an intermediate crystallite size of 311.43 nm and a dislocation density of 6.14×10^{13} m^{-2}. As deformation progressed to 20% strain, all samples exhibited a general trend of crystallite refinement and an associated increase in dislocation density. The As-built sample's crystallite size decreased significantly to 223.01 nm, with a corresponding rise in dislocation density to 9.62×10^{13} m^{-2}. A similar response was observed in the LTA_280 sample, where the crystallite size decreased to 242.85 nm and dislocation density increased to 8.88×10^{13} m^{-2}. In contrast, the LTA_300 sample demonstrated a distinct microstructural response under severe deformation. At the maximum strain, the crystallite size reduced dramatically to 59.3 nm, while the dislocation density escalated to 1.48×10^{14} m^{-2}, the highest among all conditions.

Overall, an inverse correlation between crystallite size and dislocation density was observed, consistent with classical strain hardening behavior, where smaller crystallites serve as more effective barriers to dislocation motion. Furthermore, an inverse trend was noted between dislocation density and yield strength at maximum compressive strains. The As-built sample, with the highest yield strength, exhibited the lowest dislocation density at fracture, fracturing at 35.1% strain. Conversely, the LTA_300 sample, despite its lower yield strength, sustained up to 47.2% strain, accompanied by extensive dislocation accumulation. To further elucidate the interplay between cellular network morphology and dislocation evolution, complementary EBSD and TEM analyses were performed, as discussed in the following sections.

4.3.4 Microstructure at 5% strain

To analyze the early-stage microstructural response of the alloy to mechanical loading, EBSD investigations were conducted after 5% compressive strain. The IPF-Z maps and corresponding grain size distributions are presented in **Figure 53** for the As-built, LTA_280, and LTA_300 conditions. In the As-built sample (**Figure 53A**), the post-deformation microstructure retains the characteristic columnar morphology aligned along the build direction, similar to the undeformed state. However, the average grain area is observed to reduce to 162.1 ± 167.4 μm^2. Similarly, the LTA_280 sample (**Figure 53B**) also preserves its pre-existing columnar grain

structure following compression, reflecting a limited degree of grain morphological evolution. The average grain area decreases to $93.8 \pm 101.1\ \mu m^2$, suggesting moderate internal deformation within grains but without a substantial transformation of the overall grain morphology. In contrast, the LTA_300 sample demonstrates a different response. As shown in **Figure 53C**, the microstructure undergoes a notable transformation from columnar to more equiaxed grains, indicative of higher plastic strain accommodation. The directional grain alignment characteristic of the as-built condition is largely lost, and the average grain area is significantly reduced to $42.2 \pm 43.8\ \mu m^2$.

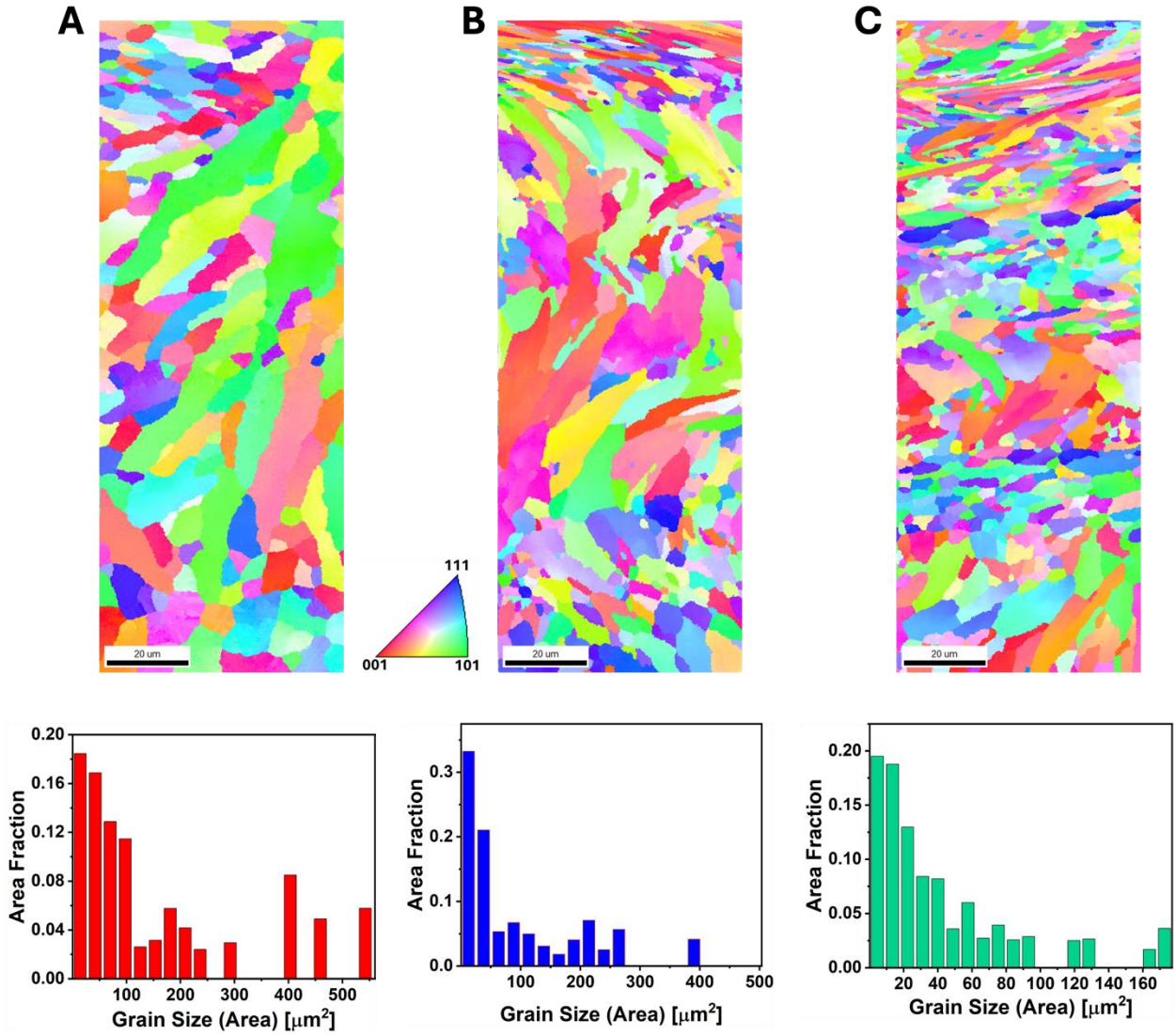

Figure 53. EBSD IPF-Z maps and grain size distribution analysis of the samples after 5% strain compression A. As-built, **B**. LTA_280, and **C**. LTA_300

Grain boundary and misorientation angle analysis were carried out following 5% compressive deformation and the results are presented in **Figure 54**. In the As-built sample (**Figure 54A**), the fraction of LAGBs (misorientation angles between 2° and 15°) increased significantly to 61.8%, with the remaining 38.2% comprising HAGBs (misorientations >15°). Conversely, the LTA_280 sample (**Figure 54B**) exhibited a decrease in LAGB content to 22.1%, with a corresponding increase in HAGBs to 77.9% after deformation. The LTA_300 sample (**Figure 54C**), which displayed a more deformed grain morphology, showed an intermediate behavior. The LAGB fraction increased moderately to 32.7%, while HAGBs constituted 67.3% of all boundaries.

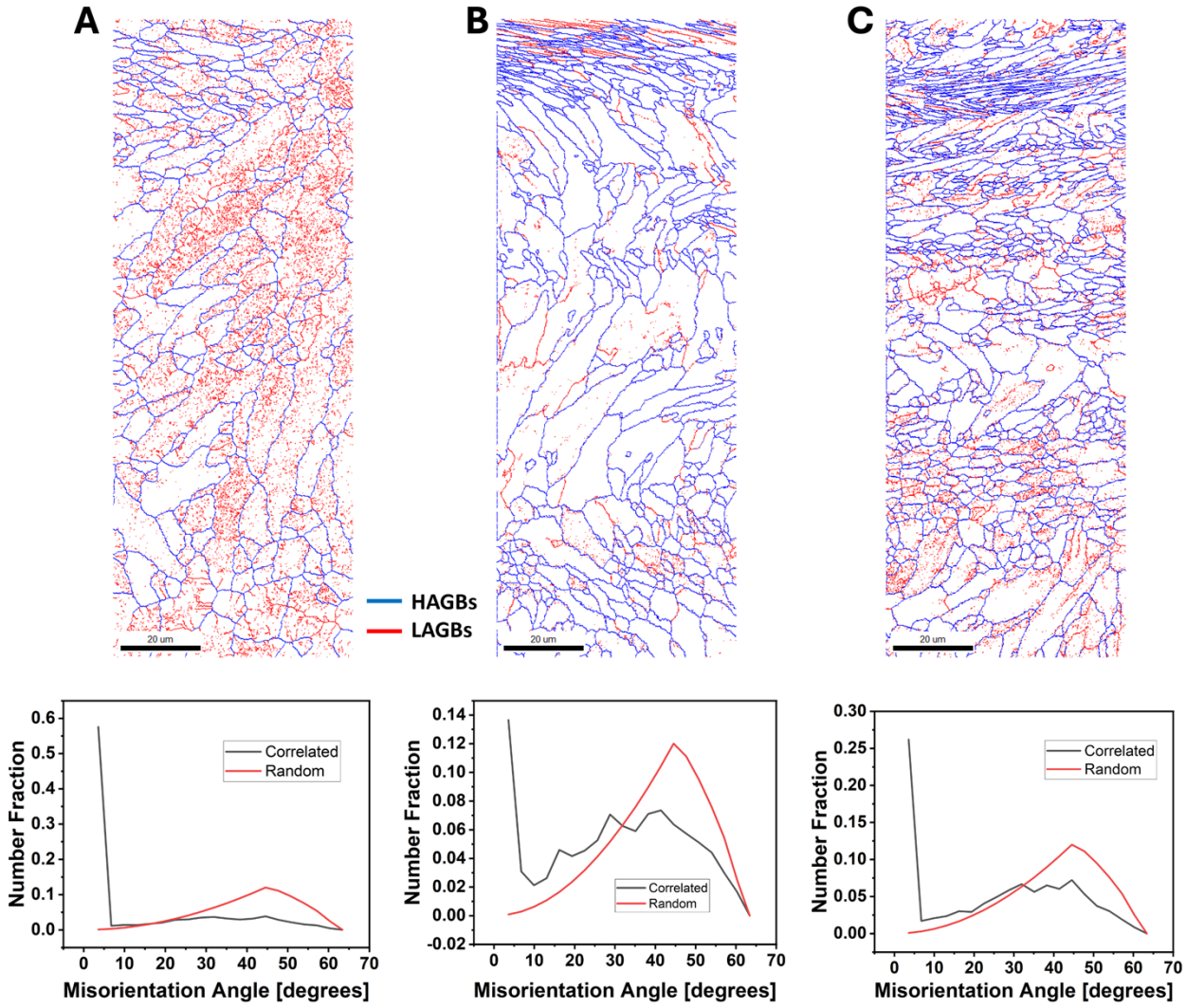

Figure 54. Grain boundary and misorientation angle distribution analysis of the samples after 5% strain compression A. As-built, **B**. LTA_280, and **C**. LTA_300

Kernel average misorientation (KAM) maps were plotted to assess the degree of GNDs accumulation following 5% compressive deformation. The results are presented in **Figure 55**. Among the investigated samples, the As-built condition (**Figure 55A**) exhibited the highest average KAM value of 0.85°, indicative of significant local misorientations. This elevated KAM suggests a high density of GNDs, consistent with a substantial GNDs accumulation at the cell boundaries during plastic deformation. The result emphasizes that a continuous and well-preserved cellular network, characteristic of the As-built microstructure, acts as an effective barrier to dislocation motion, thereby promoting dislocation pile-ups and local strain gradients. In contrast, the LTA_280 and LTA_300 samples demonstrated lower average KAM values (**Figures 55B and 55C**, respectively), reflecting reduced dislocation accumulation. This can be attributed to the thermally induced degradation of the eutectic cellular network during annealing, specifically, the partial rupture of the cellular network in LTA_280 and the extensive fragmentation observed in LTA_300, which diminishes the number of dislocation barriers during compression.

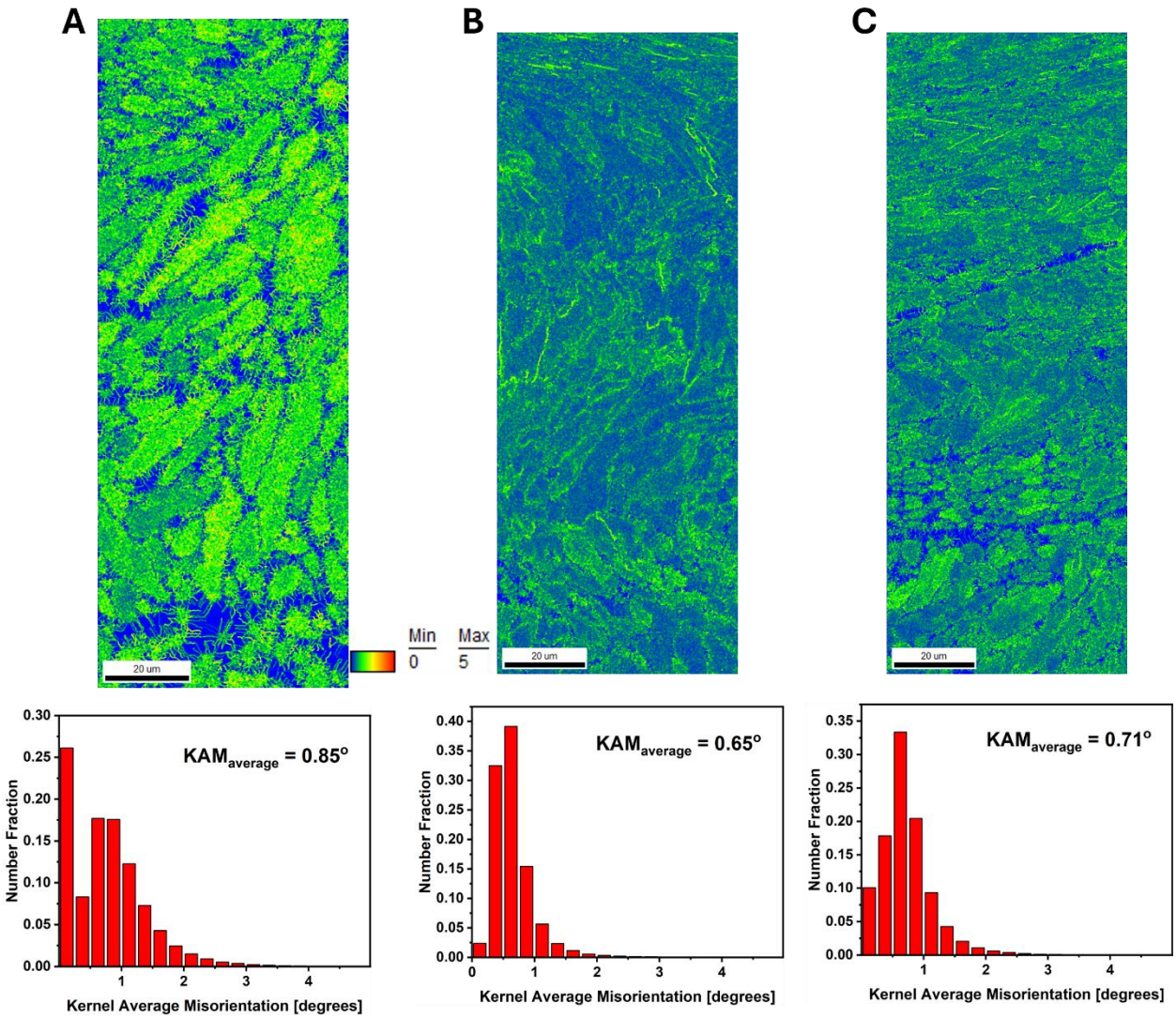

Figure 55. Kernel average misorientation (KAM) analysis of the samples after 5% strain compression A. As-built, **B**. LTA_280, and **C**. LTA_300

4.3.5 Microstructure of Compressed Samples

Observation of the post-compression As-built sample was conducted using TEM, with bright-field (BF) and dark-field (DF) images acquired and presented in **Figures 56A and 56B**, respectively. These images reveal a fragmentation of the continuous cellular structure that occurred during deformation. Additionally, numerous subgrains were observed, with an average diameter of 190 $\pm$ 50 nm. The corresponding selected area electron diffraction (SAED) pattern for **Figures 56A and 56B** is presented in **Figure 56C**. Detailed inspection of the fragmented boundary regions, further corroborated by EDS analyses shown in **Figures 56D and 56E**, confirms that silicon

remains concentrated at these fragmented boundaries. Within the refined grains, discrete silicon particulates are evident, which are presumed to have originated from the fragmentation of cell boundaries during compressive deformation. High-magnification BF and DF images (**Figures 56F and 56G**) of regions adjacent to an intragranular Si particle reveal pronounced dislocation pileups. This observation suggests both the ability of dislocations to traverse the fragmented cellular boundaries and the significant role of Si particles in acting as effective obstacles to dislocation mobility. The SAED pattern corresponding to the area shown in **Figure 56F** is displayed in **Figure 56H.**

Figure 57A presents an HRTEM image capturing a localized deformation zone, where dislocation boundaries are observed to form an ellipsoidal configuration approximately 51 nm in length. The associated SAED pattern (**Figure 57B**) confirms the presence of the face-centered cubic (FCC) aluminum phase. Complementary fast Fourier transforms (FFTs) computed from micro-areas 1 and 3 within the region exhibit patterns that match the SAED data, further substantiating the coherent crystalline orientation across the imaged zone. An inverse FFT reconstruction of region B (**Figure 57C**) shows the formation of dislocation dipoles (outlined by the yellow dashed ellipse), which are preferentially arranged along the observed dislocation boundaries.

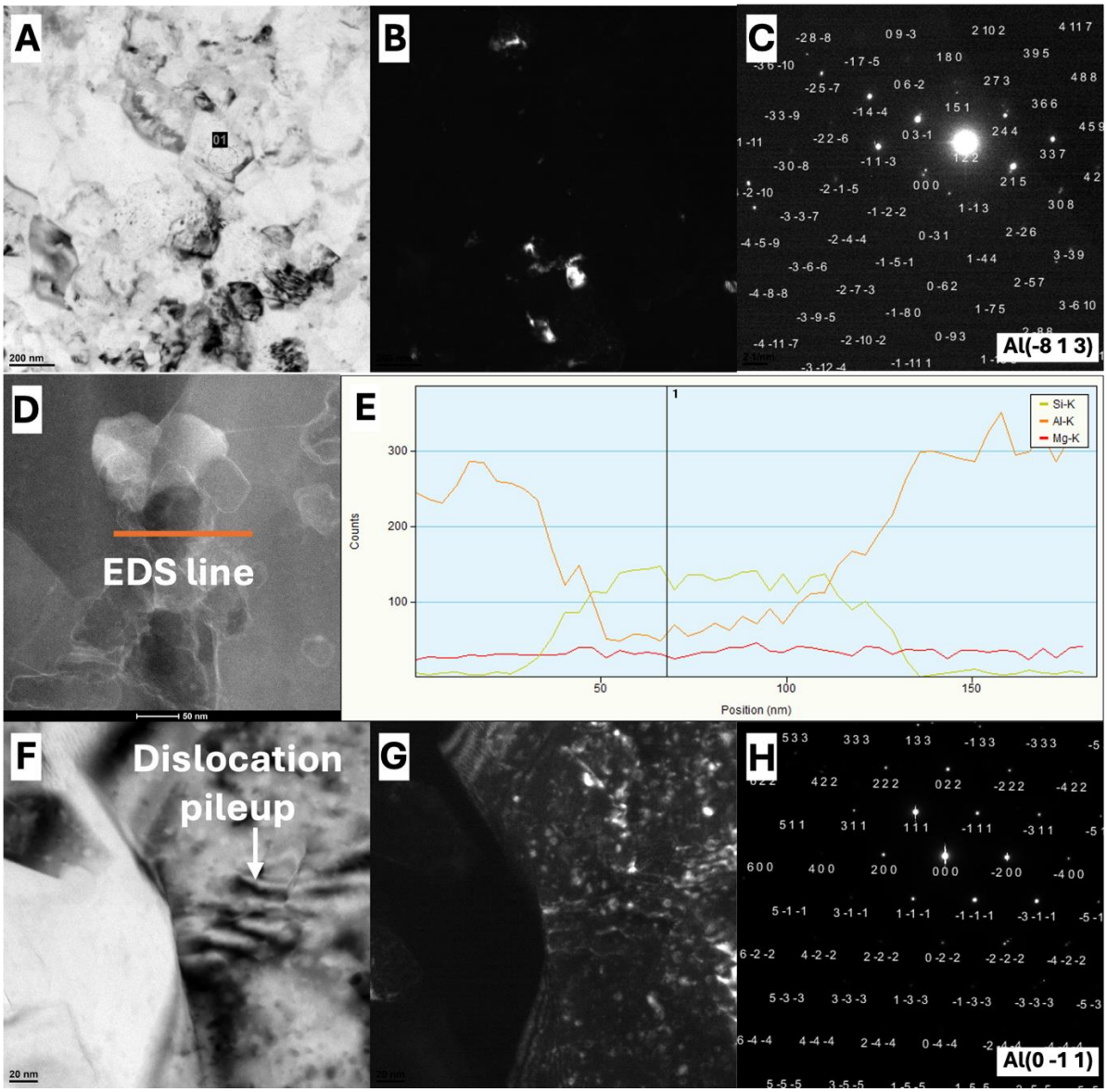

Figure 56. Transmission Electron Microscopy (TEM) analysis of compressed As-built sample **A**. Bright field TEM image, **B**. Dark field TEM image, **C**. SAED corresponding to the BF and DF images, **D**. TEM image used for EDS analysis, the orange line shows the EDS region of interest for line scan and the results displayed in the spectra in **E, F**. BF TEM image of the cell boundary showing an area with dislocation pileup, **G**. DF TEM image of F, and **H** is indexed SAED pattern corresponding to F and G.

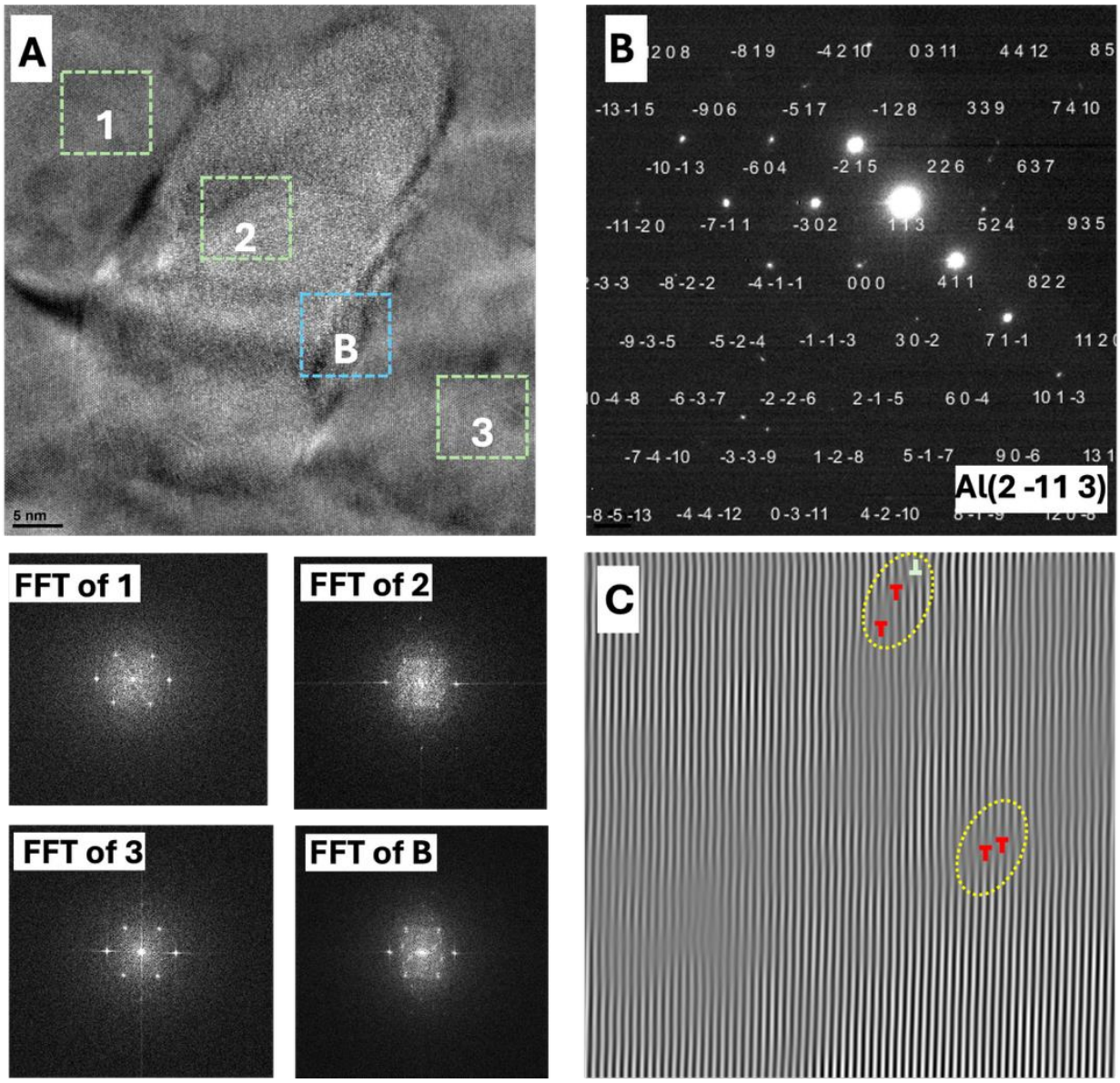

Figure 57. High-Resolution TEM (HRTEM) analysis of compressed As-built sample A. HRTEM image of dislocation boundaries captured from the grain interior and FFTs calculated from the regions marked by dashed square shapes, **B**. Indexed SAED pattern corresponding to A, **C**. Inverse FFT of the dislocation boundaries marked by the blue dashed square shape in A, showing dislocation dipoles.

Further insights into the microstructure are revealed in **Figure 58A**, which displays an HRTEM image of a silicon precipitate embedded within the aluminum matrix. The higher magnification image of the precipitate-matrix interface (**Figure 58B**) depicts a dislocation wall

adjacent to an α-Si phase, demarcated by blue dotted lines. Additionally, HRTEM analyses of an interior grain region (**Figures 58C and 58D**) reveal the presence of multiple stacking faults (SFs). These defects are indicative of partial dislocation activity, likely nucleated from Al/Si phase interfaces or high-angle grain boundaries. The coexistence of stacking faults with slip traces of perfect dislocations suggests a mixed-mode deformation behavior, where the motion of partial dislocations contributes to the overall plastic response, particularly in regions of high stress concentration. Together, these HRTEM findings provide evidence for the activation of multiple deformation mechanisms including dislocation dipole formation, stacking fault generation from the emission of partial dislocations, all of which contribute to the strain hardening and mechanical performance of the heterogeneous PBF-LB/M AlSi10Mg alloy system.

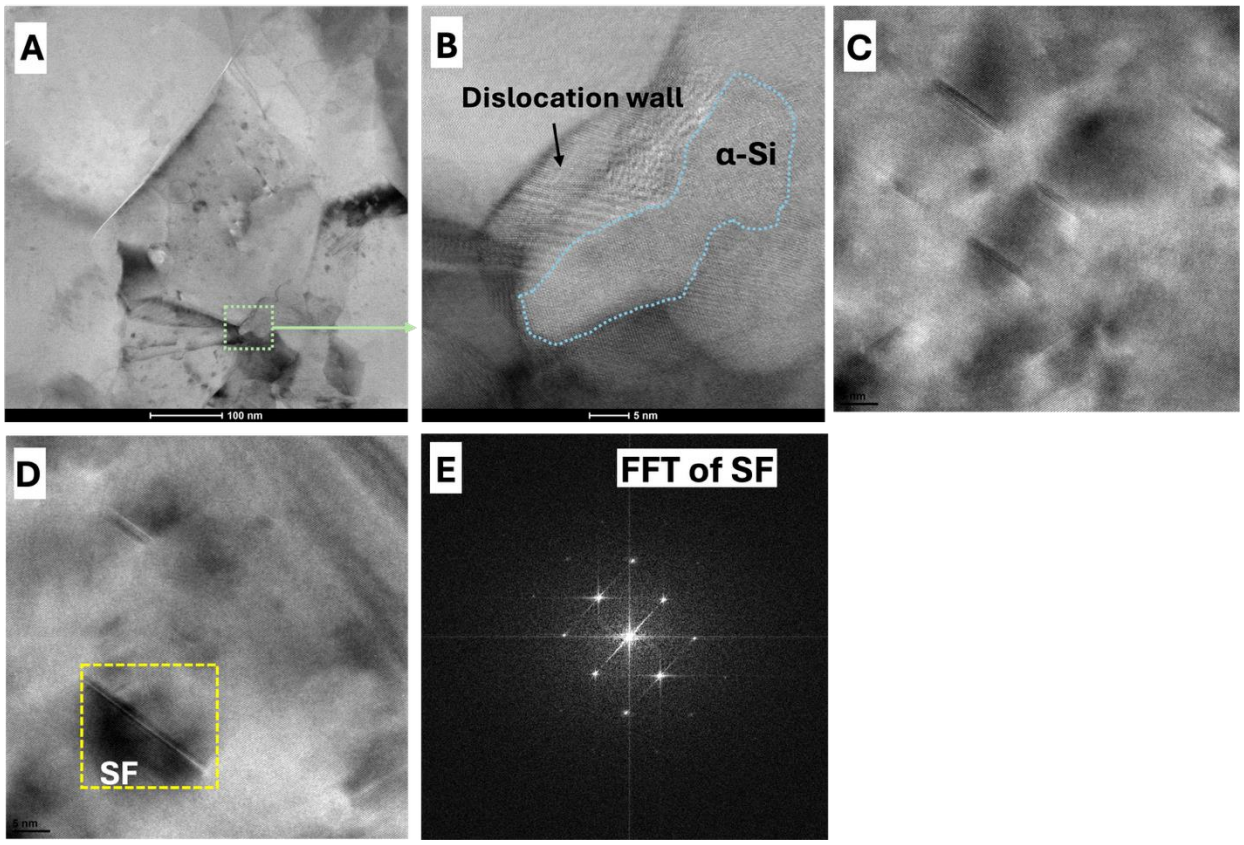

Figure 58. High-Resolution TEM (HRTEM) analysis of compressed As-built sample A. HRTEM image of silicon precipitate and a magnified section shown in **B** depicting a dislocation wall right next to an a-Si phase, **C**. HRTEM image showing stacking faults formed in a grain interior, **D**. Magnified view of the SF and the FFT of the SF calculated and presented in **E**.

Figure 59 presents TEM analysis results of the compressed LTA_300 sample. The BF and DF scanning transmission electron microscopy using high-angle annular dark-field (STEM-HAADF) images (**Figures 59A and 59B**) reveal a highly refined microstructure consisting of fragmented cellular boundaries and equiaxed grains with an average diameter of 225 ± 30 nm. **Figure 59C**, acquired via STEM, highlights these Si particles as indicated by the arrows. Numerous dislocation lines and zones of dislocation accumulation are evident around these particles, signifying that the fragmented cellular structure no longer acts as a continuous barrier to dislocation motion. Instead, dislocations traverse through the divorced Si network, interacting with the dispersed Si phase. Further BF and DF TEM imaging (**Figures 59D and 59E**) with the corresponding SAED pattern (**Figure 59F**) corroborates the presence of a high density of dislocations both within the grain interiors and along the fragmented cellular boundaries. HRTEM (**Figure 59G**) reveals the presence of stacking faults (SFs) within the grain interiors and near dislocation boundary zones, further indicating the activation of partial dislocation mechanisms. Notably, A dislocation pile-up, forming a dense dislocation wall (DDW) is evident at this Al/Si interface (**Figure 59H**)

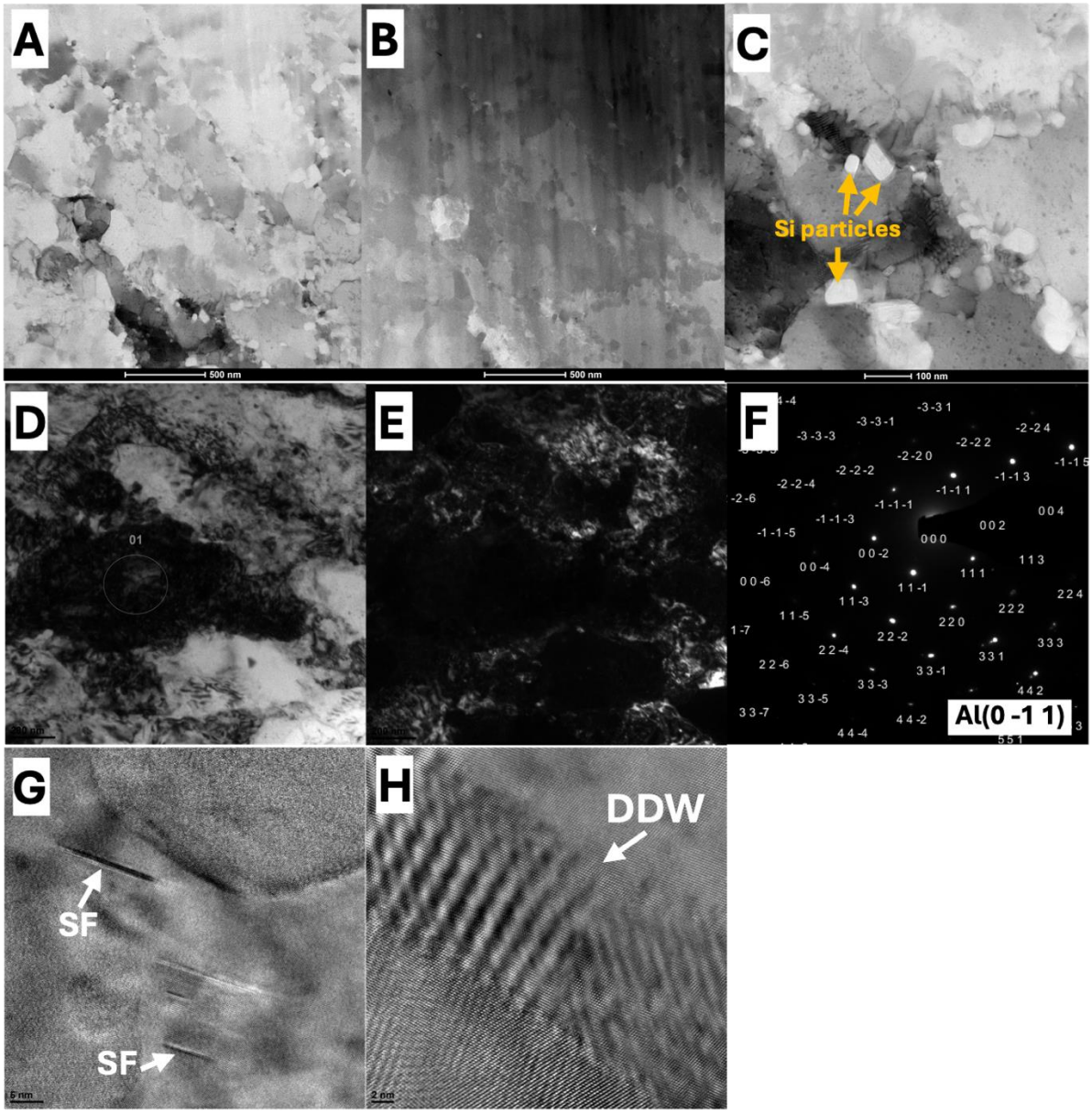

Figure 59. TEM analyses of compressed LTA_300 sample A,B Bright and Dark field STEM-HAADF images, **C**. STEM image of particulate Si surrounded by multiple dislocations, **D,E**. BF and DF TEM images with corresponding indexed SAED patterns in **F**, **G**. HRTEM image showing stacking faults (SF) in the sample, and **H**. A dense dislocation wall (DDW) captured within the sample.

4.4 Equal Channel Angular Pressing (ECAP) Processing

4.4.1 Microstructural Evolution Following ECAP Processing

ECAP was employed to assess the effects of prior heat treatments and the continuity of the Si-rich cellular network on the microstructural evolution and mechanical response of the PBF-LB/M AlSi10Mg alloy subjected to severe plastic deformation. The LOM micrographs of the ECAP-processed samples – As-built_ECAP, LTA_280_ECAP, and LTA_300_ECAP – are presented in **Figures 60, 61, and 62**, respectively. The results reveal that, despite the intense shear strain imposed during ECAP, the characteristic "fish-scale" microstructure, indicative of overlapping MPBs formed during laser melting, remains discernible in all samples. However, a comparison with their respective pre-ECAP counterparts indicates a slight reduction in MP dimensions as a result of the plastic deformation. On average, the post-ECAP MPs exhibit widths of 111 ± 20 µm and depths of 38 ± 10 µm, reflecting a degree of microstructural refinement induced by the ECAP process. The results suggest that while ECAP introduces substantial strain into the material, sufficient to alter mesoscale features, the original melt pool topology characteristic of the PBF-LB/M process is not entirely modified.

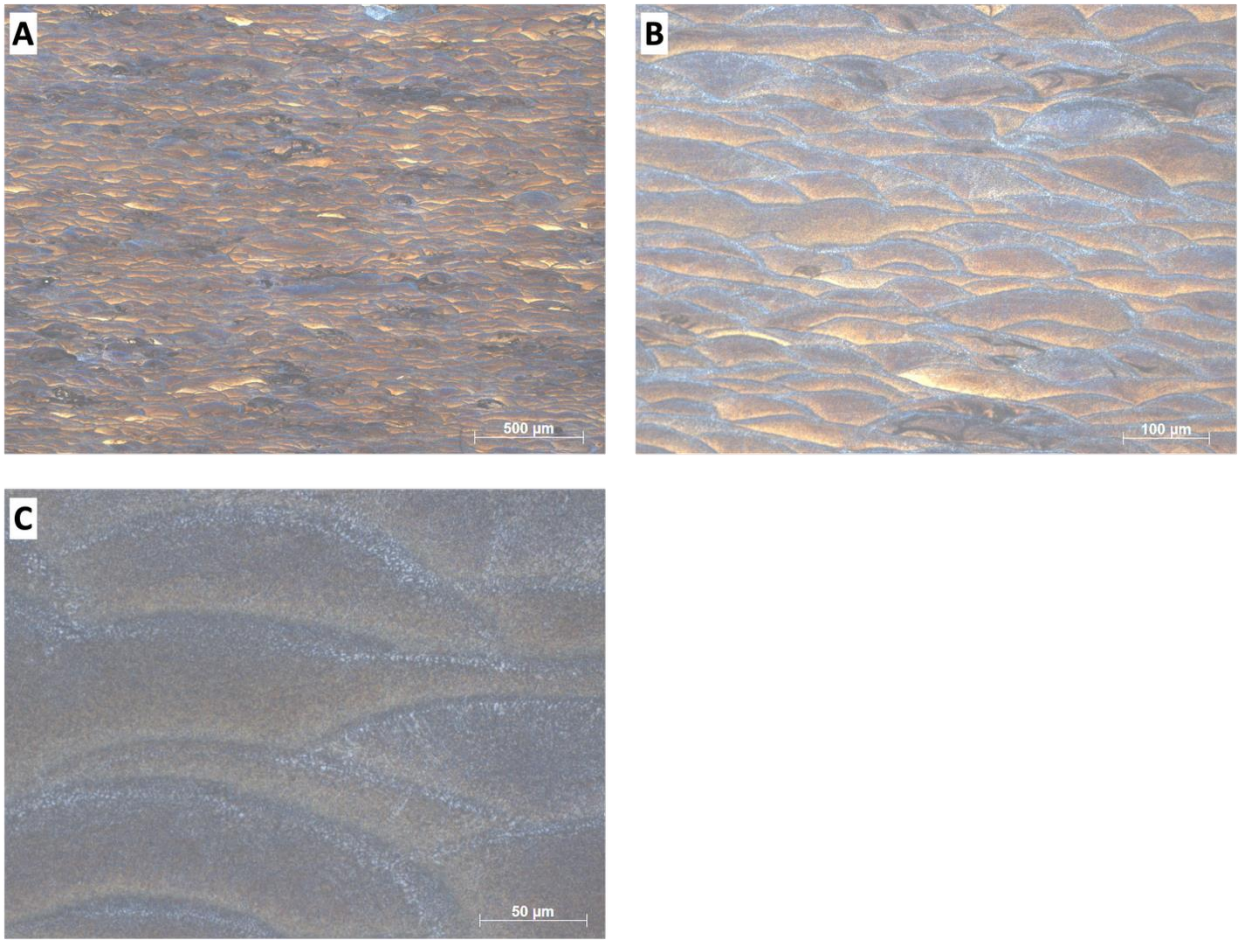

Figure 60. LOM microstructure of As-built_ECAP at different magnifications A. 50X, **B**. 200X, and **C.** 500X

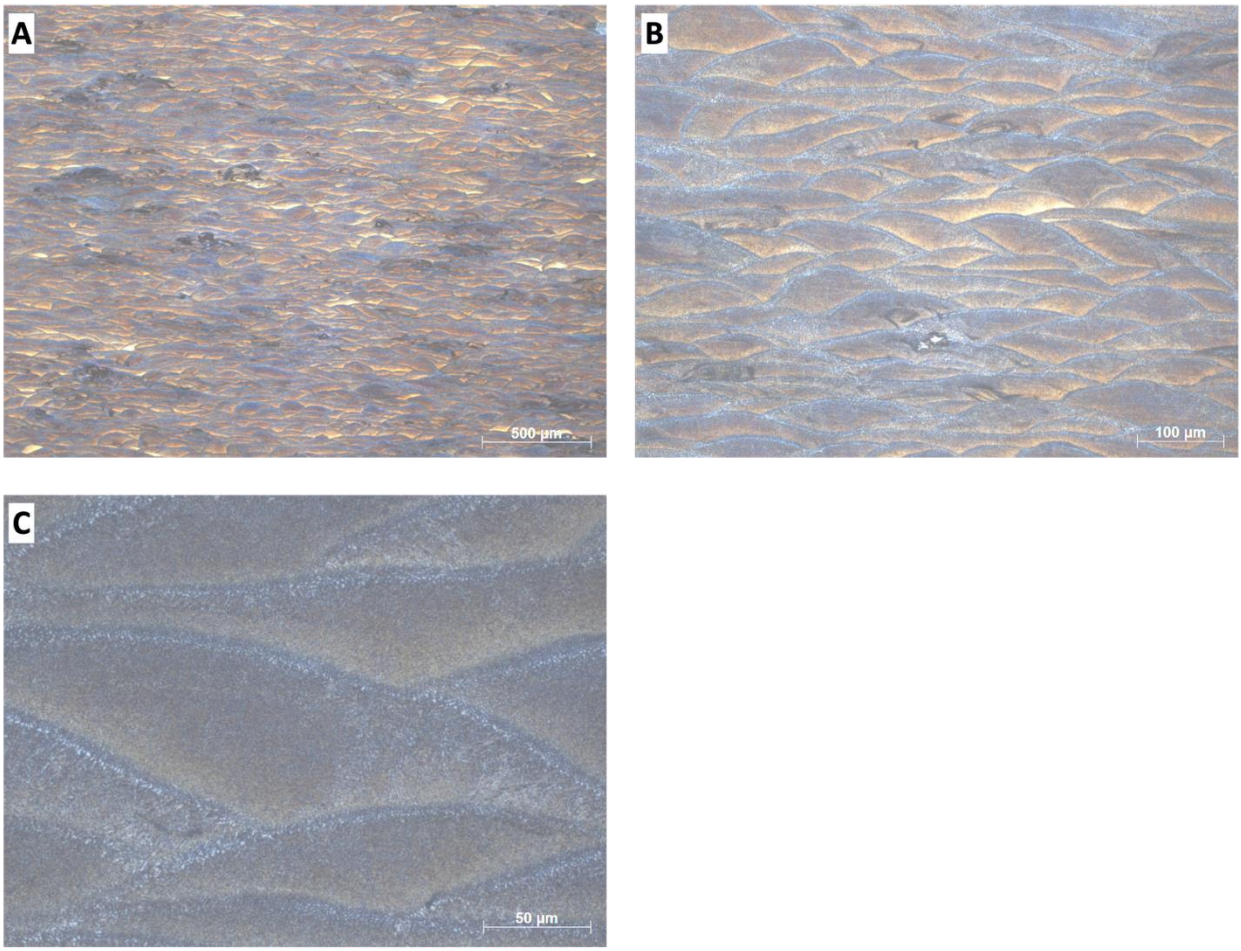

Figure 61. LOM microstructure of LTA_280_ECAP at different magnifications A. 50X, **B**. 200X, and **C.** 500X

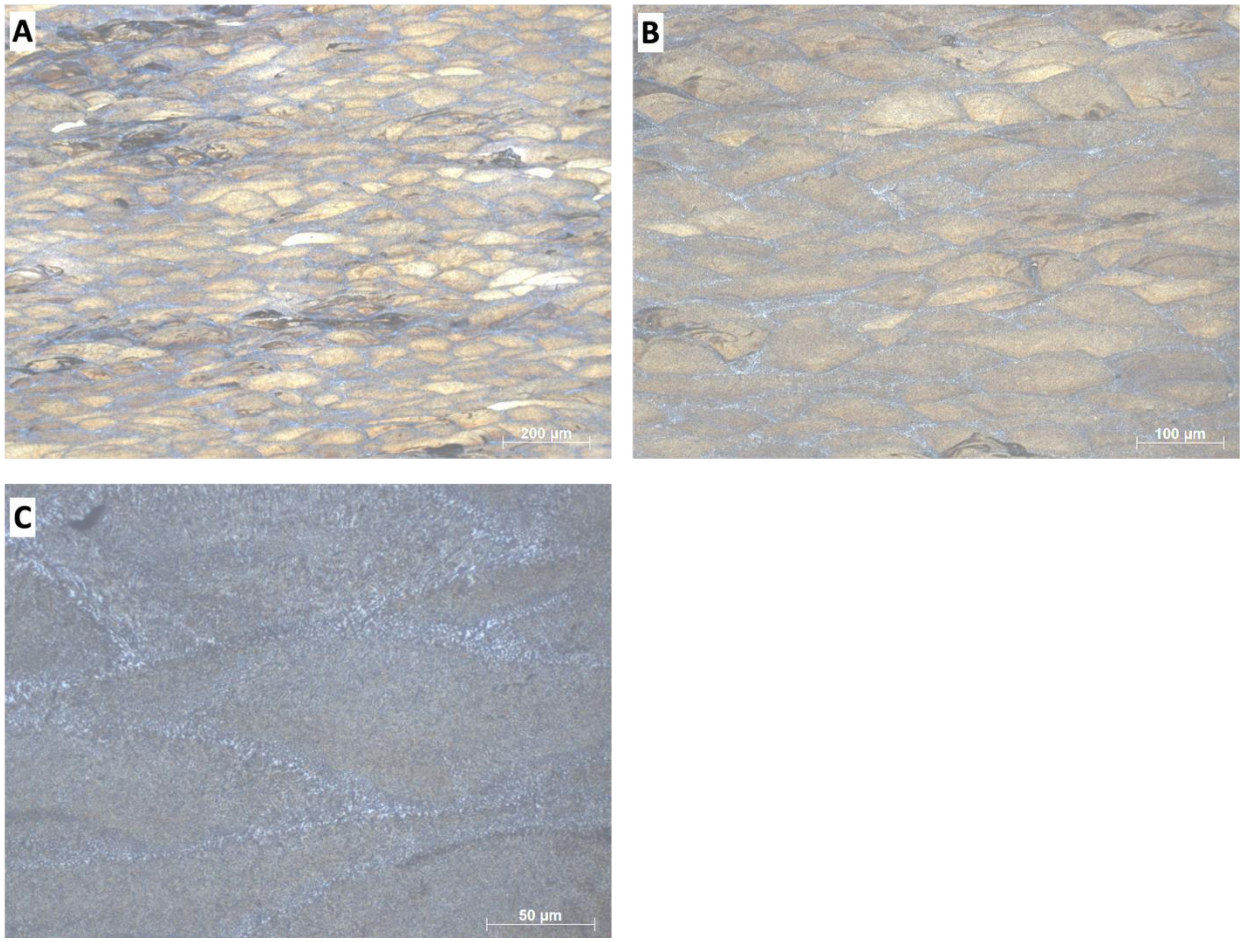

Figure 62. LOM microstructure of LTA_300_ECAP at different magnifications A. 50X, **B**. 200X, and **C.** 500X

The SEM micrograph of the As-built_ECAP sample (**Figure 63**) reveals that while some fragmentation of the cellular structure has occurred due to the imposed shear strain, a substantial portion of the cellular network remains largely intact, with cell sizes still ranging from 300 nm to 900 nm, similar to the pre-ECAP condition. In contrast, the LTA_280_ECAP sample (**Figure 64**) exhibits a significantly more fragmented network relative to its pre-ECAP state, arising from a cumulative effect of heat treatment and SPD on the eutectic structure. For the LTA_300_ECAP sample (**Figure 65**), the cellular structure remains highly fragmented, consistent with its condition prior to ECAP. However, the SEM analysis highlights the presence of discrete silicon particulates, measuring 49 ± 6 nm, dispersed throughout the aluminum matrix. These particulates are presumed to have originated from the fragmentation of former eutectic cell boundaries and were redistributed during the intense shear deformation imparted by ECAP.

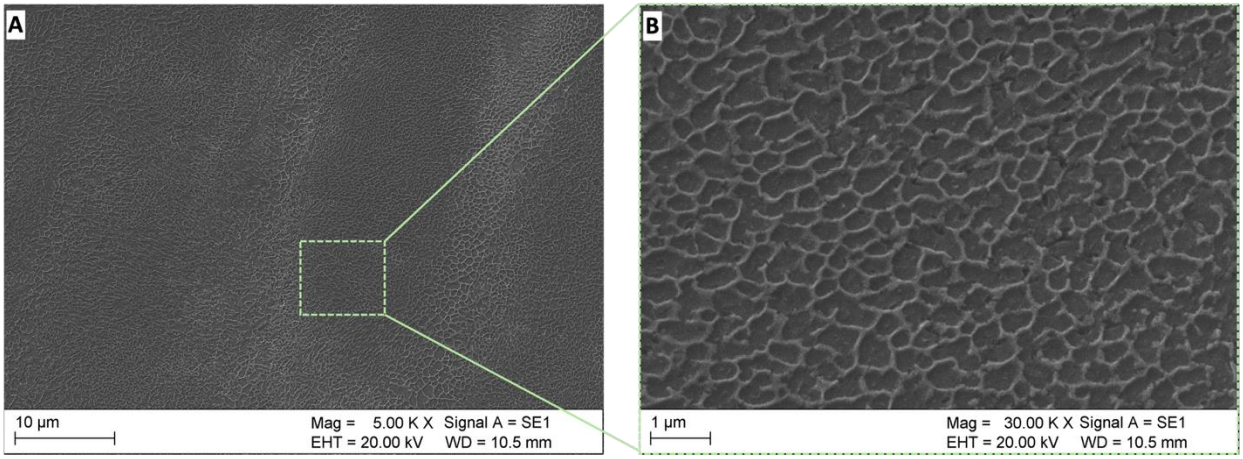

Figure 63. SEM microstructure of As-built_ECAP at different magnifications A. 5000X, **B**. 30000X

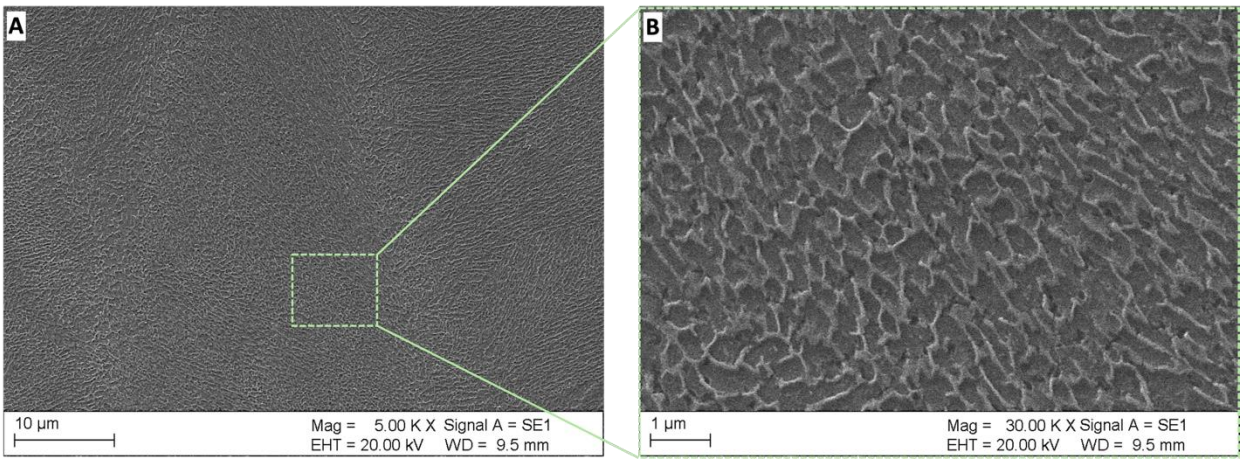

Figure 64. SEM microstructure of LTA_280_ECAP at different magnifications A. 5000X, **B**. 30000X

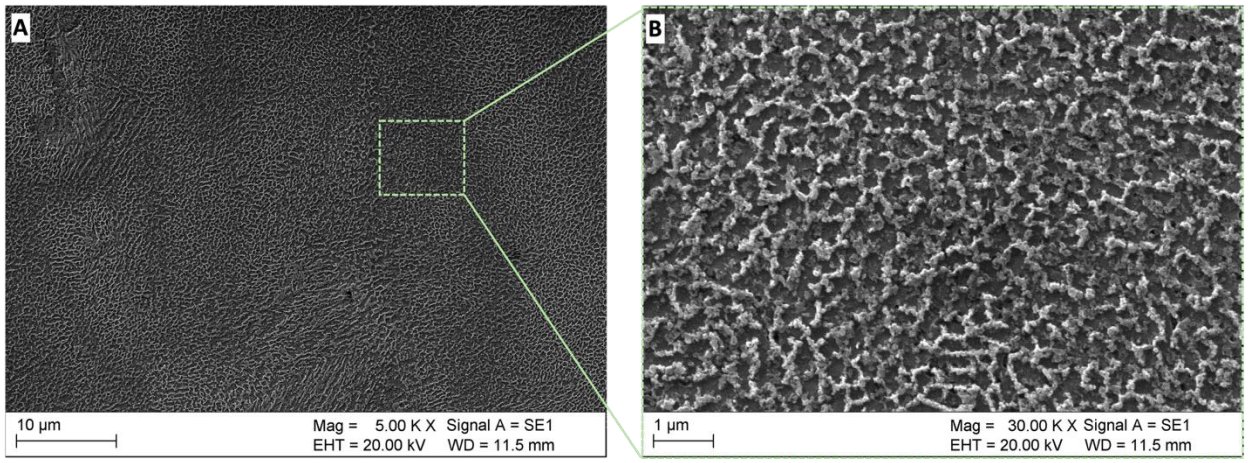

Figure 65. SEM microstructure of LTA_300_ECAP at different magnifications A. 5000X, **B**. 30000X

The IPF-Z map of the As-built_ECAP sample (**Figure 66A**) reveals a markedly refined and equiaxed grain structure, in sharp contrast to the predominantly columnar grains observed in the pre-ECAP state. Quantitative analysis confirms this grain refinement, with an average grain size of 5.70 ± 8.72 µm^2 (**Figure 66B**). Similarly, the LTA_280_ECAP sample (**Figure 66C**) shows a transition toward equiaxed grains and a reduced grain size, averaging 9.19 ± 11.46 µm^2 (**Figure 66D**). Notably, the LTA_300_ECAP sample (**Figure 66E**) exhibited the highest degree of grain refinement among the investigated samples, with a significantly reduced average grain size of 2.77 ± 6.11 µm^2 (**Figure 66F**). It is important to acknowledge the EBSD technique's inability to distinguish between crystalline grains and secondary phase particles such as silicon. As a result, the extremely fine silicon particles dispersed throughout the α-Al matrix may be misidentified as individual grains. This artifact can contribute to an underestimation of the true average grain size, particularly in samples like LTA_300_ECAP, which contain highly fragmented Si networks.

Grain boundary characterization, illustrated in **Figure 67**, indicates that the As-built_ECAP sample contained 61.7% HAGBs and 38.3% LAGBs (**Figures 67A and 67B**). In contrast, the LTA_280_ECAP sample exhibited a higher fraction of LAGBs (58.1%), with HAGBs accounting for 41.9% (**Figures 67C and 67D**). Conversely, the LTA_300_ECAP sample, with its ultrafine and equiaxed grain morphology, showed a dominant HAGB fraction of 78.4%, with LAGBs reduced to 21.6% (**Figures 67E and 67F**).

KAM analysis was used to assess the accumulation of GNDs in the post-ECAP state and the results are presented in **Figure 68**. The As-built_ECAP sample exhibited the highest average

KAM value of 1.05° (**Figures 68A and 68B**), consistent with the high integrity of the original cellular structure. In comparison, the LTA_280_ECAP and LTA_300_ECAP samples showed progressively lower KAM values, with the LTA_300_ECAP sample registering the lowest average KAM of 0.53° (**Figures 68E and 68F**). This trend aligns with the observations at low strain levels (5% compression) and showcases the role of cellular network continuity in providing dislocation accumulation sites and dictating dislocation storage during ECAP processing.

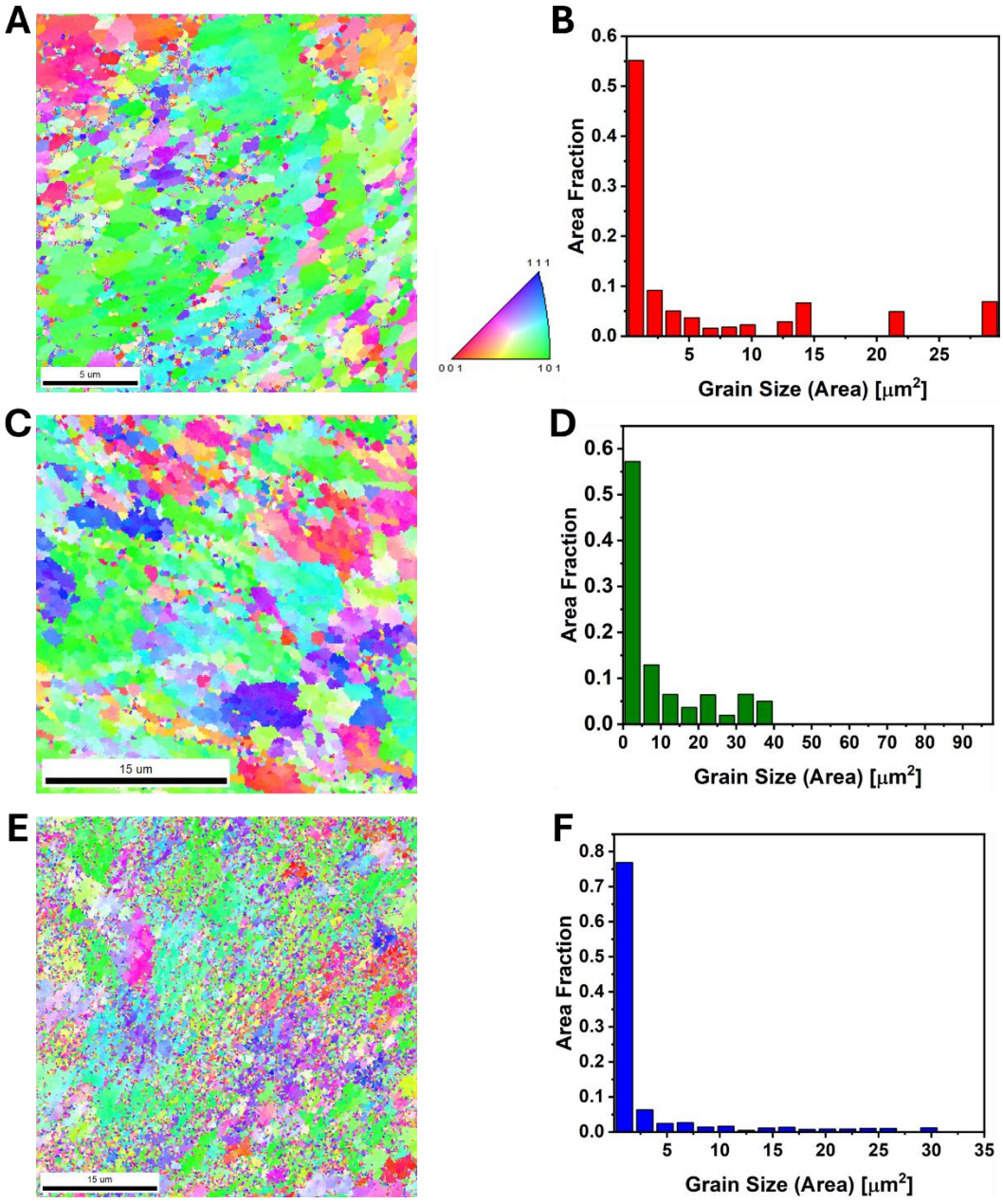

Figure 66. IPF-Z maps and corresponding grain size distribution plots for the ECAP-processed samples A,B. As-built ECAP, **C,D**. LTA_280_ECAP, and **E,F.** LTA_300_ECAP

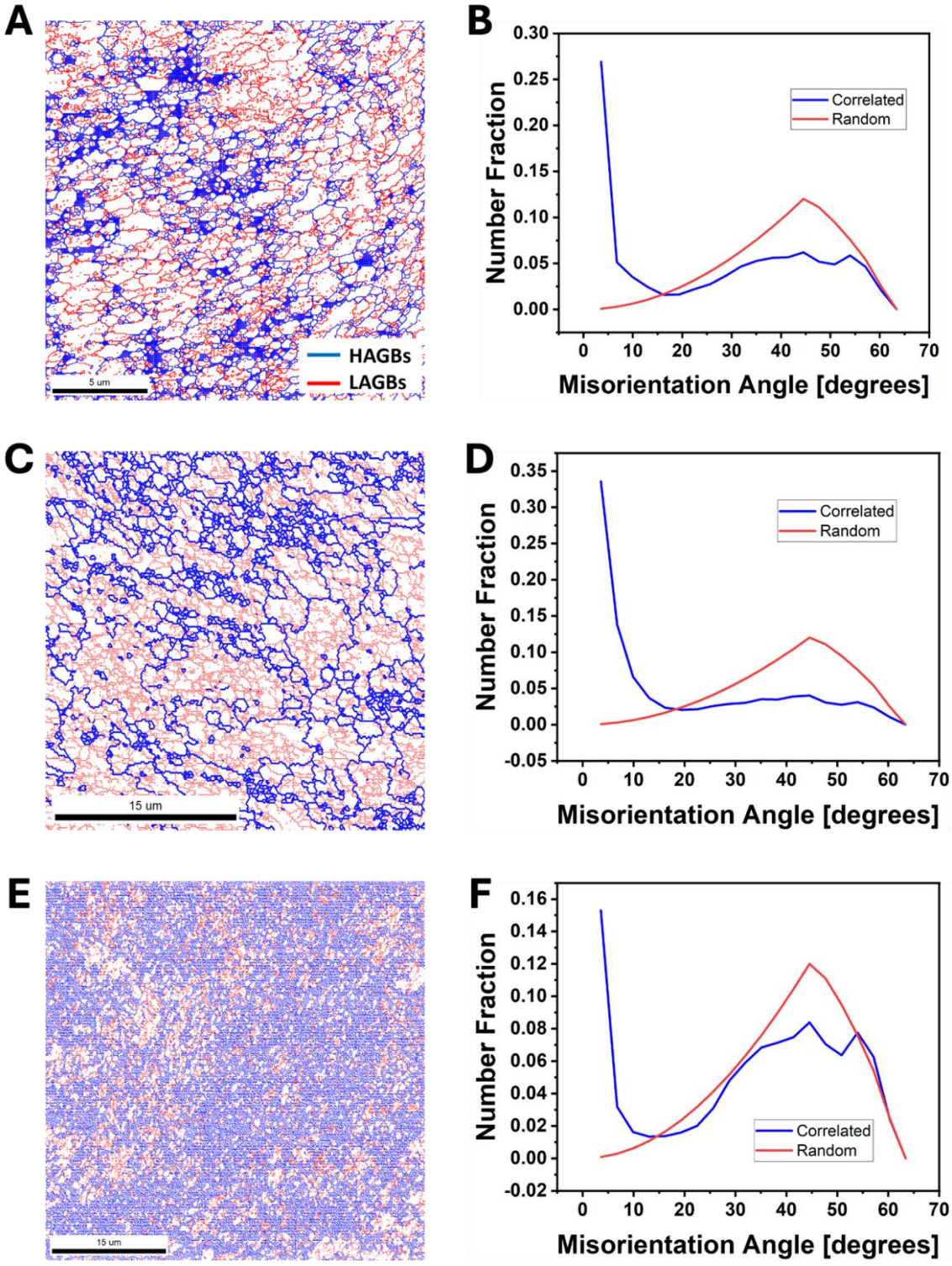

Figure 67. Grain boundary maps and corresponding misorientation angle distribution plots for the ECAP-processed samples A,B. As-built ECAP, **C,D**. LTA_280_ECAP, and **E,F.** LTA_300_ECAP

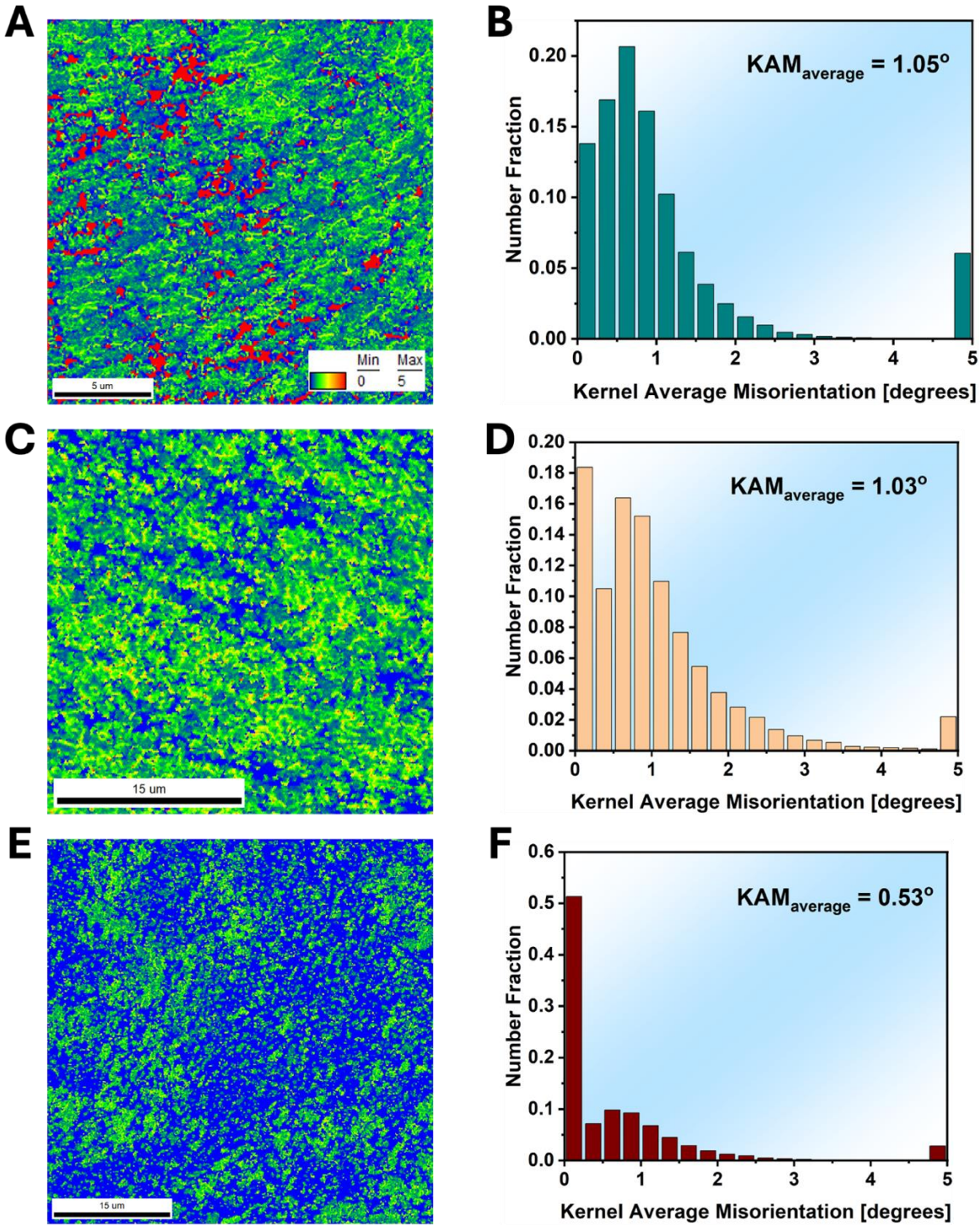

Figure 68. Kernel average misorientation (KAM) and corresponding KAM distribution plots for the ECAP-processed samples A,B. As-built ECAP, **C,D**. LTA_280_ECAP, and **E,F.** LTA_300_ECAP

TEM analysis of the As-built_ECAP sample (**Figure 69**) confirms significant grain refinement following ECAP processing. BF and DF TEM images (**Figures 69A and 69B**) reveal equiaxed grains with an average diameter of 500 ± 120 nm. Dislocations are prominently observed around the former eutectic cell boundaries, often concentrated near Si particles, which are still present and partially retained along the boundaries, as indicated by the arrows. STEM-HAADF imaging (**Figure 69D**) reveals dislocation boundaries within grain interiors, exhibiting average dimensions of approximately 267 ± 6 nm. Higher-magnification TEM images (**Figures 69E and 69F**) provide detailed views of these dislocation boundaries, which show dislocation pile-ups forming dense dislocation walls (DDWs). These walls are characteristic of the development of very low-angle grain boundaries during SPD processing.

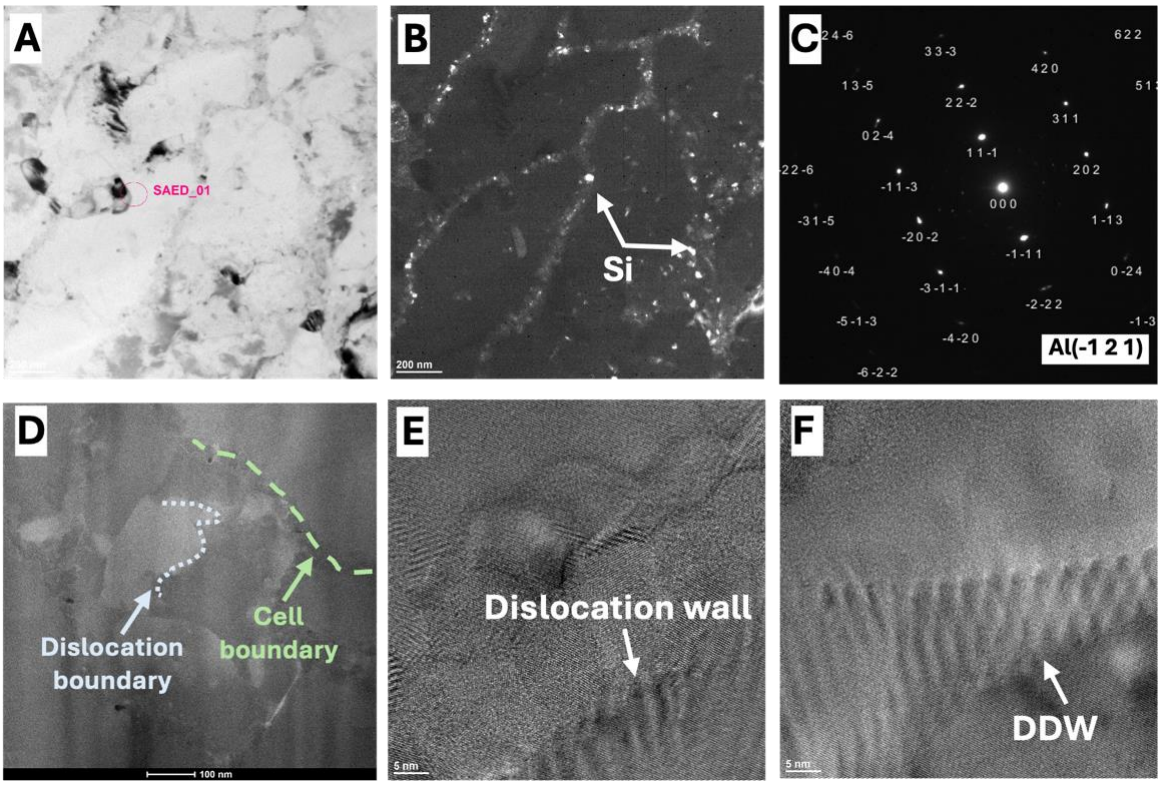

Figure 69. TEM analysis of As-built_ECAP sample. A. BF TEM image, **B.** DF TEM image showing Si precipitates at cell boundaries, **C**. Indexed SAED from zone axis Al(-1 2 1), **D**. HAADF image showing dislocation boundaries formed within the grain interior, and **E,F**. Dislocation walls (DDW – dense dislocation walls) captured from the sample.

TEM analysis of the LTA_300_ECAP sample reinforces the EBSD observations, confirming substantial grain refinement and the formation of an ultrafine-grained microstructure. STEM-HAADF images (**Figures 70A and 70B**) reveal equiaxed grains with an average size of

172.8 ± 52.4 nm. Dislocation boundaries are visible within these ultrafine grains (**Figure 70C**), attributed to dislocation pileups induced by the severe plastic deformation imposed during ECAP. HRTEM imaging (**Figure 70D**) of these regions reveals the formation of dense dislocation walls (DDWs) in the LTA_300_ECAP sample.

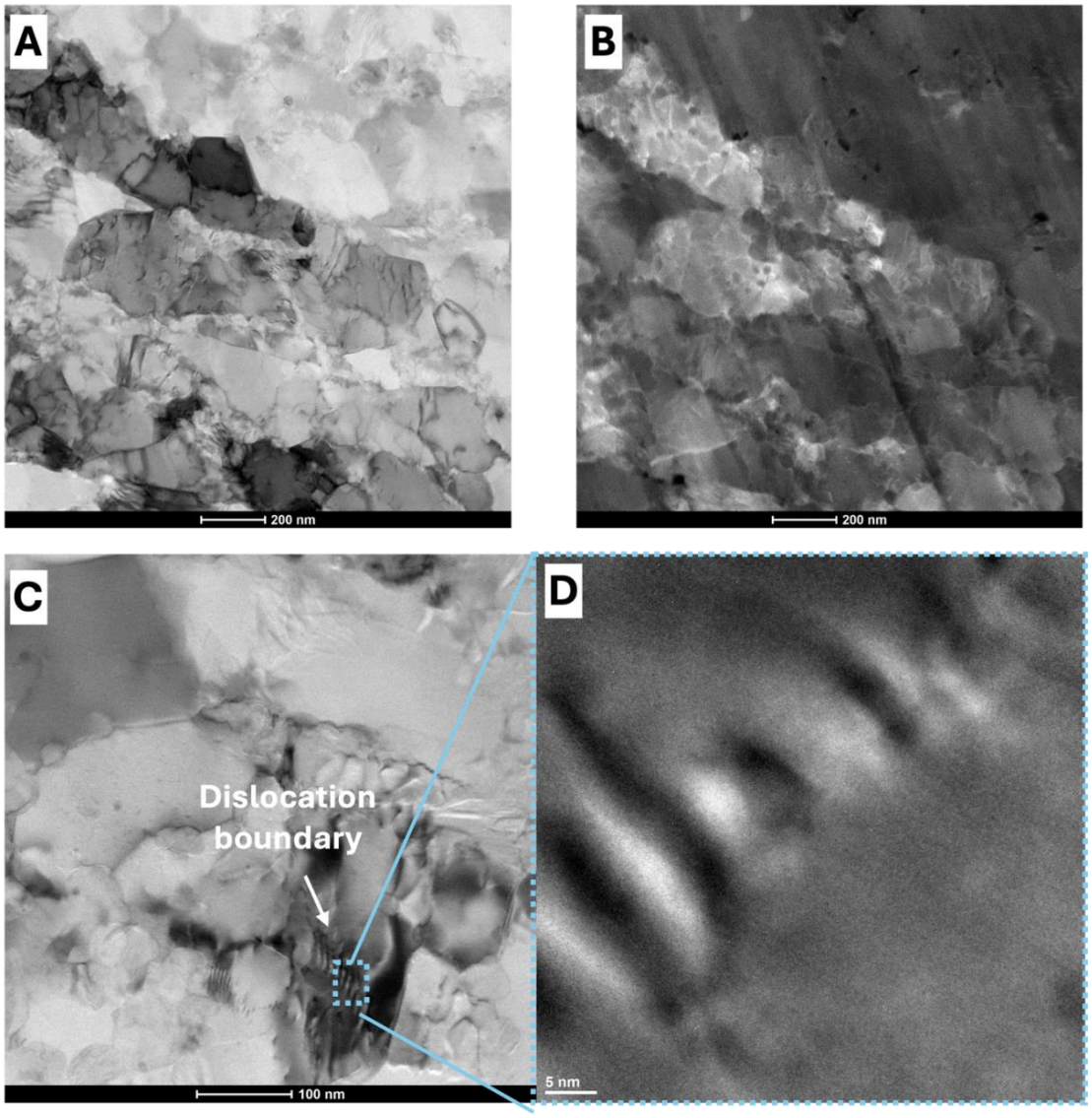

Figure 70. TEM analysis of the LTA_300_ECAP sample A,B. STEM-HAADF images showing UFG microstructure, **C**. HAADF image showing regions with a pile-up of dislocations forming dislocation boundaries, **D**. Magnified HRTEM image showing the pile up of dislocations, a DDW, at the dislocation boundary.

4.4.2 Mechanical Properties Evolution After ECAP Processing

4.4.2.1 Hardness

Figure 71 presents the Vickers microhardness profiles across the cross-sections of the samples following ECAP processing. The As-built_ECAP sample (**Figure 71A**), which retained a partially ruptured yet predominantly continuous Si cellular network, exhibited the highest average microhardness of 131.6 ± 2.3 $HV_{0.3}$, reflecting a 13.6% increase relative to its pre-ECAP condition. The LTA_280_ECAP sample (**Figure 71B**) demonstrated a 22.9% increase in hardness, rising from 105.5 ± 6.1 $HV_{0.3}$ to 129.7 ± 2.7 $HV_{0.3}$, while the LTA_300_ECAP sample (**Figure 71C**) also experienced a notable 22.4% increase, reaching 120.0 ± 3.0 $HV_{0.3}$ from its initial state.

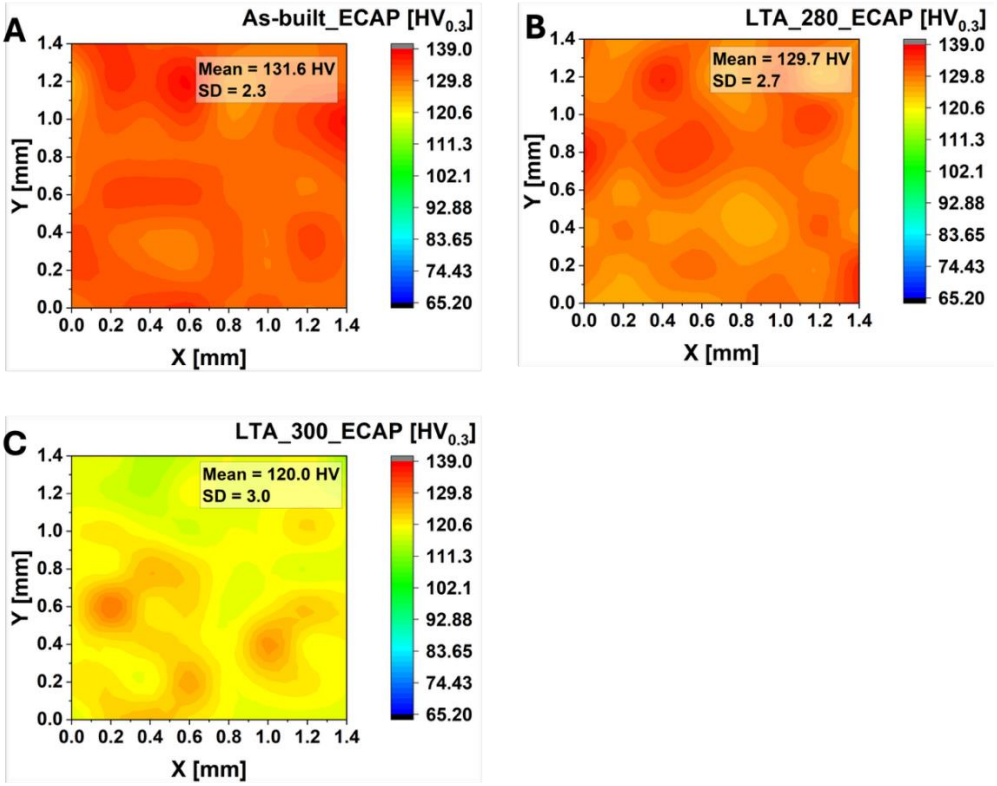

Figure 71. Vickers microhardness test results measured along the cross-section of the ECAP-processed samples A. As-built_ECAP, **B**. LTA_280_ECAP, and **C**. LTA_300_ECAP

This trend illustrates that ECAP processing enhances microhardness in all samples primarily due to grain refinement, which increases grain boundary area and impedes dislocation motion (Hall–Petch effect). Moreover, the influence of the initial Si network continuity on post-ECAP hardness is also elucidated by these results. The As-built_ECAP sample, with its more intact

cellular structure, achieved the highest post-ECAP hardness, whereas the LTA_300_ECAP sample, characterized by fragmented Si and a more disrupted microstructure, exhibited the lowest.

4.4.2.2 Strain Hardening

The mechanical behavior of the samples after ECAP processing was further evaluated through uniaxial compressive testing. The corresponding engineering and true stress–strain curves are presented in **Figures 72A and 72B**, respectively. The yield strength trends post-ECAP closely mirrored those observed in the pre-ECAP condition. Specifically, the As-built_ECAP sample exhibited the highest yield strength of 425 MPa, followed by the LTA_280_ECAP sample at 410 MPa, and the LTA_300_ECAP sample at 390 MPa. Despite its relatively lower yield strength, the LTA_300_ECAP sample demonstrated the highest ductility, failing at a true strain of 51.4%. In contrast, the As-built_ECAP and LTA_280_ECAP samples fractured at 23.4% and 25.5%, respectively. These results emphasize the significant enhancement in ductility conferred by the fragmentation of the Si network in the LTA_300_ECAP sample.

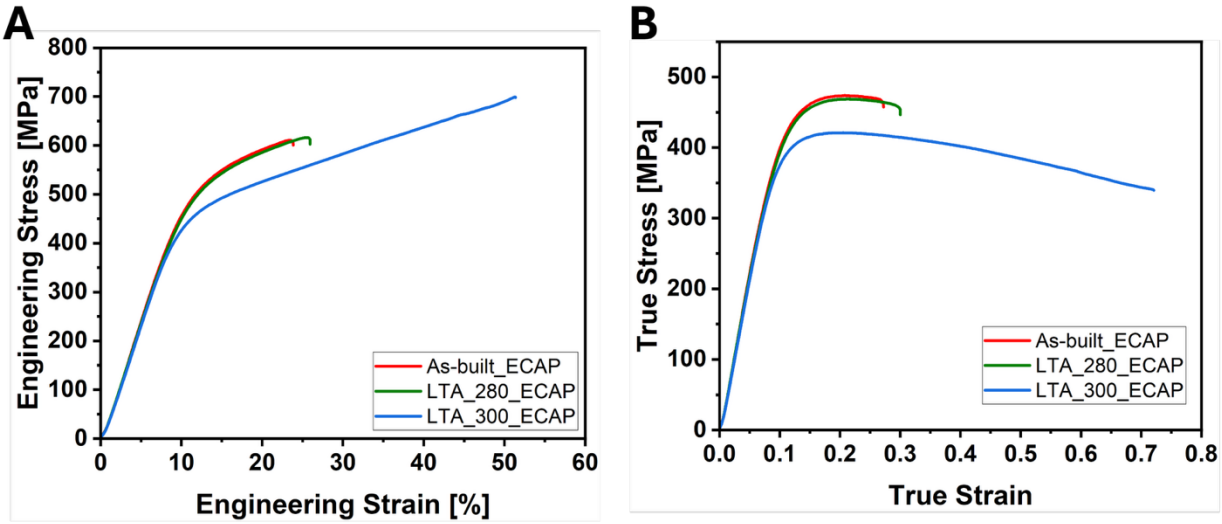

Figure 72. Engineering (**A**) and True (**B**) stress-strain plots of compressed ECAP-processed samples

The strain hardening behavior of the ECAP-processed samples was further examined by the strain hardening exponent (n) via linear regression in the log–log plots of true stress versus true plastic strain, as shown in **Figures 73 – 75**. The As-built_ECAP and LTA_280_ECAP samples exhibited comparable strain hardening exponents of 0.261 and 0.244, respectively, indicating their relatively higher capacity for sustained resistance to plastic deformation during straining. In contrast, the

LTA_300_ECAP sample had a lower strain hardening exponent of 0.218, consistent with its more fragmented cellular microstructure at the early stages of deformation.

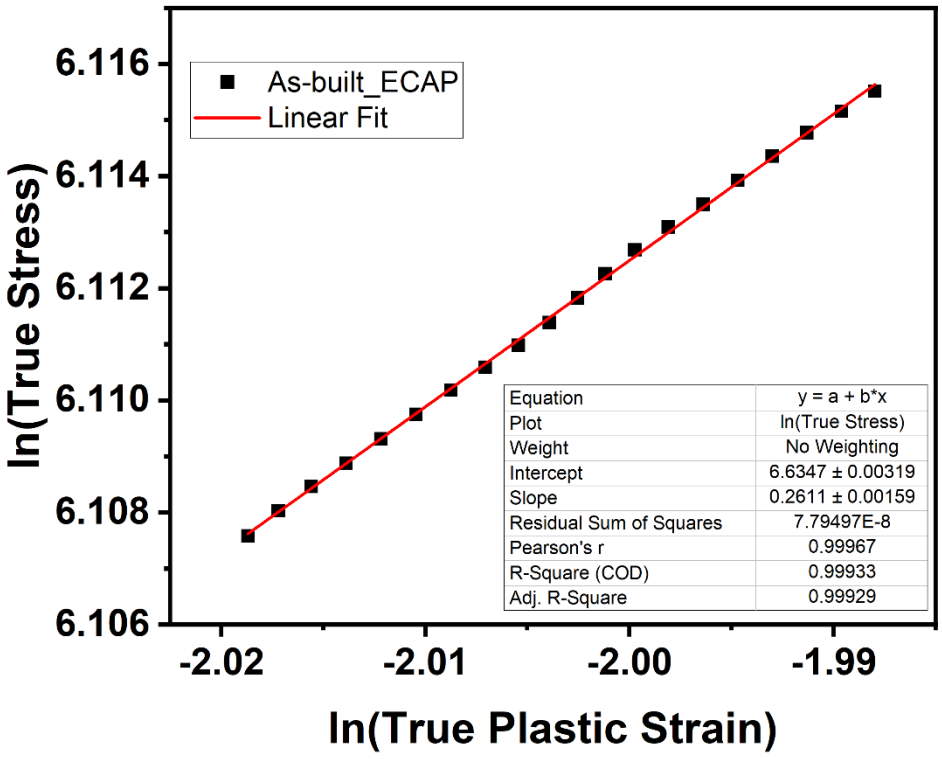

Figure 73. Strain hardening exponent plot for the As-built_ECAP sample

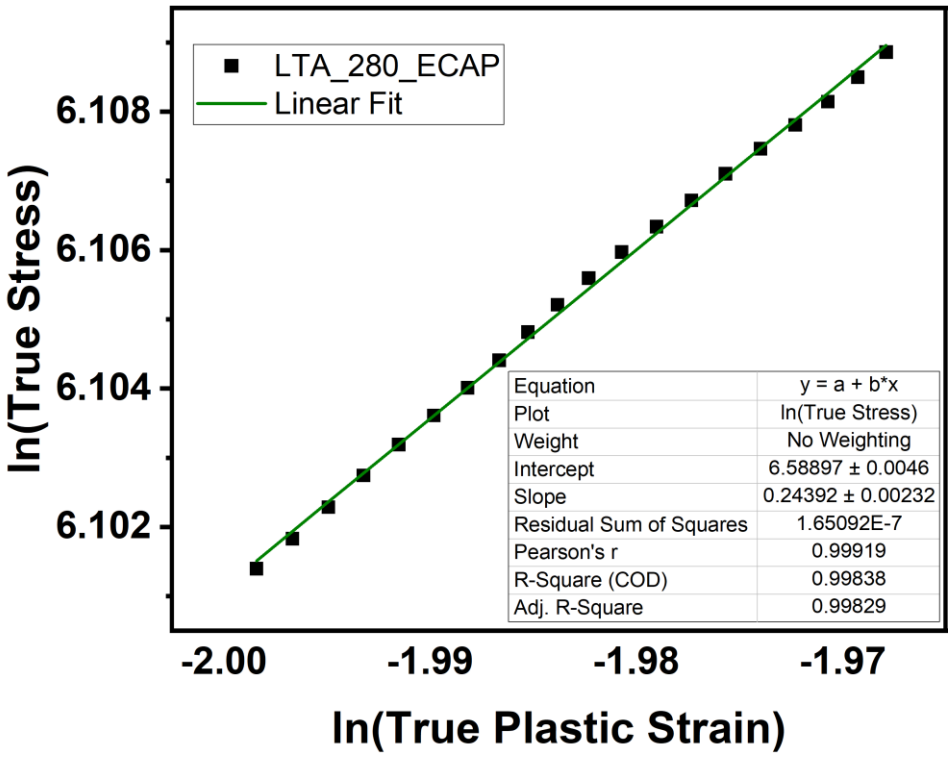

Figure 74. Strain hardening exponent plot for the LTA_280_ECAP sample

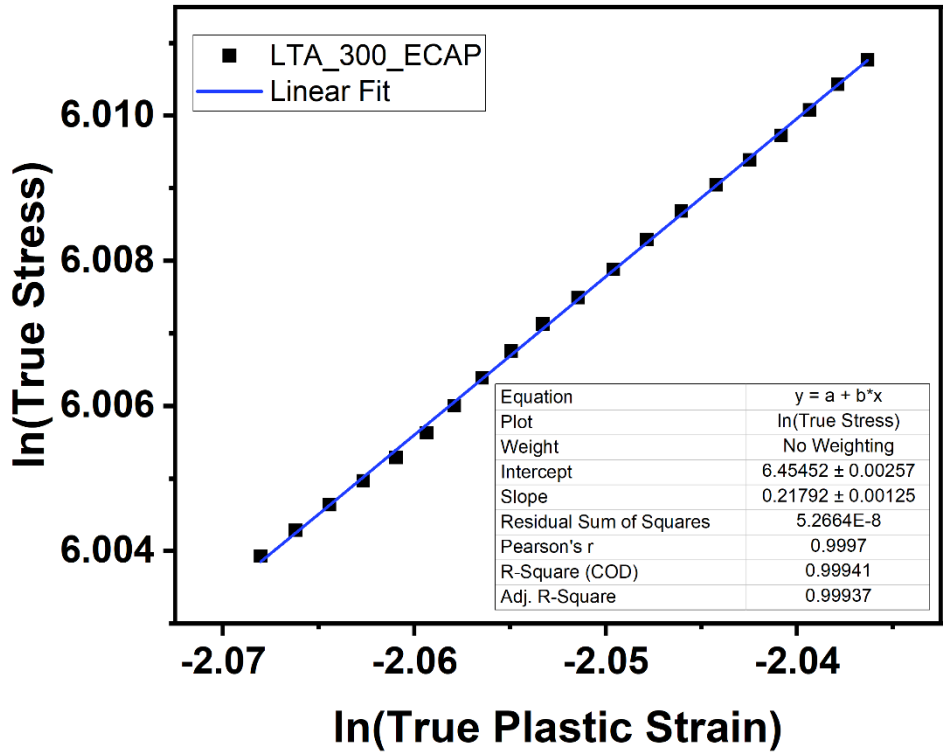

Figure 75. Strain hardening exponent plot for the LTA_300_ECAP sample

Table 6 presents a summary of the mechanical properties of the room temperature ECAP-processed samples.

Table 6. Mechanical Properties of the ECAP-processed samples

Sample ID	**Hardness [$HV_{0.3}$]**	**Yield strength (σ_y) [MPa]**	**UCS [MPa]**	**Total strain at failure (ε_f) [%]**	**n**
As-built_ECAP	131.6 ± 2.3	425	610.8	23.4	0.261
LTA_280_ECAP	129.7 ± 2.7	410	615.9	25.5	0.244
LTA_300_ECAP	120.0 ± 3.0	390	697.8	51.4	0.218

4.4.2.3 Kinematic Hardening

To further elucidate the role of kinematic hardening in the overall mechanical response, LUR compression tests were conducted, with results presented in **Figure 76**. The engineering and true stress–strain curves obtained from the LUR cycles are shown in **Figures 76A and 76B**, respectively. The evolution of back stress, σ_b, a direct measure of the material's kinematic hardening, was calculated using **Equation 11** and plotted against true strain at the unload point of each loading cycle in **Figure 77**.

$$\sigma_b = \frac{\sigma_u + \sigma_r}{2} \tag{11}$$

Where σ_u and σ_r are the yield strength values upon unloading and reloading at each LUR cycle respectively.

Zhu and Wu [149] postulated that the difference in hardness between the Si-rich eutectic network and the Al matrix induces a notable Bauschinger effect and back stress. The LUR test effectively quantifies this effect, with larger hysteresis loops indicating stronger Bauschinger effect [49]. The As-built_ECAP and LTA_280_ECAP samples with fully or partially continuous cellular networks exhibited larger hysteresis loops than the LTA_300_ECAP sample, with the As-built_ECAP sample exhibiting the highest back stress, reaching approximately 351 MPa at a true strain of 0.24. In contrast, the LTA_300_ECAP sample, which had a more fragmented Si network, consistently showed the lowest back stress. This behavior is primarily attributed to long-range

interactions among mobile dislocations [5], where the Si network acts as an effective site for such interactions. These sites are reduced upon fragmentation of the network in the LTA_300_ECAP sample.

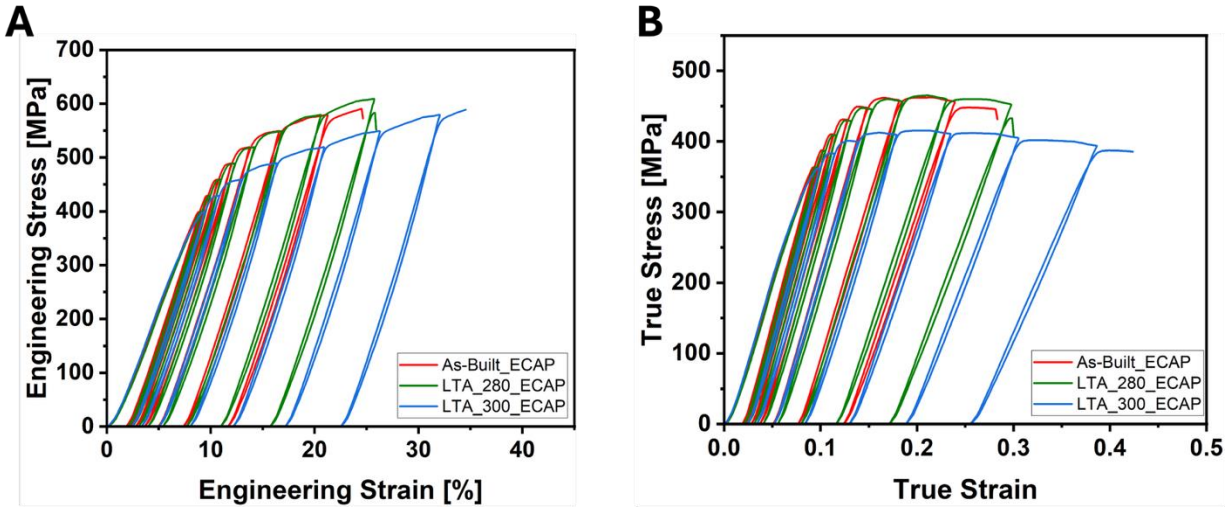

Figure 76. Engineering (**A**) and True (**B**) stress-strain plots from loading-unloading-reloading (LUR) tests for the ECAP-processed samples

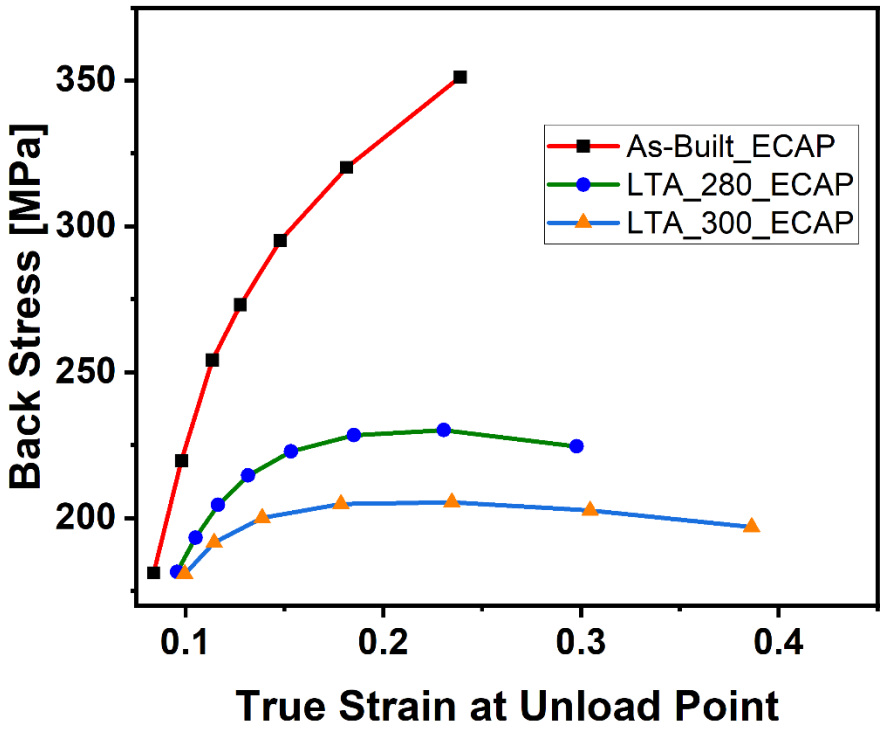

Figure 77. Back stress estimated from each LUR cycle for the ECAP-processed samples

4.5 High Temperature ECAP Processing

To complement the earlier investigations, additional ECAP processing of the PBF-LB/M AlSi10Mg alloy was conducted without prior heat treatment, this time at elevated processing temperatures of 350 °C (As-built_ECAP350), 400 °C (As-built_ECAP400), and 450 °C (As-built_ECAP450). These experiments were designed to provide deeper understanding into the microstructural evolution and mechanical response of the alloy under different processing conditions, specifically, by comparing SPD applied at room temperature following prior heat treatment with SPD performed directly at elevated temperatures. This comparative approach enables a clearer understanding of the degree of control that different processing conditions exert over the continuity of the nanoscale Si-rich cellular structure, and how this, in turn, influences the alloy's mechanical performance. Ultimately, these investigations aim to elucidate the interplay between processing temperature, thermal history, and the resulting microstructure – property relationships in PBF-LB/M AlSi10Mg alloys.

4.5.1 Microstructure

The LOM analysis of the As-built_ECAP350 sample (**Figure 78**) reveals a deformed MP structure and MPBs at the mesoscale. The melt pools appear significantly smaller compared to the as-built condition, with dimensions reduced to 60 ± 28 µm in width and 23 ± 7 µm in depth. In the As-built_ECAP400 sample (**Figure 79**), the deformation is even more pronounced, with more severely distorted MPs and MPBs observed. The MPs in this condition are also reduced in size, now measuring 98 ± 29 µm in width and 17 ± 4 µm in depth. Following ECAP processing at 450 °C, the mesoscale melt pool features and boundaries become no longer discernible under LOM in the As-built_ECAP450 sample (**Figure 80**), necessitating higher-resolution characterization using SEM to further investigate the microstructural evolution.

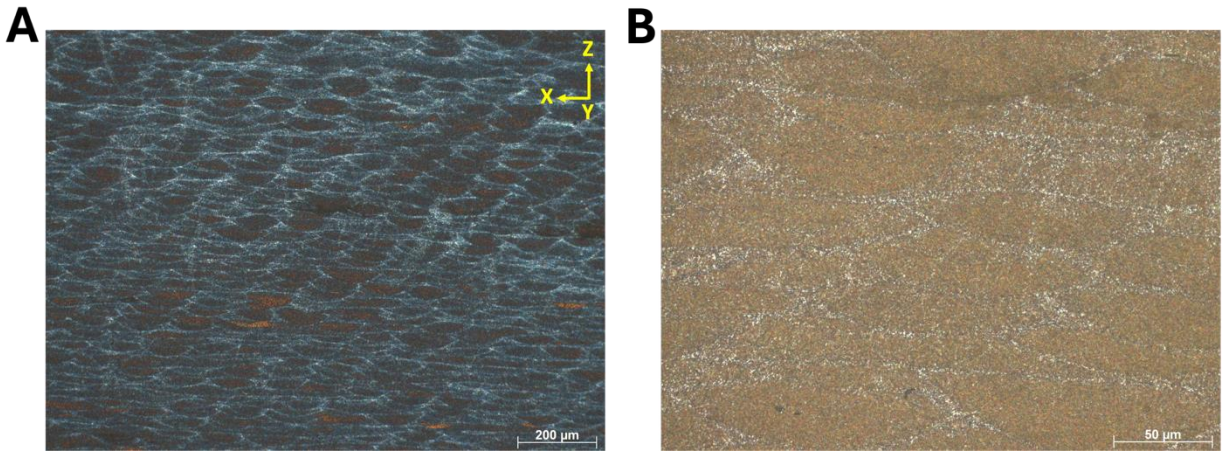

Figure 78. LOM Microstructure of **As-built_ECAP350** in the X-Z plane at different magnifications **A**. 25X, and **B**. 500X

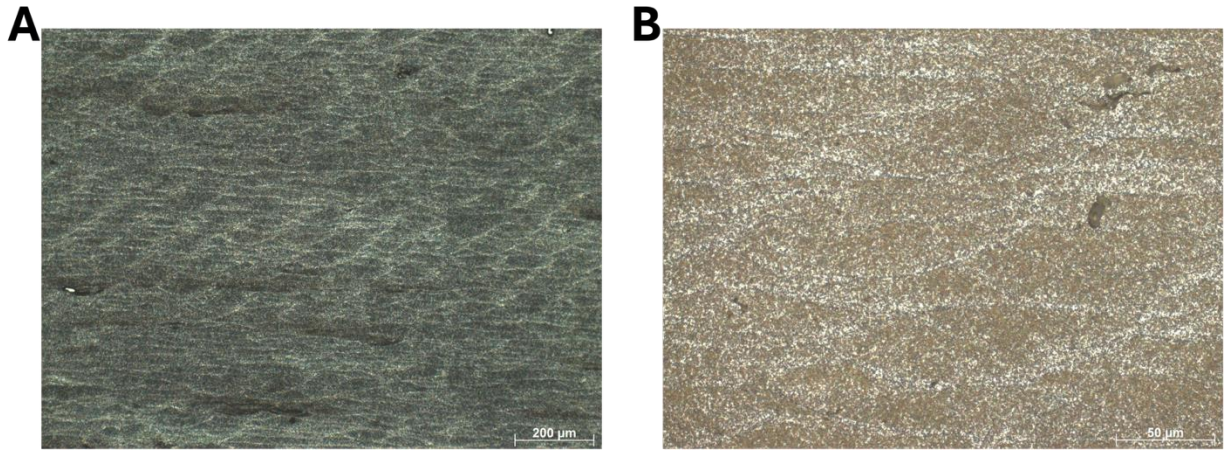

Figure 79. LOM Microstructure of **As-built_ECAP400** in the X-Z plane at different magnifications **A**. 25X, and **B**. 500X

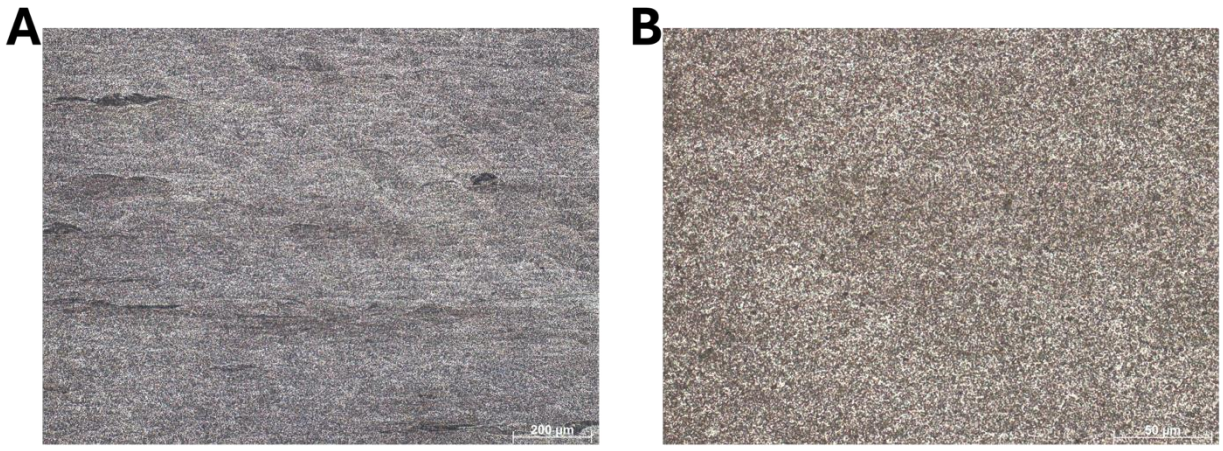

Figure 80. LOM Microstructure of **As-built_ECAP450** in the X-Z plane at different magnifications **A**. 25X, and **B**. 500X

The microstructure of the As-built_ECAP350 sample observed under the SEM (**Figure 81**) reveals a significantly more homogeneous appearance compared to the heterogenous cellular structure observed prior to ECAP processing. This enhanced uniformity results from the complete disintegration of the eutectic cellular Si network, which is transformed into discrete, spheroidized Si particles uniformly dispersed within the α-Al matrix. The characteristic cellular morphology is entirely absent, and the average size of the Si particles is measured to be 0.19 ± 0.09 μm (**Figure 81D**). A similar microstructural evolution is observed in the As-built_ECAP400 (**Figure 82**) and As-built_ECAP450 (**Figure 83**) samples. Notably, an increase in ECAP processing temperature leads to a progressive coarsening of the dispersed Si particles. In the As-built_ECAP400 sample, the Si particles exhibit an average size of 0.25 ± 0.12 μm, while in the As-built_ECAP450 sample, they further coarsen to 0.36 ± 0.18 μm. This trend suggests a temperature-dependent coarsening behavior driven by enhanced diffusion kinetics at elevated processing temperatures.

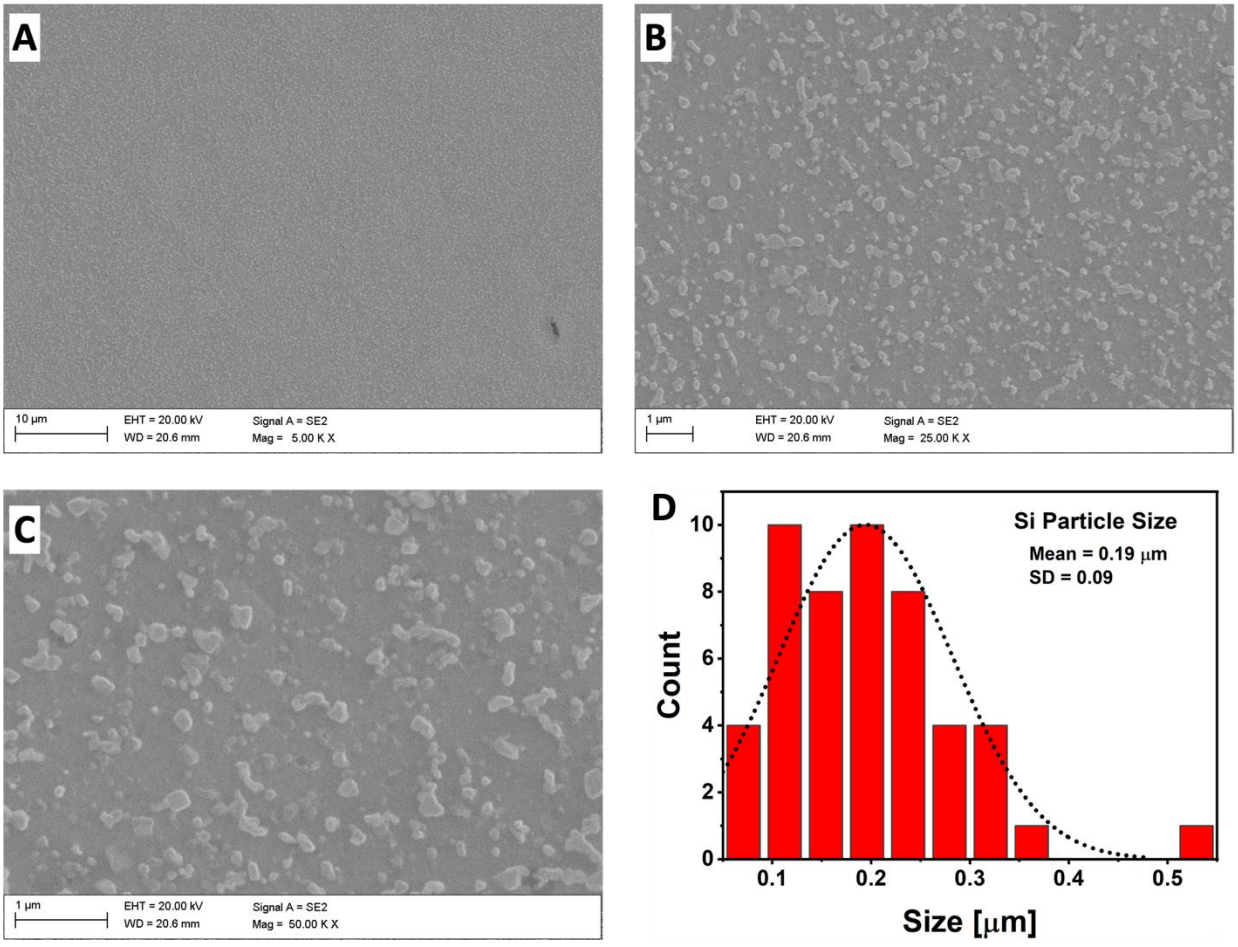

Figure 81. A-C. SEM microstructure of As-built_ECAP350 at different magnifications, and **D**. Silicon particle size distribution.

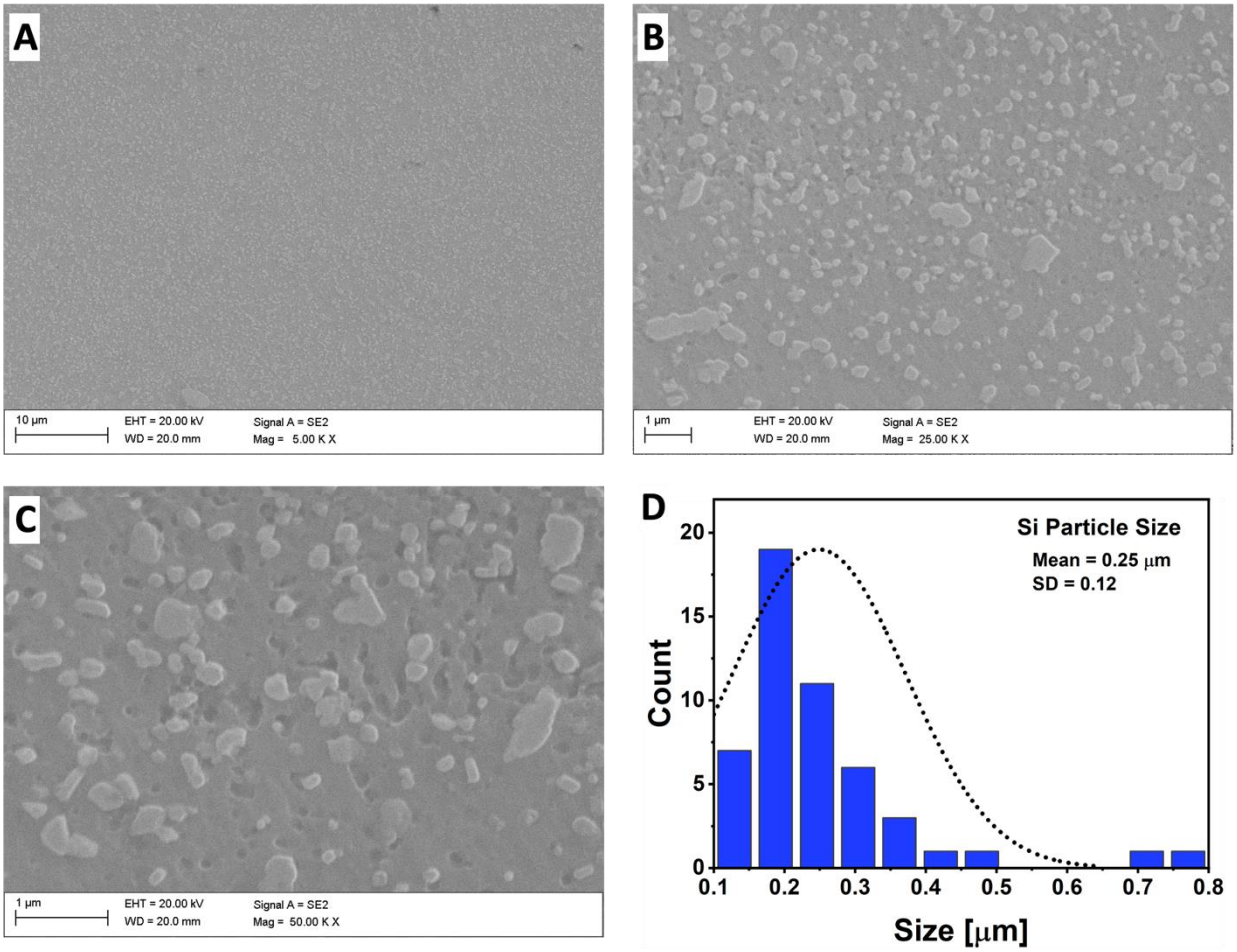

Figure 82. A-C. SEM microstructure of As-built_ECAP400 at different magnifications, and **D**. Silicon particle size distribution.

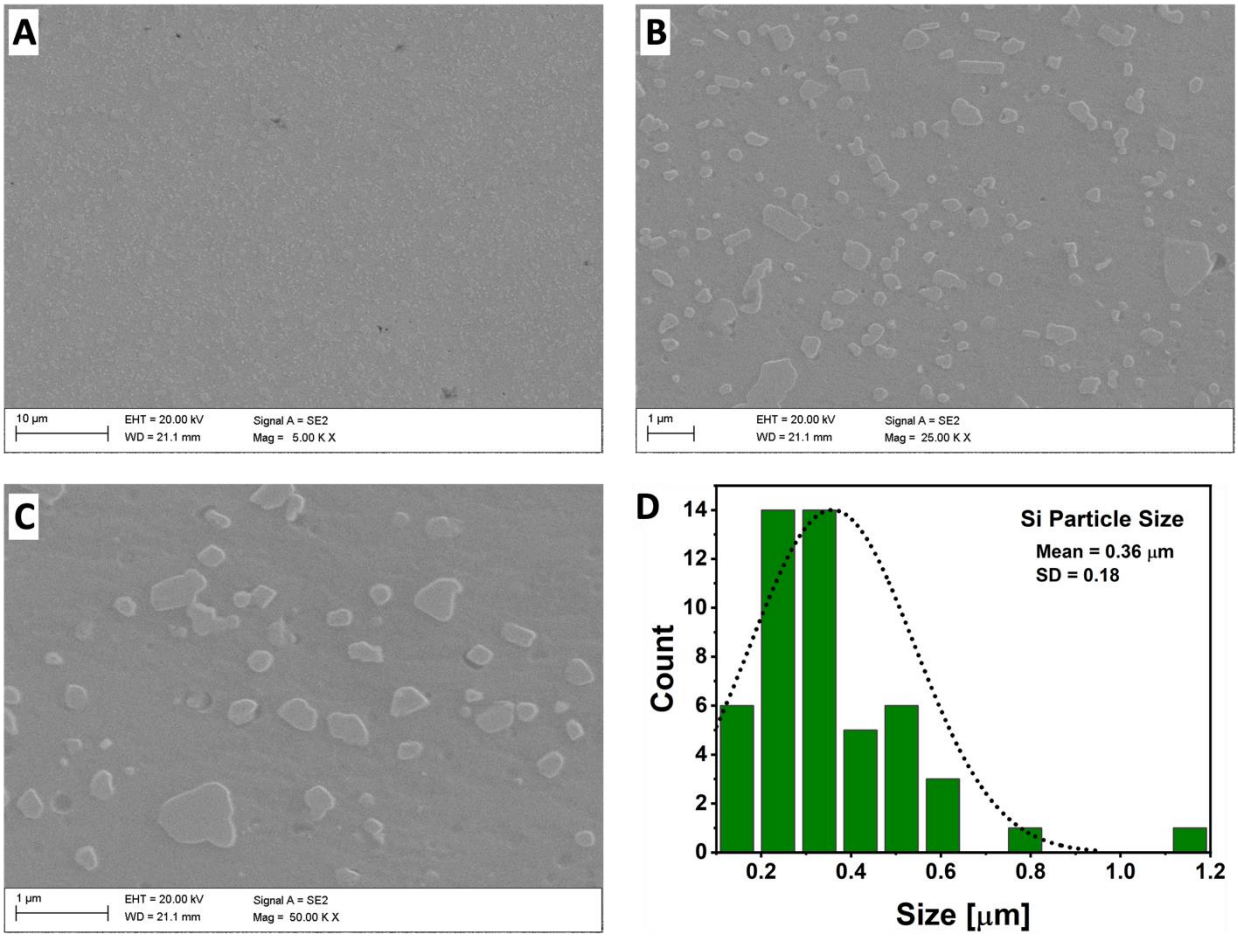

Figure 83. A-C. SEM microstructure of As-built_ECAP450 at different magnifications, and **D**. Silicon particle size distribution.

The EBSD analysis results of the ECAP-processed samples are presented in **81 and 82**. The As-built_ECAP350 sample exhibits a relatively coarse and partially columnar grain structure (**Figure 84A**), with an average grain area of $32.7 \pm 25.7\ \mu m^2$ (**Figure 84B**). This grain size is approximately six times larger than that of the room temperature ECAP-processed sample (As-built_ECAP). Interestingly, regions of finer grains are observed along curved zones in the IPF maps, which correspond to the former melt pool HAZs, suggesting partial structural retention from the initial build. The grain boundary character distribution for As-built_ECAP350 (**Figures 85A and 85B**) reveals a predominance of HAGBs at 62.3%, with LAGBs accounting for 37.7%. Increasing the ECAP processing temperature to 400 °C (As-built_ECAP400) results in a reduction in average grain size to $27.8 \pm 26.2\ \mu m^2$ (**Figures 84C and 84D**). However, the proportion of LAGBs and HAGBs remains nearly unchanged at 37.4% and 62.6%, respectively (**Figures 85C**

and 85D). This suggests that the fundamental grain boundary character distribution remains largely unaffected at this temperature range. At the highest processing temperature of 450 °C (As-built_ECAP450), the mesoscale melt pool boundaries are no longer visible in the microstructure (**Figure 84E**), indicating substantial microstructural homogenization. The average grain size decreases slightly to $25.2 \pm 24.7\ \mu m^2$ (**Figure 84F**), yet the most notable change is in the grain boundary distribution. The LAGB fraction increases significantly to 47.5%, while HAGBs decrease to 52.5% (**Figures 85E and 85F**).

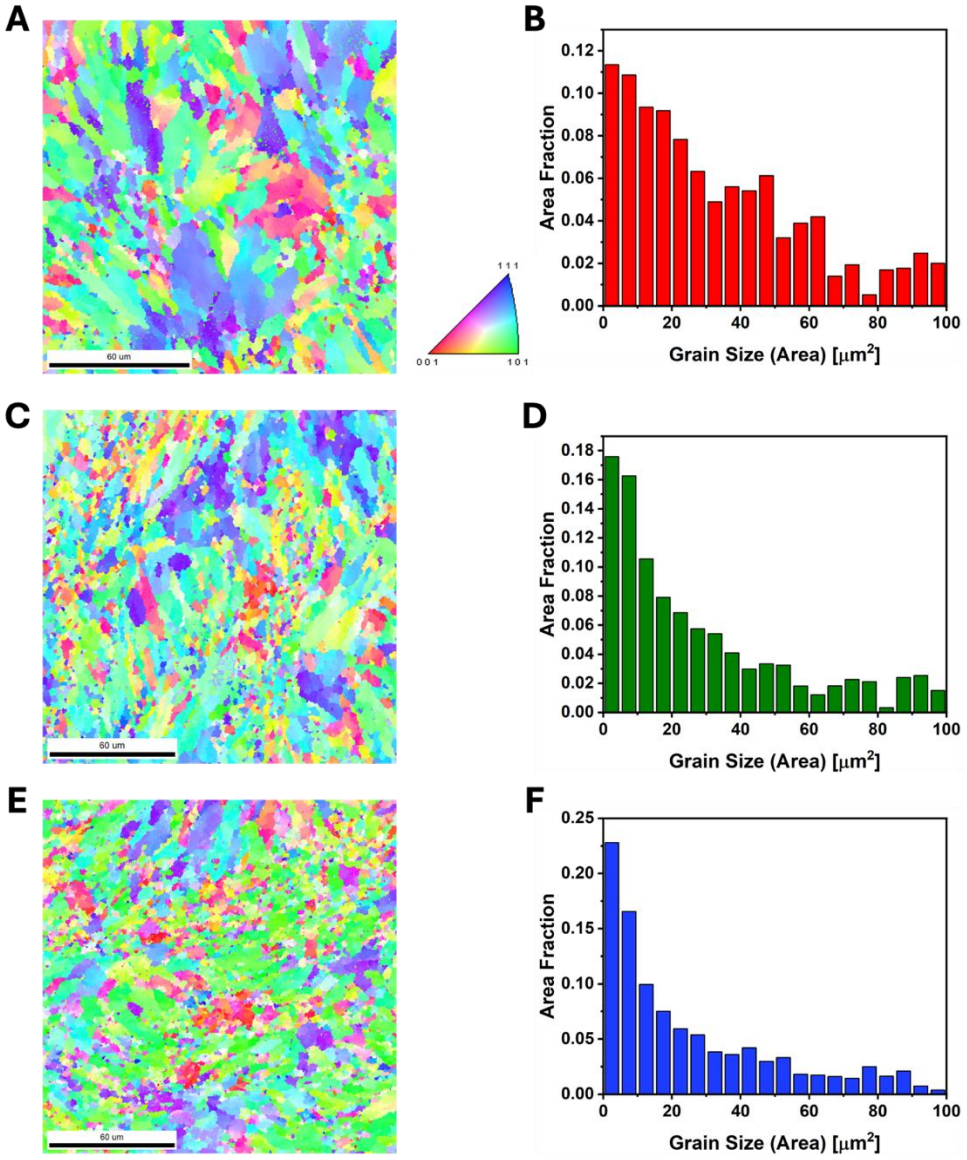

Figure 84. IPF-Z maps and corresponding grain size distribution plots for the high temperature ECAP-processed samples A,B. As-built_ECAP350, **C,D**. As-built_ECAP400, and **E,F.** As-built_ECAP450

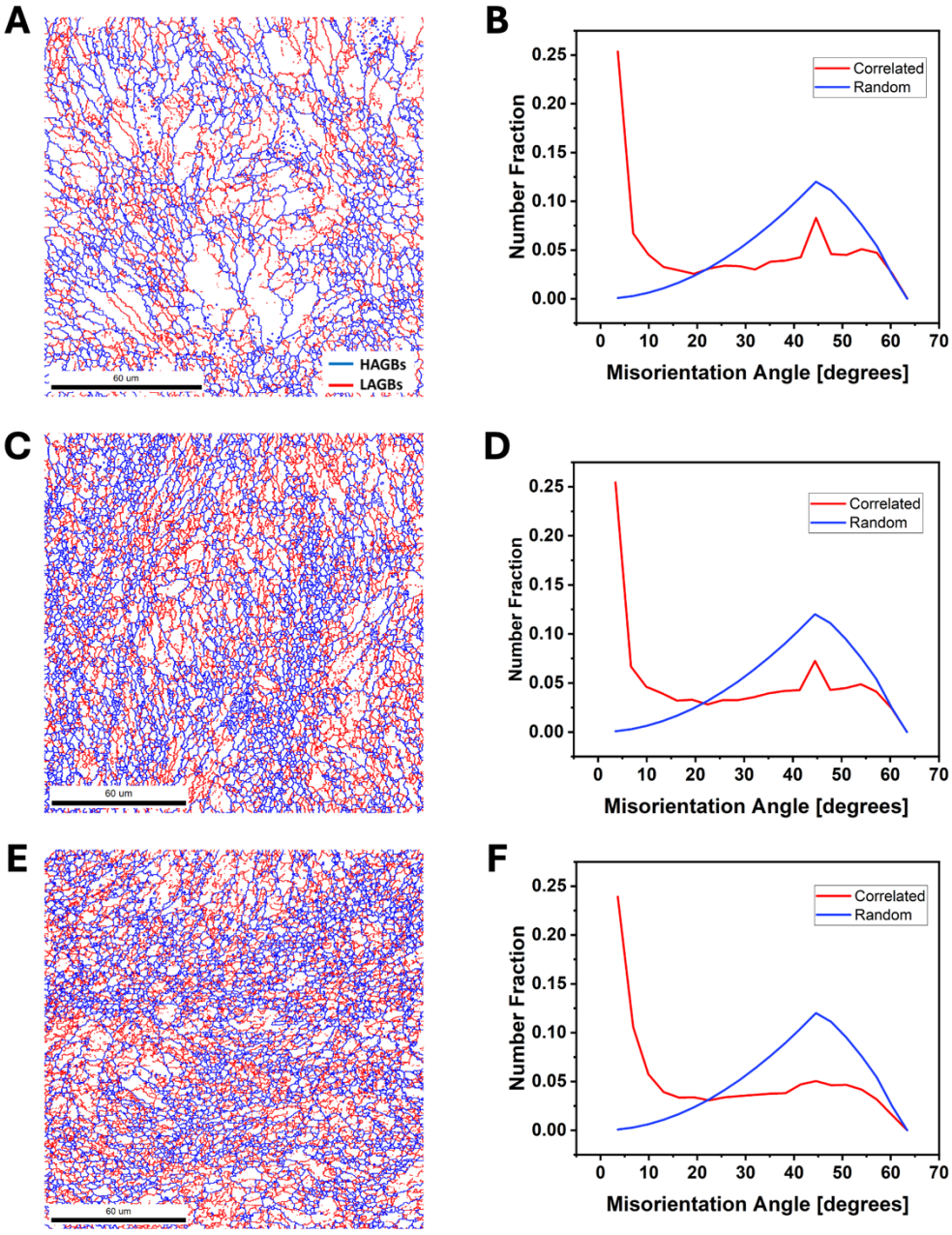

Figure 85. Grain boundary maps and corresponding misorientation angle distribution plots for the high temperature ECAP-processed samples A,B. As-built_ECAP350, **C,D**. As-built_ECAP400, and **E,F.** As-built_ECAP450

Microstructural analysis in this section has revealed that the observed transformation of the alloy's structure, particularly the evolution of the eutectic cellular network, deviated from the expectations outlined in the study's goals. The intended goal was to achieve a controlled modification of the nanoscale cellular network while preserving the mesoscale features of the alloy,

such as the melt pool morphology. While the research trajectory supports fragmentation of the cellular network to enhance mechanical performance, the complete disintegration of this structure, especially following ECAP processing at elevated temperatures, was identified as an unfavorable outcome. To assess the extent to which this microstructural degradation may compromise mechanical performance, further investigations were carried out by evaluating the mechanical properties, including microhardness measurements and compressive testing.

4.5.2 Mechanical Properties

Room temperature Vickers microhardness results for the ECAP-processed samples at elevated temperatures are presented as hardness maps in **Figure 86**. The data reveal a significant reduction in hardness by over 25% relative to the as-built condition, and more than 34% when compared to the room temperature ECAP-processed state. Moreover, an inverse relationship between ECAP processing temperature and hardness was observed. Specifically, the As-built_ECAP350 sample exhibited an average hardness of 86.2 ± 1.4 $HV_{0.1}$, which decreased to 69.4 ± 2.1 $HV_{0.1}$ in the As-built_ECAP400 sample, and further declined to 60.1 ± 2.3 $HV_{0.1}$ in the As-built_ECAP450 sample.

Compression testing results (**Figure 87**) corroborated these findings, showing a substantial reduction in YS with increasing ECAP temperature. The As-built_ECAP350 sample recorded the highest YS among the high-temperature processed states, approximately 187 MPa, which is about three times lower than the YS of the alloy in both the as-built and room temperature ECAP-processed conditions. The As-built_ECAP400 and As-built_ECAP450 samples exhibited even lower YS values of 161 MPa and 141 MPa, respectively.

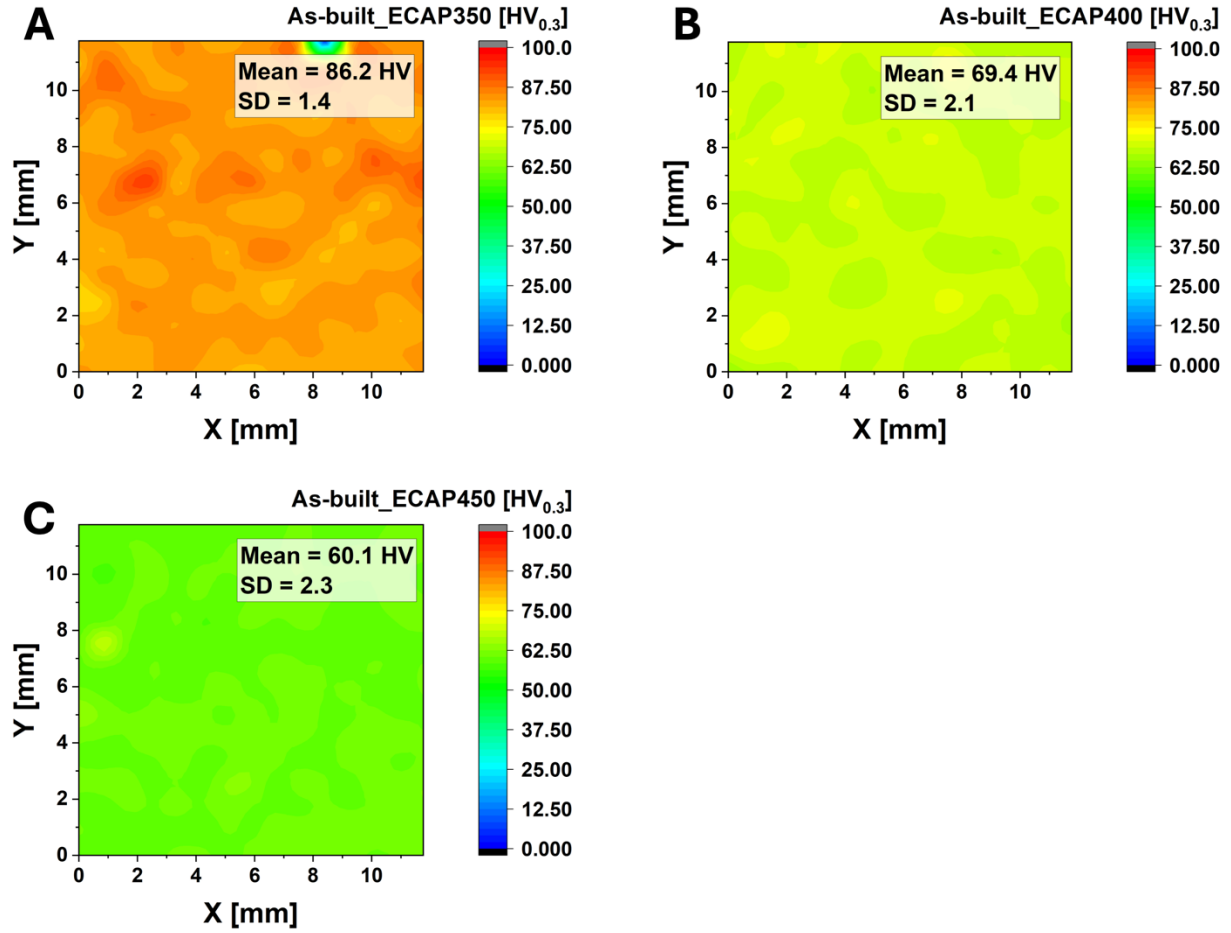

Figure 86. Vickers microhardness test results measured along the cross-section of the ECAP-processed samples A. As-built_ECAP350, **B**. As-built_ECAP400, and **C**. As-built_ECAP450

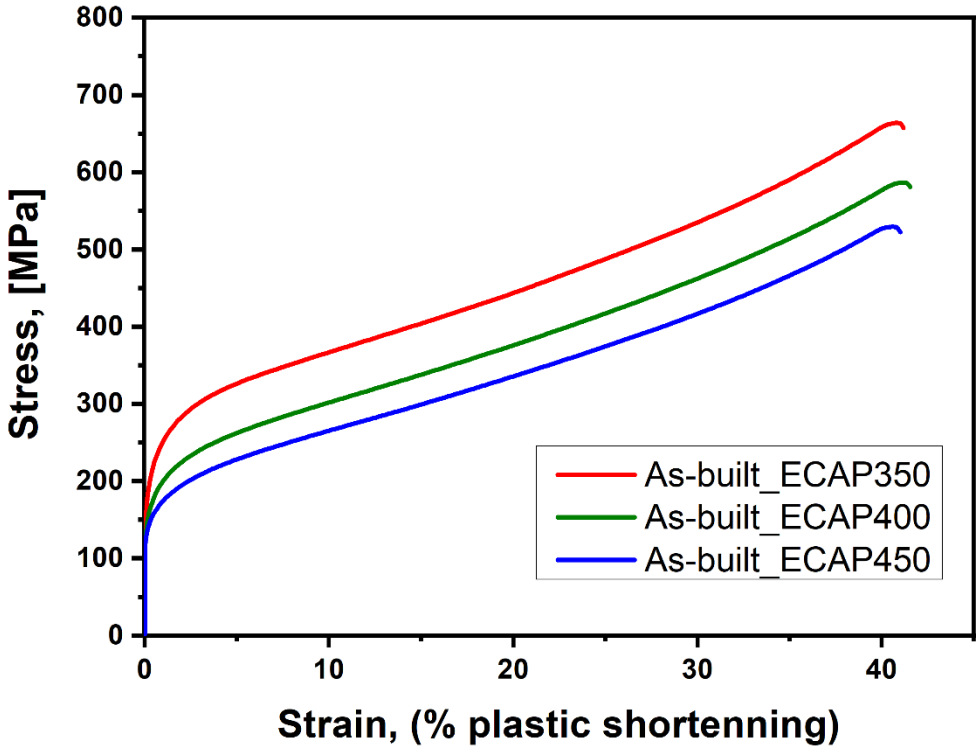

Figure 87. Compressive stress-strain results of the high temperature ECAP-processed samples

4.6 Twist Channel Angular Pressing (TCAP)

This section presents the results of TCAP applied to both as-built and heat-treated PBF-LB/M AlSi10Mg samples. TCAP was performed at elevated temperatures, specifically below the eutectic temperature of the alloy, to enable effective plastic deformation while preserving the material's mesoscale structural integrity. Two categories of samples were processed in this study. The first group underwent a single TCAP pass at 100 °C. The second group underwent two TCAP passes: the first at 100 °C and the second at a higher temperature – 250 °C for the as-built sample and 150 °C for the heat-treated samples. The justification for this variation in deformation temperature is stated in **Section 3.7**.

4.6.1 Microstructure

4.6.1.1. Single-Pass TCAP (1TCAP)

The microstructures of the As-built_1TCAP sample, as observed under bright field and polarized light optical microscopy, are presented in **Figure 88**. The micrographs reveal that single-pass TCAP processing did not significantly alter the mesoscale MP morphology of the alloy. However, a reduction in MP dimensions was observed. The MPs in the As-built_1TCAP sample measured 125.5 ± 44.8 μm in width and 26.2 ± 6.3 μm in depth, representing a 17.8% decrease in size relative to the pre-TCAP state. Similarly, the LOM images of the LTA_280_1TCAP sample (**Figure 89**) show that the melt pool morphology was largely preserved following TCAP processing. The MP dimensions remained comparable to those of the As-built_1TCAP sample, measuring 128.5 ± 22.2 μm in width and 28.1 ± 5.1 μm in depth. In the case of the LTA_300_1TCAP sample (**Figure 90**), LOM analysis also confirms the preservation of overall melt pool morphology. However, the melt pool boundaries (MPBs) appear less distinct after chemical etching when compared to the MPBs in the As-built_1TCAP and LTA_280_1TCAP samples. The MP dimensions for this sample were also similar, with an average width of 124.1 ± 28.0 μm and a depth of 25.3 ± 6.0 μm.

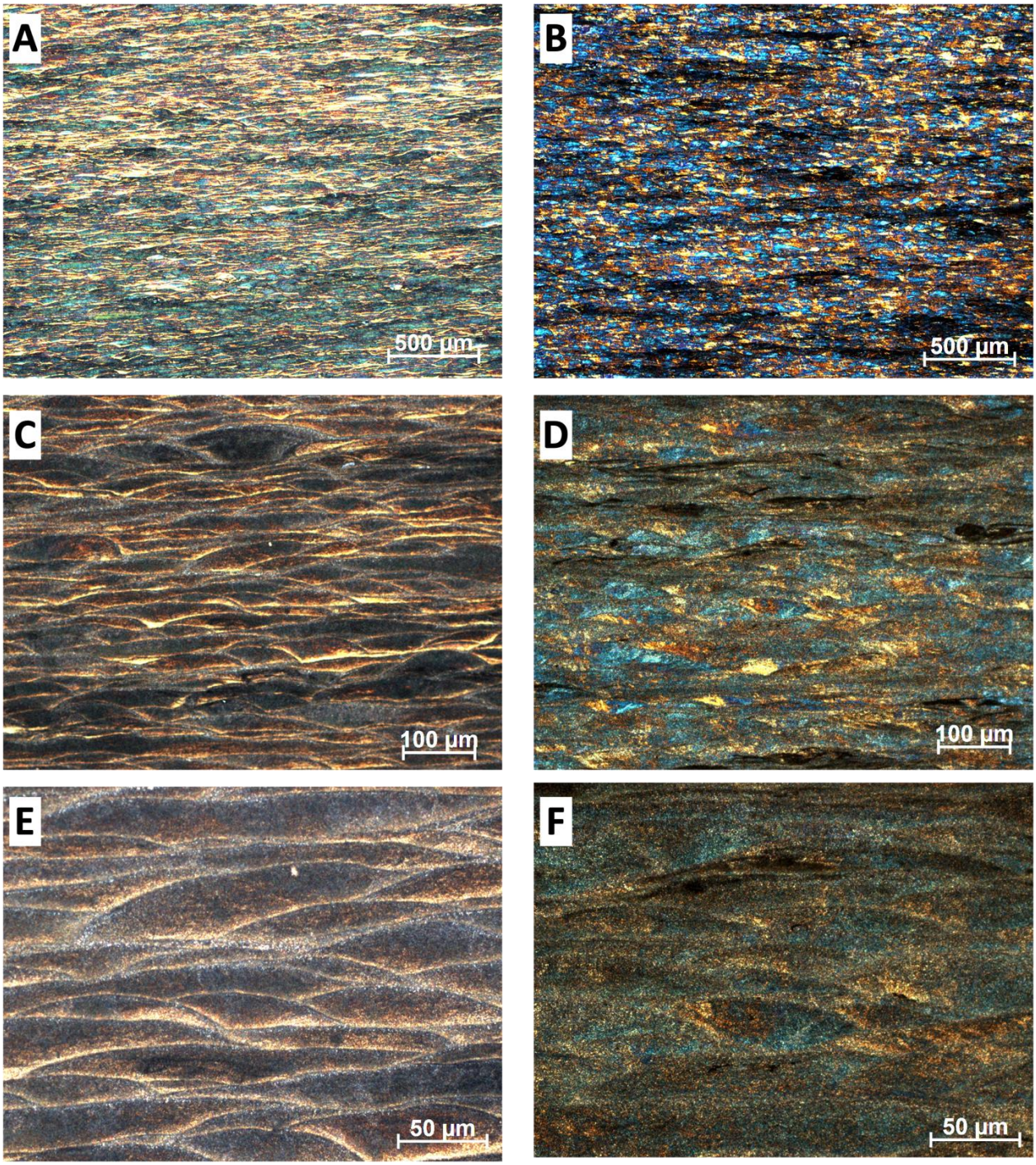

Figure 88. LOM bright field (left) and polarized light (right) microstructure of As-built_1TCAP along the X-Z plane at different magnifications **A,B.** 50X, **C,D.** 200X, and **E,F.** 500X

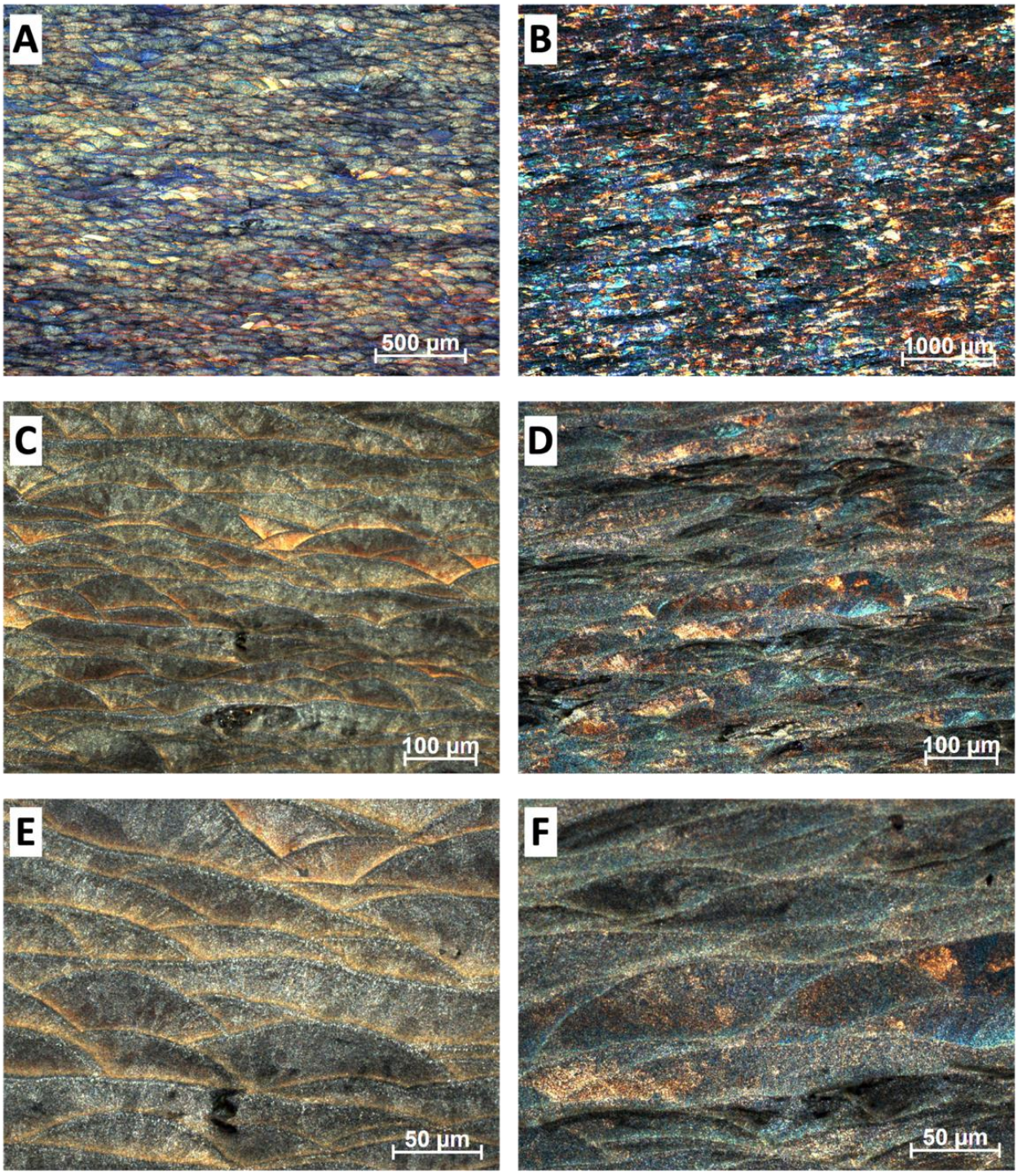

Figure 89. LOM bright field (left) and polarized light (right) microstructure of LTA_280_1TCAP along the X-Z plane at different magnifications **A,B.** 50X, **C,D.** 200X, and **E,F.** 500X

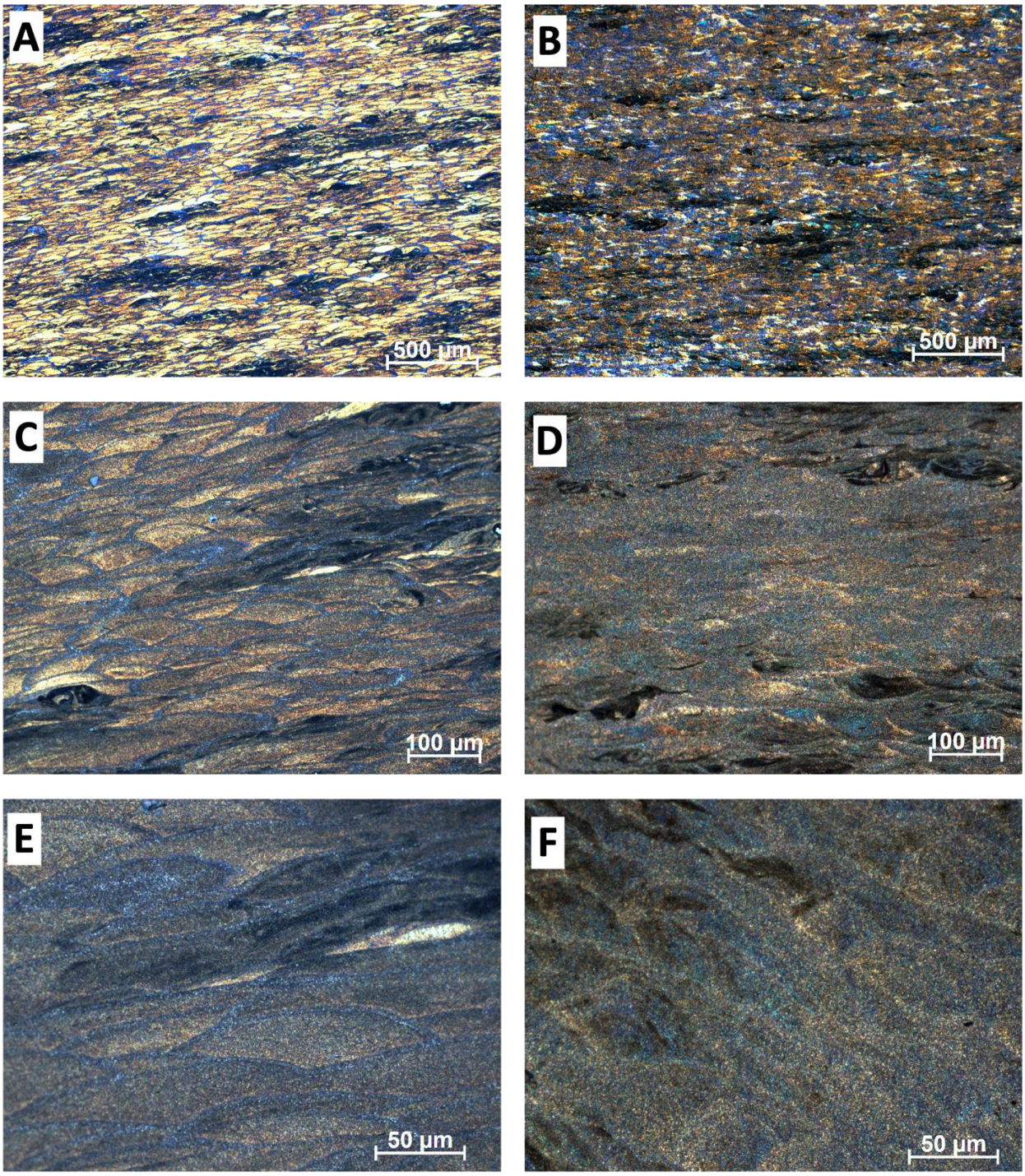

Figure 90. LOM bright field (left) and polarized light (right) microstructure of LTA_300_1TCAP along the X-Z plane at different magnifications **A,B.** 50X, **C,D.** 200X, and **E,F.** 500X

SEM observations of the As-built_1TCAP sample (**Figure 91**) reveal that the microstructure retains its characteristic heterogeneity, comprising both fine and coarse MPs as well as HAZ. Notably, there are more regions exhibiting partial discontinuities in the eutectic Si network compared to the pre-TCAP condition. The cellular structure appears slightly coarser, with an average cell size of 0.69 ± 0.24 μm and cell walls measuring 0.25 ± 0.09 μm. The SEM micrographs of the LTA_280_1TCAP sample (**Figure 92**) reveal a similar overall morphology. However, this sample exhibits a more pronounced fragmentation of the eutectic cellular network than the As-built_1TCAP sample. The average cell size increased slightly to 0.81 ± 0.22 μm, while the cell wall thickness also increased, measuring 0.43 ± 0.17 μm.

In contrast, the LTA_300_1TCAP sample (**Figure 93**) shows a significant breakdown of the eutectic cellular network. The cellular morphology is no longer visible, and instead, the microstructure is characterized by the presence of finely dispersed particulate silicon embedded within the aluminum matrix. These Si particles have an average size of 0.19 ± 0.05 μm (**Figure 93D**).

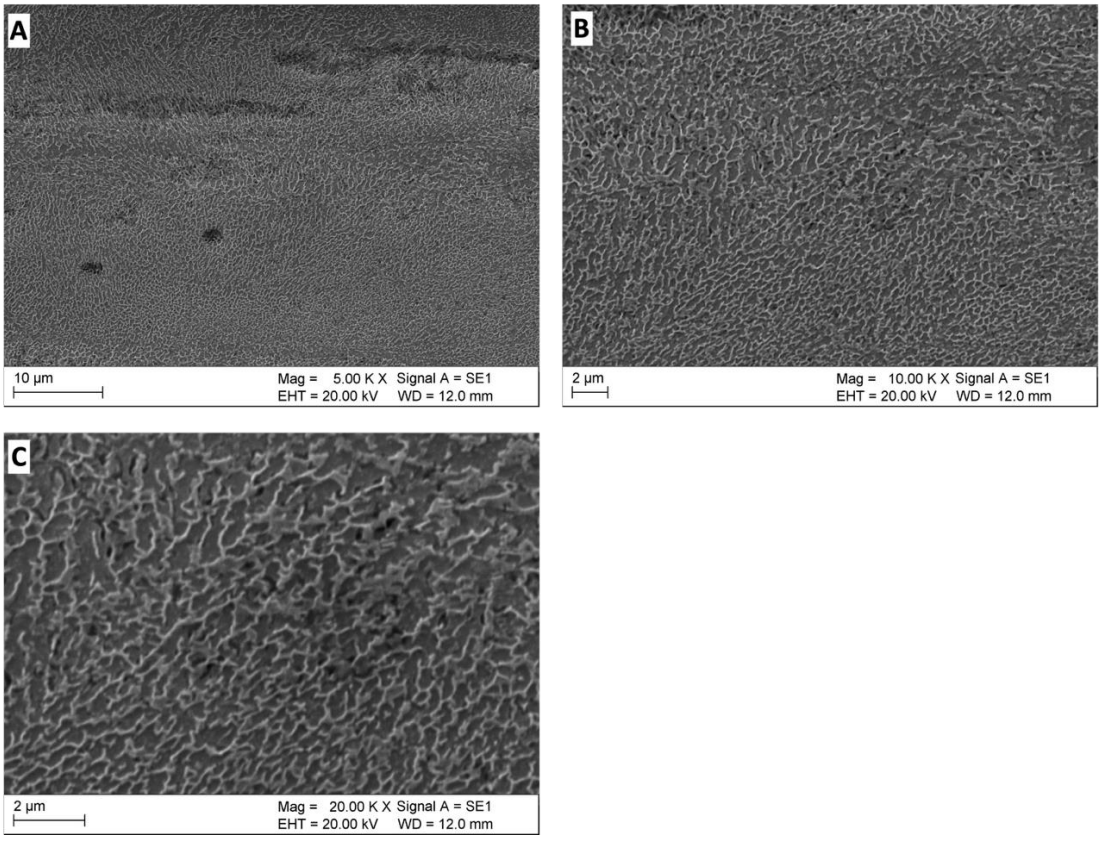

Figure 91. SEM microstructure of As-built_1TCAP at different magnifications **A**. 5000X, **B**. 10000X, and **C**. 20000X

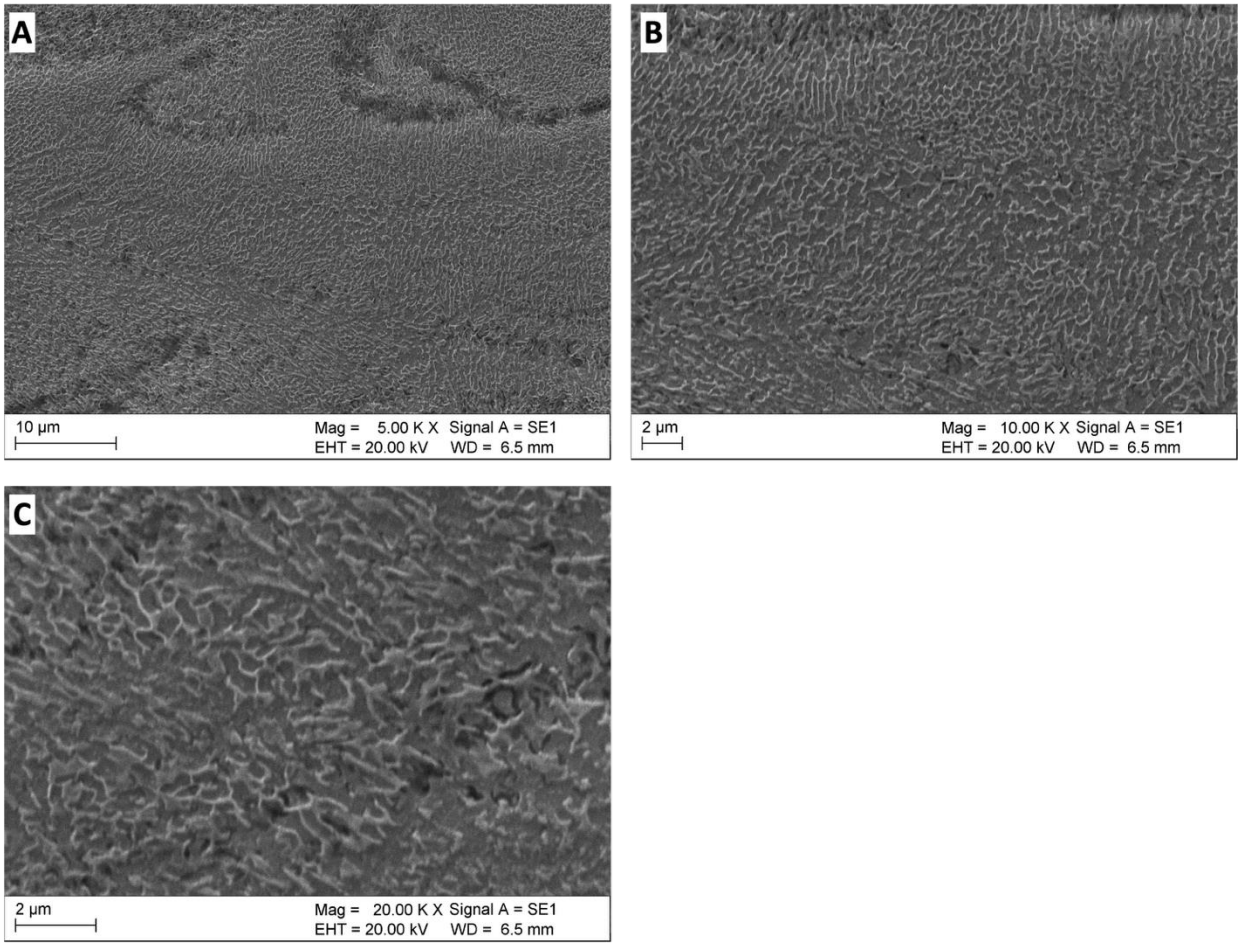

Figure 92. SEM microstructure of LTA_280_1TCAP at different magnifications **A**. 5000X, **B**. 10000X, and **C**. 20000X

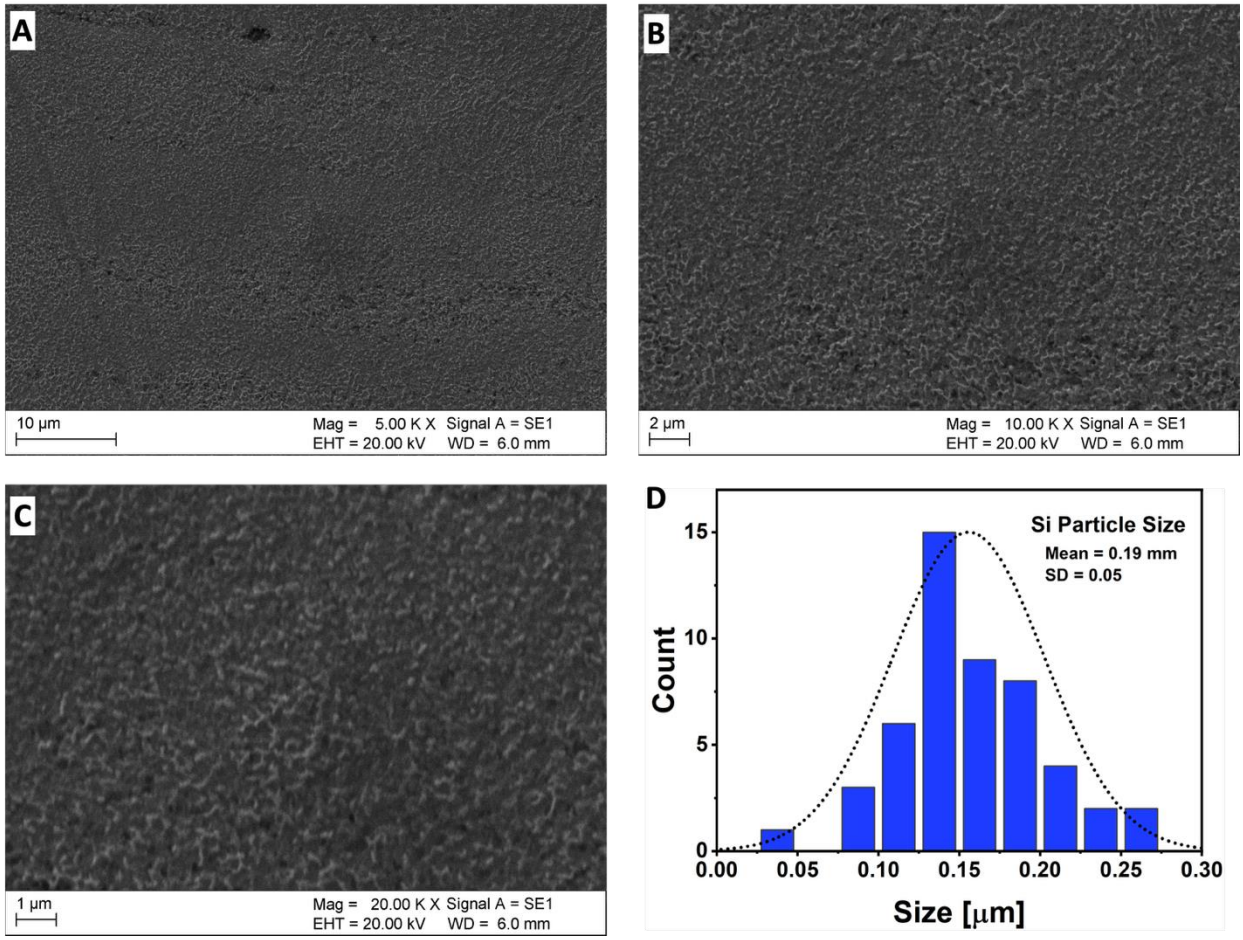

Figure 93. SEM microstructure of LTA_300_1TCAP at different magnifications **A**. 5000X, **B**. 10000X, and **C**. 20000X

The evolution of grain morphology and grain boundaries following the single-pass TCAP processing was assessed through EBSD analysis. Due to the comparable microstructural features observed in both LOM and SEM for the As-built_1TCAP and LTA_280_1TCAP samples, only the As-built_1TCAP sample was selected as a representative for EBSD characterization, in addition to the LTA_300_1TCAP sample.

The EBSD results are presented in **Figure 94** for the As-built_1TCAP sample and in **Figure 95** for the LTA_300_1TCAP sample. The IPF map of the As-built_1TCAP sample (**Figure 94A**) reveals a predominantly columnar grain structure. However, the grains exhibit significant refinement relative to the pre-TCAP condition, with an average grain area of 29.35 ± 27.69 µm^2, suggesting effective grain refinement induced by the single-pass TCAP process. Grain boundary

analysis indicates that LAGBs constitute 67.2%, while HAGBs account for 32.8% of the total boundaries (**Figures 94C and 94D**).

In contrast, the LTA_300_1TCAP sample demonstrates more extensive grain refinement, with grain sizes falling within the UFG regime. The average grain area was measured to be $18.4 \pm 24.8\ \mu m^2$ (**Figure 95A**). This sample exhibited a substantially higher fraction of HAGBs, approximately 85.1%, while LAGBs were reduced to 14.9% (**Figures 95C and 95D**).

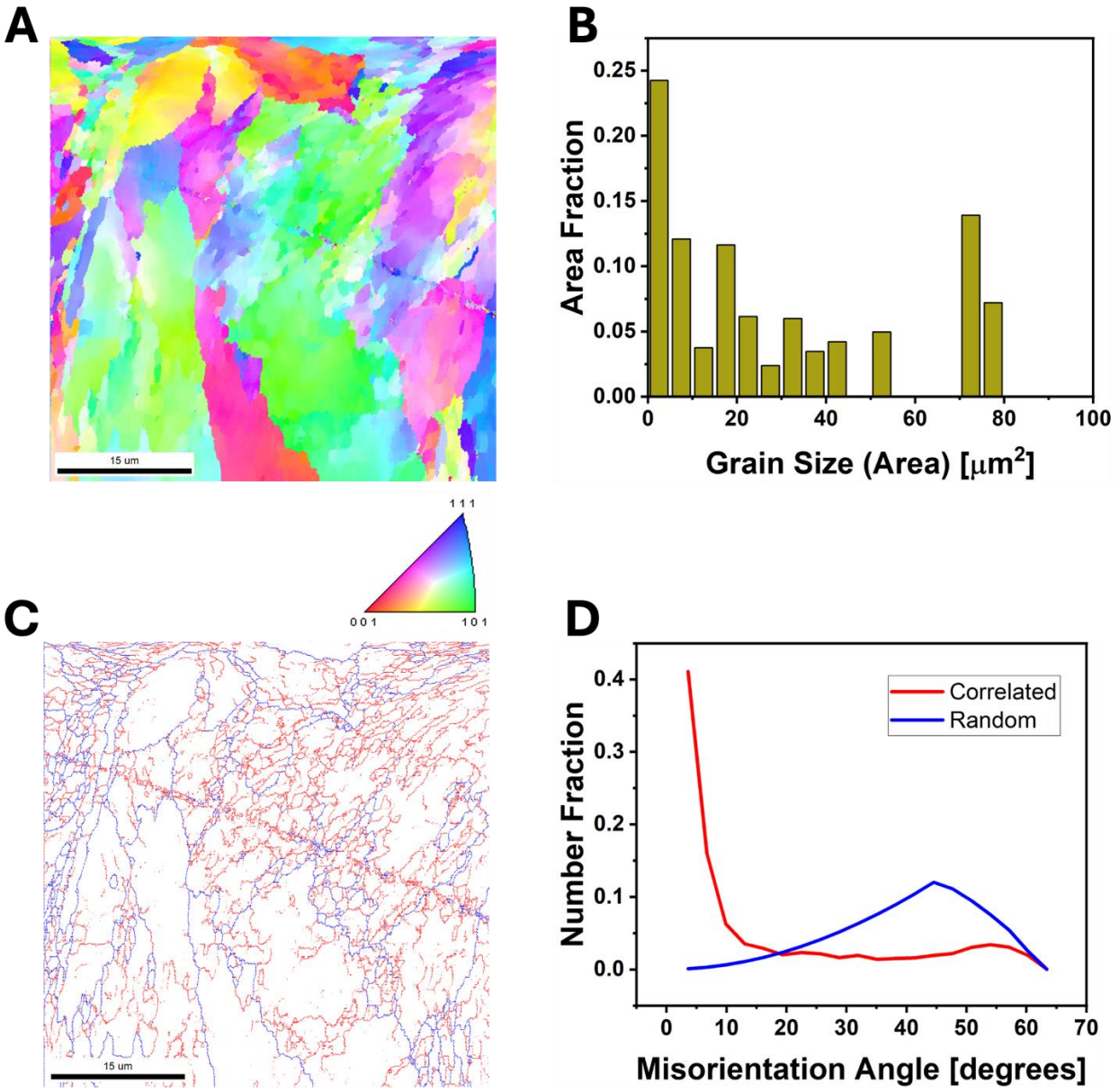

Figure 94. **Microstructure of As-built_1TCAP from EBSD analysis. A**. EBSD IPF-Z map of the sample, **B**. Grain size (area) histogram of the sample, **C**. Grain boundary map of the sample, and **D**. Misorientation angle histogram of the sample.

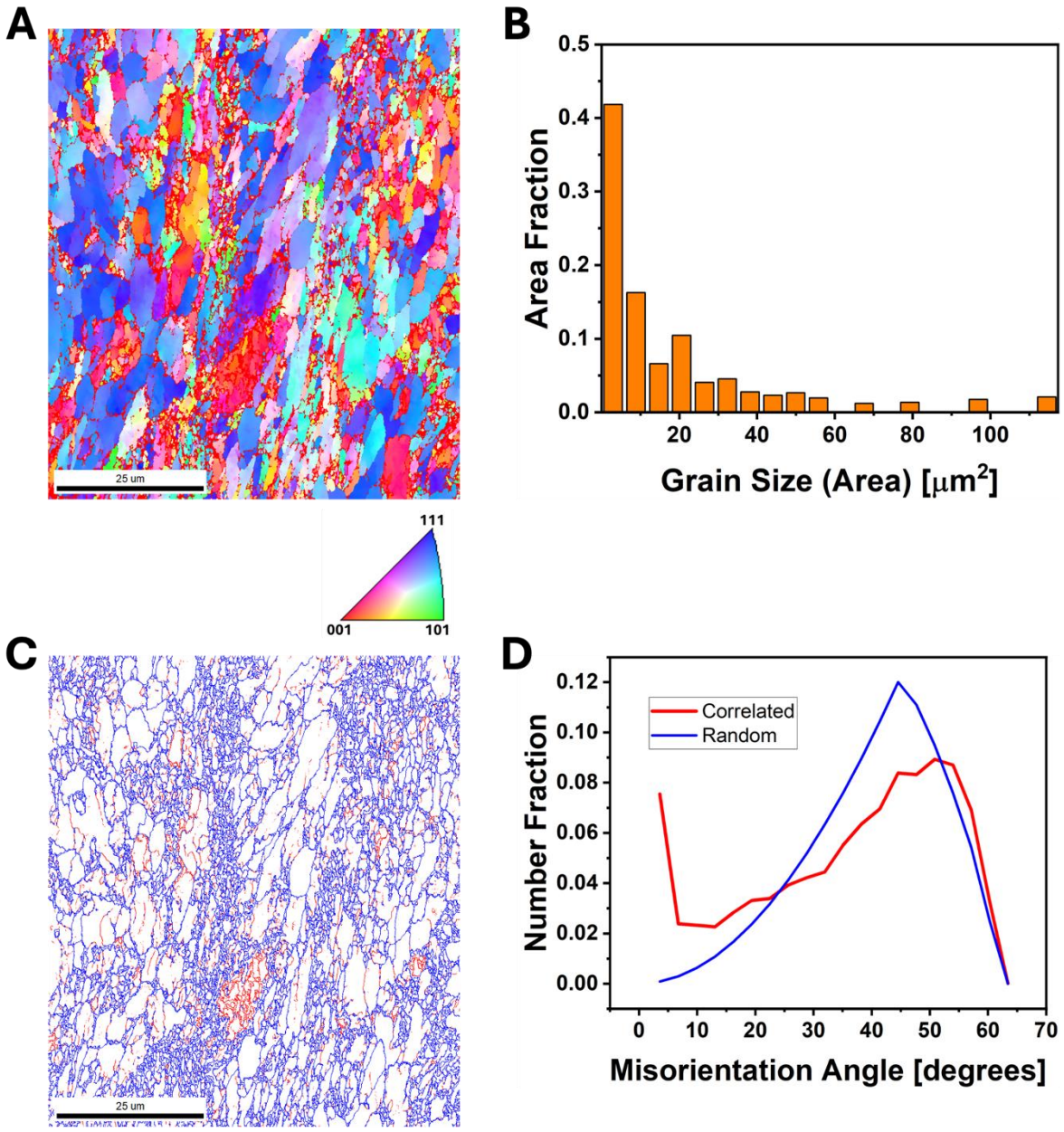

Figure 95. **Microstructure of LTA_300_1TCAP from EBSD analysis. A**. EBSD IPF-Z map of the sample, **B**. Grain size (area) histogram of the sample, **C**. Grain boundary map of the sample, and **D**. Misorientation angle histogram of the sample.

The microstructural evolution of the LTA_300_1TCAP sample was further investigated using TEM, with the results presented in **Figure 96**. The results reveal a refined grain structure, with an average grain size of 396 ± 71 nm (**Figure 96A**), corroborating the grain refinement previously observed via EBSD analysis. The results further show an intricate network of

dislocations distributed both within the refined grains and along the fragmented remnants of the former cellular boundaries. EDS mapping across the fragmented regions (**Figure 96D**) confirms that silicon remains preferentially concentrated along these boundaries. Moreover, the BF and DF TEM images (**Figures 96E and 96F**), along with the corresponding SAED pattern (**Figure 96G**), show that within the refined α-Al grains, the presence of discrete, nanosized Si particles, measuring approximately 108 ± 8 nm in diameter, was observed. These Si particles are presumed to have evolved from the further fragmentation and spheroidization of the original cell walls during the TCAP deformation.

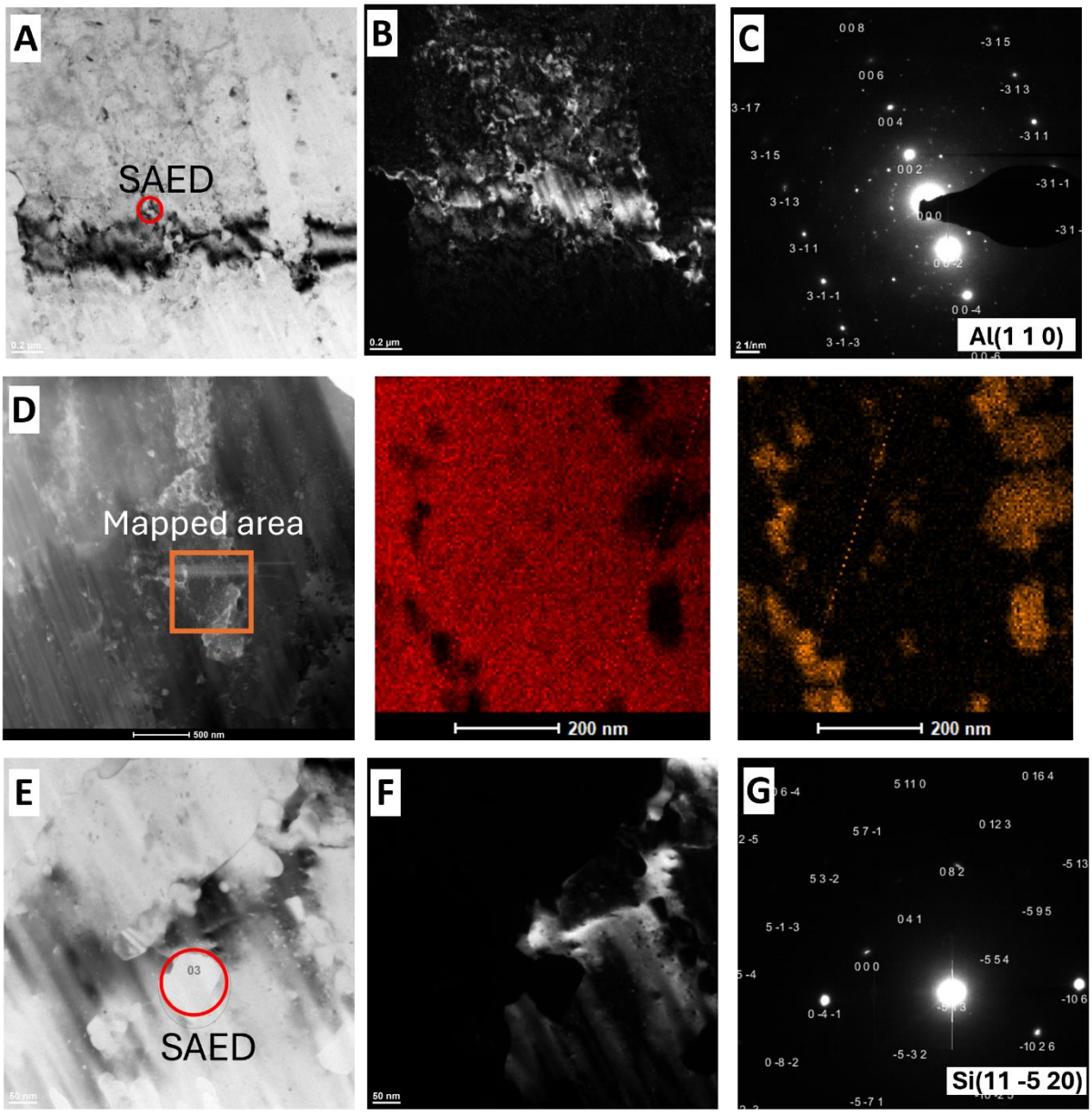

Figure 96. TEM analysis of the microstructure of LTA_300_1TCAP A,B. BF and DF TEM images showing the grain structure, **C**. Indexed SAED pattern corresponding to the indicated area in B, **D**. EDS chemical composition mapping of the fragmented cell boundaries, **E,F**. BF and DF TEM images showing particulate Si and the indexed SAED pattern of the indicated Si particle is presented in **G**.

4.6.2 Two Passes TCAP (2TCAP)

The results of microstructural evolution of the samples following the second pass of TCAP (2TCAP) as examined using BF and polarized LOM, are presented in **Figures 97, 98 and 99** for the As-built_2TCAP, LTA_280_2TCAP, and LTA_300_2TCAP samples, respectively. The As-built_2TCAP sample retained the characteristic mesoscale MP morphology following the second deformation pass. However, the overall MP dimensions were altered: the average MP width was significantly reduced to 79.80 ± 9.28 μm, while the depth slightly increased to 32.8 ± 12.13 μm. In the LTA_280_2TCAP sample, although the characteristic "fish-scale" MP morphology was still discernible, the MP geometry was modified in the opposite manner. The average MP depth decreased to 22.6 ± 7.5 μm, while the width increased to 162.8 ± 34.2 μm.

Conversely, the LTA_300_2TCAP sample exhibited porosity in several regions after the second TCAP pass (**Figure 99A**). The average MP width and depth were measured as 49.30 ± 7.47 μm and 40.74 ± 18.12 μm, respectively. These values corroborate the more compact and vertically elongated MP profile depicted in **Figure 99C**.

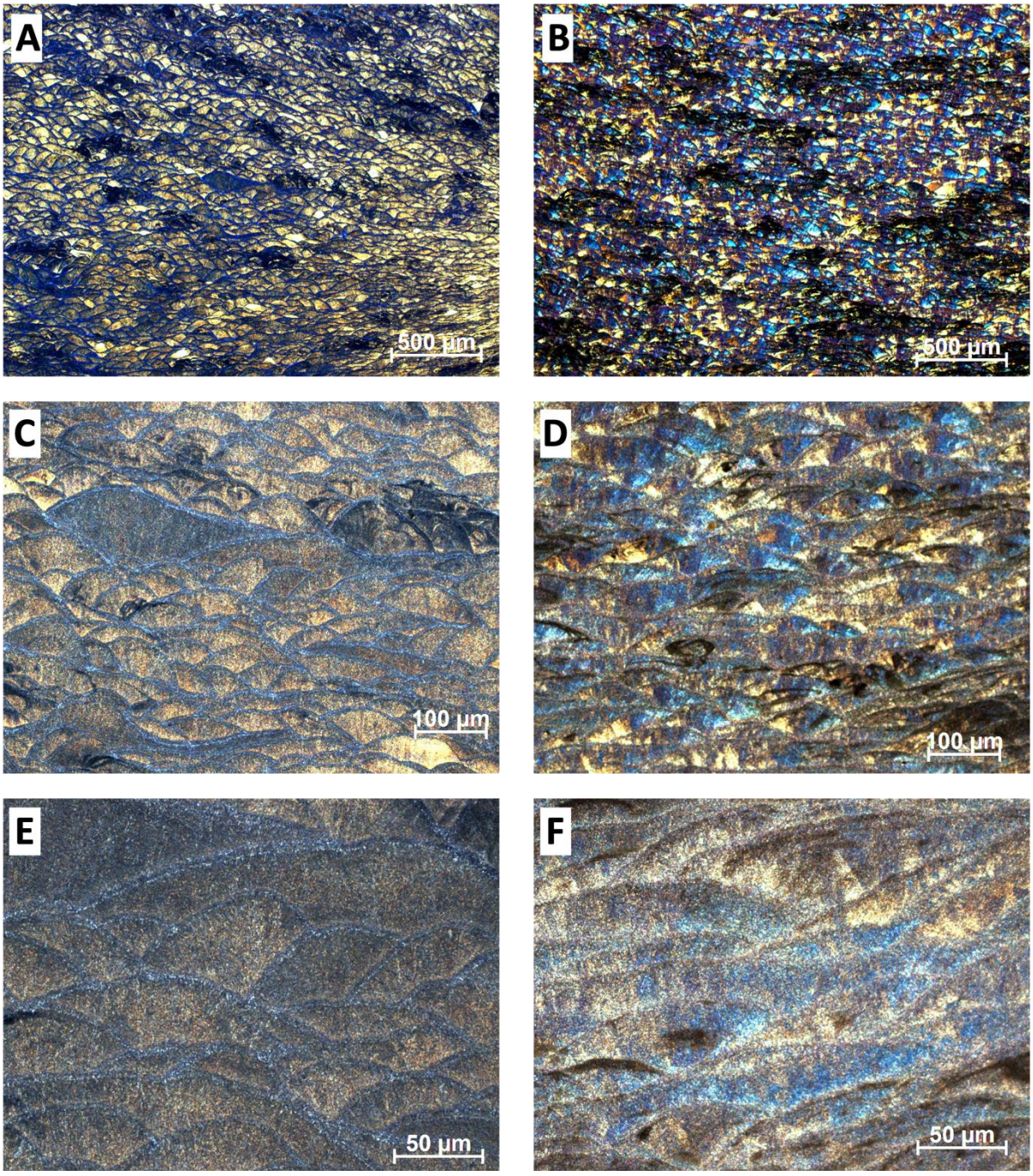

Figure 97. LOM bright field (left) and polarized light (right) microstructure of As-built_2TCAP along the X-Z plane at different magnifications **A,B.** 50X, **C,D.** 200X, and **E,F.** 500X

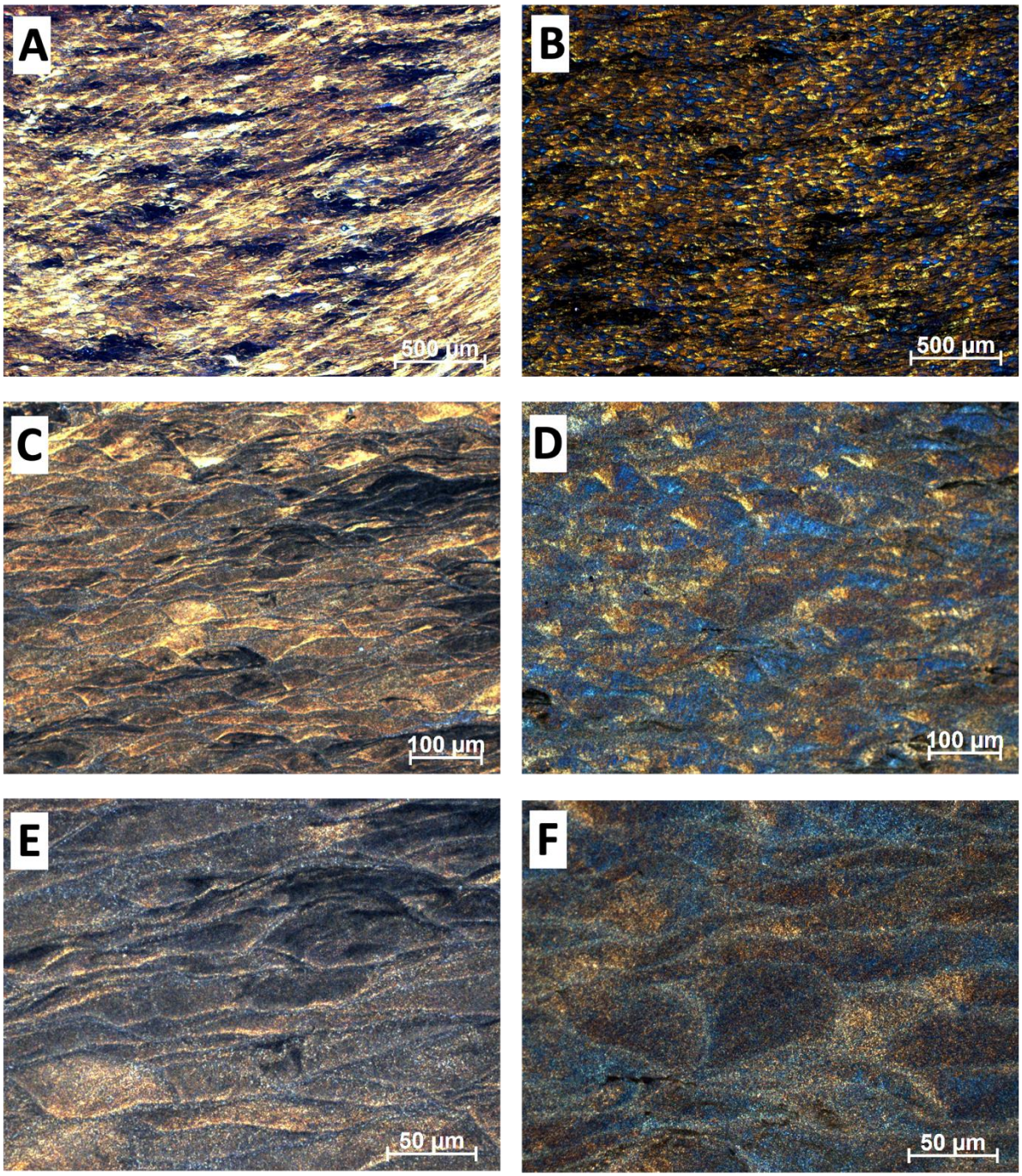

Figure 98. LOM bright field (left) and polarized light (right) microstructure of LTA_280_2TCAP along the X-Z plane at different magnifications **A,B.** 50X, **C,D.** 200X, and **E,F.** 500X

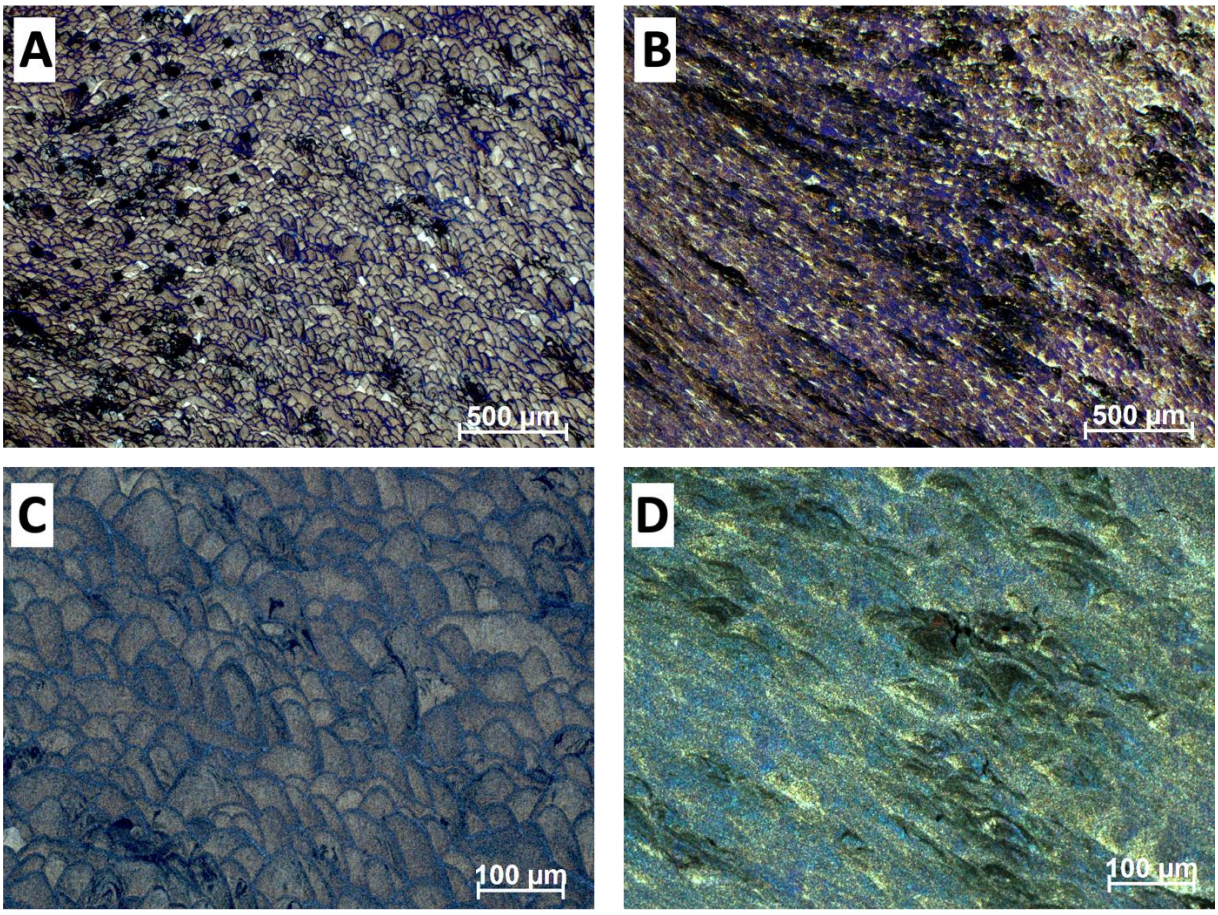

Figure 99. LOM bright field (left) and polarized light (right) microstructure of LTA_300_2TCAP along the X-Z plane at different magnifications **A,B.** 50X, and **C,D.** 200X

SEM observations of the As-built_2TCAP sample (**Figure 100**) revealed substantial fragmentation of the eutectic cellular network following the second TCAP processing pass, resulting in a predominantly non-cellular morphology. Residual fragments of the former cell walls were observed, with an average thickness of 0.20 ± 0.04 µm. The LTA_280_2TCAP sample (**Figure 101**) exhibited a comparable microstructural appearance to that of the As-built_2TCAP state. The eutectic network was similarly disrupted, and the structure was characterized by dispersed fragments of the cellular architecture. The average thickness of these fragmented cell walls was measured to be 0.23 ± 0.06 µm, suggesting a similar degree of structural refinement and homogenization despite the prior low-temperature annealing.

In the case of the LTA_300_2TCAP sample, the SEM micrographs (**Figure 102**) revealed a fully non-cellular microstructure, with uniformly dispersed particulate Si embedded within the

aluminum matrix, consistent with the microstructural condition observed after the first TCAP pass. Moreover, the average Si particle size remained essentially unchanged after the second deformation cycle (**Figure 102D**), indicating that further plastic deformation did not significantly alter the particulate coarsening or morphology established in the prior 1TCAP state.

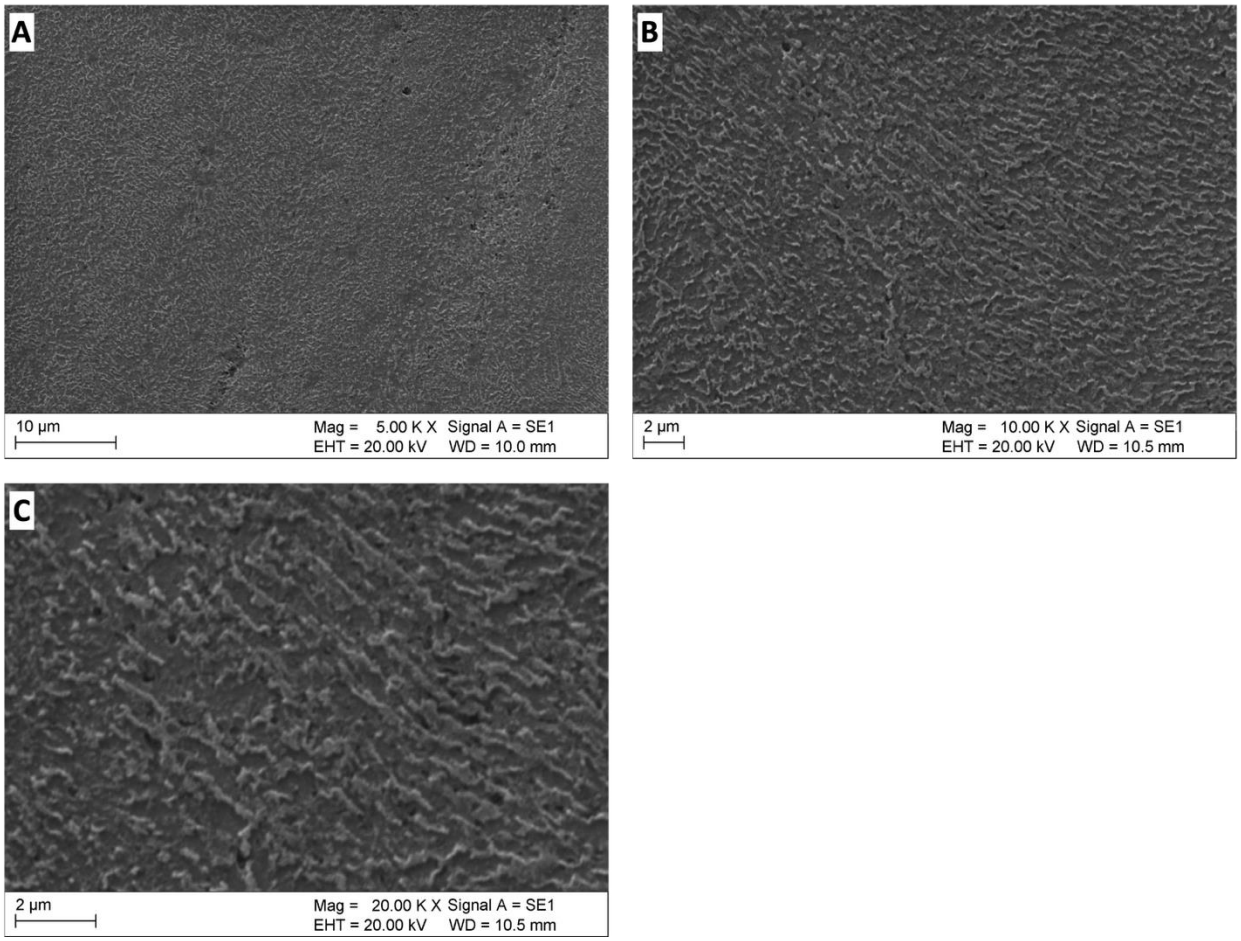

Figure 100. SEM microstructure of As-built_2TCAP at different magnifications **A**. 5000X, **B**. 10000X, and **C**. 50000X

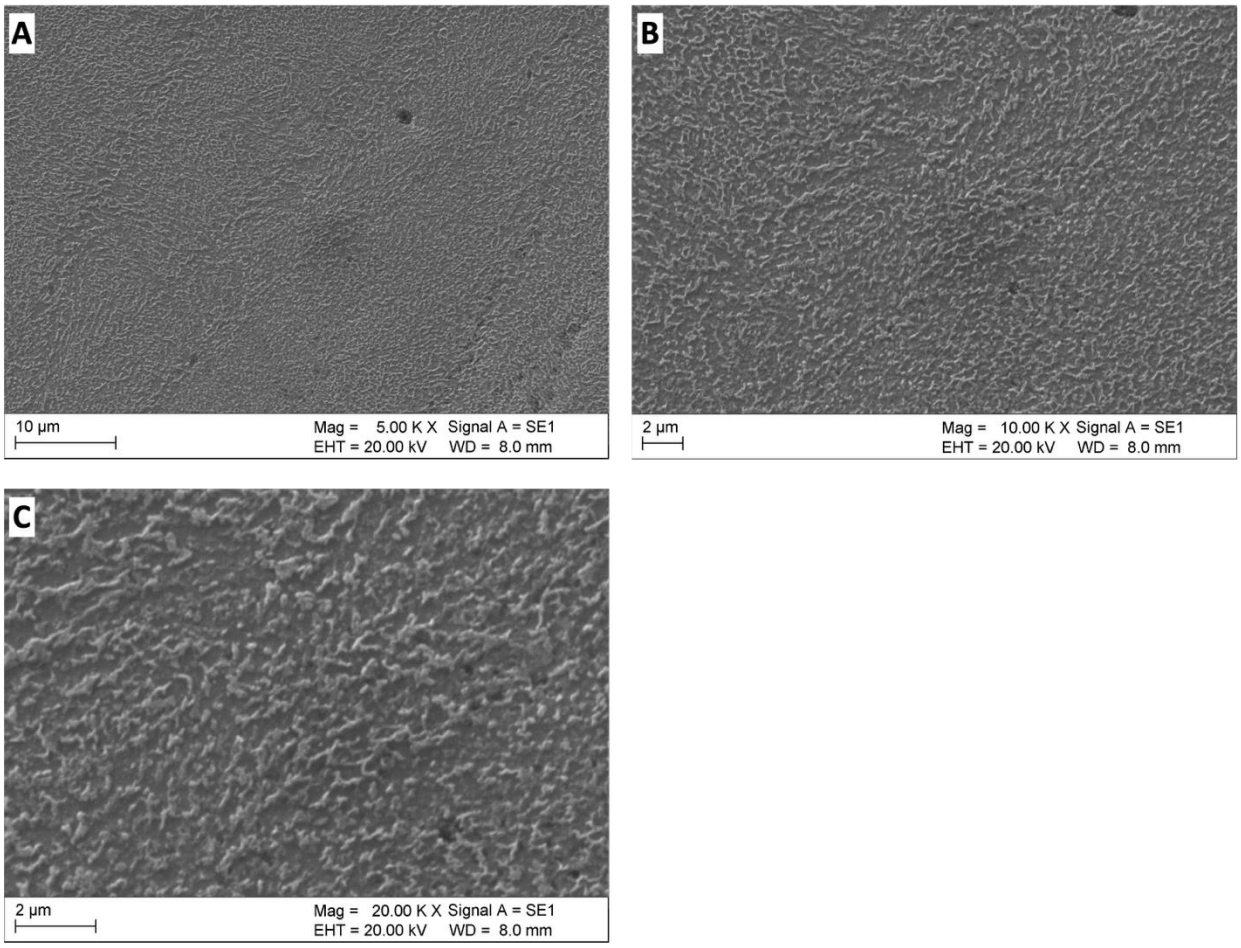

Figure 101. SEM microstructure of LTA_280_2TCAP at different magnifications **A**. 5000X, **B**. 10000X, and **C**. 20000X

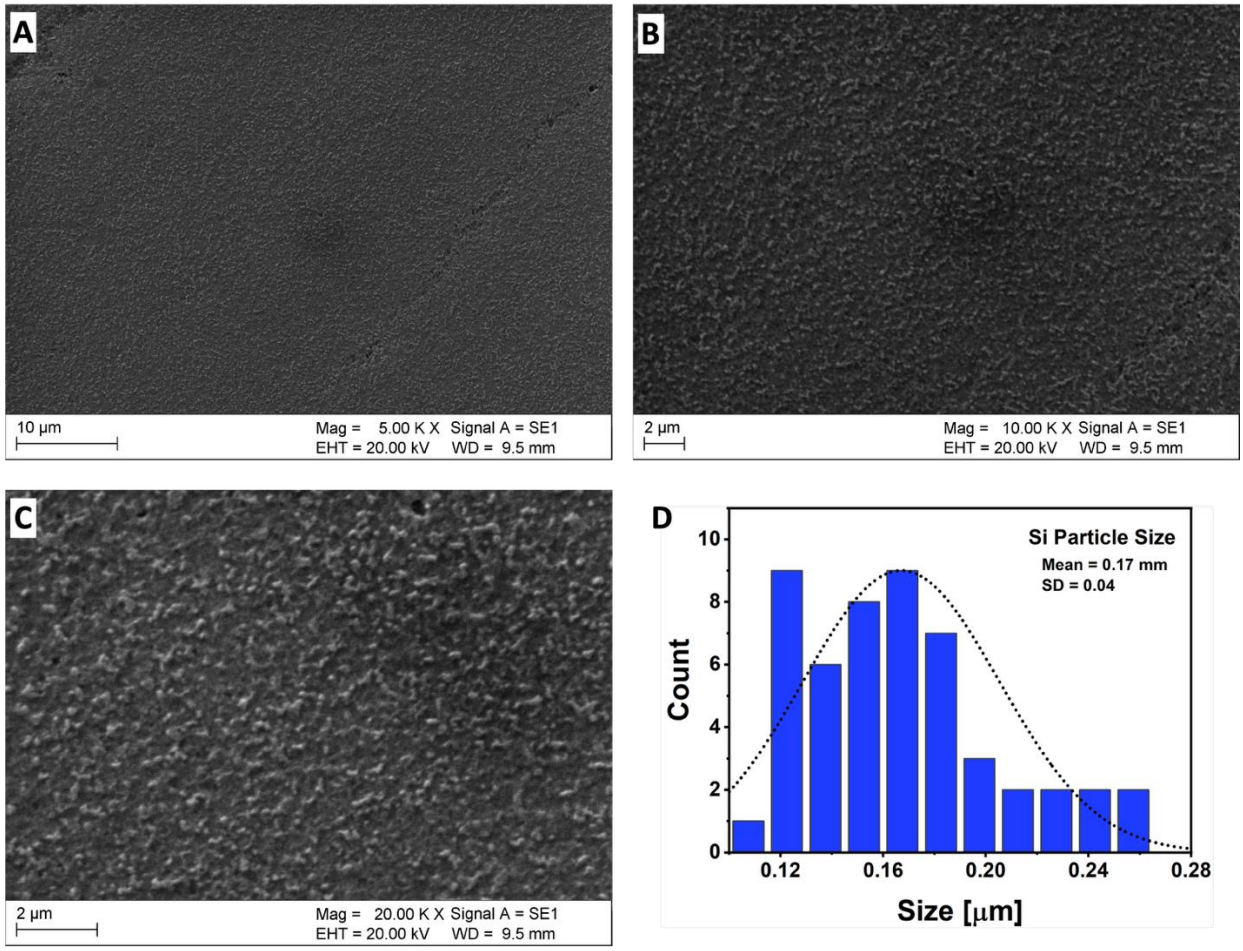

Figure 102. SEM microstructure of LTA_300_2TCAP at different magnifications **A**. 5000X, **B**. 10000X, **C**. 20000X, **D**. Si particle size distribution

EBSD analyses of the As-built_2TCAP and LTA_300_2TCAP samples are presented in **Figures 102 and 103**, respectively. The IPF map of the As-built_2TCAP sample (**Figure 103A**) reveals a microstructure characterized predominantly by partial columnar grains, alongside a localized region of finer equiaxed grains typically associated with the HAZ of the MP. This observation aligns with the preservation of the MP morphology previously noted in the LOM analysis. The average grain area was estimated at 7.4 ± 12.2 µm^2, indicating substantial grain refinement relative to the pre-TCAP state. Furthermore, grain boundary analysis revealed a higher proportion of LAGBs at 55.7%, while HAGBs accounted for 44.3%.

In contrast, the IPF map of the LTA_300_2TCAP sample (**Figure 104A**) shows a further refined, equiaxed grain structure, indicative of even more extensive grain refinement during the second TCAP pass. The average grain size was significantly reduced to 2.6 ± 5.0 µm^2. The grain

boundary statistics reveal a dominant fraction of HAGBs (83.6%) and a reduced fraction of LAGBs (16.4%).

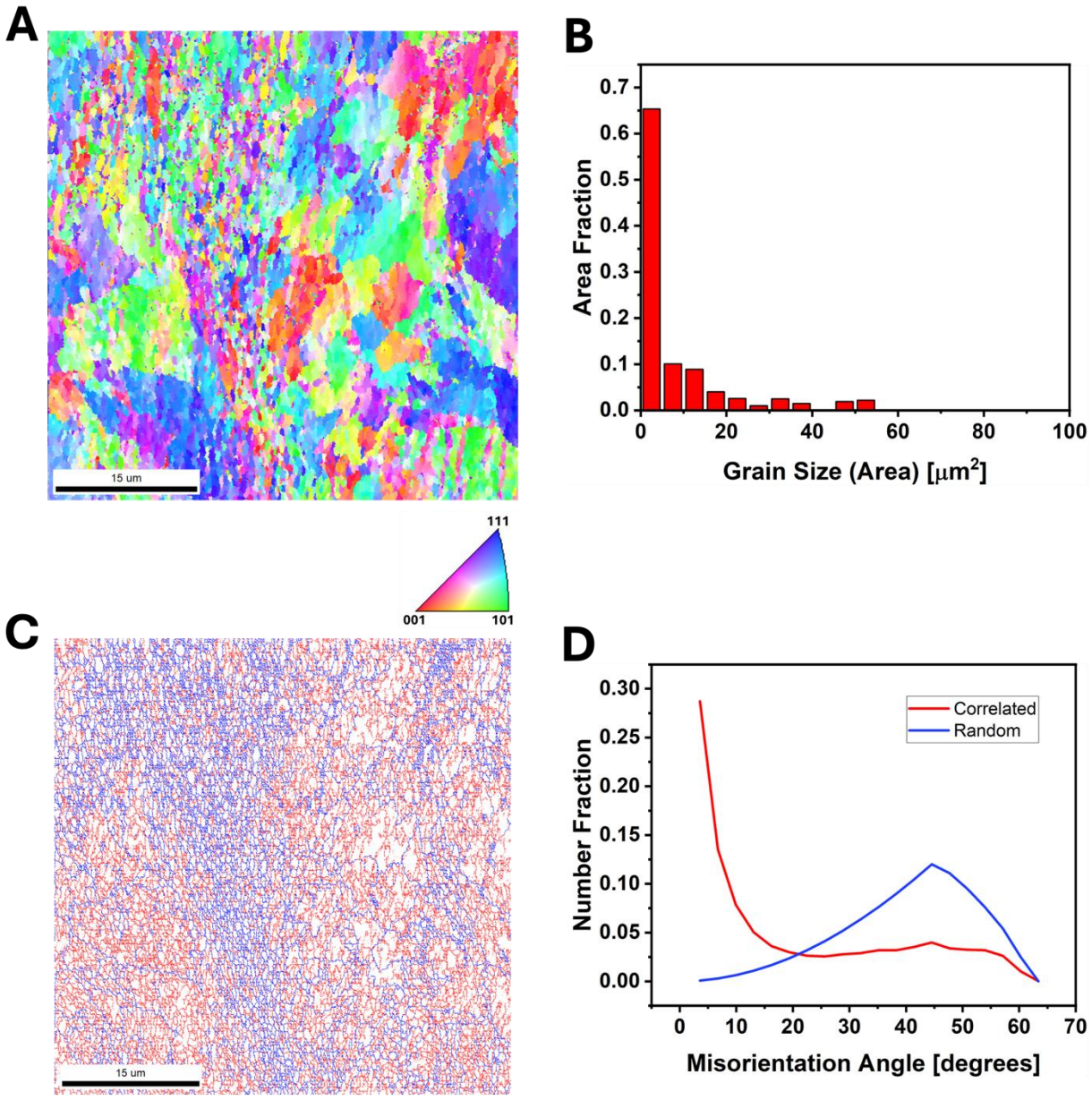

Figure 103. **Microstructure of As-built_2TCAP from EBSD analysis. A**. EBSD IPF-Z map of the sample, **B**. Grain size (area) histogram of the sample, **C**. Grain boundary map of the sample, and **D**. Misorientation angle histogram of the sample.

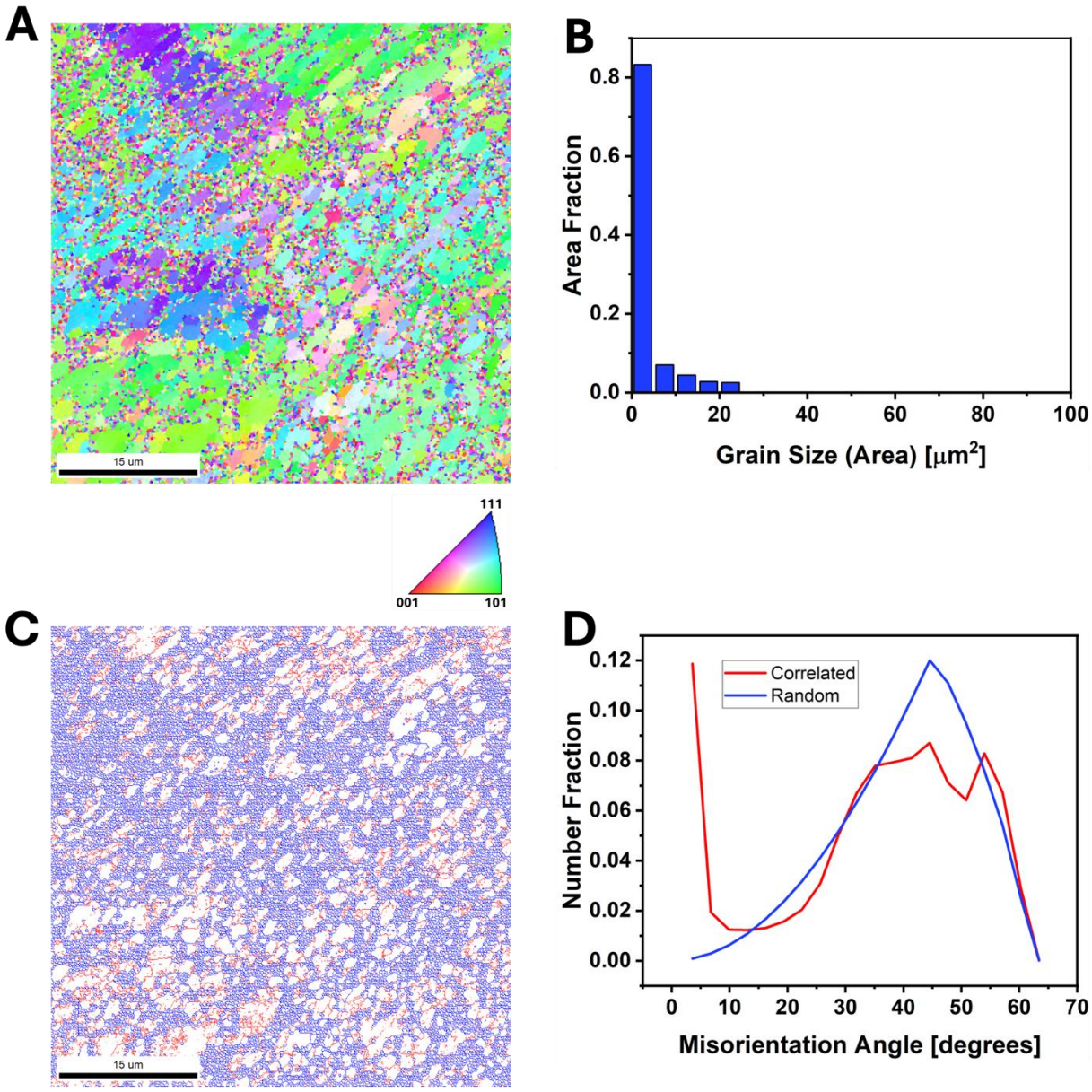

Figure 104. Microstructure of LTA_300_2TCAP from EBSD analysis. A. EBSD IPF-Z map of the sample, **B**. Grain size (area) histogram of the sample, **C**. Grain boundary map of the sample, and **D**. Misorientation angle histogram of the sample

4.6.3. Mechanical Properties

4.6.3.1. Hardness

The room temperature Vickers microhardness results of the TCAP-processed samples are presented as hardness contour maps in **Figure 105**. The data reveal that the highest hardness values were achieved by the As-built_1TCAP and LTA_280_1TCAP samples, both recording average

hardness values of approximately 130 $HV_{0.3}$. However, following the second TCAP pass, a general reduction in microhardness was observed for both samples. Notably, the LTA_280_2TCAP sample retained the highest hardness among the 2TCAP-processed specimens, with an average value of 121 ± 3.3 $HV_{0.3}$, while the As-built_2TCAP sample recorded a slightly lower hardness of 113.9 ± 4.0 $HV_{0.3}$, comparable to its pre-TCAP state.

In contrast, the LTA_300_2TCAP sample exhibited the lowest hardness values among all groups, with 108.2 ± 4.3 $HV_{0.3}$ after the first pass and 105.0 ± 3.7 $HV_{0.3}$ after the second pass. These findings are consistent with previous hardness results obtained for the as-built, heat-treated, and ECAP-processed samples. Specifically, samples retaining a continuous or partially continuous eutectic cellular structure exhibited superior hardness, while those that underwent complete disintegration of the cellular network, such as the LTA_300 variants, demonstrated reduced hardness. To further elucidate the effect of TCAP processing on mechanical performance, compression testing was conducted on all samples.

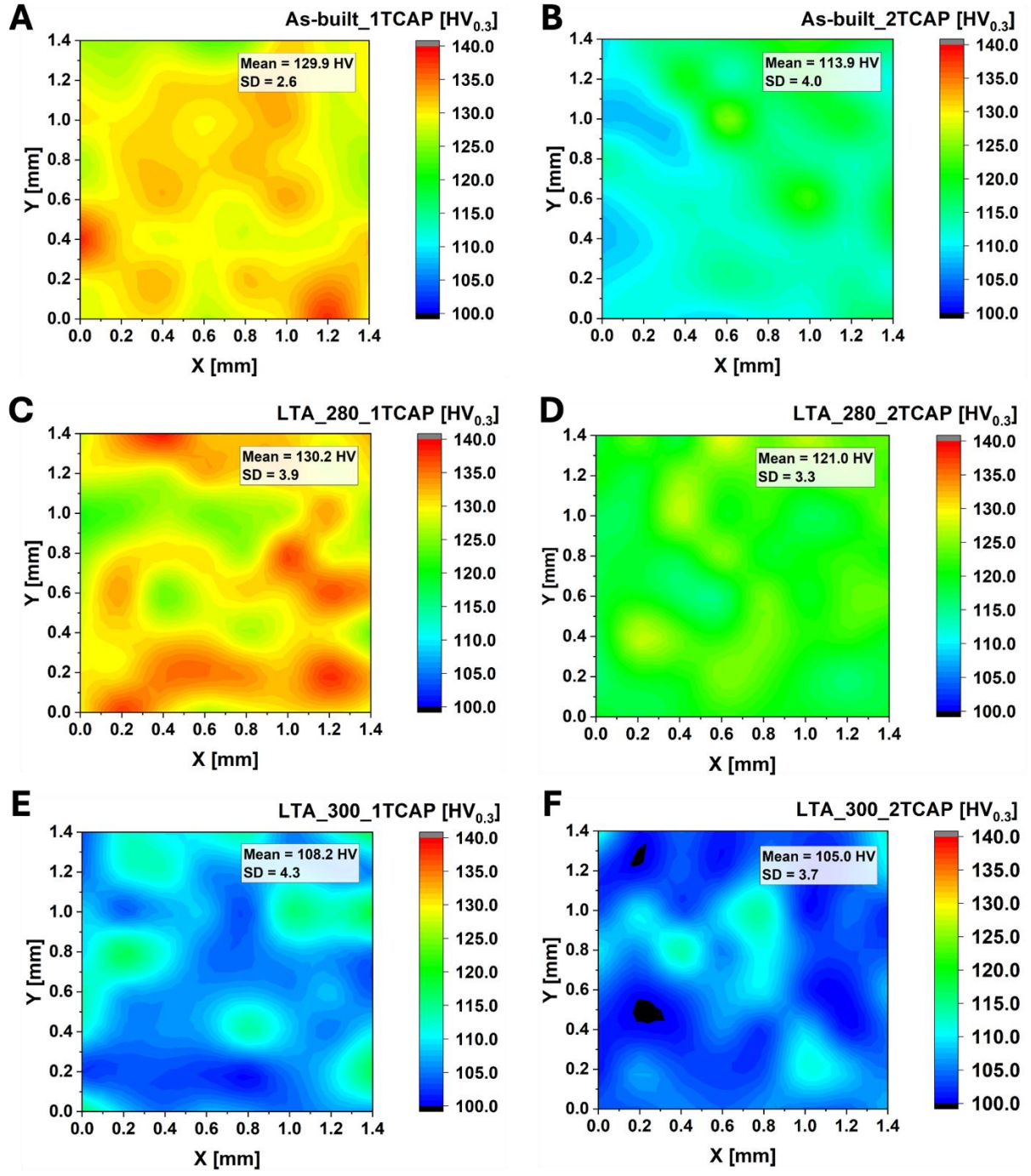

Figure 105. Vicker's microhardness of the TCAP processed samples. **A,C,E**. Single-pass TCAP, and **B,D,F.** 2-pass TCAP

4.6.3.2. Strain and Kinematic Hardening after 1TCAP

The compressive stress–strain responses of the samples processed via single-pass TCAP (1TCAP) are presented in **Figure 106**. Among the tested specimens, the LTA_280_1TCAP sample exhibited the highest yield strength (YS) of 506 MPa, followed by the As-built_1TCAP sample at 482 MPa, and the LTA_300_1TCAP sample, which showed the lowest YS of 392 MPa. This strength hierarchy aligns with earlier mechanical property trends observed in the pre-SPD and post-ECAP states, where samples retaining continuous or partially continuous cellular networks consistently demonstrated superior strength.

In terms of ductility, the inverse trend was observed. The LTA_300_1TCAP sample, which exhibited a highly fragmented eutectic cellular structure, demonstrated the highest failure strain of 38.3%, indicative of enhanced ductility. This was followed by the As-built_1TCAP sample with 35.5%, while the LTA_280_1TCAP sample had the lowest ductility, failing at 26.2%.

The strain hardening exponent (n) correlated positively with the yield strength across all samples. The LTA_280_1TCAP, which had the highest YS, also had the highest n value of 0.282 (**Figure 108**). This was followed by the As-built_1TCAP sample with an n value of 0.274 (**Figure 107**), while the LTA_300_1TCAP sample had the lowest n value of 0.223 (**Figure 109**), consistent with its relatively lower yield strength.

LUR tests further confirmed the superior ductility of the LTA_300_1TCAP sample (**Figure 110**), corroborating its highest failure strain observed during uniaxial compression testing. However, this sample also exhibited the lowest kinematic hardening capacity, as indicated by a maximum back stress of approximately 196 MPa before failure (**Figure 111**). In contrast, the LTA_280_1TCAP sample demonstrated the highest back stress, peaking at 242 MPa, followed by the As-built_1TCAP sample with 227 MPa.

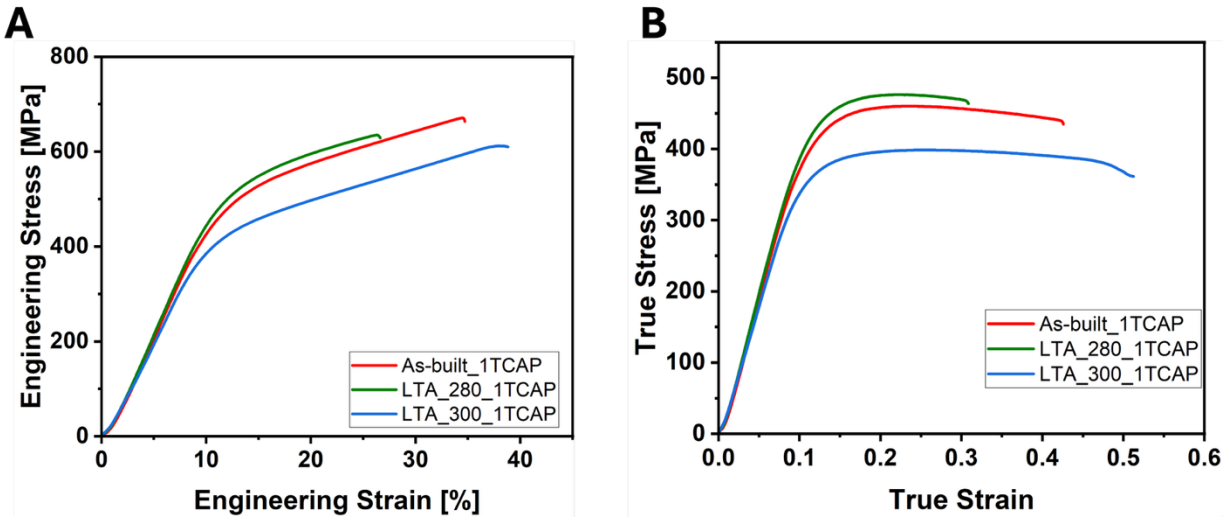

Figure 106. Engineering (**A**) and True (**B**) stress-strain plots of compressed single-pass TCAP-processed samples

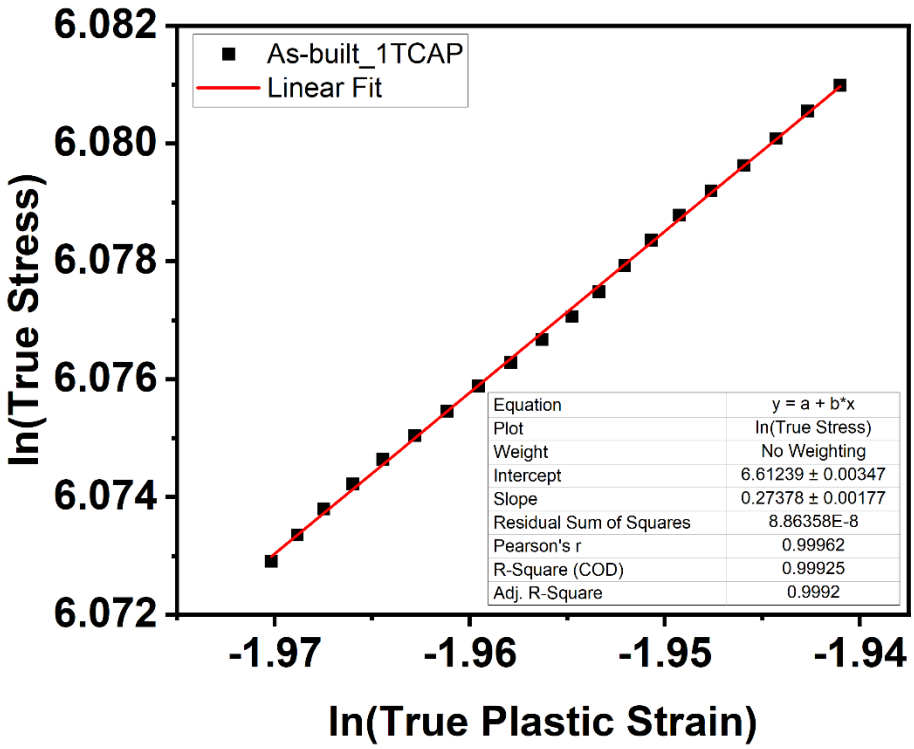

Figure 107. Strain hardening exponent plot for the As-built_1TCAP sample

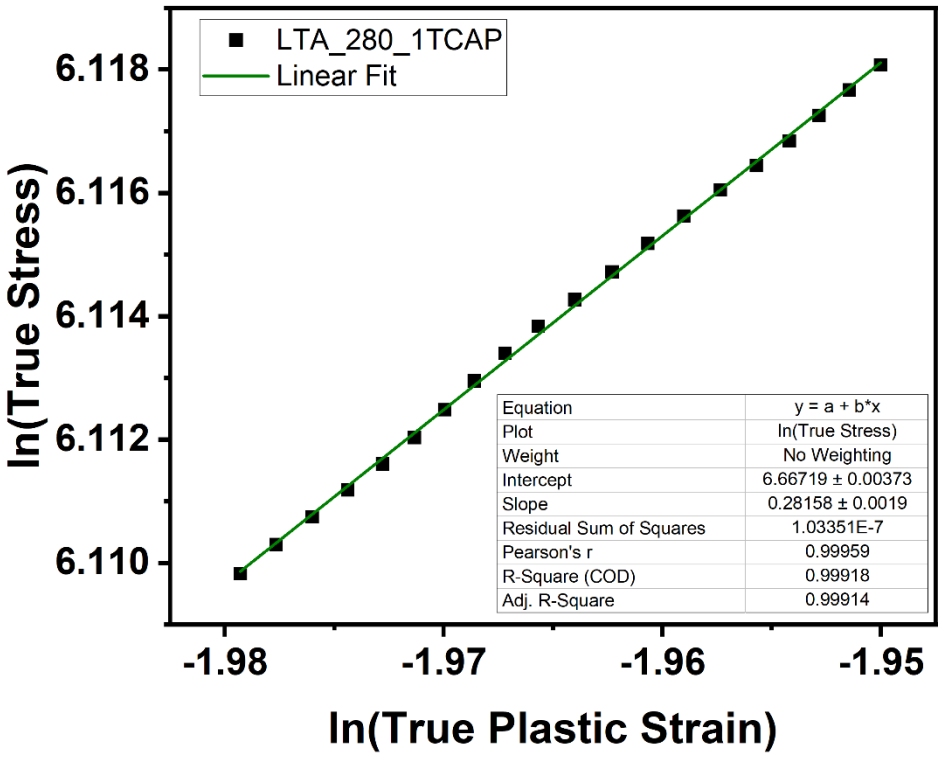

Figure 108. Strain hardening exponent plot for the LTA_280_1TCAP sample

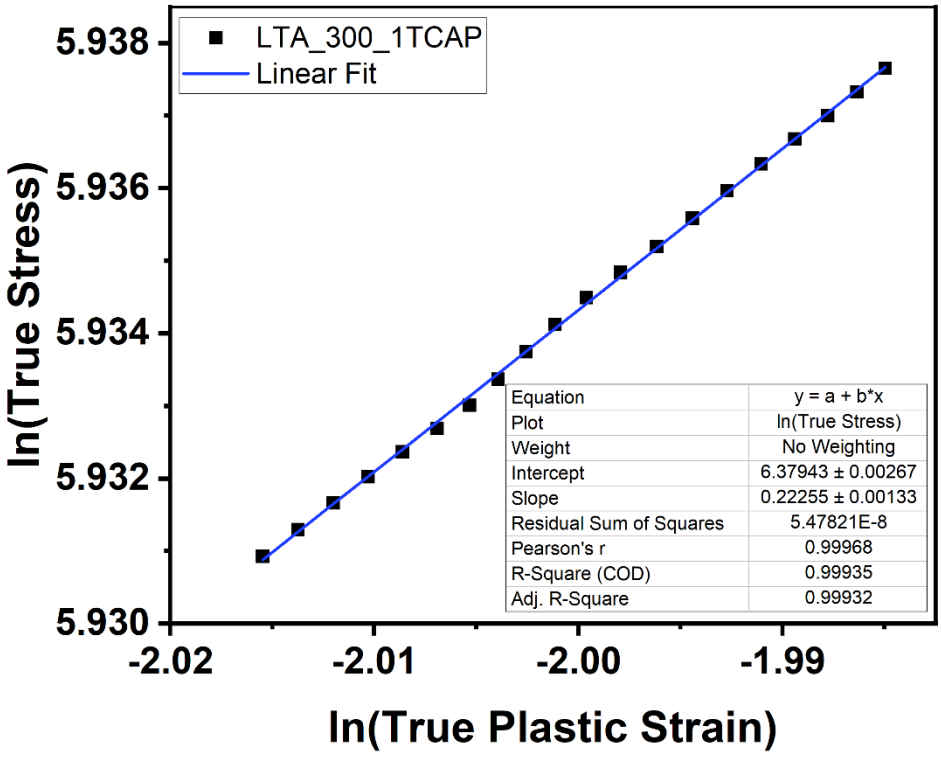

Figure 109. Strain hardening exponent plot for the LTA_300_1TCAP sample

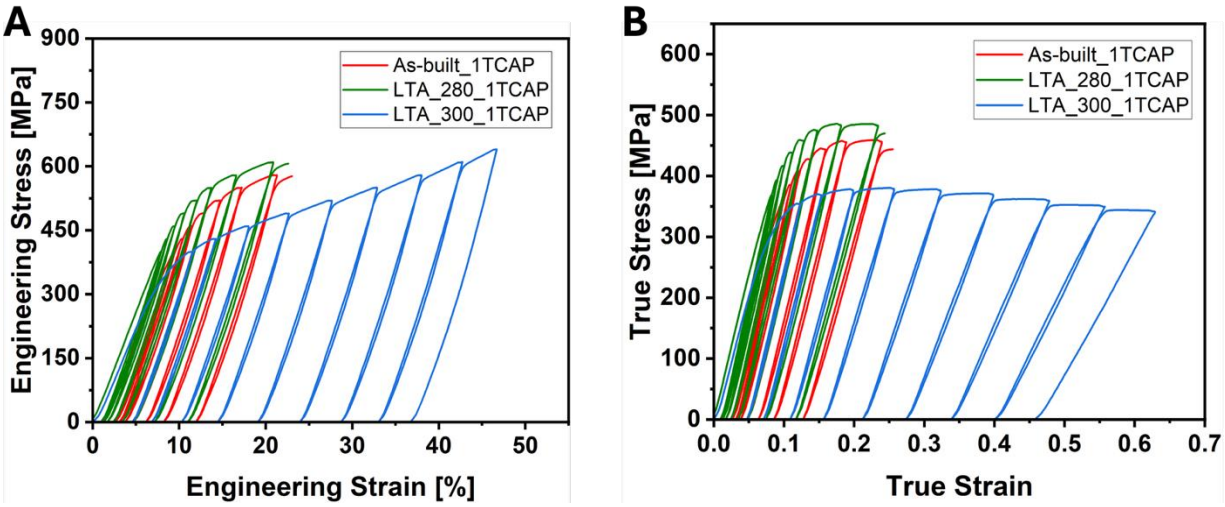

Figure 110. Engineering (**A**) and True (**B**) stress-strain plots from loading-unloading-reloading (LUR) tests for the single-pass TCAP-processed samples

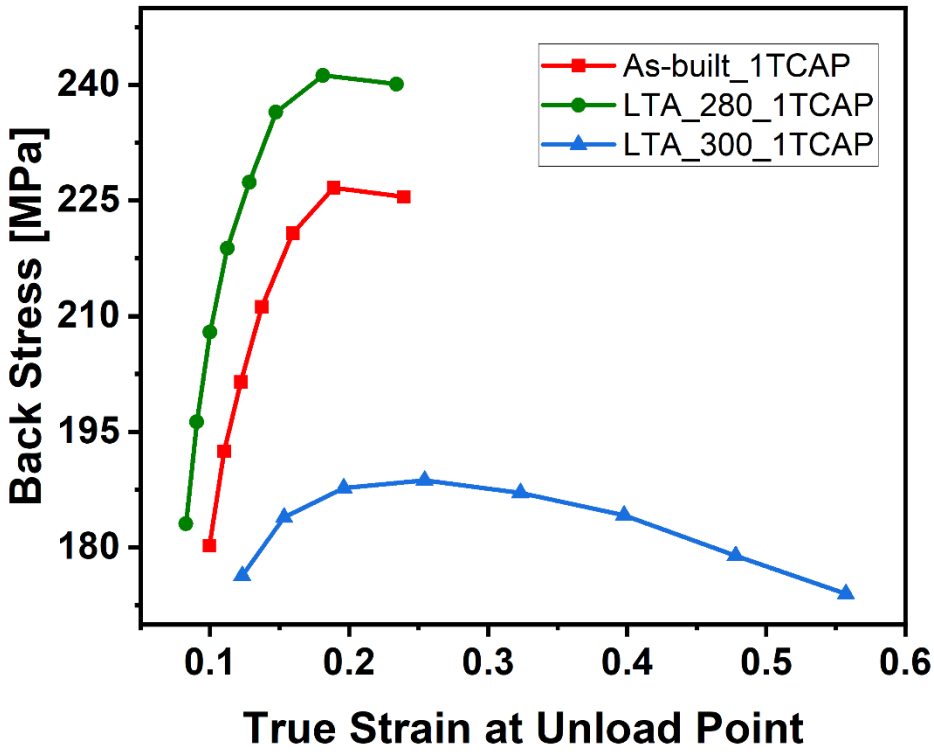

Figure 111. Back stress estimated from each LUR cycle for the single-pass TCAP-processed samples

4.6.3.3. Strain and Kinematic Hardening after 2TCAP

The mechanical performance of the samples after two-pass TCAP (2TCAP) was evaluated through uniaxial compression and LUR testing to investigate their stress–strain behavior, strain hardening, and kinematic hardening capacities. The engineering and true stress–strain curves presented in **Figure 112** show that the 2TCAP-processed samples exhibited comparable yield strengths (YS), ranging between 400 and 500 MPa. Despite this convergence, trends similar to those observed after 1TCAP were maintained. The LTA_280_2TCAP sample exhibited the highest YS of 455 MPa with a failure strain of 45.1%. This was followed by the As-built_2TCAP sample, with a YS of 422 MPa and failure strain of 48.3%, while the LTA_300_2TCAP sample recorded the lowest YS of 403 MPa, which nonetheless represents an improvement of ~11 MPa compared to its 1TCAP counterpart, along with a failure strain of 51.3%.

The strain hardening exponent (n) showed varied evolution after the second TCAP pass. The As-built_2TCAP sample exhibited a reduction in n to 0.255 (**Figure 113**), as did the LTA_280_2TCAP, which decreased to 0.253 (**Figure 114**). Conversely, the LTA_300_2TCAP sample demonstrated a slight increase in n to 0.243 (**Figure 115**), which corresponds with its observed increase in yield strength.

LUR testing results (**Figure 116**) corroborated the uniaxial test outcomes, reflecting similar mechanical behavior trends across the samples. However, the evolution of back stress after 2TCAP processing, presented in **Figure 117**, revealed nuanced differences. While the LTA_300_2TCAP sample continued to exhibit the lowest back stress, peaking at 193 MPa, a slight reversal in the hierarchy was observed between the other two samples. The As-built_2TCAP sample slightly surpassed the LTA_280_2TCAP in back stress, reaching a maximum of 204 MPa, compared to 202 MPa for the latter.

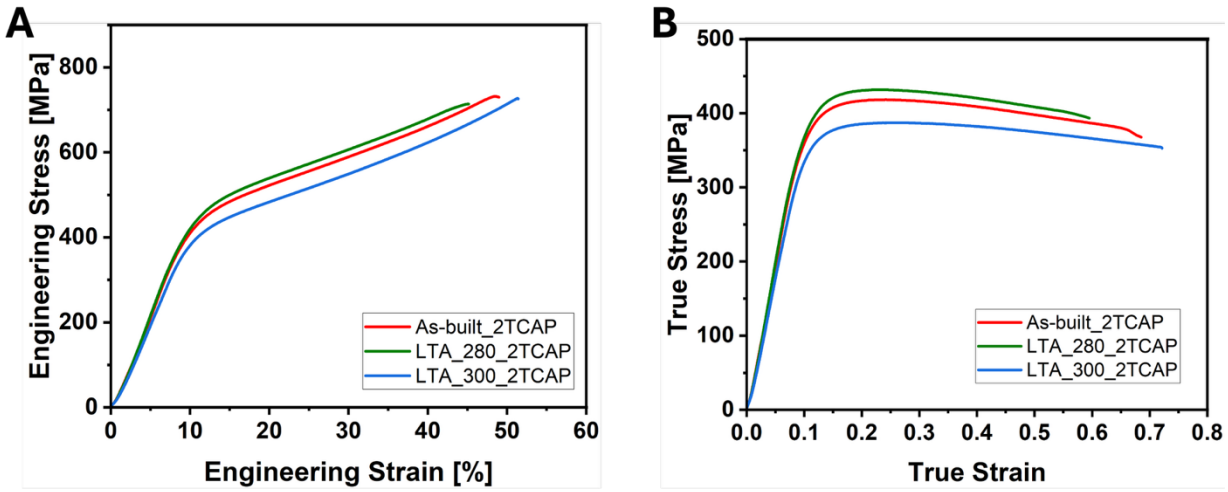

Figure 112. Engineering (**A**) and True (**B**) stress-strain plots of compressed 2-pass TCAP-processed samples

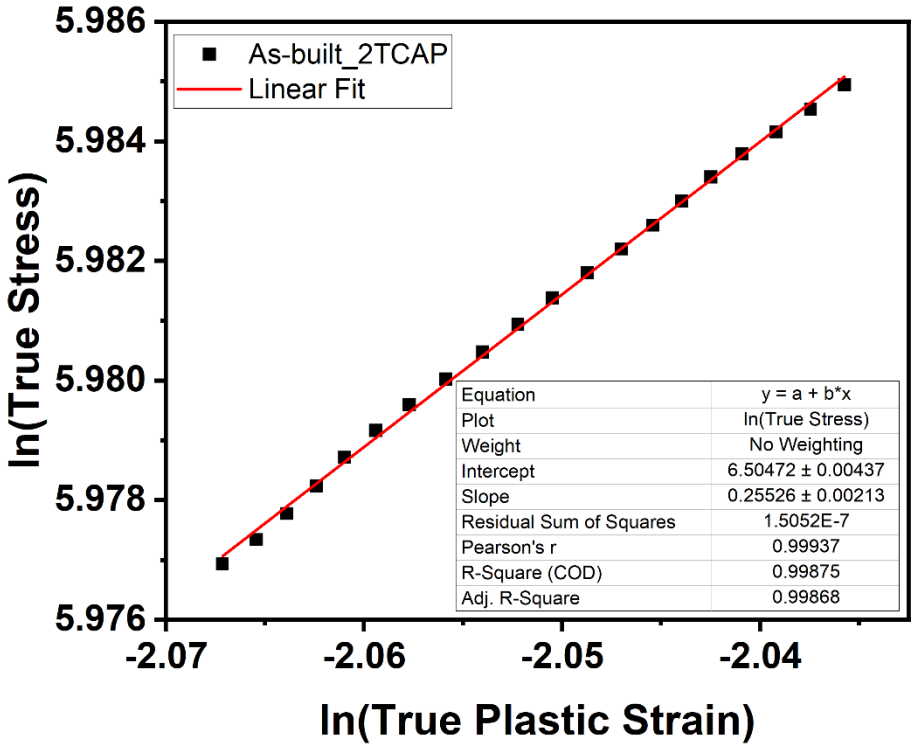

Figure 113. Strain hardening exponent plot for the As-built_2TCAP sample

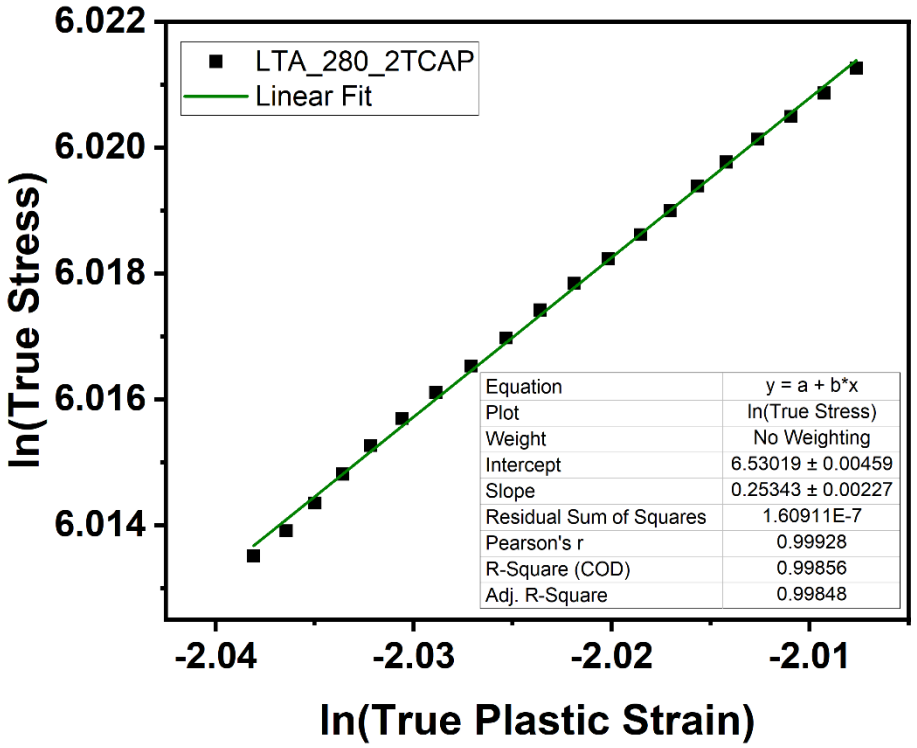

Figure 114. Strain hardening exponent plot for the LTA_280_2TCAP sample

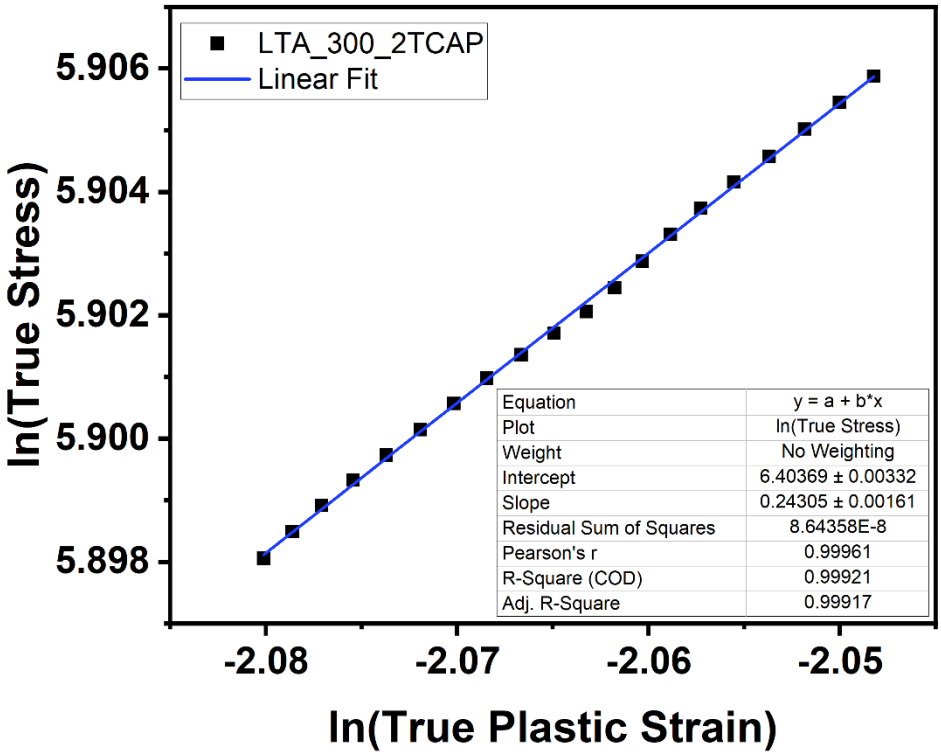

Figure 115. Strain hardening exponent plot for the LTA_300_2TCAP sample

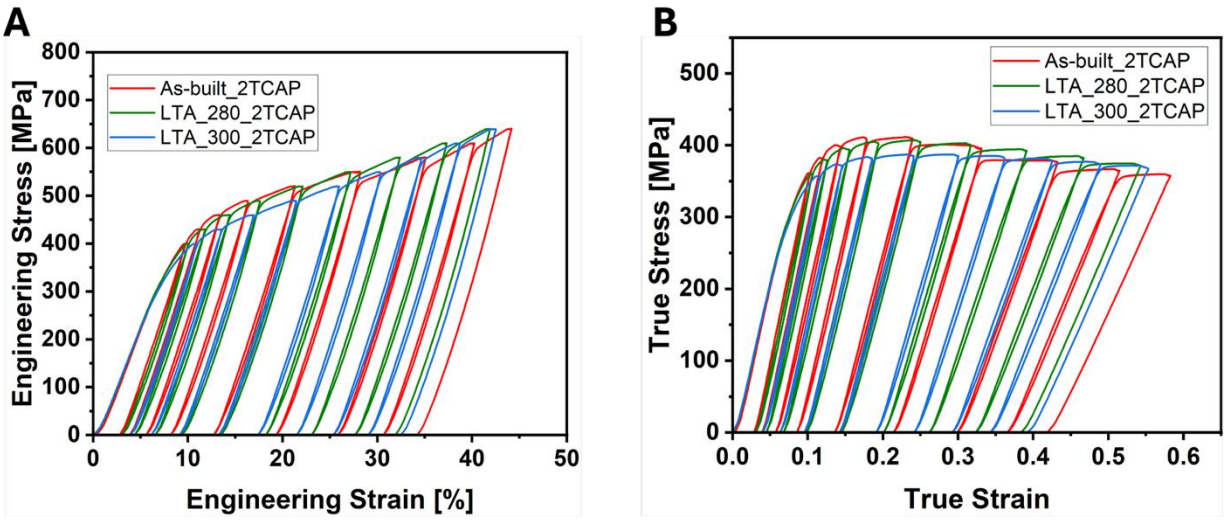

Figure 116. Engineering (**A**) and True (**B**) stress-strain plots from loading-unloading-reloading (LUR) tests for the 2-pass TCAP-processed samples

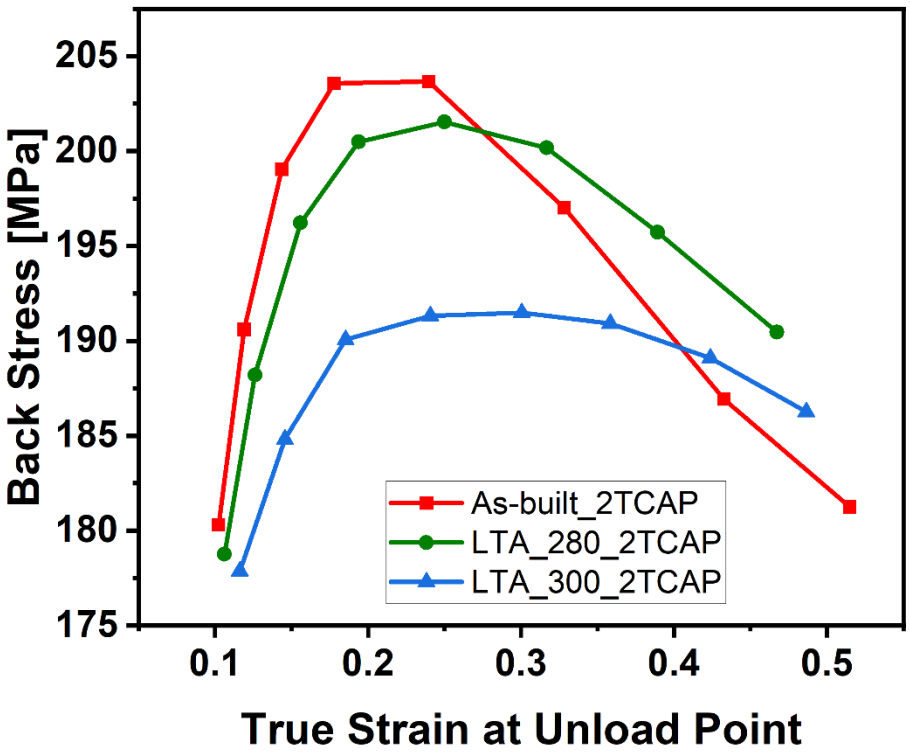

Figure 117. Back stress estimated from each LUR cycle for the 2-pass TCAP-processed samples

A summary of the mechanical properties of the TCAP processed samples is given in **Table 7**.

Table 7. Mechanical Properties of the TCAP-processed samples

Sample ID	**Hardness [$HV_{0.3}$]**	**Yield strength (σ_y) [MPa]**	**UCS [MPa]**	**Total strain at failure (ε_f) [%]**	**n**
As-built_1TCAP	129.9 ± 2.6	482	670.8	34.5	0.274
LTA_280_1TCAP	130.2 ± 3.9	506	634.8	26.2	0.282
LTA_300_1TCAP	108.2 ± 4.3	392	701.6	38.3	0.223
As-built_2TCAP	113.9 ± 4.0	422	740.8	45.1	0.255
LTA_280_2TCAP	121.0 ± 3.3	455	742.0	45.1	0.253
LTA_300_2TCAP	105.0 ± 3.7	403	727.2	51.3	0.243

Chapter Five

5.0 Discussion

This chapter provides a comprehensive analysis and interpretation of the experimental results presented in **Chapter 4**. The discussion aims to elucidate the intricate relationships between alloy composition, thermal history, and deformation processing on the microstructural evolution and resultant mechanical properties of additively manufactured Al-Si-Mg alloys. The findings are contextualized within the established principles of physical metallurgy, dislocation theory, and severe plastic deformation.

5.1 Influence of Alloy Composition on As-Built PBF-LB/M Microstructure and Properties

The initial phase of this investigation involved a comparative assessment of three Al-Si-Mg alloys (AlSi7Mg, AlSi10Mg, and AlSi12Mg) to establish a baseline and justify the selection of AlSi10Mg for subsequent, more intensive study. The results from this comparative analysis, detailed in **Section 4.1**, demonstrate that the selection of AlSi10Mg is fundamentally justified by its superior combination of processability and as-built properties, which are intrinsically linked to its near-eutectic composition.

The processability of a metallic powder in PBF-LB/M is paramount, as it directly influences the stability of the melt pool, the uniformity of layer deposition, and the final density of the component [150]. The powder characterization revealed that the AlSi10Mg powder possessed the most uniform particle size distribution, with a span of 1.06, compared to 1.20 for AlSi7Mg and 1.30 for AlSi12Mg (**Figure 21**). A narrow and consistent particle size distribution is known to enhance powder bed packing density and flowability [151], which are critical for minimizing process-induced defects. This superior powder quality, combined with the alloy's near-eutectic nature, translates directly into improved melt pool behavior. The approximately 10% silicon content enhances melt fluidity and narrows the solidification range, which is crucial for mitigating defects such as hot tearing and lack-of-fusion porosity that are common in alloys with wider solidification intervals [74].

This theoretical advantage is empirically validated by the porosity analysis presented in **Figure 30**. The hypo-eutectic AlSi7Mg alloy exhibited a high porosity of approximately 2.4%, likely due to a combination of lower fluidity and a wider solidification range that promotes defect

formation [152]. In contrast, both the AlSi10Mg and AlSi12Mg alloys achieved high relative densities, with porosity levels of only 0.46% and 1.76%, respectively. This confirms that a silicon content near or above the eutectic composition is essential for achieving sound, dense parts under the PBF-LB/M conditions employed in this study.

While both AlSi10Mg and AlSi12Mg demonstrate excellent processability, a closer examination of their microstructures reveals a critical distinction. The relationship between silicon content and the resulting as-built microstructure is non-monotonic. The extreme cooling rates inherent to PBF-LB/M, estimated to be on the order of 10^5 to 10^7 k/s create a unique, non-equilibrium cellular structure. The morphology and scale of this structure are governed by the local solidification conditions, specifically the ratio of the thermal gradient (G) to the solidification rate (R) [153]. The present work shows that AlSi10Mg produces the finest cellular structure, with an average cell size of 0.88 ± 0.17 μm (**Figure 29**). In contrast, the AlSi7Mg and AlSi12Mg exhibited a coarser cellular structures with average sizes of 1.06 ± 0.25 μm and 1.36 ± 0.38 μm respectively. This suggests that while increasing Si content up to the eutectic point refines the cellular structure by influencing the G/R ratio favorably, further increases may alter the solidification kinetics in a way that promotes cellular coarsening rather than refinement.

This difference in cellular refinement is the primary determinant of the as-built mechanical properties. The fine, interconnected Si-rich network at the cell boundaries acts as a significant barrier to dislocation motion, leading to strengthening via a mechanism analogous to the Hall-Petch effect, where the cell size acts as the characteristic length scale. Consequently, the AlSi10Mg alloy, with its finer cellular structure, exhibited the highest Vickers microhardness of 115.77 $HV_{0.3}$, surpassing both the porous AlSi7Mg (96.77 $HV_{0.3}$) and the coarser-celled AlSi12Mg (106.69 $HV_{0.3}$) (**Figure 31**). This finding aligns with literature reporting that the exceptional strength of as-built PBF-LB/M AlSi10Mg stems directly from this unique, fine-scale hierarchical microstructure [95], [154], [155], [156]. Therefore, AlSi10Mg was selected for this study as it represents an optimal balance: its composition ensures excellent processability leading to near-fully dense parts, while simultaneously producing the most refined and potent strengthening cellular microstructure among the common Al-Si PBF-LB/M alloys. This makes it the ideal model system for investigating how this inherent heterogeneity can be controlled through post-processing to achieve superior mechanical performance.

5.2 Thermal Stability and Microstructural Evolution during Low-Temperature Annealing (LTA)

The application of post-process heat treatments is a standard industrial practice for PBF-LB/M components, primarily aimed at relieving the residual stresses that accumulate during the rapid, localized heating and cooling cycles [157]. However, the results of this study demonstrate that LTA treatments are not merely stress-relief steps but are, more importantly, microstructural conditioning processes that fundamentally alter the material's strengthening architecture and subsequent deformation behavior. The choice of annealing parameters; temperature and time, governs the kinetics of Si network decomposition, which in turn dictates the balance between strength and ductility.

The LTA_280 treatment, a short anneal at 280 °C for 9 minutes, represents a subtle but significant modification of the as-built state. As shown in **Figures 37** and **39**, the mesoscale features, including the melt pool morphology and the columnar grain structure, remain largely intact, indicating that this thermal exposure is insufficient to trigger significant grain growth or recrystallization. This is consistent with studies showing the high thermal stability of the PBF-LB/M grain structure at temperatures below 350 °C [158], [159]. However, at the microscale, SEM analysis reveals the initiation of microstructural degradation, evidenced by localized ruptures in the continuous eutectic Si network (**Figure 35C**). This observation suggests the onset of thermally activated recovery processes and the diffusion of silicon atoms [30], [160], which begin to disrupt the integrity of the cellular architecture. This partial breakdown of the strengthening network is sufficient to cause a noticeable decrease in hardness from 115.8 $HV_{0.3}$ in the as-built state to 105.5 $HV_{0.3}$.

In contrast, the LTA_300 treatment, a longer anneal at a slightly higher temperature of 300 °C for 30 minutes, induces a notable microstructural transformation. While the mesoscale grain structure remains stable (**Figure 37**), the nanoscale cellular network undergoes notable fragmentation. The continuous Si network disintegrates and spheroidizes into discrete, fine Si particles with an average size of 95 – 130 nm, which are dispersed throughout the α-Al matrix (**Figures 41 and 42**). This phenomenon, according to studies by Tabatabael et al. [147] and Hu et al. [161], is a classic example of Ostwald ripening, a diffusion-controlled coarsening process driven by the reduction of the total interfacial energy between the Si particles and the Al matrix. This is consistent with literature observations of PBF-LB/M AlSi10Mg alloys following heat

treatment [162], [163], [164]. The kinetics of this process are highly sensitive to both temperature and time; the parameters for LTA_300 were sufficient to drive the fragmentation to completion, whereas those for LTA_280 were not.

This dramatic change in the Si phase morphology fundamentally alters the material's strengthening mechanisms. The transition from a continuous network to dispersed particles represents a shift from a cellular network-reinforced composite to a particle-reinforced composite. The loss of the continuous, load-bearing Si network significantly weakens the Hall-Petch-like strengthening from the cell boundaries and the Orowan-like strengthening from the network itself, resulting in a further drop in hardness to 98.0 $HV_{0.3}$. Concurrently, recovery processes [165], which are more pronounced at the higher temperature and longer duration of the LTA_300 treatment, lead to a greater reduction in the initial dislocation density, further contributing to the observed softening.

Nonetheless, this softening is not merely a degradation of properties but rather a controlled approach to making the material more ductile. In the as-built state, the continuous and brittle Si network, while providing high strength, also acts as a preferential path for crack initiation and propagation, severely limiting the material's ductility. This is evidenced by the low fracture strain of 35.1% in the as-built sample under compression. Once this network is fragmented into discrete, rounded particles by the LTA_300 treatment, a propagating crack is no longer offered an easy, continuous path. Instead, it must navigate through the much more ductile α-Al matrix, a process that requires significantly more energy and allows for plastic deformation to blunt the crack tip [166].

This change in the failure mechanism is responsible for the dramatic increase in fracture strain to 47.2% observed in the LTA_300 sample (**Table 4**). Therefore, the LTA_300 treatment in this research is viewed as an essential pre-conditioning step that trades a predictable amount of initial strength for a massive gain in damage tolerance and deformability. This enhanced ductility is a critical prerequisite for enabling the material to withstand the extreme strains of subsequent severe plastic deformation without premature failure.

5.3 Deformation Mechanisms and Hardening Behavior under Gradual Compression

The uniaxial compression tests performed at progressive strain levels (5%, 20%, and max strain) provide a clear window into the fundamental deformation mechanisms at play and how they are governed by the microstructural state of the alloy. The results, detailed in **Sections 4.3.2 to**

4.3.5, reveal that the continuity of the Si cellular network is the dominant factor controlling the generation and storage of dislocations, which in turn dictates the strain hardening behavior and the ultimate balance of strength and ductility.

The stress-strain curves (**Figures 46, 47**) and the corresponding strain hardening rate plots (**Figure 48**) delineate two distinct behaviors. The As-built and LTA_280 samples, which retain a continuous or semi-continuous Si network, exhibit higher yield strengths and superior initial strain hardening rates. This is a direct consequence of the Si network acting as a potent barrier to dislocation motion, a characteristic feature of PBF-LB/M AlSi10Mg. In contrast, the LTA_300 sample, with its fragmented Si network, shows a lower yield strength and a reduced initial hardening rate, as dislocations can more easily traverse the matrix, encountering only discrete particle obstacles as observed from TEM analysis (**Figures 56 and 59**).

A deeper, mechanistic understanding emerges from the analysis of the dislocation substructure evolution. During plastic deformation, two types of dislocations are generated: SSDs, which arise from random trapping events and contribute to isotropic hardening, and GNDs, which are required to accommodate plastic strain gradients and maintain lattice continuity across heterogeneities. In the AlSi10Mg system, the significant plastic strain incompatibility between the hard Si phase and the soft Al matrix necessitates the storage of GNDs to maintain lattice continuity at their interface. The generation of all dislocations, contributing to both the GND and SSD populations, occurs via mechanisms such as the operation of Frank-Read sources, which are particularly active in the high-stress regions near these interfaces. Direct evidence for this localized GND accumulation is provided by KAM analysis. At 5% strain, the As-built sample exhibits the highest average KAM value of 0.85°, significantly higher than the 0.65° observed in the LTA_300 sample (**Figure 55**). This finding is consistent with literature [76], [167], as the large strain gradients imposed by the continuous Al/Si network in the As-built sample drive the formation of a high-density GND population. These GNDs, in turn, generate long-range internal back stresses that oppose further dislocation motion, thereby producing the high strain hardening rate observed. Conversely, in the LTA_300 sample, the more homogeneous deformation associated with dispersed, spheroidized particles results in lower strain gradients and, consequently, a reduced density of GNDs.

This interpretation can be applied to the observations from dislocation density measurements. While KAM analysis indicates fewer GNDs in the LTA_300 sample at low strain,

XRD analysis of the samples deformed to fracture shows that the LTA_300 sample possesses the highest SSDs density, reaching 1.48×10^{14} m^{-2} (**Table 5**). This can be understood by considering the different roles of the Si network in hardening versus ductility. In the As-built sample, the high density of GNDs provides powerful back-stress hardening, reflected in the high strain hardening exponent (n = 0.250). However, the intense dislocation pile-ups at the continuous network also act as powerful stress concentrators, leading to premature damage initiation and fracture at a relatively low total strain (35.1%), thus limiting the overall amount of dislocation storage the material can accommodate. Conversely, the fragmented network in the LTA_300 sample generates less back-stress hardening, with a lower n value (n = 0.215) but allows the ductile Al matrix to deform to a much greater extent (failure strain of 47.2%). This extensive, more homogeneous plastic flow provides a much larger capacity for the accumulation and storage of SSDs throughout the matrix, resulting in a higher total dislocation density at fracture.

Therefore, two main phenomena can be inferred from these results. Firstly, the high strain hardening in the As-built state is primarily driven by GND-induced back-stress hardening, emanating from the continuous heterostructure. In contrast, the second phenomenon is that the exceptional ductility and high total dislocation storage in the LTA_300 state are enabled by a high SSD storage capacity within the ductile matrix, which is unlocked by fragmenting the brittle network.

5.4 Microstructural Tailoring and Mechanical Response via Severe Plastic Deformation (SPD)

The application of SPD techniques, namely ECAP and TCAP, represents the final stage in the thermomechanical processing route designed to achieve an optimal combination of strength and ductility. The results from these experiments, detailed in **Sections 4.4 to 4.6**, showcase the importance of the initial microstructural state, as determined by the LTA pre-treatment, in dictating the final properties of the SPD-processed alloy.

5.4.1 The Interplay of Pre-Treatment and SPD on Microstructure and Properties

The primary effect of SPD is the imposition of massive shear strains, which drives significant grain refinement in all samples, a well-documented outcome of such processes as reported by Snopiński et al. [80]. However, the efficiency of this refinement and, more importantly, the resulting mechanical response are profoundly influenced by the starting microstructure. The

LTA_300 samples, which possess a pre-fragmented Si network, consistently achieve the most refined grain structures. After one pass of TCAP, the LTA_300_1TCAP sample exhibits an average grain size of just 396 ± 71 nm (**Figure 96A**) qualifying as an ultrafine-grained (UFG) structure. This microstructural advantage translates into a remarkable mechanical performance. While the As-built and LTA_280 samples exhibit higher strength after a single TCAP pass, a notable divergence occurs in their ductility. After both ECAP and TCAP, the LTA_300-conditioned samples demonstrate consistent superior ductility, with failure strains exceeding 51% (**Tables 6 and 7**). In contrast, the As-built and LTA_280 samples, which enter the SPD process with a more continuous Si network, become relatively more brittle, fracturing at strains around 23-26% after ECAP.

This behavior reveals a crucial processing principle for heterostructured materials. During SPD, the intense shear strain acts upon the existing microstructure. In the As-built and LTA_280 samples, this strain forcibly breaks the remaining continuous or semi-continuous Si network into fragments. These newly created, hard fragments act as potent stress risers within a now heavily work-hardened and mechanically robust matrix, providing ideal sites for crack initiation and leading to premature failure. For the LTA_300 sample, however, the brittle phase is already stabilized in the form of fine, rounded particles before SPD is applied. The subsequent SPD process then primarily deforms and refines the ductile Al matrix around these stable particles. This allows the material to reap the benefits of UFG strengthening from grain refinement without introducing a new, detrimental failure mechanism [166], [168].

Therefore, the LTA_300 treatment is not merely a softening step but a critical enabling step. It strategically pre-conditions the microstructure by homogenizing the brittle phase, which is essential for achieving a desirable outcome from subsequent SPD. The combined processing route of LTA_300 followed by two passes of TCAP successfully produces a material with a high yield strength of 403 MPa and an exceptional failure strain of 51.3%. This outstanding combination of properties, which overcomes the classic strength-ductility paradox, is unachievable through any other processing route investigated in this work and highlights the necessity of this multi-stage, synergistic approach.

5.4.2 Kinematic Hardening and the Bauschinger Effect

The LUR compression tests provide direct, quantitative evidence of the kinematic hardening behavior of the alloy and its dependence on the microstructural state. Kinematic

hardening, which manifests macroscopically as the Bauschinger effect, describes the phenomenon where plastic deformation in one direction leads to a reduced yield strength upon load reversal. This effect is attributed to the development of long-range internal stresses, or back stresses, which are generated by the pile-up of dislocations at impenetrable obstacles [9], [169], [170].

The results from the LUR tests on the ECAP-processed samples (**Figure 77**) are particularly enlightening. The As-built_ECAP sample, which retains the most continuous Si network fragments, develops the highest back stress, reaching approximately 351 MPa. In contrast, the LTA_300_ECAP sample, with its dispersed Si particles, consistently exhibits the lowest back stress. A similar trend is observed after TCAP processing (**Figures 111 and 117**), where the As-built and LTA_280 conditions show significantly higher back stress than the LTA_300 condition. These results provide a clear link between the microstructural heterogeneity and the magnitude of kinematic hardening. The continuous Si network in the As-built and LTA_280 samples acts as a strong, long-range barrier. During forward loading, dislocations generated in the soft α-Al matrix pile up against this network, creating a potent back stress in the Al matrix and a corresponding forward stress in the Si phase (**Figure 1**). This internal stress field assists the motion of dislocations upon load reversal, lowering the reverse yield strength and producing a pronounced Bauschinger effect. When the network is fragmented into discrete particles, as in the LTA_300 condition, dislocation interaction is more localized. Dislocations are more likely to bypass particles via Orowan looping rather than forming extensive, long-range pile-ups. This results in lower internal back stress and, consequently, a reduced Bauschinger effect and less kinematic hardening [171].

This research successfully uses back stress measurements as a mechanical proxy to quantify the influence of the Si network's continuity. It demonstrates that for this alloy system, the hard Si network is the dominant source of the long-range internal stresses that drive kinematic hardening. This finding has significant implications for material design. For applications involving cyclic plastic deformation, such as in low-cycle fatigue scenarios, a microstructure that minimizes kinematic hardening (like that of the LTA_300-processed material) may be preferable to avoid the premature softening associated with the Bauschinger effect. Conversely, the high back stress generated in structures with continuous hard phases could be strategically harnessed to produce what is known as hetero-deformation induced (HDI) strengthening, a key feature of advanced heterostructured materials [9], [172], [173], [174].

5.5 Analysis of SPD Processing Parameters

The effectiveness of any SPD process is not only dependent on the material's initial state but also on the specific processing parameters employed, particularly deformation temperature and the number of deformation passes. This study evaluates these parameters to establish a robust processing window for PBF-LB/M AlSi10Mg.

5.5.1 Impact of High-Temperature ECAP

While applying SPD at elevated temperatures can lower processing forces and enhance material formability, the results from **Section 4.5** show that for PBF-LB/M AlSi10Mg, high-temperature ECAP (at 350 °C, 400 °C, and 450 °C) is fundamentally detrimental. This processing route leads to a substantial loss of strength that outweighs any potential benefits. The primary reason for this degradation is the activation of thermally-driven softening mechanisms that completely erase the unique and beneficial microstructure imparted by the PBF-LB/M process. At these elevated temperatures, which are well within the hot-working regime for aluminum alloys (typically > $0.5T_m$, where T_m is the melting temperature), diffusion kinetics are accelerated. This leads to two concurrent and deleterious microstructural changes. First, the fine eutectic Si network, and even the fragmented particles, undergo rapid coarsening via Ostwald ripening (**Figures 81-83**). The Si particles grow from an average size of 0.19 μm at 350 °C to 0.36 μm at 450 °C, drastically reducing their effectiveness as Orowan strengthening obstacles, consistent with similar observations in literature for other alloys [175], [176], [177].

Second, instead of the desired grain refinement, high-temperature ECAP promotes grain coarsening relative to the room-temperature ECAP condition (**Figure 84**). This occurs because the thermal energy allows dynamic recovery (DRV) and dynamic recrystallization (DRX) to become the dominant restoration mechanisms, overpowering the work hardening effect of the deformation. DRV facilitates the annihilation and rearrangement of dislocations into low-energy subgrains, which then have sufficient thermal energy to grow, preventing the accumulation of the high dislocation density required to form a stable UFG structure [178], [179], [180].

The combined effect of Si particle coarsening and grain coarsening results in a massive drop in mechanical properties. Hardness plummets to as low as 60.1 $HV_{0.1}$, and yield strength significantly drops to 141 MPa at 450°C (**Figures 86, 87**). This represents a strength reduction of over 70% compared to the as-built state and completely negates the purpose of using advanced

manufacturing and post-processing. This finding establishes a clear processing boundary: to leverage SPD for strengthening PBF-LB/M AlSi10Mg, the process must be conducted in the "cold" or "warm" working regime (e.g., < 200 °C), where strain-induced hardening and refinement dominate over thermally-induced softening. The LTA + cold/warm SPD route is thus validated as a superior strategy to a single hot SPD step.

5.5.2 A Comparative Assessment of SPD Processes and Passes

This study employed two different SPD techniques, ECAP and TCAP, allowing for a comparative assessment of their effectiveness. TCAP is designed to impart a more complex strain path, combining the simple shear of ECAP with a torsional component, expected to result in greater accumulated strain and more efficient grain refinement per pass [181], [182]. The results of this work support this expectation. A single pass of TCAP at 100 °C was sufficient to induce substantial fragmentation of the Si network and achieve a UFG structure in the LTA_300 sample (average grain area of 18.4 μm^2) (**Figure 95**). This level of refinement appears superior to that achieved with a single ECAP pass, confirming TCAP as a more potent SPD method for this alloy system.

The effect of multiple TCAP passes, however, reveals a complex relationship between continued strain hardening and thermal softening. The second TCAP pass, which required higher processing temperatures (150 °C for LTA samples, 250 °C for the As-built sample) to overcome the increased deformation resistance, led to a further reduction in grain size, particularly for the LTA_300 sample (**Figure 105**). Yet, this additional deformation did not uniformly translate to increased strength. The As-built_2TCAP and LTA_280_2TCAP samples were actually weaker and less hard than their single-pass counterparts (**Table 7, Figure 106**).

This counterintuitive result can be explained by the competing effects of strain hardening and thermal softening. For the As-built and LTA_280 samples, the higher temperatures used for the second pass (especially the 250 °C for the As-built sample) were sufficient to activate in-situ recovery and further Si network degradation, leading to a net softening effect that outweighed the benefits of the additional strain. In contrast, the LTA_300 microstructure, with its already stabilized, fragmented Si particles, proved more resistant to thermal degradation at 150 °C. It was therefore able to benefit more fully from the additional grain refinement and dislocation accumulation of the second pass, resulting in a slight increase in yield strength (from 392 MPa to 403 MPa) and a significant improvement in ductility (from 38.3% to 51.3% strain).

Chapter Six

Conclusions

This thesis has systematically investigated the optimization of microstructural heterogeneity in PBF-LB/M AlSi10Mg alloy through a multi-stage thermomechanical processing route, with the ultimate aim of overcoming the strength-ductility trade-off. By integrating advanced manufacturing with tailored heat treatments and severe plastic deformation, this work has elucidated the fundamental deformation mechanisms and established a clear pathway for producing a high-performance, lightweight structural material. The principal findings, their broader implications, and recommendations for future research are summarized below.

6.1 Principal Findings

The key conclusions drawn from this comprehensive investigation are as follows:

- Among the Al-Si-Mg alloys investigated, AlSi10Mg provides the optimal starting point for this work. Its near-eutectic composition ensures excellent processability and low porosity in PBF-LB/M, while its unique solidification kinetics result in the finest and most potent as-built cellular strengthening network compared to AlSi7Mg and AlSi12Mg.
- LTA is not merely a stress-relief step but a critical microstructural conditioning process. The LTA_300 treatment (300 °C for 30 minutes) effectively transforms the strengthening architecture from a continuous, brittle Si network to a dispersion of fine, spheroidized Si particles. This fragmentation formed the key to unlocking the material's ductility, making it an essential prerequisite for subsequent severe plastic deformation.
- The continuity of the Si cellular network is the primary factor governing strain hardening behavior. A continuous network (As-built condition) promotes high hetero-deformation induced (HDI) hardening via the generation of GNDs and significant back stress. A fragmented network (LTA_300 condition) minimizes back stress but allows for a much greater strain accommodation capacity through the extensive storage of SSDs, leading to superior uniform elongation.
- Severe plastic deformation is a powerful tool for grain refinement, but its success is critically dependent on the initial microstructure. Applying SPD to the as-built material with its continuous Si network leads to embrittlement. In contrast, applying SPD to the LTA_300-conditioned material, with its pre-fragmented and stabilized Si phase, allows for

the full benefits of UFG strengthening to be realized without introducing new failure mechanisms, resulting in a superior final strength-ductility combination.

- Processing via ECAP at elevated temperatures (≥350°C) is fundamentally detrimental to the properties of PBF-LB/M AlSi10Mg. Thermally activated softening mechanisms, including dynamic recovery, dynamic recrystallization, and significant Si particle coarsening, dominate over work hardening, leading to a catastrophic loss of strength and erasing the unique benefits of the initial additively manufactured microstructure.

6.2 Significance of Study

6.2.1 Scientific and Technological Impact

The findings of this research carry significant implications for both fundamental materials science and applied engineering. From a scientific perspective, this work provides a comprehensive, mechanism-based understanding of the complex interplay between processing, hierarchical microstructure, and mechanical behavior in a heterostructured additively manufactured alloy. By systematically controlling the morphology of the Si network, this study successfully decouples and quantifies the distinct contributions of GND-driven back-stress hardening and SSD-driven strain capacity. The direct measurement of back stress via LUR tests and its correlation with the continuity of the reinforcing phase offers a valuable dataset for the validation and refinement of advanced crystal plasticity and continuum damage mechanics models for heterogeneous materials. The elucidation of the failure mechanisms, particularly the embrittlement caused by SPD on unprepared microstructures versus the enhanced damage tolerance of pre-conditioned ones, provides a new paradigm for the design of thermomechanical processing routes for a wide range of composite and heterostructured materials.

From a technological standpoint, this research establishes a clear and validated manufacturing strategy for producing high-performance aluminum components that overcome the performance limitations of conventionally processed alloys. The demonstrated ability to achieve a yield strength over 400 MPa combined with ductility exceeding 50% represents a significant advancement for PBF-LB/M aluminum alloys, placing them in a competitive position with higher-strength alloys for lightweight structural applications. This optimized material could be deployed in demanding sectors such as aerospace and automotive, enabling the fabrication of lightweight, damage-tolerant, and fuel-efficient components like brackets, chassis elements, and other structural parts

that are currently made from heavier materials or more complex multi-material assemblies. The single-material solution offered by this processing route also simplifies end-of-life recycling, contributing to a more sustainable manufacturing lifecycle.

6.2.2 Economic Impact

The advancements in additive manufacturing proposed in this study have the potential to significantly reduce production costs and waste, leading to more economical manufacturing practices. Enhanced properties of AlSi10Mg components mean longer lifespans and reduced need for replacements, impacting the cost-efficiency of manufacturing processes in industries such as aerospace and automotive. The development of materials with improved performance can also open up new markets for high-strength, lightweight components, potentially leading to economic growth and increased competitiveness for companies adopting these technologies.

6.2.3 Environmental Impact

By optimizing the use of materials and enhancing the life cycle of manufactured components, this research directly contributes to environmental sustainability. Improved additive manufacturing processes decrease the carbon footprint associated with production by minimizing waste and energy consumption. Additionally, the use of lightweight materials contributes to greater fuel efficiency in automotive and aerospace applications, reducing emissions and promoting the use of sustainable technologies.

6.2.4 Social Impact

The societal benefits of this research are multifaceted, ranging from increased safety and performance of vehicles and aircraft to the promotion of green manufacturing practices. By improving the reliability and efficiency of structural components, this study also supports higher standards of safety in everyday applications, directly impacting public welfare. Furthermore, the dissemination of research findings through publications, workshops, and collaborations fosters an educated community that values innovation and sustainability in manufacturing.

6.3 Limitations and Recommendations for Future Work

Building upon the foundation established by this work, several avenues for future research are recommended to further advance the understanding and application of these materials, based on the limitations of this study.

- **Exploration of High-Temperature SPD Regimes** The study identified that high-temperature ECAP at temperatures greater than or equal to 350 °C was detrimental to the material's properties, leading to substantial strength loss due to thermally activated softening mechanisms like dynamic recovery, dynamic recrystallization, and significant Si particle coarsening. While this finding establishes a critical processing boundary, it suggests that a detailed understanding or exploration of optimal high-temperature SPD regimes that might avoid or mitigate such softening was not within the primary scope.
- **Development of Predictive Models**: The extensive quantitative data generated in this thesis on microstructural evolution (grain size, cell morphology, dislocation density) and mechanical response (hardening exponents, back stress) provides a rich dataset. This data should be used to develop and validate advanced, physically-based crystal plasticity finite element models (CPFEM) capable of predicting the mechanical behavior of these complex heterostructures, which would accelerate the design of new alloys and processes.
- **Investigation of Anisotropy**: This study focused on mechanical properties in a single orientation. SPD processes are known to induce strong crystallographic textures, which can lead to significant mechanical anisotropy. A thorough investigation of the anisotropic tensile, compressive, and fatigue properties of the TCAP-processed materials is necessary for their reliable application in components subjected to multi-axial stress states.
- **Application to other Alloy Systems**: The core principle established in this work, including the strategic pre-conditioning of a brittle phase prior to SPD of the ductile matrix, is a broadly applicable concept. Future research should explore applying this methodology to other important PBF-LB/M systems with inherent heterogeneity, such as Ti-6Al-4V (with its α/β lamellar structure) or various metal-matrix composites, to unlock their full performance potential.

References

[1] D. Mayer, T. Bein, H. Buff, B. Götz, O. Schwarzhaupt, and D. Spancken, "Enhanced lightweight design by composites–Results of the EU project ENLIGHT," *J. Reinf. Plast. Compos.*, vol. 37, no. 19, pp. 1217–1224, 2018.

[2] Z. Wang *et al.*, "Ultrastrong lightweight compositionally complex steels via dual-nanoprecipitation," *Sci. Adv.*, vol. 6, no. 46, p. eaba9543, 2020.

[3] E. Ma and X. Wu, "Tailoring heterogeneities in high-entropy alloys to promote strength–ductility synergy," *Nat. Commun.*, vol. 10, no. 1, p. 5623, 2019.

[4] X. Liu, H. Zhang, and K. Lu, "Strain-induced ultrahard and ultrastable nanolaminated structure in nickel," *Science*, vol. 342, no. 6156, pp. 337–340, 2013.

[5] X. Wu *et al.*, "Heterogeneous lamella structure unites ultrafine-grain strength with coarse-grain ductility," *Proc. Natl. Acad. Sci.*, vol. 112, no. 47, pp. 14501–14505, 2015.

[6] T. Fang, W. Li, N. Tao, and K. Lu, "Revealing extraordinary intrinsic tensile plasticity in gradient nano-grained copper," *Science*, vol. 331, no. 6024, pp. 1587–1590, 2011.

[7] C. Sawangrat, S. Kato, D. Orlov, and K. Ameyama, "Harmonic-structured copper: performance and proof of fabrication concept based on severe plastic deformation of powders," *J. Mater. Sci.*, vol. 49, pp. 6579–6585, 2014.

[8] M. Ashby, "The deformation of plastically non-homogeneous materials," *Philos. Mag. J. Theor. Exp. Appl. Phys.*, vol. 21, no. 170, pp. 399–424, 1970.

[9] Y. Zhu and X. Wu, "Perspective on hetero-deformation induced (HDI) hardening and back stress," *Mater. Res. Lett.*, vol. 7, no. 10, pp. 393–398, 2019.

[10] V. Manakari, G. Parande, and M. Gupta, "Selective laser melting of magnesium and magnesium alloy powders: a review," *Metals*, vol. 7, no. 1, p. 2, 2016.

[11] S. Liu *et al.*, "Influence of laser process parameters on the densification, microstructure, and mechanical properties of a selective laser melted AZ61 magnesium alloy," *J. Alloys Compd.*, vol. 808, p. 151160, 2019.

[12] H. Rao, S. Giet, K. Yang, X. Wu, and C. H. Davies, "The influence of processing parameters on aluminium alloy A357 manufactured by Selective Laser Melting," *Mater. Des.*, vol. 109, pp. 334–346, 2016.

[13] Y. Zhou, S. Wen, C. Wang, L. Duan, Q. Wei, and Y. Shi, "Effect of TiC content on the Al-15Si alloy processed by selective laser melting: Microstructure and mechanical properties," *Opt. Laser Technol.*, vol. 120, p. 105719, Dec. 2019, doi: 10.1016/j.optlastec.2019.105719.

[14] K. G. Prashanth *et al.*, "Microstructure and mechanical properties of Al–12Si produced by selective laser melting: Effect of heat treatment," *Mater. Sci. Eng. A*, vol. 590, pp. 153–160, 2014.

[15] A. G. Putra, A. Manaf, and A. Anawati, "Enhancing the Hardness of Mg-9Al-1Zn Cast Alloy by Solution Treatment," presented at the IOP Conference Series: Materials Science and Engineering, IOP Publishing, 2019, p. 012088.

[16] J. Delahaye, J. T. Tchuindjang, J. Lecomte-Beckers, O. Rigo, A. M. Habraken, and A. Mertens, "Influence of Si precipitates on fracture mechanisms of AlSi10Mg parts processed by Selective Laser Melting," *Acta Mater.*, vol. 175, pp. 160–170, Aug. 2019, doi: 10.1016/j.actamat.2019.06.013.

[17] T. Kimura and T. Nakamoto, "Microstructures and mechanical properties of A356 (AlSi7Mg0.3) aluminum alloy fabricated by selective laser melting," *Mater. Des.*, vol. 89, pp. 1294–1301, Jan. 2016, doi: 10.1016/j.matdes.2015.10.065.

[18] C.-L. Chen, A. Richter, and R. C. Thomson, "Mechanical properties of intermetallic phases in multi-component Al–Si alloys using nanoindentation," *Intermetallics*, vol. 17, no. 8, pp. 634–641, Aug. 2009, doi: 10.1016/j.intermet.2009.02.003.

[19] J. Fite, S. Eswarappa Prameela, J. A. Slotwinski, and T. P. Weihs, "Evolution of the microstructure and mechanical properties of additively manufactured AlSi10Mg during room temperature holds and low temperature aging," *Addit. Manuf.*, vol. 36, p. 101429, Dec. 2020, doi: 10.1016/j.addma.2020.101429.

[20] J. Fiocchi, A. Tuissi, P. Bassani, and C. A. Biffi, "Low temperature annealing dedicated to AlSi10Mg selective laser melting products," *J. Alloys Compd.*, vol. 695, pp. 3402–3409, Feb. 2017, doi: 10.1016/j.jallcom.2016.12.019.

[21] J. C. Pereira, E. Gil, L. Solaberrieta, M. San Sebastián, Y. Bilbao, and P. P. Rodríguez, "Comparison of AlSi7Mg0.6 alloy obtained by selective laser melting and investment casting processes: Microstructure and mechanical properties in as-built/as-cast and heat-treated conditions," *Mater. Sci. Eng. A*, vol. 778, p. 139124, Mar. 2020, doi: 10.1016/j.msea.2020.139124.

[22] M. Wang, B. Song, Q. Wei, and Y. Shi, "Improved mechanical properties of AlSi7Mg/nano-SiCp composites fabricated by selective laser melting," *J. Alloys Compd.*, vol. 810, p. 151926, Nov. 2019, doi: 10.1016/j.jallcom.2019.151926.

[23] N. T. Aboulkhair, I. Maskery, C. Tuck, I. Ashcroft, and N. M. Everitt, "The microstructure and mechanical properties of selectively laser melted AlSi10Mg: The effect of a conventional T6-like heat treatment," *Mater. Sci. Eng. A*, vol. 667, pp. 139–146, 2016.

[24] G. Schaffer, S. Huo, J. Drennan, and G. Auchterlonie, "The effect of trace elements on the sintering of an Al–Zn–Mg–Cu alloy," *Acta Mater.*, vol. 49, no. 14, pp. 2671–2678, 2001.

[25] Y. Wei *et al.*, "Evading the strength–ductility trade-off dilemma in steel through gradient hierarchical nanotwins," *Nat. Commun.*, vol. 5, no. 1, p. 3580, 2014.

[26] U. Rocks and H. Mecking, "Physics and phenomenology of strain hardening: the FCC case," *Prog. Mater. Sci.*, vol. 48, no. 3, pp. 171–273, 2003.

[27] R. O. Ritchie, "The conflicts between strength and toughness," *Nat. Mater.*, vol. 10, no. 11, pp. 817–822, 2011.

[28] C. Tan *et al.*, "Review on field assisted metal additive manufacturing," *Int. J. Mach. Tools Manuf.*, vol. 189, p. 104032, Jun. 2023, doi: 10.1016/j.ijmachtools.2023.104032.

[29] N. Khan and A. Riccio, "A systematic review of design for additive manufacturing of aerospace lattice structures: Current trends and future directions," *Prog. Aerosp. Sci.*, vol. 149, p. 101021, Aug. 2024, doi: 10.1016/j.paerosci.2024.101021.

[30] N. Limbasiya, A. Jain, H. Soni, V. Wankhede, G. Krolczyk, and P. Sahlot, "A comprehensive review on the effect of process parameters and post-process treatments on microstructure and mechanical properties of selective laser melting of AlSi10Mg," *J. Mater. Res. Technol.*, vol. 21, pp. 1141–1176, Nov. 2022, doi: 10.1016/j.jmrt.2022.09.092.

[31] I. Gibson *et al.*, "Powder bed fusion," *Addit. Manuf. Technol.*, pp. 125–170, 2021.

[32] D. Dev Singh, T. Mahender, and A. Raji Reddy, "Powder bed fusion process: A brief review," *2nd Int. Conf. Manuf. Mater. Sci. Eng.*, vol. 46, pp. 350–355, Jan. 2021, doi: 10.1016/j.matpr.2020.08.415.

[33] G. Liu *et al.*, "Additive manufacturing of structural materials," *Mater. Sci. Eng. R Rep.*, vol. 145, p. 100596, Jul. 2021, doi: 10.1016/j.mser.2020.100596.

[34] E. Rezvani Ghomi, F. Khosravi, R. E. Neisiany, S. Singh, and S. Ramakrishna, "Future of additive manufacturing in healthcare," *Curr. Opin. Biomed. Eng.*, vol. 17, p. 100255, Mar. 2021, doi: 10.1016/j.cobme.2020.100255.

[35] A. H. Alami *et al.*, "Additive manufacturing in the aerospace and automotive industries: Recent trends and role in achieving sustainable development goals," *Ain Shams Eng. J.*, vol. 14, no. 11, p. 102516, Nov. 2023, doi: 10.1016/j.asej.2023.102516.

[36] J. C. Vasco, "Chapter 16 - Additive manufacturing for the automotive industry," in *Additive Manufacturing*, J. Pou, A. Riveiro, and J. P. Davim, Eds., Elsevier, 2021, pp. 505–530. doi: 10.1016/B978-0-12-818411-0.00010-0.

[37] M. Khorasani, A. Ghasemi, B. Rolfe, and I. Gibson, "Additive manufacturing a powerful tool for the aerospace industry," *Rapid Prototyp. J.*, vol. 28, no. 1, pp. 87–100, 2022.

[38] A. Vafadar, F. Guzzomi, A. Rassau, and K. Hayward, "Advances in metal additive manufacturing: a review of common processes, industrial applications, and current challenges," *Appl. Sci.*, vol. 11, no. 3, p. 1213, 2021.

[39] P. Durai Murugan *et al.*, "A current state of metal additive manufacturing methods: A review," *Int. Conf. Virtual Conf. Technol. Adv. Mech. Eng.*, vol. 59, pp. 1277–1283, Jan. 2022, doi: 10.1016/j.matpr.2021.11.503.

[40] W. Abd-Elaziem *et al.*, "On the current research progress of metallic materials fabricated by laser powder bed fusion process: a review," *J. Mater. Res. Technol.*, vol. 20, pp. 681–707, Sep. 2022, doi: 10.1016/j.jmrt.2022.07.085.

[41] S. R. Narasimharaju *et al.*, "A comprehensive review on laser powder bed fusion of steels: Processing, microstructure, defects and control methods, mechanical properties, current challenges and future trends," *J. Manuf. Process.*, vol. 75, pp. 375–414, Mar. 2022, doi: 10.1016/j.jmapro.2021.12.033.

[42] M. Armstrong, H. Mehrabi, and N. Naveed, "An overview of modern metal additive manufacturing technology," *J. Manuf. Process.*, vol. 84, pp. 1001–1029, Dec. 2022, doi: 10.1016/j.jmapro.2022.10.060.

[43] I. Bitharas, N. Parab, C. Zhao, T. Sun, A. Rollett, and A. Moore, "The interplay between vapour, liquid, and solid phases in laser powder bed fusion," *Nat. Commun.*, vol. 13, no. 1, p. 2959, 2022.

[44] W. Guo *et al.*, "Effect of laser scanning speed on the microstructure, phase transformation and mechanical property of NiTi alloys fabricated by LPBF," *Mater. Des.*, vol. 215, p. 110460, Mar. 2022, doi: 10.1016/j.matdes.2022.110460.

[45] S. Cao, Y. Zou, C. V. S. Lim, and X. Wu, "Review of laser powder bed fusion (LPBF) fabricated Ti-6Al-4V: process, post-process treatment, microstructure, and property," *Light Adv. Manuf.*, vol. 2, no. 3, pp. 313–332, 2021.

[46] N. Ahmed, I. Barsoum, G. Haidemenopoulos, and R. K. A. Al-Rub, "Process parameter selection and optimization of laser powder bed fusion for 316L stainless steel: A review," *J. Manuf. Process.*, vol. 75, pp. 415–434, Mar. 2022, doi: 10.1016/j.jmapro.2021.12.064.

[47] S. Chowdhury *et al.*, "Laser powder bed fusion: a state-of-the-art review of the technology, materials, properties & defects, and numerical modelling," *J. Mater. Res. Technol.*, vol. 20, pp. 2109–2172, 2022.

[48] H. Eskandari Sabzi and P. E. Rivera-Díaz-del-Castillo, "Defect prevention in selective laser melting components: compositional and process effects," *Materials*, vol. 12, no. 22, p. 3791, 2019.

[49] X. Yang, Y. Ge, J. Lehtonen, and S.-P. Hannula, "Hierarchical microstructure of laser powder bed fusion produced face-centered-cubic-structured equiatomic CrFeNiMn multicomponent alloy," *Materials*, vol. 13, no. 20, p. 4498, 2020.
[50] Z. Xiao, W. Yu, H. Fu, Y. Deng, Y. Wu, and H. Zheng, "Recent progress on microstructure manipulation of aluminium alloys manufactured via laser powder bed fusion," *Virtual Phys. Prototyp.*, vol. 18, no. 1, p. e2125880, 2023.
[51] D. Guillen, S. Wahlquist, and A. Ali, "Critical review of LPBF metal print defects detection: roles of selective sensing technology," *Appl. Sci.*, vol. 14, no. 15, p. 6718, 2024.
[52] L. Zhao *et al.*, "Review on the correlation between microstructure and mechanical performance for laser powder bed fusion AlSi10Mg," *Addit. Manuf.*, vol. 56, p. 102914, Aug. 2022, doi: 10.1016/j.addma.2022.102914.
[53] T. Maeshima, K. Oh-Ishi, and H. Kadoura, "Microstructural evolution and hardening phenomenon caused by aging of AlSi10Mg alloy by laser powder bed fusion," *Heliyon*, vol. 10, no. 6, 2024.
[54] W. H. Kan *et al.*, "A critical review on the effects of process-induced porosity on the mechanical properties of alloys fabricated by laser powder bed fusion," *J. Mater. Sci.*, vol. 57, no. 21, pp. 9818–9865, 2022.
[55] S. M. H. Hojjatzadeh *et al.*, "Pore elimination mechanisms during 3D printing of metals," *Nat. Commun.*, vol. 10, no. 1, p. 3088, 2019.
[56] S. Wang *et al.*, "Role of porosity defects in metal 3D printing: Formation mechanisms, impacts on properties and mitigation strategies," *Mater. Today*, vol. 59, pp. 133–160, 2022.
[57] N. Sanaei and A. Fatemi, "Defects in additive manufactured metals and their effect on fatigue performance: A state-of-the-art review," *Prog. Mater. Sci.*, vol. 117, p. 100724, 2021.
[58] A. Du Plessis, "Effects of process parameters on porosity in laser powder bed fusion revealed by X-ray tomography," *Addit. Manuf.*, vol. 30, p. 100871, 2019.
[59] G. Kasperovich, J. Haubrich, J. Gussone, and G. Requena, "Correlation between porosity and processing parameters in TiAl6V4 produced by selective laser melting," *Mater. Des.*, vol. 105, pp. 160–170, 2016.
[60] Q. C. Johnson, C. M. Laursen, A. D. Spear, J. D. Carroll, and P. J. Noell, "Analysis of the interdependent relationship between porosity, deformation, and crack growth during compression loading of LPBF AlSi10Mg," *Mater. Sci. Eng. A*, vol. 852, p. 143640, Sep. 2022, doi: 10.1016/j.msea.2022.143640.
[61] Z. Wu *et al.*, "The effect of defect population on the anisotropic fatigue resistance of AlSi10Mg alloy fabricated by laser powder bed fusion," *Int. J. Fatigue*, vol. 151, p. 106317, 2021.
[62] T. Ronneberg, C. M. Davies, and P. A. Hooper, "Revealing relationships between porosity, microstructure and mechanical properties of laser powder bed fusion 316L stainless steel through heat treatment," *Mater. Des.*, vol. 189, p. 108481, 2020.
[63] Z. Wu, S. Wu, X. Gao, Y. Lin, Y. Xue, and P. J. Withers, "The role of internal defects on anisotropic tensile failure of L-PBF AlSi10Mg alloys," *Sci. Rep.*, vol. 13, no. 1, p. 14681, Sep. 2023, doi: 10.1038/s41598-023-39948-z.
[64] J. Fiocchi, A. Tuissi, and C. A. Biffi, "Heat treatment of aluminium alloys produced by laser powder bed fusion: A review," *Mater. Des.*, vol. 204, p. 109651, Jun. 2021, doi: 10.1016/j.matdes.2021.109651.

[65] T. Mukherjee, H. L. Wei, A. De, and T. DebRoy, "Heat and fluid flow in additive manufacturing – Part II: Powder bed fusion of stainless steel, and titanium, nickel and aluminum base alloys," *Comput. Mater. Sci.*, vol. 150, pp. 369–380, Jul. 2018, doi: 10.1016/j.commatsci.2018.04.027.

[66] J. P. Oliveira, A. LaLonde, and J. Ma, "Processing parameters in laser powder bed fusion metal additive manufacturing," *Mater. Des.*, vol. 193, p. 108762, 2020.

[67] S. Liu, H. Zhu, G. Peng, J. Yin, and X. Zeng, "Microstructure prediction of selective laser melting AlSi10Mg using finite element analysis," *Mater. Des.*, vol. 142, pp. 319–328, Mar. 2018, doi: 10.1016/j.matdes.2018.01.022.

[68] J. Li, X. Cheng, Z. Li, X. Zong, S.-Q. Zhang, and H.-M. Wang, "Improving the mechanical properties of Al-5Si-1Cu-Mg aluminum alloy produced by laser additive manufacturing with post-process heat treatments," *Mater. Sci. Eng. A*, vol. 735, pp. 408–417, Sep. 2018, doi: 10.1016/j.msea.2018.08.074.

[69] X. Zhang, X. Zhang, W. Liu, A. Jiang, and Y. Long, "Towards Understanding Formation Mechanism of Cellular Structures in Laser Powder Bed Fused AlSi10Mg," *Materials*, vol. 17, no. 9, p. 2121, 2024.

[70] M. S. Bisht, V. Gaur, and I. Singh, "A Study of Strengthening and Hardening Micro-mechanisms in Additively Built AlSi10Mg Using Crystal Plasticity Simulations," *Met. Mater. Int.*, pp. 1–20, 2025.

[71] J. Liu and Y. Shi, "SiCp/AlSi10Mg composites with simultaneously enhanced tensile strength and ductility fabricated by laser powder bed fusion additive manufacturing," *Mater. Sci. Eng. A*, vol. 888, p. 145839, Nov. 2023, doi: 10.1016/j.msea.2023.145839.

[72] H. Chen *et al.*, "Phase-separation induced dislocation-network cellular structures in Ti-Zr-Nb-Mo-Ta high-entropy alloy processed by laser powder bed fusion," *Addit. Manuf.*, vol. 102, p. 104737, Mar. 2025, doi: 10.1016/j.addma.2025.104737.

[73] J. G. Santos Macías, T. Douillard, L. Zhao, E. Maire, G. Pyka, and A. Simar, "Influence on microstructure, strength and ductility of build platform temperature during laser powder bed fusion of AlSi10Mg," *Acta Mater.*, vol. 201, pp. 231–243, Dec. 2020, doi: 10.1016/j.actamat.2020.10.001.

[74] H. Hyer *et al.*, "Understanding the laser powder bed fusion of AlSi10Mg alloy," *Metallogr. Microstruct. Anal.*, vol. 9, pp. 484–502, 2020.

[75] H. Eskandari Sabzi and P. E. J. Rivera-Díaz-del-Castillo, "Composition and process parameter dependence of yield strength in laser powder bed fusion alloys," *Mater. Des.*, vol. 195, p. 109024, Oct. 2020, doi: 10.1016/j.matdes.2020.109024.

[76] Z. Li, Z. Li, Z. Tan, D.-B. Xiong, and Q. Guo, "Stress relaxation and the cellular structure-dependence of plastic deformation in additively manufactured AlSi10Mg alloys," *Int. J. Plast.*, vol. 127, p. 102640, 2020.

[77] M. M. Rohoman and C. Zhou, "Crystal Plasticity Modeling of Dislocation Density Evolution in Cellular Dislocation Structures," *Metals*, vol. 15, no. 4, p. 419, 2025.

[78] B. Chen *et al.*, "Strength and strain hardening of a selective laser melted AlSi10Mg alloy," *Scr. Mater.*, vol. 141, pp. 45–49, 2017.

[79] P. Snopiński, M. Kotoul, J. Petruška, S. Rusz, K. Żaba, and O. Hilšer, "Revealing the strengthening contribution of stacking faults, dislocations and grain boundaries in severely deformed LPBF AlSi10Mg alloy," *Sci. Rep.*, vol. 13, no. 1, p. 16166, 2023.

[80] P. Snopiński, K. Matus, and O. Hilšer, "Investigation of the Effects of Various Severe Plastic Deformation Techniques on the Microstructure of Laser Powder Bed Fusion AlSi10Mg Alloy," *Materials*, vol. 16, no. 23, p. 7418, 2023.
[81] S. Shi *et al.*, "Achieving superior strength-plasticity performance in laser powder bed fusion of AlSi10Mg via high-speed scanning remelting," *Mater. Res. Lett.*, vol. 12, no. 9, pp. 668–677, 2024.
[82] A. Salandari-Rabori and V. Fallah, "Heterogeneity of deformation, shear band formation and work hardening behavior of as-printed AlSi10Mg via laser powder bed fusion," *Mater. Sci. Eng. A*, vol. 866, p. 144698, Feb. 2023, doi: 10.1016/j.msea.2023.144698.
[83] A. Salandari-Rabori, B. J. Diak, and V. Fallah, "Dislocation-obstacle interaction evolution in rate dependent plasticity of AlSi10Mg as-built microstructure by laser powder bed fusion," *Mater. Sci. Eng. A*, vol. 857, p. 144043, Nov. 2022, doi: 10.1016/j.msea.2022.144043.
[84] A. Salandari Rabori and V. Fallah, "Room temperature strain rate sensitivity of as-built 3D printed AlSi10Mg by laser powder bed fusion," *Mater. Lett.*, vol. 320, p. 132395, Aug. 2022, doi: 10.1016/j.matlet.2022.132395.
[85] P. Snopiński, "Electron microscopy study of structural defects formed in additively manufactured AlSi10Mg alloy processed by equal channel angular pressing," *Symmetry*, vol. 15, no. 4, p. 860, 2023.
[86] S. Megahed, J. Bühring, T. Duffe, A. Bach, K.-U. Schröder, and J. H. Schleifenbaum, "Effect of heat treatment on ductility and precipitation size of additively manufactured alsi10mg," *Metals*, vol. 12, no. 8, p. 1311, 2022.
[87] M. Duesbery and G. Richardson, "The dislocation core in crystalline materials," *Crit. Rev. Solid State Mater. Sci.*, vol. 17, no. 1, pp. 1–46, 1991.
[88] W. D. Callister Jr and D. G. Rethwisch, *Materials science and engineering: an introduction*. John wiley & sons, 2020.
[89] C. R. Weinberger, B. L. Boyce, and C. C. Battaile, "Slip planes in bcc transition metals," *Int. Mater. Rev.*, vol. 58, no. 5, pp. 296–314, 2013.
[90] V. Celli and N. Flytzanis, "Motion of a screw dislocation in a crystal," *J. Appl. Phys.*, vol. 41, no. 11, pp. 4443–4447, 1970.
[91] M. R. Fellinger, A. M. Z. Tan, L. G. Hector Jr, and D. R. Trinkle, "Geometries of edge and mixed dislocations in bcc Fe from first-principles calculations," *Phys. Rev. Mater.*, vol. 2, no. 11, p. 113605, 2018.
[92] H. Pan, Y. He, and X. Zhang, "Interactions between dislocations and boundaries during deformation," *Materials*, vol. 14, no. 4, p. 1012, 2021.
[93] L. Priester, "'Dislocation–interface' interaction—stress accommodation processes at interfaces," *Mater. Sci. Eng. A*, vol. 309, pp. 430–439, 2001.
[94] C. Liu, Y. Wang, Y. Zhang, L.-C. Zhang, and L. Wang, "Deformation mechanisms of additively manufactured TiNbTaZrMo refractory high-entropy alloy: The role of cellular structure," *Int. J. Plast.*, vol. 173, p. 103884, Feb. 2024, doi: 10.1016/j.ijplas.2024.103884.
[95] X. X. Zhang *et al.*, "Evolution of microscopic strains, stresses, and dislocation density during in-situ tensile loading of additively manufactured AlSi10Mg alloy," *Int. J. Plast.*, vol. 139, p. 102946, Apr. 2021, doi: 10.1016/j.ijplas.2021.102946.
[96] X. Zhang *et al.*, "Quantifying internal strains, stresses, and dislocation density in additively manufactured AlSi10Mg during loading-unloading-reloading deformation," *Mater. Des.*, vol. 198, p. 109339, 2021.

[97] X. Liu, C. Zhao, X. Zhou, Z. Shen, and W. Liu, "Microstructure of selective laser melted AlSi10Mg alloy," *Mater. Des.*, vol. 168, p. 107677, Apr. 2019, doi: 10.1016/j.matdes.2019.107677.

[98] X. Zhu, Y. Ma, H. Wu, M. Li, and X. Lu, "In-situ tensile testing of fracture and strain in a selective laser melted AlSi10Mg alloy," *Heliyon*, vol. 10, no. 14, p. e34137, Jul. 2024, doi: 10.1016/j.heliyon.2024.e34137.

[99] P. Snopiński and O. Hilšer, "Mechanism of Grain Refinement in 3D-Printed AlSi10Mg Alloy Subjected to Severe Plastic Deformation," *Materials*, vol. 17, no. 16, p. 4098, 2024.

[100] H. Chen, S. Patel, M. Vlasea, and Y. Zou, "Enhanced tensile ductility of an additively manufactured AlSi10Mg alloy by reducing the density of melt pool boundaries," *Scr. Mater.*, vol. 221, p. 114954, Dec. 2022, doi: 10.1016/j.scriptamat.2022.114954.

[101] M. J. Paul *et al.*, "Fracture resistance of AlSi10Mg fabricated by laser powder bed fusion," *Acta Mater.*, vol. 211, p. 116869, Jun. 2021, doi: 10.1016/j.actamat.2021.116869.

[102] Q. Liu *et al.*, "Machine-learning assisted laser powder bed fusion process optimization for AlSi10Mg: New microstructure description indices and fracture mechanisms," *Acta Mater.*, vol. 201, pp. 316–328, Dec. 2020, doi: 10.1016/j.actamat.2020.10.010.

[103] C. Paoletti, E. Cerri, E. Ghio, E. Santecchia, M. Cabibbo, and S. Spigarelli, "Effect of low-temperature annealing on creep properties of AlSi10Mg alloy produced by additive manufacturing: experiments and modeling," *Metals*, vol. 11, no. 2, p. 179, 2021.

[104] P. Snopiński, A. N. S. Appiah, O. Hilšer, and M. Kotoul, "Investigation of Microstructure and Mechanical Properties of SLM-Fabricated AlSi10Mg Alloy Post-Processed Using Equal Channel Angular Pressing (ECAP)," *Materials*, vol. 15, no. 22, p. 7940, 2022.

[105] P. J. Konijnenberg, S. Zaefferer, and D. Raabe, "Assessment of geometrically necessary dislocation levels derived by 3D EBSD," *Acta Mater.*, vol. 99, pp. 402–414, Oct. 2015, doi: 10.1016/j.actamat.2015.06.051.

[106] H. Gao and Y. Huang, "Geometrically necessary dislocation and size-dependent plasticity," *Scr. Mater.*, vol. 48, no. 2, pp. 113–118, Jan. 2003, doi: 10.1016/S1359-6462(02)00329-9.

[107] D.-K. Kim, W. Woo, J.-H. Hwang, K. An, and S.-H. Choi, "Stress partitioning behavior of an AlSi10Mg alloy produced by selective laser melting during tensile deformation using in situ neutron diffraction," *J. Alloys Compd.*, vol. 686, pp. 281–286, Nov. 2016, doi: 10.1016/j.jallcom.2016.06.011.

[108] K. Jamali Dogahe *et al.*, "Multicale Study of the Fatigue Life of AlSi10Mg Material Produced by Laser Powder Bed Fusion (LPBF) Method: Experimental and Computational," *Fatigue Fract. Eng. Mater. Struct.*, vol. 48, no. 5, pp. 2290–2308, 2025.

[109] X. X. Zhang *et al.*, "Strain hardening behavior of additively manufactured and annealed AlSi3.5Mg2.5 alloy," *J. Alloys Compd.*, vol. 898, p. 162890, Mar. 2022, doi: 10.1016/j.jallcom.2021.162890.

[110] H. E. Sabzi *et al.*, "Grain refinement in laser powder bed fusion: The influence of dynamic recrystallization and recovery," *Mater. Des.*, vol. 196, p. 109181, Nov. 2020, doi: 10.1016/j.matdes.2020.109181.

[111]H. Proudhon, W. J. Poole, X. Wang, and Y. Brechet, "The role of internal stresses on the plastic deformation of the Al–Mg–Si–Cu alloy AA6111," *Philos. Mag.*, vol. 88, no. 5, pp. 621–640, 2008.

[112] P. Withers, W. Stobbs, and O. Pedersen, "The application of the Eshelby method of internal stress determination to short fibre metal matrix composites," *Acta Metall.*, vol. 37, no. 11, pp. 3061–3084, 1989.

[113] Z. Wang, X. Lin, N. Kang, Y. Hu, J. Chen, and W. Huang, "Strength-ductility synergy of selective laser melted Al-Mg-Sc-Zr alloy with a heterogeneous grain structure," *Addit. Manuf.*, vol. 34, p. 101260, Aug. 2020, doi: 10.1016/j.addma.2020.101260.

[114] S. Harjo, S. Kubota, W. Gong, T. Kawasaki, and S. Gao, "Neutron diffraction monitoring of ductile cast iron under cyclic tension–compression," *Acta Mater.*, vol. 196, pp. 584–594, Sep. 2020, doi: 10.1016/j.actamat.2020.07.016.

[115] A. Deschamps, B. Decreus, F. De Geuser, T. Dorin, and M. Weyland, "The influence of precipitation on plastic deformation of Al–Cu–Li alloys," *Acta Mater.*, vol. 61, no. 11, pp. 4010–4021, Jun. 2013, doi: 10.1016/j.actamat.2013.03.015.

[116] F. Chu *et al.*, "Improved Ductility by Reducing Powder Size in Laser Powder Bed Fusion of AlSi10Mg," *Addit. Manuf. Front.*, vol. 3, no. 1, p. 200122, Mar. 2024, doi: 10.1016/j.amf.2024.200122.

[117] Z. H. Xiong, S. L. Liu, S. F. Li, Y. Shi, Y. F. Yang, and R. D. K. Misra, "Role of melt pool boundary condition in determining the mechanical properties of selective laser melting AlSi10Mg alloy," *Mater. Sci. Eng. A*, vol. 740–741, pp. 148–156, Jan. 2019, doi: 10.1016/j.msea.2018.10.083.

[118] H. E. Sabzi, *Alloy and microstructure design for additive manufacturing*. Lancaster University (United Kingdom), 2022.

[119] P. Snopiński and K. Matus, "Characterisation of Microstructure and Special Grain Boundaries in LPBF AlSi10Mg Alloy Subjected to the KoBo Extrusion Process," *Symmetry*, vol. 15, no. 9, p. 1634, 2023.

[120] H. E. Sabzi, X.-H. Li, C. Zhang, H. Fu, D. San-Martín, and P. E. J. Rivera-Díaz-del-Castillo, "Deformation twinning-induced dynamic recrystallization during laser powder bed fusion," *Scr. Mater.*, vol. 207, p. 114307, Jan. 2022, doi: 10.1016/j.scriptamat.2021.114307.

[121] S. M. Yusuf, M. Hoegden, and N. Gao, "Effect of sample orientation on the microstructure and microhardness of additively manufactured AlSi10Mg processed by high-pressure torsion," *Int. J. Adv. Manuf. Technol.*, vol. 106, pp. 4321–4337, 2020.

[122] P. Snopiński, K. Matus, M. Łagoda, A. N. S. Appiah, and J. Hajnyš, "Engineering an ultra-fine grained microstructure, twins and stacking faults in PBF-LB/M Al-Si alloy via KoBo extrusion method," *J. Alloys Compd.*, vol. 970, p. 172576, Jan. 2024, doi: 10.1016/j.jallcom.2023.172576.

[123] P. Snopiński, A. Woźniak, and M. Pagáč, "Microstructural Evolution, Hardness, and Strengthening Mechanisms in SLM AlSi10Mg Alloy Subjected to Equal-Channel Angular Pressing (ECAP)," *Materials*, vol. 14, no. 24, p. 7598, 2021.

[124] E. Ghio and E. Cerri, "Work hardening of heat-treated alsi10mg alloy manufactured by single and double laser selective laser melting: Effects of layer thickness and hatch spacing," *Materials*, vol. 14, no. 17, p. 4901, 2021.

[125] S. Yu *et al.*, "Heterogeneous microstructure and mechanical behaviour of Al-8.3 Fe-1.3 V-1.8 Si alloy produced by laser powder bed fusion," *Virtual Phys. Prototyp.*, vol. 18, no. 1, p. e2155197, 2023.

[126] K. Ma *et al.*, "Mechanical behavior and strengthening mechanisms in ultrafine grain precipitation-strengthened aluminum alloy," *Acta Mater.*, vol. 62, pp. 141–155, Jan. 2014, doi: 10.1016/j.actamat.2013.09.042.

[127] P. Van Cauwenbergh *et al.*, "Unravelling the multi-scale structure–property relationship of laser powder bed fusion processed and heat-treated AlSi10Mg," *Sci. Rep.*, vol. 11, no. 1, p. 6423, Mar. 2021, doi: 10.1038/s41598-021-85047-2.

[128] H. Qin, Q. Dong, V. Fallah, and M. R. Daymond, "Rapid solidification and non-equilibrium phase constitution in laser powder bed fusion (LPBF) of AlSi10Mg alloy: analysis of nano-precipitates, eutectic phases, and hardness evolution," *Metall. Mater. Trans. A*, vol. 51, pp. 448–466, 2020.

[129] R. Montanari and A. Varone, "Processing–Structure–Property Relationships in Metals," *Metals*, vol. 9, no. 8, p. 907, 2019.

[130] D. P. Cann, "Fundamentals of Materials Science: The Microstructure-Property Relationship Using Metals as Model Systems, by Eric J. Mittemeijer, Springer Nature Switzerland AG 2021," *J. Mater. Sci.*, vol. 57, no. 14, pp. 7127–7130, 2022.

[131] M. Albu, R. Krisper, J. Lammer, G. Kothleitner, J. Fiocchi, and P. Bassani, "Microstructure evolution during in-situ heating of AlSi10Mg alloy powders and additive manufactured parts," *Addit. Manuf.*, vol. 36, p. 101605, 2020.

[132] P. Snopiński, K. Matus, F. Tatiček, and S. Rusz, "Overcoming the strength-ductility trade-off in additively manufactured AlSi10Mg alloy by ECAP processing," *J. Alloys Compd.*, p. 165817, 2022.

[133] C. Xu, M. Furukawa, Z. Horita, and T. G. Langdon, "Using ECAP to achieve grain refinement, precipitate fragmentation and high strain rate superplasticity in a spray-cast aluminum alloy," *Acta Mater.*, vol. 51, no. 20, pp. 6139–6149, 2003.

[134] P. Snopiński, T. Tański, K. Matus, and S. Rusz, "Microstructure, grain refinement and hardness of Al-3% Mg aluminium alloy processed by ECAP with helical die," *Arch. Civ. Mech. Eng.*, vol. 19, no. 2, pp. 287–296, 2019.

[135] A. S. Nivarthi, "Multiscale modeling and characterization of additively manufactured materials," 2024.

[136] G. Sander *et al.*, "Corrosion of additively manufactured alloys: a review," *Corrosion*, vol. 74, no. 12, pp. 1318–1350, 2018.

[137] V. Romanova *et al.*, "Multiscale deformation-induced surface pattern in 3D-printed AlSi10Mg under uniaxial compression," *Mater. Sci. Eng. A*, vol. 923, p. 147684, Feb. 2025, doi: 10.1016/j.msea.2024.147684.

[138] J. Mei *et al.*, "Improving the comprehensive mechanical property of the AlSi10Mg alloy via parameter adaptation of selective laser melting and heat treatment," *J. Alloys Compd.*, vol. 981, p. 173623, Apr. 2024, doi: 10.1016/j.jallcom.2024.173623.

[139] H. Chen, P. Liu, X. Ren, and A. A. Volinsky, "Fatigue and corrosion fatigue performance of selective laser melted AlSi10Mg and die cast A360 aluminum alloys," *Corros. Sci.*, vol. 245, p. 112711, Apr. 2025, doi: 10.1016/j.corsci.2025.112711.

[140] S. Wang *et al.*, "Preparation of porous anorthite-spinel composite ceramics with spherical pores via direct foaming method: Role of fused magnesia as pore structure stabilizer," *Ceram. Int.*, May 2025, doi: 10.1016/j.ceramint.2025.05.300.

[141] M. Bartošák *et al.*, "Low-cycle fatigue of laser powder bed fusion-processed AlSi10Mg using recycled powder: Experiments and machine learning-assisted lifetime prediction," *Mater. Des.*, vol. 253, p. 113926, May 2025, doi: 10.1016/j.matdes.2025.113926.

[142] E. O. Olakanmi, "Selective laser sintering/melting (SLS/SLM) of pure Al, Al–Mg, and Al–Si powders: Effect of processing conditions and powder properties," *J. Mater. Process.*

Technol., vol. 213, no. 8, pp. 1387–1405, Aug. 2013, doi: 10.1016/j.jmatprotec.2013.03.009.

[143] J. Zhang *et al.*, "Ultrauniform, strong, and ductile 3D-printed titanium alloy through bifunctional alloy design," *Science*, vol. 383, no. 6683, pp. 639–645, 2024.

[144] R. F. Fernandes, J. S. Jesus, R. Branco, L. P. Borrego, J. D. Costa, and J. A. M. Ferreira, "Effect of low-temperature stress relieving heat treatments on fatigue behaviour and failure mechanisms of L-PBF AlSi10Mg aluminium alloy," *Eng. Fail. Anal.*, vol. 169, p. 109210, Mar. 2025, doi: 10.1016/j.engfailanal.2024.109210.

[145] N. Jeyaprakash, S. Q. Moinuddin, K. Alnamasi, and A. Alsharif, "Effect of post-heat treatment cooling strategies on Si morphology and nano-mechanical behavior of additively manufactured AlSi10Mg alloy," *J. Mater. Res. Technol.*, vol. 36, pp. 8308–8324, May 2025, doi: 10.1016/j.jmrt.2025.05.046.

[146] R. Ramesh, S. Gairola, R. Jayaganthan, and M. Kamaraj, "Effects of post-processing on the microstructural evolution and mechanical behaviour of an additively manufactured AlSi10Mg alloy," *J. Mater. Res. Technol.*, vol. 34, pp. 2802–2813, Jan. 2025, doi: 10.1016/j.jmrt.2024.12.248.

[147] N. Tabatabaei, A. Zarei-Hanzaki, A. Moshiri, and H. R. Abedi, "The effect of heat treatment on the room and high temperature mechanical properties of AlSi10Mg alloy fabricated by selective laser melting," *J. Mater. Res. Technol.*, vol. 23, pp. 6039–6053, Mar. 2023, doi: 10.1016/j.jmrt.2023.02.086.

[148] C. Li, W. X. Zhang, H. O. Yang, J. Wan, X. X. Huang, and Y. Z. Chen, "Microstructural origin of high strength and high strain hardening capability of a laser powder bed fused AlSi10Mg alloy," *J. Mater. Sci. Technol.*, vol. 197, pp. 194–206, Oct. 2024, doi: 10.1016/j.jmst.2024.01.067.

[149] Y. Zhu and X. Wu, "Heterostructured materials," *Prog. Mater. Sci.*, vol. 131, p. 101019, 2023.

[150] F. Sajadi, J.-M. Tiemann, N. Bandari, A. Cheloee Darabi, J. Mola, and S. Schmauder, "Fatigue improvement of AlSi10Mg fabricated by laser-based powder bed fusion through heat treatment," *Metals*, vol. 11, no. 5, p. 683, 2021.

[151] M. Park *et al.*, "Effect of particle size distribution on the sidewall surface roughness of AlSi10Mg parts manufactured by laser powder bed fusion," *Results Eng.*, vol. 26, p. 105532, Jun. 2025, doi: 10.1016/j.rineng.2025.105532.

[152] J. Singh *et al.*, "Role of particle size distribution on microstructure, defects, and mechanical properties in laser-based powder bed fusion of Scalmalloy®," *J. Manuf. Sci. Eng.*, pp. 1–30, 2025.

[153] N. Rojas-Arias, L. Unti, D. Valim, A. Gabriel, E. Fonseca, and E. Lopes, "Microstructural Evolution of PBF-LB AlSi10Mg under Different Heat Treatment Conditions," *Mater. Res.*, vol. 28, no. Suppl 1, p. e20250146, 2025.

[154] A. Hadadzadeh, B. Shalchi Amirkhiz, A. Odeshi, J. Li, and M. Mohammadi, "Role of hierarchical microstructure of additively manufactured AlSi10Mg on dynamic loading behavior," *Addit. Manuf.*, vol. 28, pp. 1–13, Aug. 2019, doi: 10.1016/j.addma.2019.04.012.

[155] L. Song, L. Zhao, Y. Zhu, S. Liang, M. Huang, and Z. Li, "Uncovering the role of hierarchical and heterogeneous structures on strength anisotropy and strain localization of laser powder bed fusion AlSi10Mg," *J. Alloys Compd.*, vol. 1010, p. 178213, Jan. 2025, doi: 10.1016/j.jallcom.2024.178213.

[156] L. Song *et al.*, "How heterogeneous microstructure determines mechanical behavior of laser powder bed fusion AlSi10Mg," *Mater. Sci. Eng. A*, vol. 909, p. 146845, Sep. 2024, doi: 10.1016/j.msea.2024.146845.

[157] B. J. Mfusi, N. R. Mathe, L. C. Tshabalala, and P. A. Popoola, "The effect of stress relief on the mechanical and fatigue properties of additively manufactured AlSi10Mg parts," *Metals*, vol. 9, no. 11, p. 1216, 2019.

[158] S. Chen, X. Huang, L. Shuai, G. Wu, T. Huang, and X. Huang, "Annealing behavior of AlSi10Mg alloy fabricated by laser powder bed fusion," presented at the Journal of Physics: Conference Series, IOP Publishing, 2023, p. 012036.

[159] G. Di Egidio, L. Tonelli, M. Zanni, D. Carosi, A. Morri, and L. Ceschini, "Direct artificial aging of the PBF-LB AlSi10Mg alloy designed to enhance the trade-off between strength and residual stress relief," *J. Alloys Metall. Syst.*, vol. 5, p. 100063, Mar. 2024, doi: 10.1016/j.jalmes.2024.100063.

[160] S. Heilgeist, B. Heine, M. Merkel, L. Hitzler, Z. Javanbakht, and A. Öchsner, "The influence of post-heat treatments on the tensile strength and surface hardness of selectively laser-melted AlSi10Mg," *Mater. Werkst.*, vol. 50, no. 5, pp. 546–552, 2019.

[161] Z. Hu, Z. Zhao, X. Deng, Z. Lu, J. Liu, and Z. Qu, "Microstructure and mechanical behavior of TiCN reinforced AlSi10Mg composite fabricated by selective laser melting," *Mater. Chem. Phys.*, vol. 283, p. 125996, May 2022, doi: 10.1016/j.matchemphys.2022.125996.

[162] F. Alghamdi, X. Song, A. Hadadzadeh, B. Shalchi-Amirkhiz, M. Mohammadi, and M. Haghshenas, "Post heat treatment of additive manufactured AlSi10Mg: On silicon morphology, texture and small-scale properties," *Mater. Sci. Eng. A*, vol. 783, p. 139296, 2020.

[163] C. Gao, Z. Liu, Z. Xiao, W. Zhang, K. Wong, and A. H. Akbarzadeh, "Effect of heat treatment on SLM-fabricated TiN/AlSi10Mg composites: Microstructural evolution and mechanical properties," *J. Alloys Compd.*, vol. 853, p. 156722, Feb. 2021, doi: 10.1016/j.jallcom.2020.156722.

[164] A. Iturrioz, E. Gil, M. Petite, F. Garciandia, A. Mancisidor, and M. San Sebastian, "Selective laser melting of AlSi10Mg alloy: influence of heat treatment condition on mechanical properties and microstructure," *Weld. World*, vol. 62, pp. 885–892, 2018.

[165] E. Cerri and E. Ghio, "On the work-hardening behaviour of the additively manufactured Al-Si-Mg alloys: Composite-like versus networked microstructure," *Materialia*, vol. 38, p. 102282, Dec. 2024, doi: 10.1016/j.mtla.2024.102282.

[166] G. Di Egidio, C. Martini, J. Börjesson, E. Ghassemali, L. Ceschini, and A. Morri, "Influence of microstructure on fracture mechanisms of the heat-treated AlSi10Mg alloy produced by laser-based powder bed fusion," *Materials*, vol. 16, no. 5, p. 2006, 2023.

[167] L. Song *et al.*, "Microstructure and loading direction dependent hardening and damage behavior of laser powder bed fusion AlSi10Mg," *Mater. Sci. Eng. A*, vol. 832, p. 142484, Jan. 2022, doi: 10.1016/j.msea.2021.142484.

[168] J. Boban and A. Ahmed, "Defect mitigation and surface enhancement of additively manufactured AlSi10Mg internal features using electro-thermal post-treatment," *Mater. Lett.*, vol. 353, p. 135267, 2023.

[169] J. Toribio *et al.*, "Analysis of the Bauschinger effect in cold drawn pearlitic steels," *Metals*, vol. 10, no. 1, p. 114, 2020.

[170] J. B. Jordon, M. Horstemeyer, K. Solanki, and Y. Xue, "Damage and stress state influence on the Bauschinger effect in aluminum alloys," *Mech. Mater.*, vol. 39, no. 10, pp. 920–931, 2007.

[171] Y. Zhu *et al.*, "Heterostructured materials: superior properties from hetero-zone interaction," *Mater. Res. Lett.*, vol. 9, no. 1, pp. 1–31, 2021.

[172] Y. Qi, S. Li, and B. Gu, "Experimental analysis on Bauschinger effects under cryogenically cyclic loading of AA7075 alloy sheets in different heat treatment conditions," *Mater. Sci. Eng. A*, vol. 927, p. 147945, Apr. 2025, doi: 10.1016/j.msea.2025.147945.

[173] J. Li, G. Wang, M. Zhang, J. Li, X. Fang, and X. Ma, "Strengthening mechanisms of a heterostructured pure aluminum with extraordinary mechanical properties," *Mater. Charact.*, vol. 202, p. 113049, Aug. 2023, doi: 10.1016/j.matchar.2023.113049.

[174] J. Hu *et al.*, "Synergy of tensile strength and ductility in a novel additively manufactured Al-Mg-Mn-Er-Zr alloy with a trilevel equiaxed heterogeneous structure," *Virtual Phys. Prototyp.*, vol. 20, no. 1, p. e2440039, 2025.

[175] C. Shi, J. Lai, and X.-G. Chen, "Microstructural evolution and dynamic softening mechanisms of Al-Zn-Mg-Cu alloy during hot compressive deformation," *Materials*, vol. 7, no. 1, pp. 244–264, 2014.

[176] H. Zhang, G. Y. Lin, D. S. Peng, L. B. Yang, and Q. Q. Lin, "Dynamic and static softening behaviors of aluminum alloys during multistage hot deformation," *J. Mater. Process. Technol.*, vol. 148, no. 2, pp. 245–249, May 2004, doi: 10.1016/j.jmatprotec.2003.12.020.

[177] Q. Yang, X. Liu, Y. Liu, X. Fan, and M. Shu, "The flow softening behavior and deformation mechanism of AA7050 aluminum alloy," *Mater. Trans.*, vol. 60, no. 9, pp. 2041–2047, 2019.

[178] Y. Wu, H. Liao, J. Yang, and K. Zhou, "Effect of Si content on dynamic recrystallization of Al–Si–Mg alloys during hot extrusion," *J. Mater. Sci. Technol.*, vol. 30, no. 12, pp. 1271–1277, 2014.

[179] D. Hu, L. Wang, and H. Wang, "Dynamic recrystallization behavior and processing map of the 6082 aluminum alloy," *Materials*, vol. 13, no. 5, p. 1042, 2020.

[180] H. J. McQueen and W. Blum, "Dynamic recovery: sufficient mechanism in the hot deformation of Al (<99.99)," *Mater. Sci. Eng. A*, vol. 290, no. 1, pp. 95–107, Oct. 2000, doi: 10.1016/S0921-5093(00)00933-3.

[181] L. Kunčická and R. Kocich, "Structure development after twist channel angular pressing," *Acta Phys Pol A*, vol. 134, pp. 681–685, 2017.

[182] O. Hilšer *et al.*, "Study of the microstructure, tensile properties and hardness of AZ61 magnesium alloy subjected to severe plastic deformation," *Metals*, vol. 8, no. 10, p. 776, 2018.

List of Figures

List of Tables